

**The Search for Higgs Boson Production in Association  
with a Top-Quark Pair in  $pp$  Collisions at  $\sqrt{s} = 8$  TeV in  
the Lepton Plus Jets Final State**

John Garland Wood  
Charlottesville, VA

B.S., The University of California, Berkeley, 2008

A Dissertation presented to the Graduate Faculty  
of the University of Virginia in Candidacy for the Degree of  
Doctor of Philosophy

Department of Physics

University of Virginia  
May, 2015

## Abstract

The most important goal of the Large Hadron Collider (LHC) is to elucidate the mechanism of electroweak symmetry breaking. The Standard Model (SM) Higgs boson is thought to be a prime candidate for this. The newly discovered boson announced on July 4th, 2012, with a mass of  $\sim 125$  GeV/c $^2$ , has so far been shown to be consistent with a SM Higgs. However, the final confirmation of this new particle as the SM Higgs depends on subsequent measurements of all of its properties. The observation of this new particle in association with top-quark pairs would allow the couplings of this particle to top and bottom quarks to be directly measured.  $t\bar{t}H$  , with Higgs decaying to  $b\bar{b}$  is an excellent channel to explore due to the dominant branching ratio of Higgs to  $b\bar{b}$  and the kinematic handle the  $t\bar{t}$  system offers on the event. However, it presents a plethora of difficult challenges due to a low signal to background ratio and uncertainties on kinematically similar SM backgrounds. This work discusses the search for Higgs boson production in association with a top-quark pair in  $pp$  collisions at  $\sqrt{s} = 8$  TeV, collected by the Compact Muon Solenoid (CMS) experiment at the LHC. The search has been performed and published in two stages. The first analysis used the first 5.1 fb $^{-1}$ , and was followed up by the second analysis with the full 2012 dataset, using a total integrated luminosity of 19.5 fb $^{-1}$

We approve the dissertation of John Garland Wood.

Date of Signature

---

Supervisor: Dr. Christopher Neu

---

Committee Chair: Dr. Bradley Cox

---

Committee Member: Dr. Hank Thacker

---

PhD Committee Chair: Dr. Astronomy Person

# Contents

<b>Contents</b>	<b>iv</b>
<b>List of Figures</b>	<b>vii</b>
<b>List of Tables</b>	<b>xix</b>
<b>1 Introduction</b>	<b>1</b>
<b>2 Theoretical Background</b>	<b>4</b>
2.1 An Overview of Quantum Field Theory . . . . .	4
2.2 Abelian Gauge Theories of Particle Interactions . . . . .	7
2.3 Non-Abelian Gauge Theories of Particle Interactions . . . . .	9
2.4 The Higgs Mechanism in an Abelian Theory . . . . .	12
2.5 The Higgs Mechanism in a non-Abelian Theory . . . . .	14
2.6 Glashow Weinberg Salam Theory . . . . .	16
2.7 The Standard Model of Particle Physics . . . . .	22
2.8 Higgs Production in $pp$ Collisions at the LHC . . . . .	24
2.9 $t\bar{t}H$ Production in $pp$ Collisions at the LHC . . . . .	26
2.10 Background Processes to $t\bar{t}H$ . . . . .	27
2.11 Potential BSM Effects on $t\bar{t}H$ production . . . . .	30
<b>3 The Large Hadron Collider</b>	<b>32</b>
3.1 The LHC Accelerator Complex . . . . .	34
3.2 LHC Magnets . . . . .	42
3.3 LHC RF Technology . . . . .	48
3.4 The LHC Cryogen System . . . . .	51
3.5 The LHC Vacuum System . . . . .	52
<b>4 The Compact Muon Solenoid</b>	<b>54</b>
4.1 The Tracker . . . . .	56

4.1.1	The Silicon Pixel Detector . . . . .	58
4.1.2	The Silicon Strip Detector . . . . .	60
4.2	The Electromagnetic Calorimeter . . . . .	63
4.2.1	Vacuum Photo-Triodes . . . . .	67
4.2.2	Test Rig at UVa . . . . .	68
4.2.3	Results of UVa Tests . . . . .	69
4.3	The Hadronic Calorimeter . . . . .	72
4.4	Muon Chambers . . . . .	77
4.5	Data Collection Overview . . . . .	81
<b>5</b>	<b>Particle Reconstruction at CMS</b>	<b>85</b>
5.1	Iterative Tracking . . . . .	85
5.2	Calorimeter Clustering . . . . .	86
5.3	Calorimeter Energy Calibration . . . . .	87
5.4	Linking . . . . .	89
5.5	Physics Object Reconstruction . . . . .	90
5.5.1	Muon Reconstruction . . . . .	90
5.5.2	Electron Reconstruction . . . . .	91
5.5.3	Charged Hadron Reconstruction . . . . .	92
5.5.4	Photon and Neutral Hadron Reconstruction . . . . .	92
5.5.5	Jet Reconstruction . . . . .	93
5.5.6	Missing Transverse Energy Reconstruction . . . . .	95
<b>6</b>	<b>Analysis I: The first <math>5.08 \text{ fb}^{-1}</math> of 8 TeV data</b>	<b>97</b>
6.1	Data and Simulated Samples . . . . .	99
6.1.1	Data Samples . . . . .	100
6.1.2	Signal Samples . . . . .	101
6.1.3	Background Samples . . . . .	101
6.1.4	MC pileup reweighting . . . . .	102
6.1.5	Additional Pileup Corrections . . . . .	103
6.2	Event Selection . . . . .	105
6.2.1	Event cleaning . . . . .	105
6.2.2	Trigger . . . . .	106
6.2.3	Muon Selection . . . . .	106
6.2.4	Electron Selection . . . . .	107
6.2.5	Lepton selection and trigger efficiencies . . . . .	108

6.2.6	Jet selection . . . . .	109
6.2.7	<i>b</i> -tagging selection . . . . .	111
6.2.8	Lepton + Jets Selection . . . . .	113
6.3	Multivariate Analysis . . . . .	116
6.3.1	Artificial Neural Network Overview . . . . .	117
6.3.2	MVA Input Variables, Data to Monte Carlo Comparisons . . . . .	121
6.3.3	MVA Output, Data to Monte Carlo Comparisons . . . . .	138
6.4	Systematic Uncertainties . . . . .	140
6.5	Statistical Methods . . . . .	146
6.6	Results and Conclusions . . . . .	148
<b>7</b>	<b>Analysis II: The Complete <math>19.5 \text{ fb}^{-1}</math> of 8 TeV data</b>	<b>150</b>
7.1	Data and Simulated Samples . . . . .	150
7.1.1	Data Samples . . . . .	151
7.1.2	Signal Samples . . . . .	151
7.1.3	Background Samples . . . . .	151
7.1.4	MC pileup reweighting . . . . .	154
7.1.5	Top $p_T$ Reweighting . . . . .	154
7.2	Event Selection . . . . .	155
7.2.1	<i>b</i> -tag discriminant reweighting . . . . .	156
7.2.2	Lepton + Jets Selection . . . . .	157
7.3	Multivariate Analysis . . . . .	159
7.3.1	Boosted Decision Tree Overview . . . . .	159
7.3.2	MVA Input Variables, Data to Monte Carlo Comparisons . . . . .	161
7.3.3	MVA Output, Data to Monte Carlo Comparisons . . . . .	175
7.4	Systematic Uncertainties . . . . .	175
7.5	Statistical Methods . . . . .	183
7.6	Results and Conclusions . . . . .	185
<b>8</b>	<b>Analysis Improvements</b>	<b>187</b>
8.1	aMC@NLO, MadSpin, and Pythia8 Monte Carlo . . . . .	187
8.2	Analysis Techniques Under Development . . . . .	189
<b>Bibliography</b>		<b>193</b>
<b>List of Acronyms</b>		<b>202</b>

# List of Figures

1.1	The CMS experiment has observed a new boson at $m \sim 125 \text{ GeV}/c^2$ . . . . .	1
1.2	A Feynman diagram of the $t\bar{t}H$ process, with Higgs $\rightarrow b\bar{b}$ , and the $t\bar{t}$ -system decaying semi-leptonically . . . . .	3
2.1	Leading and Next to Leading Order Feynman diagrams for the coulomb scattering process . . . . .	6
2.2	The global average of $\alpha_s$ , the QCD coupling constant. . . . .	7
2.3	A visual representation of the Higgs potential . . . . .	12
2.4	Experimental milestones of the Standard Model . . . . .	23
2.5	Higgs production cross-sections at the LHC, for 7-14 TeV $pp$ collisions . . . . .	24
2.6	Feynman diagrams for the three largest Higgs production modes at the LHC . . . . .	25
2.7	Feynman diagram for $t\bar{t}H$ production . . . . .	26
2.8	Feynman diagrams for the semileptonic $t\bar{t}H$ process and its irreducible background, $t\bar{t} + b\bar{b}$ . . . . .	27
2.9	Feynman diagrams for the $t\bar{t}W$ and $t\bar{t}Z$ background processes . . . . .	28
2.10	Feynman diagrams for the single $t$ s,t, and $tW$ background processes . . . . .	28
2.11	Feynman diagrams for the $W, Z$ plus jets, and diBoson ( $WW, WZ, ZZ$ ) production. . . . .	29
2.12	Measurements of $t\bar{t}H$ backgrounds at CMS . . . . .	29
2.13	The cancellation of the divergent Higgs mass from a loop of top-quarks is cancelled by a loop of supersymmetric top-quarks, stop-quarks, . . . . .	31
3.1	Aerial view of the LHC complex, spanning the French-Swiss border [1] . . . . .	32
3.2	Integrated Luminosity delived to the CMS experiment from 2010-12 . . . . .	34
3.3	The LHC accelerator complex, taking protons from a bottle of Hydrogen at the Linac2, all the way to the LHC ring . . . . .	35
3.4	Features of the Linac2, the first stage of acceleration in the LHC injection chain . . . . .	36
3.5	Features of the PS booster, the second stage of the LHC injection chain . . . . .	37
3.6	Features of the PS, the third stage of the LHC injection chain . . . . .	40

3.7	Features of the SPS, the fourth and final stage of the LHC injection chain . . . . .	41
3.8	The LHC ring is divided into eight octants . . . . .	43
3.9	The single turn injection scheme. A septum magnet makes the initial alignment. The kicker magnet times the injection and makes the final alignment. Bumper magnets align the LHC beam with the injected beam. . . . .	44
3.10	Layout of Interaction Region 8, where one proton beam is injected into the LHC ring. A transfer line from the SPS bring a proton in from the right. In green, a septum magnet aligns the beam horizontally with the LHC. In blue, a kicker magnet makes the final vertical alignment into the LHC, and is timed to fill one of the 400 MHz buckets of the RF capture system . . . . .	44
3.11	The initial filling of 6 batches of protons from the PSB to the PS, leaves 12 empty buckets in the PS bunch structure. The rise time of the SPS magnet creates an additonal gap in the SPS bunch structure. Additional gaps emerge due to the rise time of the LHC injection and dumping kicker magnets . . . . .	45
3.12	Features of the dipole magnets used in the LHC . . . . .	46
3.13	Features of the dipole magnets used in the LHC . . . . .	47
3.14	Features of the 400 MHz superconducting RF system used in the LHC . . . . .	48
3.15	A klystron uses a weak RF signal coupled to a resonace cavity to bunch an electron beam, which in turn creates an amplified RF signal as it passes through a second resonance cavity tuned to the same frequency. . . . .	49
3.16	One of sixteen 300 kW, 400 MHz klystrons that power the superconducting RF cavities that accelerate the proton beam. . . . .	50
3.17	Layout of the five cryogenic islands, which are home to the eight facilities that provide liquid helium to the LHC . . . . .	51
3.18	Features of the 4.5 K refridgeration system . . . . .	51
3.19	Cross section schematic of the cryogenic distribution system in the LHC tunnel .	52
3.20	Beam screen for the LHC, with slits to allow for easy pumping of residual gas molecules in the beampipe. . . . .	53
4.1	A cutaway diagram of the CMS detector. Two humans are present at the bottom of the image to provide scale. . . . .	54
4.2	A slice of the CMS detector showing how various particles interact and deposit energy. The trajectory of charged particles is measured in the tracker; electrons and photons deposit most of their energy in the ECAL; charged and neutral hadrons deposit most of their energy in the HCAL; the muon chambers measures the trajectory of muons or long-lived charged particles . . . . .	55

4.3 A side view of the tracker. The pixel detector is the innermost sub-system, with three concentric rings of detectors in the barrel, and two in the endcap. The tracker inner barrel (TIB) is a silicon strip detector, with four concentric rings. The tracker inner disks (TID) are three layers deep. The tracker outer barrel (TOB) is six concentric rings and the tracker end caps (TEC) are nine layers deep.	57
4.4 A head-on view of the beamline and barrel components of the tracker. . . . .	57
4.5 The three barrel and two disk layers of the silicon pixel tracker provide coverage of $ \eta  < 2.5$ . . . . .	58
4.6 The readout electronics chain for the pixel detector . . . . .	59
4.7 In 2012 $pp$ collisions at $\sqrt{s} = 8$ TeV, the pixel detector performed with a resolution of $11.8 \mu\text{m}$ . The above is a plot of the residual difference between a pixel and the results of a fit to a particle track. . . . .	60
4.8 A silicon strip module, with two $500 \mu\text{m}$ thick sensors. . . . .	61
4.9 Schematic of the readout sequence of the silicon strip detector. . . . .	62
4.10 Measurements of the performance of the silicon strip track using $pp$ collisions from 2011 at $\sqrt{s} = 7$ TeV . . . . .	62
4.11 Layout of the ECAL sub-detector . . . . .	63
4.12 Typical Lead Tungstate crystal, with APD attached to the rear face in the left frame, and a VPT attached in the right frame. . . . .	63
4.13 A simulation of the evolution of an electromagnetic shower being initiated by an electron entering the center of the front face. . . . .	64
4.14 A module of 500 crystals (25 crystals wide by 20 crystal tall). . . . .	65
4.15 Schematic of the On-Detector Readout for the ECAL . . . . .	66
4.16 A section of the ECAL end-cap, a Dee. Two Dees form a disk with an inner bore for the beam-line to pass through. 5x5 modules, or supercrystals, are mounted in preparation for installation at CMS . . . . .	67
4.17 Vacuum Photo-Triode devices used in the ECAL end-caps (EE) . . . . .	67
4.18 Features of the UVa VPT test stand . . . . .	70
4.19 3 runs of 5 VPTs, exposed to blue LED light, and fit to a sum of two exponentials. . . . .	71
4.20 3 runs of 5 VPTs, exposed to orange LED light, and fit to a sum of two exponentials. . . . .	72
4.21 Longitudinal cross-section of the HCAL with the four sub-systems labeled . . . . .	73

4.22 Closeup of the HCAL barrel section. The center section of each of the 18 wedges are labeled, optical cables lay accross the joint of the center and staggered edge sections of each wedge. The blue lines show the apporximate azimuthal division of the wedge. . . . .	74
4.23 Over 1 million Russian shells of military artillery were re-processed in the construction of the HCAL . . . . .	75
4.24 Optical readout chain of the HCAL scintillator tiles . . . . .	75
4.25 HCAL endcap, 18 azimuthal divisions of alternating layers of brass and plastic scintillator. . . . .	76
4.26 Longitudinal cross-section of the HCAL forward calorimetry, the HF . . . . .	76
4.27 Longitudinal cross-section of one of the 5 wheels of the muon system. Drift tubes are placed in 4 concentric layers, with 2 being placed inside the return yoke of the magnet, and 12 azimuthal divisions. . . . .	78
4.28 A cross-section view of a drift cell. The anode wire is held at 3600 V, creating a potential difference with the walls. Electric field lines are shown in blue. . . . .	79
4.29 RPC layout for the barrel and endcaps . . . . .	79
4.30 Exploded diagram of an RPC . . . . .	80
4.31 Cross-section of one quarter of the muon endcap system, with the 4 disks of CSC systems shown in red . . . . .	80
4.32 A CSC station with 7 layers, making 6 gas chambers. Cathode strips are shown in yellow, perpendicular to the vertical anode wires in orange. . . . .	81
4.33 A block diagram of the L1 trigger . . . . .	82
4.34 A schematic of the $e/\gamma$ trigger algorithm . . . . .	82
4.35 Layout of the CMS DAQ . . . . .	83
 5.1 Results of the uncertainty on the ECAL intercalibration coefficients for the barrel (left) and endcaps (right) . . . . .	88
5.2 Instantaneous luminosity response to the crystals as measured by the laser and LED system. Additional crystal calibration constants are derived to normalize the crystal reponse over the range of collected data . . . . .	89
5.3 Results of using a $\chi^2$ minimization procedure to estimate the neutral hadron energy contribution in the HCAL using simulated events . . . . .	90
5.4 Muon validation plots for the particle-flow reconstruction . . . . .	91
5.5 Electron validation plots for the particle-flow reconstruction . . . . .	92
5.6 The anti-kt jet clustering algorithm with distance parameter R=1.0 . . . . .	93

5.7	Commissioning of the particle-flow algorithm on jets, involved comparing the energy measured from charged hadron tracks, to energy measured in calorimeter clusters linked to the tracks . . . . .	94
5.8	A $b$ -meson will travel a distance $L_{xy}$ before decaying and creating a secondary vertex. The impact parameter, $d_0$ measures the longitudinal displacement of the two vertices . . . . .	95
6.1	This figure shows the breakdown of jet-to-parton assignments for the two jets with the minimum $\Delta R$ separation in the event for events with greater or equal 4 $b$ -tagged jets. . . . .	98
6.2	Comparison of number of reconstructed vertices for data (black) and the $t\bar{t}$ MC sample before (blue) and after (red) pileup reweighting. After pileup reweighting, the MC matches the data well. . . . .	103
6.3	$H_T$ distribution for 8 TeV lepton plus jet events with $\geq 4$ jets and $\geq 2$ tags shown for different amounts of pileup. The left-hand plot shows low pileup, the middle plot shows medium pileup, and the right-hand plot shows high pileup. . . . .	104
6.4	$H_T$ distribution for 8 TeV lepton plus jet events with $\geq 4$ jets and $\geq 2$ tags. The left-hand plot shows the distribution before correction. The right-hand plot shows the distribution after correction. Note that the ratio in the right-hand plot is flatter than the left-hand plot. . . . .	105
6.5	Muon and electron ID, isolation selection and trigger efficiency scale factors in bins of $p_T$ and $\eta$ . . . . .	109
6.6	Number of jets (left) and number of $b$ -tagged jets (right) in data and simulation for events with $\geq 4$ jets + $\geq 2$ $b$ -tags in the lepton+jets channel at 8 TeV. The background is normalized to the SM expectation; the uncertainty band (shown as a hatched band in the stack plot and a green band in the ratio plot) includes statistical and systematic uncertainties that affect both the rate and shape of the background distributions. The $t\bar{t}H$ signal ( $m_H = 125 \text{ GeV}/c^2$ ) is normalized to $30 \times$ SM expectation. . . . .	116
6.7	A simple example of a MLP type ANN, with one layer of input neurons that make connections to a hidden layer, which is connected to the output layer . . . . .	117
6.8	The CFMlpANN architechture used in this analysis features two hidden layers, and 10 input variables for each jet/tag category (11 variables for the $\geq 6$ jets, $\geq 4$ $b$ -tags category) . . . . .	118
6.9	Comparisons of the testing and training samples used to optimize the CFMlpANN weights for each jet/tag category . . . . .	120

6.10 Lepton + jets data/MC comparison for the $\geq 6$ jets + 2 tag category. The uncertainty band includes statistical and systematic uncertainties that affect both the rate and shape of the background distributions. . . . .	125
6.11 Lepton + jets data/MC comparison for the $\geq 6$ jets + 2 tag category. The uncertainty band includes statistical and systematic uncertainties that affect both the rate and shape of the background distributions. . . . .	126
6.12 Lepton + jets data/MC comparison for the 4 jets + 3 tag category. The uncertainty band includes statistical and systematic uncertainties that affect both the rate and shape of the background distributions. . . . .	127
6.13 Lepton + jets data/MC comparison for the 4 jets + 3 tag category. The uncertainty band includes statistical and systematic uncertainties that affect both the rate and shape of the background distributions. . . . .	128
6.14 Distributions of the five ANN input variables with rankings 1 through 5, in terms of separation, for the 5 jets + 3 b-tags category of the lepton+jets channel at 8 TeV. Definitions of the variables are given in the text. The background is normalized to the SM expectation; the uncertainty band (shown as a hatched band in the stack plot and a green band in the ratio plot) includes statistical and systematic uncertainties that affect both the rate and shape of the background distributions. The $t\bar{t}H$ signal ( $m_H = 125 \text{ GeV}/c^2$ ) is normalized to the total background yield, for easier comparison of the shapes. . . . .	129
6.15 Distributions of the five ANN input variables with rankings 6 through 10, in terms of separation, for the 5 jets + 3 b-tags category of the lepton+jets channel at 8 TeV. Definitions of the variables are given in the text. The background is normalized to the SM expectation; the uncertainty band (shown as a hatched band in the stack plot and a green band in the ratio plot) includes statistical and systematic uncertainties that affect both the rate and shape of the background distributions. The $t\bar{t}H$ signal ( $m_H = 125 \text{ GeV}/c^2$ ) is normalized to the total background yield, for easier comparison of the shapes. . . . .	130
6.16 Lepton + jets data/MC comparison for the $\geq 6$ jets + 3 tag category. The uncertainty band includes statistical and systematic uncertainties that affect both the rate and shape of the background distributions. . . . .	131
6.17 Lepton + jets data/MC comparison for the $\geq 6$ jets + 3 tag category. The uncertainty band includes statistical and systematic uncertainties that affect both the rate and shape of the background distributions. . . . .	132

6.18 Lepton + jets data/MC comparison for the 4 jets + 4 tag category. The uncertainty band includes statistical and systematic uncertainties that affect both the rate and shape of the background distributions. . . . .	133
6.19 Lepton + jets data/MC comparison for the 4 jets + 4 tag category. The uncertainty band includes statistical and systematic uncertainties that affect both the rate and shape of the background distributions. . . . .	134
6.20 Lepton + jets data/MC comparison for the 5 jets + 4 tag category. The uncertainty band includes statistical and systematic uncertainties that affect both the rate and shape of the background distributions. . . . .	135
6.21 Lepton + jets data/MC comparison for the 5 jets + 4 tag category. The uncertainty band includes statistical and systematic uncertainties that affect both the rate and shape of the background distributions. . . . .	136
6.22 Lepton + jets data/MC comparison for the $\geq 6$ jets + 4 tag category. The uncertainty band includes statistical and systematic uncertainties that affect both the rate and shape of the background distributions. . . . .	137
6.23 Lepton + jets data/MC comparison for the $\geq 6$ jets + 4 tag category. The uncertainty band includes statistical and systematic uncertainties that affect both the rate and shape of the background distributions. . . . .	138
6.24 The distributions of the CFMlpANN output for lepton+jets events at 8 TeV in the various analysis categories. Background-like events have a low CFMlpANN output value. Signal-like events have a high CFMlpANN output value. The background is normalized to the SM expectation; the uncertainty (shown as a hatched band in the stack plot and a green band in the ratio plot) includes statistical and systematic uncertainties that affect both the rate and shape of the background distributions. The $t\bar{t}H$ signal ( $m_H = 125 \text{ GeV}/c^2$ ) is normalized to $30 \times \text{SM}$ expectation. . . . .	139
6.25 Comparison of the MVA discriminator for JES shift upwards (red) and downwards (blue) relative to the nominal (black) shape for the $t\bar{t}H(120)$ signal (left) and the main background sample $t\bar{t}+$ light flavor (right). The plots shown are from the $\geq 6$ jet $\geq 4$ tag category in the lepton+jets channel. All plots are normalized to unit area. . . . .	141

6.26 Comparison of the MVA discriminator for $b$ -tag scale factor shift upwards (red) and downwards (blue) relative to the nominal (black) shape for the $t\bar{t}H(120)$ signal (left) and the main background sample $t\bar{t} + \text{light flavor}$ (right). The plots are from the $\geq 6$ jets + $\geq 4$ tags category in the lepton+jets channel. All plots are normalized to unit area. . . . .	142
6.27 Comparison of the MVA discriminator for additional PU correction systematic upwards (red) and downwards (blue) relative to the nominal (black) shape for the $t\bar{t}H(120)$ signal (left) and the main background sample $t\bar{t} + \text{light flavor}$ (right). The plots are from the $\geq 6$ jets + $\geq 4$ tags category in the lepton+jets channel. All plots are normalized to unit area. . . . .	143
6.28 The rate and shape variations for selected categories due to the $Q^2$ uncertainty. . . . .	145
6.29 A dedicated CFMlpANN trained to isolate $t\bar{t} + b\bar{b}$ from $t\bar{t} + \text{jets}$ . The left plot shows is for the case of nominal $t\bar{t} + b\bar{b}$ cross-section, the right plot shows the case for $x2 t\bar{t} + b\bar{b}$ cross-section. The left-most region of both plots is the most sensitivite to the $t\bar{t}+b\bar{b}$ normalization, and shows no significant improment in data to MC agreement, justifying the reasoning that an uncertainty larger than 50% is needed. . . . .	146
6.30 The expected and observed 95% CL upper limits on the signal strength parameter $\mu = \sigma/\sigma_{SM}$ for the lepton+jets channel using the 2012 dataset. These limits were extracted using the asymptotic method. . . . .	149
7.1 Comparison of number of reconstructed vertices for data (black) and the sum of all background MC samples before (red) and after (blue) pileup reweighting. After pileup reweighting, the MC matches the data well. . . . .	154
7.2 The scale factors from top differential crosse section group, the fitting as well as the $\pm 1\sigma$ variations. . . . .	155
7.3 Leading jet $p_T$ distribution for 8 TeV lepton plus jet events with $\geq 4$ jets and $\geq 2$ tags. The left-hand plot shows the distribution before top $p_T$ reweighting. The right-hand plot shows the distribution after top $p_T$ reweighting. Note that the ratio in the right-hand plot is flatter than the left-hand plot. . . . .	156
7.4 Comparison of yields for the different categories (top), number of jets (bottom left), and number of tagged jets (bottom right) in data and Monte Carlo for events with one lepton $\mu$ or $e$ , $\geq 4$ jets and $\geq 2$ tags. . . . .	158
7.5 Example of a decision tree, which chooses a set of variables to cut on, in order to produce a region of events with high signal purity . . . . .	160

7.6 Comparisons of the testing and training samples used to optimize the BDT weights for each jet/tag category . . . . .	162
7.7 Data/MC comparisons for events with one lepton and $\geq 6$ jets + 2b- tags. The uncertainty band includes statistical and systematic uncertainties that affect both the rate and shape of the background distributions. . . . .	165
7.8 Data/MC comparisons for events with one lepton and 4 jets + 3 b-tags. The uncertainty band includes statistical and systematic uncertainties that affect both the rate and shape of the background distributions. . . . .	166
7.9 Data/MC comparisons for events with one lepton and 5 jets + 3 b-tags. The uncertainty band includes statistical and systematic uncertainties that affect both the rate and shape of the background distributions. . . . .	167
7.10 Data/MC comparisons for events with one lepton and $\geq 6$ jets + 3 b-tags. The uncertainty band includes statistical and systematic uncertainties that affect both the rate and shape of the background distributions. . . . .	168
7.11 Data/MC comparisons for events with one lepton and $\geq 6$ jets + 3 b-tags. The uncertainty band includes statistical and systematic uncertainties that affect both the rate and shape of the background distributions. . . . .	169
7.12 Data/MC comparisons for events with one lepton and 4 jets + 4 b-tags. The uncertainty band includes statistical and systematic uncertainties that affect both the rate and shape of the background distributions. . . . .	170
7.13 Data/MC comparisons for events with one lepton and 5 jets + $\geq 4$ b-tags. The uncertainty band includes statistical and systematic uncertainties that affect both the rate and shape of the background distributions. . . . .	171
7.14 Data/MC comparisons for events with one lepton and 5 jets + $\geq 4$ b-tags. The uncertainty band includes statistical and systematic uncertainties that affect both the rate and shape of the background distributions. . . . .	172
7.15 Data/MC comparisons for events with one lepton and $\geq 6$ jets + $\geq 4$ b-tags. The uncertainty band includes statistical and systematic uncertainties that affect both the rate and shape of the background distributions. . . . .	173
7.16 Data/MC comparisons for events with one lepton and $\geq 6$ jets + $\geq 4$ b-tags. The uncertainty band includes statistical and systematic uncertainties that affect both the rate and shape of the background distributions. . . . .	174

7.17 Final BDT output for lepton + jet events. Background-like events have a low BDT output value. Signal-like events have a high BDT output value. The uncertainty band includes statistical and systematic uncertainties that affect both the rate and shape of the background distributions. The top, middle and, bottom rows are events with 4, 5, and $\geq 6$ jets, respectively, while the left, middle, and right-hand columns are events with 2, 3, and $\geq 4$ b-tags, respectively. The $t\bar{t}H$ signal ( $m_H = 125$ GeV) is normalized to $30 \times$ SM expectation. . . . .	176
7.18 Comparison of the MVA discriminator for JES shift upwards (red) and downwards (blue) relative to the nominal (black) shape for the $t\bar{t}H(125)$ signal (left) and the main background sample $t\bar{t} + b\bar{b}$ (right). The plots are from the $\geq 6$ jet $\geq 4$ tag category in the lepton+jets channel. All plots are normalized to unit area. . . . .	177
7.19 Comparison of the MVA discriminator when shifting the light flavor contamination in the heavy flavor scale factor determination shift upwards (red) and downwards (blue) relative to the nominal (black) shape for the $t\bar{t}H(125)$ signal (top row) and $t\bar{t} + b\bar{b}$ and $t\bar{t} + \text{LF}$ background samples (middle row and bottom row respectively). The plots are from the LJ $\geq 6$ jet $\geq 4$ category. All plots are normalized to unit area. . . . .	178
7.20 Comparison of the MVA discriminator when shifting the heavy flavor contamination in the light flavor scale factor determination shift upwards (red) and downwards (blue) relative to the nominal (black) shape for the $t\bar{t}H(125)$ signal (top row) and $t\bar{t} + b\bar{b}$ and $t\bar{t} + \text{LF}$ background samples (middle row and bottom row respectively). The plots are from the LJ $\geq 6$ jet $\geq 4$ category. All plots are normalized to unit area. . . . .	178
7.21 Comparison of the MVA discriminator when shifting to account for the statistical uncertainty on the heavy flavor scale factor extraction. Two classes of distortion in the scale factor are considered: linear distortions (labeled “Stat. Error 1”) and nonlinear distortions (labeled “Stat. Error 2”). Both shift upwards (red) and downwards (blue) relative to the nominal (black) shape for the $t\bar{t}H(125)$ signal (top row) and $t\bar{t} + b\bar{b}$ and $t\bar{t} + \text{LF}$ background samples (middle row and bottom row respectively) are shown. The plots are from the $\geq 6$ jet $\geq 4$ category. All plots are normalized to unit area. . . . .	179

7.22 Comparison of the MVA discriminator when shifting to account for the statistical uncertainty on the light flavor scale factor extraction. Two classes of distortion in the scale factor are considered: linear distortions (labeled “Stat. Error 1”) and nonlinear distortions (labeled “Stat. Error 2”). Both shift upwards (red) and downwards (blue) relative to the nominal (black) shape for the $t\bar{t}H(125)$ signal (top row) and $t\bar{t} + b\bar{b}$ and $t\bar{t} + \text{LF}$ background samples (middle row and bottom row respectively) are shown. The plots are from the $\geq 6$ jet $\geq 4$ category. All plots are normalized to unit area. . . . .	179
7.23 Comparison of the MVA discriminator when shifting to account for the uncertainty on the charm jets scale factor extraction. Two classes of distortion in the scale factor are considered: linear distortions (labeled “Error 1”) and nonlinear distortions (labeled “Error 2”). Both shift upwards (red) and downwards (blue) relative to the nominal (black) shape for the $t\bar{t}H(125)$ signal (top row) and $t\bar{t} + c\bar{c}$ and $t\bar{t} + \text{LF}$ background samples (middle row and bottom row respectively) are shown. The plots are from the $\geq 6$ jet $\geq 4$ category. All plots are normalized to unit area. . . . .	180
7.24 Comparison of the MVA discriminator for shifts in top quark $p_T$ reweighting upwards (red) and downwards (blue) relative to the nominal (black) shape for the $t\bar{t} + \text{LF}$ background (left) and the $t\bar{t} + b\bar{b}$ (right). The plots are from the $\geq 6$ jets $+ \geq 4$ tags category in the lepton+jets channel. All plots are normalized to unit area. . . . .	181
7.25 Comparison of the MVA discriminator when shifting the $Q^2$ scale up and down by its uncertainties. Shown are the shift upwards (red) and downwards (blue) relative to the nominal (black) shape for the $t\bar{t} + b\bar{b}$ (top row) $t\bar{t} + b$ (middle row) and $t\bar{t} + \text{LF}$ (bottom) background samples. The plots are from the $\text{LJ} \geq 6$ jet $\geq 4$ category. All plots are normalized to unit area. . . . .	182
7.26 The expected and observed 95% CL upper limits on the signal strength parameter $\mu = \sigma/\sigma_{SM}$ for the lepton+jets channel using the 2012 dataset. These limits were extracted using the asymptotic method. . . . .	185
8.1 The number of reconstructed jets passing selection (left) and that have additionally been $b$ -tagged (right) for $t\bar{t}H$ , $t\bar{t} + jets$ , and $t\bar{t} + b\bar{b}$ samples generated with the aMC@NLO and Pythia 8 framework . . . . .	189
8.2 The invariant mass of the $W$ boson in the $t\bar{t}$ decay for the case of the MC truth (red), correctly associated reconstructed jets (blue), and incorrectly associated reconstructed jets (green) . . . . .	190

8.3	The cosine of the angle between the momentum three-vectors for the $b$ -quarks from the top decays (left), the lepton and the up-type $W$ boson daughter (center), and the lepton and the down-type $W$ boson daughter (right) . . . . .	190
8.4	The difference in the $\phi$ coordinate between the momentum three-vectors for the $b$ -quarks from the top decays (left), the lepton and the up-type $W$ boson daughter (center), and the lepton and the down-type $W$ boson daughter (right) . . . . .	191
8.5	Jet times lepton charge, for the $b$ -jet associated with the same top as the lepton. Green shows incorrectly associated reconstructed jets, blue shows correctly associated jets, and red is the MC truth . . . . .	192

# List of Tables

2.1	The quantum numbers Isospin and Hypercharge are assigned for each of the $SU(2)$ and $U(1)$ symmetries respectively . . . . .	20
4.1	Fit Results for VPT Conditioning Studies at U.Va. and Brunel, Blue Reference LED . . . . .	71
4.2	Fit Results for VPT Conditioning Studies at U.Va., Orange LED . . . . .	72
6.1	The datasets analyzed for this analysis. . . . .	101
6.2	List of signal MC datasets and cross sections used to determine the SM expectation. . . . .	101
6.3	List of background MC datasets and cross sections used for normalization. . . . .	102
6.4	List of lepton+jets triggers . . . . .	106
6.5	Tight and loose muon definition . . . . .	108
6.6	Tight and loose muon definition . . . . .	108
6.7	Jet definition . . . . .	110
6.8	Jet Energy Resolution (JER) scale factors . . . . .	110
6.9	Expected event yields in $5 \text{ fb}^{-1}$ for signal and backgrounds in the $\mu+\text{jets}$ channel. . . . .	114
6.10	Expected event yields in $5 \text{ fb}^{-1}$ for signal and backgrounds in the $e+\text{jets}$ channel. . . . .	114
6.11	Expected event yields in $5 \text{ fb}^{-1}$ for signal and backgrounds in the $\mu+\text{jets}$ channel. . . . .	115
6.12	The ANN inputs for the nine jet-tag categories in the 8 TeV $t\bar{t}H$ analysis in the lepton+jets and dilepton channels. The choice of inputs is optimized for each category. Definitions of the variables are given in the text. The best input variable for each jet-tag category is denoted by $\star$ . . . . .	122
6.13	Summary of the systematic uncertainties considered on the inputs to the limit calculation. Except where noted, each row in this table will be treated as a single, independent nuisance parameter. . . . .	140
6.14	Relative yield change due to JES shift up/down for the $\geq 6$ jets + $\geq 4$ tags category in the lepton+jets channel. . . . .	141

6.15 Relative yield change due to $b$ -tag scale factor shift up/down for the $\geq 6$ jets + $\geq 4$ tags category in the lepton+jets channel. . . . .	142
6.16 Cross section uncertainties used for the limit settings. Each column in the table is an independent source of uncertainty, except for the last column which represents uncertainties uncorrelated with any others. Uncertainties in the same column for two different processes (different rows) are completely correlated. . . . .	144
6.17 Expected and observed upper limits for SM Higgs for lepton + jets channel using the first $5.1 \text{ fb}^{-1}$ of the 2012 dataset. These limits were extracted using the asymptotic method. . . . .	148
7.1 The datasets analyzed for this analysis. . . . .	151
7.2 List of signal MC datasets and cross sections used to determine the SM expectation.	152
7.3 List of background MC datasets and cross sections used for normalization. . . . .	153
7.4 Observed data event yields, expected event yields in $19.5 \text{ fb}^{-1}$ for signal and backgrounds in the lepton+jets channel. . . . .	158
7.5 Event variables used in dilepton and lepton+jets BDT training and their descriptions. . . . .	163
7.6 BDT input variable assignments for the lepton+jets categories. . . . .	164
7.7 List of variables used as inputs in each of the ttbb/ttH BDTs. See table 7.5 for definitions. . . . .	164
7.8 Relative yield change due to JES shift up/down for the $\geq 3$ tag category in the dilepton channel and the $\geq 6$ jets + $\geq 4$ tags category in the lepton+jets channel. . . . .	175
7.9 This table summarizes the rate effect of the six independent nuisance parameters that characterize the $b$ -tag uncertainties. (Note: The $b$ -tag rate uncertainties associated with JES variations are already included with the JES rate uncertainties in Table 6.14. The impact of statistical uncertainties is in the heavy-flavor and light-flavor scale factor extraction is incorporated using two separate nuisance parameters, as described above. The uncertainty labeled “Stat. Err. 1” represents statistical uncertainties resulting a linear distortion of the CSV scale factor, while the one labeled “Stat. Err. 2” corresponds to nonlinear distortions. . . . .	180
7.10 Relative yield change due to varying the top quark $p_T$ reweighting. The “up” variation corresponds to apply twice as much correction to the top quark $p_T$ distribution as the nominal, while the “down” correction corresponds to applying no correction to the default MC top quark $p_T$ distribution. . . . .	181

7.11 Cross section uncertainties used for the limit settings. Each column in the table is an independent source of uncertainty, except for the last column which represents uncertainties uncorrelated with any others. Uncertainties in the same column for two different processes (different rows) are completely correlated. . . . .	182
7.12 This table summarizes the rate effect of shifting $Q^2$ scale uncertainty for Madgraph. Note that the shifts are made independently for the following topologies: $t\bar{t} + 0p$ , $t\bar{t} + 1p$ , $t\bar{t} + 2p$ , $t\bar{t} + c\bar{c}$ , $t\bar{t} + b$ , and $t\bar{t} + b\bar{b}$ . . . . .	182
7.13 Summary for the of the systematic uncertainties considered on the inputs to the limit calculation. Except where noted, each row in this table will be treated as a single, independent nuisance parameter. . . . .	183
7.14 Specific effect of systematics on predicted background yields for events with $\geq 6$ jets and $\geq 4$ b-tags. Here we only consider the sum of the largest backgrounds, $t\bar{t} + lf$ , $t\bar{t} + b$ , $t\bar{t} + b\bar{b}$ , and $t\bar{t} + c\bar{c}$ . These three backgrounds account for 94% of all background events. The signal is 3.5% of the yield of the three main backgrounds. The signal fraction is directly comparable to the variations of the background in the table. The table shows that the signal is much smaller than many of the background variations. . . . .	184
7.15 Expected and observed upper limits for SM Higgs for lepton + jets channel using the 2012 dataset. These limits were extracted using the asymptotic method. . . . .	185



# <sup>1</sup> Chapter 1

## <sup>2</sup> Introduction

<sup>3</sup> On July 4th, 2012, the Compact Muon Solenoid (CMS) and A Toroidal LHC Apparatus (ATLAS)  
<sup>4</sup> experiments announced the discovery of a new boson of mass  $\sim 125 \text{ GeV}/c^2$  [2] [3]. The particle  
<sup>5</sup> has been shown to be increasingly consistent with the description of the boson predicted by the  
<sup>6</sup> Higgs mechanism of the SM, as measurements on its mass, width, and quantum numbers are  
<sup>7</sup> completed. However, there are several properties of this new boson, which remain to be tested.  
<sup>8</sup> Figure 1.1 shows a consistent mass peak between the  $H \rightarrow ZZ$  and  $H \rightarrow \gamma\gamma$  channels at the  
<sup>9</sup> CMS experiment.

<sup>10</sup> The Yukawa coupling of the Higgs boson to the top-quark in the SM is the largest coupling  
<sup>11</sup> among the fundamental particles and is well predicted - thus offering an excellent test of the  
<sup>12</sup> nature of the coupling of the Higgs to fermions, as well as a potential probe into physics Beyond  
<sup>13</sup> the Standard Model (BSM) that would alter this value from the SM prediction. The production  
<sup>14</sup> of the Higgs boson in association with top-quark pairs is the best production mode at the LHC  
<sup>15</sup> that offers direct access to the top-Higgs coupling. The dominant production mode of Higgs  
<sup>16</sup> at the LHC, gluon-gluon fusion, involves a triangle loop of strongly-coupled fermions, which

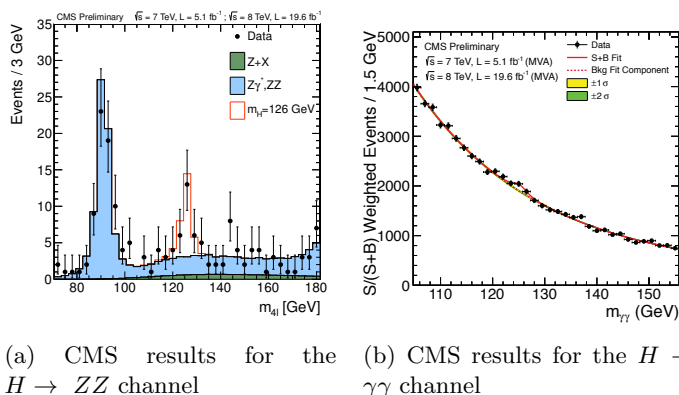


Figure 1.1: The CMS experiment has observed a new boson at  $m \sim 125 \text{ GeV}/c^2$

<sup>17</sup> includes all of the other quarks, as well as the potential for BSM particles.

<sup>18</sup>       $t\bar{t}H$  production also has the ability to constrain some extensions of the SM that would not  
<sup>19</sup> modify the Higgs branching fractions enough to be seen within current experimental precision.  
<sup>20</sup> Such models include Little Higgs models, models with extra dimensions, top-color models, and  
<sup>21</sup> composite Higgs models that introduce a vector-like top partner, a  $t'$ , that can decay to  $tH$ ,  
<sup>22</sup>  $bW$ , or  $tZ$  states. Both  $t't'$  and  $t't$  production would produce a  $t\bar{t}H$  final state, or one that is  
<sup>23</sup> indistinguishable from it ( $tHbW$ ). Upper limits on  $t\bar{t}H$  production would also provide limits  
<sup>24</sup> on the previously described models, which would be complementary to existing direct searches  
<sup>25</sup> for  $t'$  particles, which attempt to reconstruct the  $t'$  resonance.

<sup>26</sup>      The  $t\bar{t}H$  channel has a rich set of possible final states. Each top-quark will decay to a  
<sup>27</sup>  $b$ -quark and a  $W$  boson. The  $W$  boson will subsequently decay to two quarks, or a lepton and  
<sup>28</sup> a neutrino. These decays are classified as either hadronic, semi-leptonic, or di-leptonic for zero,  
<sup>29</sup> one, or both  $t$  quarks decaying leptonically respectively. The Higgs may decay to  $b$ -quark,  $W$ ,  
<sup>30</sup>  $Z$ ,  $\tau$ , or  $\gamma$  pairs. In fact, this is one of the only production modes at the LHC which has access  
<sup>31</sup> to every Higgs decay mode, as other production mechanisms are swamped by large backgrounds  
<sup>32</sup> preventing measurements of all Higgs decay types.

<sup>33</sup>      The search is performed with the CMS experiment, a modern, general purpose particle  
<sup>34</sup> detector capable of reconstructing and identifying hadronic jets, photons, electrons, muons,  
<sup>35</sup> and tau leptons. The hermetic design, and its high precision and efficiency in reconstructing  
<sup>36</sup> and tracking every particle in a  $pp$  collision, also makes it suitable for reconstructing missing  
<sup>37</sup> transverse energy from the calculated momentum imbalance of all of the measured particles in  
<sup>38</sup> the event. This missing transverse energy is often the signature of a neutrino, which is the  
<sup>39</sup> only SM particle capable of escaping detection. The detector uses a 3.8 T axial magnetic field,  
<sup>40</sup> produced by the solenoid it is named after, to bend charged particles as they travel through  
<sup>41</sup> the detector. The measured curvature of their tracks allows the momentum of the particles to  
<sup>42</sup> be calculated with to a high precision. Tracks are formed and particles are reconstructed by a  
<sup>43</sup> combination of sub-detector systems which work together to form the final reconstructed  
<sup>44</sup> image of each particle in the collision.

<sup>45</sup>      This thesis will focus on a semi-leptonic decay of the top-quarks, with the Higgs decaying to a  
<sup>46</sup>  $b$ -quark pair. Figure 1.2 is Feynman diagram of the  $t\bar{t}H$  process. The largest background to this  
<sup>47</sup> process is top-quark pair production with extra jets originating from Initial State Radiation (ISR)  
<sup>48</sup> or Final State Radiation (FSR) radiation,  $t\bar{t} + jets$ . The irreducible background is formed by  
<sup>49</sup> top-quark pairs, where a gluon is radiated and decays to  $b$ -quark pairs,  $t\bar{t} + b\bar{b}$ . In addition to the  
<sup>50</sup> large backgrounds, the high jet multiplicity in the  $t\bar{t}H$  final state gives rise to a combinatorics  
<sup>51</sup> problem in associating each jet with its role in the  $t\bar{t}H$  system. This inevitably leads to

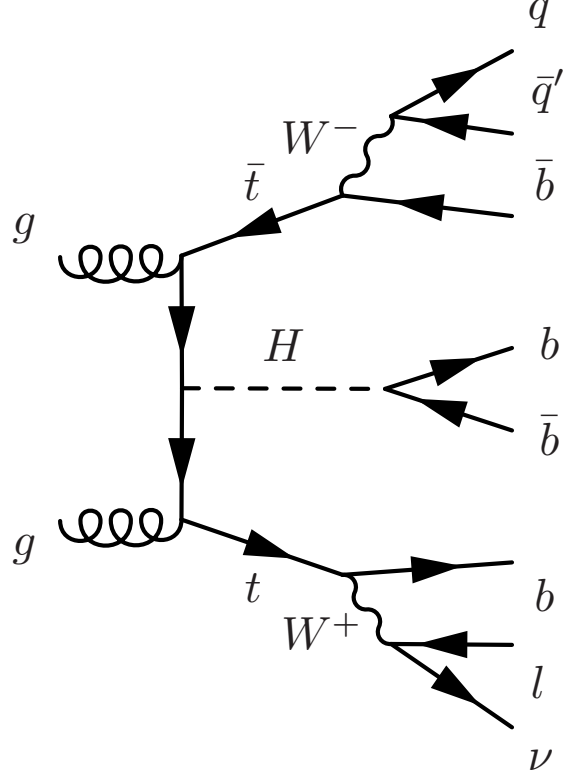


Figure 1.2: A Feynman diagram of the  $t\bar{t}H$  process, with  $H \rightarrow b\bar{b}$ , and the  $t\bar{t}$ -system decaying semi-leptonically

misidentifying which jets are the decay product of the Higgs, and thus additionally smears out the resolution on the mass of the Higgs. Due to the similarity of the  $t\bar{t} + b\bar{b}$  background and the combinatorics issue, no single variable is suitable for signal extraction. A Multi-Variate Analysis (MVA) technique is used in an attempt to isolate the  $t\bar{t}H$  signal from the  $t\bar{t} + jets$  background. The MVA provides a one-dimensional discriminant based on several input variables related to the kinematics of the event. This discriminant is then used to perform signal extraction and set upper-limits on  $t\bar{t}H$  production. The results of two searches will be presented. The first result used the first  $5.1 \text{ fb}^{-1}$  of the 2012 dataset, with center of mass energy of 8 TeV, and was published in the Journal of High Energy Physics (JHEP), May 2013. The second result was update with the full  $19.4 \text{ fb}^{-1}$  8 TeV dataset, and was published in JHEP, September 2014.

## <sup>62</sup> Chapter 2

# <sup>63</sup> Theoretical Background

<sup>64</sup> The Standard Model (SM) of particle physics represents the sum of knowledge of the fundamen-  
<sup>65</sup> tal particles and their interactions with each other. It is a Quantum Field Theory (QFT) that  
<sup>66</sup> represents the interactions of each of the fundamental forces through the symmetry of a mathe-  
<sup>67</sup> matical object known as a Lie group. It is the theory that dictates the rate that the  $t\bar{t}H$  process  
<sup>68</sup> is produced, as well as the kinematics of every particle involved. As such, its predictions are  
<sup>69</sup> critical for modeling the characteristic signature of the  $t\bar{t}H$  signal in the CMS detector, as well as  
<sup>70</sup> the background processes, like  $t\bar{t} + b\bar{b}$  which leave a kinematically similar final state signature.

### <sup>71</sup> 2.1 An Overview of Quantum Field Theory

<sup>72</sup> Quantum Field Theory (QFT) was developed out of the need for a relativistic description of  
<sup>73</sup> quantum mechanics. Since the Einstein relation  $E = mc^2$  allows for the creation of particle-  
<sup>74</sup> antiparticle pairs, the single-particle description used in non-relativistic quantum mechanics,  
<sup>75</sup> fails describe this phenomenon [4]. This additionally fails when considering that Heisenberg's  
<sup>76</sup> uncertainty relation,  $\Delta E \cdot \Delta t = \hbar$ , allows for an arbitrary number of intermediate, virtual  
<sup>77</sup> particles to be created. By quantizing a field representing a certain type of particle, multiparticle  
<sup>78</sup> states are naturally described as discrete excitations of that field.

<sup>79</sup> Lorentz invariance, and the need to preserve causality, also define a fundamental relationship  
<sup>80</sup> between matter and antimatter. The propagation of a particle across a space-like interval is  
<sup>81</sup> treated equivalently to the an anti-particle propagating in the opposite direction [4]. This is  
<sup>82</sup> done so that the net probability amplitude for the particles to have an effect on a measurement  
<sup>83</sup> occurring across a space-like interval cancel each other, thus preserving causality. This cancel-  
<sup>84</sup> lation requirement additionally implies that the particle and anti-particle have the same mass,  
<sup>85</sup> with opposite quantum numbers such as spin or electric charge.

86 The Lorentz transformations for a scalar field are different than for a field with internal de-  
 87 grees of freedom, such as spin. A rotation on a vector field, will affect both its location, as well  
 88 as it's orientation [4]. This means the Lorentz invariant equation of motion describring a scalar  
 89 field will have a different form than equations of motion for a field with spin. The most relevant  
 90 equations describe the particles of SM, which contain spins of 0, 1/2, and 1. They are described  
 91 by the Klein-Gordan, Dirac, and Proca equations respectively.

92

Klein-Gordon equation, for scalar (spin 0) fields

$$(\partial^2 + m^2)\phi = 0 \quad (2.1)$$

Dirac equation, for spinor (spin 1/2) fields

$$(i\gamma^\mu \partial_\mu - m)\psi = 0 \quad (2.2)$$

Proca equation, for vector (spin 1) fields

$$\partial_\mu(\partial^\mu A^\nu - \partial^\nu A^\mu) + m^2 A^\nu = 0 \quad (2.3)$$

93 With these equations, one can build a theory of free particles. The Lagrangian formulation is  
 94 the most appropriate since all expressions are explicitly Lorentz invariant [4]. The Lagrangians  
 95 for the Klein-Gordon, Dirac, and Proca equations are given as:

96

Klein-Gordon Lagrangian, for real and complex scalar fields

$$\begin{aligned} \mathcal{L} &= \partial_\mu \partial^\mu \phi^2 - \frac{1}{2} m^2 \phi^2 \\ \mathcal{L} &= (\partial_\mu \phi)^*(\partial^\mu \phi) - m^2 (\phi)^*(\phi) \end{aligned} \quad (2.4)$$

Dirac Lagrangian, for spinor fields

$$\mathcal{L} = i\bar{\psi} \gamma^\mu \partial_\mu \psi - m\bar{\psi} \psi \quad (2.5)$$

Proca Lagrangian, for vector fields

$$\mathcal{L} = -\frac{1}{4} F_{\mu\nu} F^{\mu\nu} + m^2 A^\nu A_\nu \quad (2.6)$$

97 where  $F_{\mu\nu}$ , is the field strength tensor, defined as  $F_{\mu\nu} = \partial_\mu A_\nu - \partial_\nu A_\mu$

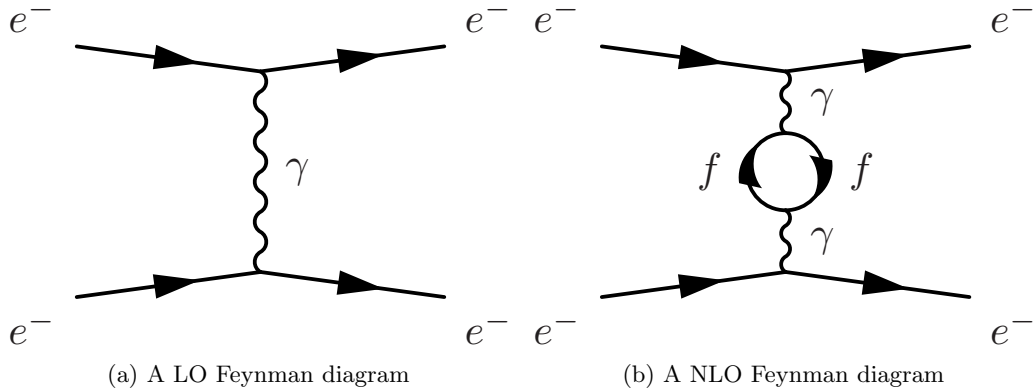


Figure 2.1: Leading and Next to Leading Order Feynman diagrams for the coulomb scattering process

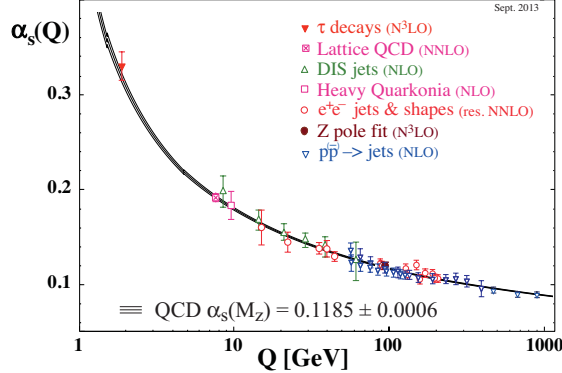
Interactions are generated by coupling multiple fields together in a single term, such as  $ieA_\mu\bar{\psi}\psi$  and treating it as a perturbation to the free field theory. This implies every interaction between particles is carried out by a virtual mediating particle. When two electrons scatter off one another, they are really exchanging a virtual photon, the mediator of the electromagnetic force. The  $W^\pm$  and  $Z$  bosons mediate the weak force, while the gluons mediate the strong force.

$$\mathcal{L} = \mathcal{L}_{Free} + \mathcal{L}_{Interacting} \quad (2.7)$$

In order to calculate the probability and dynamics of two particles interacting with one another, an integral, constrained by energy and momentum conservation, over the phase space of outgoing particles and the scattering amplitude,  $\mathcal{M}$ , is evaluated. The scattering amplitude is calculated by using the propagator (Green's function of the free particle theory) for the incoming, mediating, and outgoing particles, with an appropriate weighting function, or vertex factor, for each point the particles interact in the scattering process, and then integrating over the momentum of the mediating particle. Richard Feynmann developed a set of rules for the writing down the propagators and vertex factors directly from the Lagrangian, and easily computing the scattering amplitude. He also introduced an elegant pictographic notation useful for visualizing particle interactions, known as Feynmann diagrams.

With these tools, one can calculate the probability amplitudes of a given process occurring to Leading Order (LO) without any difficulties. However, when calculations in Next to Leading Order (NLO) are performed, and loop diagrams of virtual particles are considered, the probability amplitudes associated with a given process diverge to infinity. This occurs when one integrates over all of the possible momentum allowed by intermediate, loops of virtual particles, which due to Heisenberg's uncertainty principle, are allowed to take on any value of momentum. Figure 2.1 shows an example of a LO and NLO process.

The systematic removal of divergences from a theory is called renormalization. The di-

Figure 2.2: The global average of  $\alpha_s$ , the QCD coupling constant.

vergences are absorbed into the definitions of the free parameters of the theory, making the parameters a function of the energy scale the process occurs at, instead of a constant. This allows for the calculations of fundamental processes to completed, as long as the energy scale of the interaction is known. A modern interpretation of renormalization was provided by Kenneth Wilson [5] [6]. Instead of seeing the effects of high momentum calculations after moving to NLO in perturbation theory, one uses an effective Lagrangian, computed by integrating out shells of momentum beginning at the energy cutoff of the theory, where the NLO effects begin the dominate. The dimensions of integration are then rescaled and the result of evaluating the integral over the momentum shell is absorbed into the definition of free parameters. The processes is iterated until the energy scale of the interaction is reached. The functional dependence of the parameters is then directly present in the resulting effective Lagrangian, instead of appearing suddenly when accounting for the one-loop contributions at NLO. Regardless of how strange this procedure seem, the running of the coupling constant as a function of interaction engergy has been validated experimentally time and time and again, as shown in Figure 2.2 [7].

## 2.2 Abelian Gauge Theories of Particle Interactions

In 1930, Herman Weyl introduced the idea that the interactions between fields can be generated by requiring them to be invariant under guage tansformations of a local symmetry [8]. For electromagnetism, the local symmetry is that of the Lie group,  $U(1)$ . It is an abelian group, which has the property that the generators of the group symmetry commutes with themselves. The  $U(1)$  symmetry is invariant under phase rotations. By requiring local guage invariance, the Lagrangian must be unchanged under the

$$\psi(x) \rightarrow e^{i\alpha(x)}\psi(x). \quad (2.8)$$

<sup>142</sup> Consider the Lagrangian for a free spin 1/2 particle:

$$\mathcal{L} = \bar{\psi}(i\gamma^\mu \partial_\mu - m)\psi \quad (2.9)$$

<sup>143</sup> The first term in the Lagrangian, involving the derivative, acts on  $\alpha(x)$ , creating a new term in  
<sup>144</sup> the Lagrangian, breaking its invariance under the local phase transformation.

$$\mathcal{L} \rightarrow \mathcal{L} - (\partial_\mu \alpha) \bar{\psi} \gamma^\mu \psi \quad (2.10)$$

<sup>145</sup> Thus, a new term must be added to the original Lagrangian to cancel out the term arising from  
<sup>146</sup> the local phase transformation. This is achieved by defining the covariant derivative:

$$D_\mu = \partial_\mu + ieA_\mu \quad (2.11)$$

<sup>147</sup> where  $A_\mu$  is a new vector field that transforms as follows:

$$A_\mu(x) \rightarrow A_\mu(x) - \frac{1}{e}\partial_\mu \alpha(x) \quad (2.12)$$

<sup>148</sup> The covariant derivative thus transforms like

$$\begin{aligned} D_\mu \psi(x) &\rightarrow [\partial_\mu + ie(A_\mu - \frac{1}{e}\partial_\mu \alpha)] e^{i\alpha(x)} D_\mu \psi(x) \\ &= e^{i\alpha(x)} [\partial_\mu + ie(A_\mu - \frac{1}{e}\partial_\mu \alpha + \frac{1}{e}\partial_\mu \alpha)] D_\mu \psi(x) \\ &= e^{i\alpha(x)} (\partial_\mu + ieA_\mu) \psi(x) \\ &= e^{i\alpha(x)} D_\mu \psi(x) \end{aligned} \quad (2.13)$$

<sup>149</sup> This covariant derivative transforms in the same way that  $\psi(x)$  does, and the new locally gauge  
<sup>150</sup> invariant Lagrangian becomes

$$\begin{aligned} \mathcal{L} &= \bar{\psi}(i\gamma^\mu D_\mu - m)\psi - \frac{1}{4}F^{\mu\nu}F_{\mu\nu} \\ &= i\bar{\psi}\gamma^\mu \partial_\mu \psi - \bar{\psi}\gamma^\mu \psi A_{\mu u} - m\bar{\psi}\psi - \frac{1}{4}F^{\mu\nu}F_{\mu\nu} \end{aligned} \quad (2.14)$$

<sup>151</sup> where

$$F^{\mu\nu} = (\partial^\mu A^\nu - \partial^\nu A^\mu) \quad (2.15)$$

<sup>152</sup> and  $\frac{1}{4}F^{\mu\nu}F_{\mu\nu}$  is the kinetic energy term of the Proca equation for the new vector field.

<sup>153</sup> This new Lagrangian is identical to the QED Lagrangian, except it was derived beginning  
<sup>154</sup> with a free Dirac theory and requiring the field to be locally gauge invariant under  $U(1)$  transfor-  
<sup>155</sup> mations. This necessitated the introduction of a new vector field,  $A_\mu$ , as well as an interaction

<sup>156</sup> term with it. This implies that the electromagnetic force can be represented by the requirement  
<sup>157</sup> of local  $U(1)$  symmetry on a free Dirac particle.

<sup>158</sup> It should be noted, that if the photon had mass, an additional term from the Proca equation  
<sup>159</sup> would have to be added to the Lagrangian,  $m^2 A_\mu A^\mu$ . This term complicates the picture since  
<sup>160</sup> it is not invariant under local phase transformations, and cannot be compensated for through a  
<sup>161</sup> different choice of  $A_\mu$ . This implies that the bosons of a gauge theory must be massless in order  
<sup>162</sup> to preserve local gauge invariance.

### <sup>163</sup> 2.3 Non-Abelian Gauge Theories of Particle Interactions

<sup>164</sup> In 1954, Yang and Mills worked to extend this idea to symmetries of different gauge groups [9].  
<sup>165</sup> Their most important accomplishment was developing this procedure for non-abelian groups.  
<sup>166</sup> These are groups, where the transformation does not involve a simple variable  $\alpha(x)$ , but rather an  
<sup>167</sup> entire matrix of dimension  $n > 2$ . These matrices do not commute with each other, and their work  
<sup>168</sup> developed the procedure for applying local gauge invariance described above to the more complex,  
<sup>169</sup> higher dimensional symmetries, such as  $SU(2)$  and  $SU(3)$ . Consider the case of  $SU(2)$  symmetry.  
<sup>170</sup> The theory is appropriate for describing the dynamics of two fermion fields, represented as a  
<sup>171</sup> doublet:

$$\psi = \begin{pmatrix} \psi_1(x) \\ \psi_2(x) \end{pmatrix} \quad (2.16)$$

<sup>172</sup> this will transform under the  $SU(2)$  transformation as a two-component spinor:

$$\psi \rightarrow \exp\left(i\alpha^i \frac{\sigma_i}{2}\right) \psi \quad (2.17)$$

<sup>173</sup> where  $\sigma^i$  are the Pauli matrices:

$$\sigma^1 = \begin{pmatrix} 0 & 1 \\ 1 & 0 \end{pmatrix}, \sigma^2 = \begin{pmatrix} 0 & -i \\ i & 0 \end{pmatrix}, \sigma^3 = \begin{pmatrix} 1 & 0 \\ 0 & -1 \end{pmatrix} \quad (2.18)$$

<sup>174</sup> and have the commutation relation defined by:

$$\left[ \frac{\sigma^i}{2}, \frac{\sigma^j}{2} \right] = i\epsilon^{ijk} \frac{\sigma^k}{2} \quad (2.19)$$

<sup>175</sup> Similar to the case of the  $U(1)$  Abelian symmetry, in order to form a lagrangian that is locally  
<sup>176</sup> gauge invariant, three vector fields,  $A_\mu^i$ ,  $i = 1, 2, 3$ , are introduced, and coupled to  $\psi$  through the  
<sup>177</sup> covariant derivative:

$$D_\mu = (\partial_\mu - igA_\mu^i \frac{\sigma^i}{2}) \quad (2.20)$$

<sup>178</sup> to ensure that the derivative covaries with the transformation, the fields,  $A_\mu^i$  will transform like:

$$A_\mu^i \frac{\sigma^i}{2} \rightarrow A_\mu^i \frac{\sigma^i}{2} + \frac{1}{g}(\partial_\mu \alpha^i) \frac{\sigma^i}{2} + i \left[ \frac{\alpha^i \sigma^i}{2}, A_\mu^i \frac{\sigma^i}{2} \right] \quad (2.21)$$

<sup>179</sup> The third term, which was absent from the abelian form of the transformation, is necessary to  
<sup>180</sup> account for the non-commutation of the pauli matrices. This non-communtation also changes  
<sup>181</sup> the form of the field strength tensor,  $F_{\mu\nu}^i$ :

$$F_{\mu\nu}^i = \partial_\mu A_\nu^i - \partial_\nu A_\mu^i + g\epsilon^{ijk} A_\mu^j A_\nu^k \quad (2.22)$$

<sup>182</sup> The entire  $SU(2)$  invariant Lagrangian can then be written as:

$$\begin{aligned} \mathcal{L}_{Yang-Mills} &= -\frac{1}{4}F_{\mu\nu}^i F^{i\mu\nu} + \bar{\psi}(i\gamma^\mu D_\mu)\psi \\ &= -\frac{1}{4}F_{\mu\nu}^i F^{i\mu\nu} + \bar{\psi}(i\gamma^\mu \partial_\mu - igA_\mu^i \frac{\sigma^i}{2})\psi \end{aligned} \quad (2.23)$$

<sup>183</sup> This procedure generalizes to any continuous group of symmetries. The basic steps involve  
<sup>184</sup> idenitifying the generators of the transformation:

$$\psi(x) \rightarrow e^{i\alpha^a t^a} \psi \quad (2.24)$$

<sup>185</sup> where  $t^a$  are a set of matrices with the commutation relationship:

$$[t^a, t^b] = if^{abc}t^c \quad (2.25)$$

<sup>186</sup> where  $f^{abc}$  is the structure constant for the goup. The covariant derivative is then defined as:

$$D_\mu = \partial_\mu - igA_\mu^a t^a \quad (2.26)$$

<sup>187</sup> where the fields,  $A_\mu^a$ , transform like:

$$A_\mu^a \rightarrow A_\mu^a + \frac{1}{g}\partial_\mu \alpha^a + f^{abc}A_\mu^b \alpha^c \quad (2.27)$$

<sup>188</sup> the field strength tensor is then formed as:

$$F_{\mu\nu}^a = \partial_\mu A_\nu^a - \partial_\nu A_\mu^a + f^{abc} A_\mu^b A_\nu^c \quad (2.28)$$

<sup>189</sup> and finally, the locally, gauge invariant Lagrangian will have the form:

$$\begin{aligned}\mathcal{L}_{\text{General, non-Abelian}} &= -\frac{1}{4}F_{\mu\nu}^a F^{a\mu\nu} + \bar{\psi}(i\gamma^\mu D_\mu)\psi \\ &= -\frac{1}{4}F_{\mu\nu}^a F^{a\mu\nu} + \bar{\psi}(i\gamma^\mu \partial_\mu - ig A_\mu^a t^a)\psi\end{aligned}\quad (2.29)$$

190 In 1964, Murray Gell-Mann and Zweig independently developed a model of hadron interactions,  
 191 that described the spectrum of baryons and mesons in terms of combinations of fundamental  
 192 particles, which Gell-Mann named quarks [10] [11] [12]. In their model, three quarks:  $u, d, s$   
 193 formed an  $SU(3)$  flavor symmetry. However, this did not explain the appearance of only two and  
 194 three quark combinations, the mesons and baryons. It also could not explain the spin statistics  
 195 of the baryons. The  $\Delta^{++}$ ,  $\Delta^-$ , and  $\Omega^-$ , particles all have  $uuu$ ,  $ddd$ ,  $sss$  quark combinations,  
 196 respectively, with their spins aligned. That is to say, these baryons seem to violate the Pauli-  
 197 exclusion principle since all three quarks seem to occupy the same quantum state simultaneously.

198 In 1964, O.W. Greenberg solved this problem by proposing that quarks also have an additional  
 199 quantum number, *color*, that come in three types: red, green, blue [13]. The requirement that  
 200 all stable hadrons be color neutral: either possessing equal amounts of all three colors in  $qqq$   
 201 combinations, or a  $q\bar{q}$  pair sharing the same color, also explained the observation of only 2 and  
 202 3 quark combinations in experiments. These three colors form an  $SU(3)$  symmetry, and is the  
 203 gauge symmetry describing the interactions of quarks and leptons. This theory is known as  
 204 Quantum Chromodynamics (QCD). Its derivation follows from the procedure outlined above.  
 205 This group has eight generators, known as the Gell-Mann matrices, and are defined as:

$$\begin{aligned}t^1 &= \frac{1}{2} \begin{pmatrix} 0 & 1 & 0 \\ 1 & 0 & 0 \\ 0 & 0 & 0 \end{pmatrix}, \quad t^2 = \frac{1}{2} \begin{pmatrix} 0 & -i & 0 \\ i & 0 & 0 \\ 0 & 0 & 0 \end{pmatrix}, \quad t^3 = \frac{1}{2} \begin{pmatrix} 1 & 0 & 0 \\ 0 & -1 & 0 \\ 0 & 0 & 0 \end{pmatrix} \\ t^4 &= \frac{1}{2} \begin{pmatrix} 0 & 0 & 1 \\ 0 & 0 & 0 \\ 1 & 0 & 0 \end{pmatrix}, \quad t^5 = \frac{1}{2} \begin{pmatrix} 0 & 0 & -i \\ 0 & 0 & 0 \\ i & 0 & 0 \end{pmatrix} \\ , \quad t^6 &= \frac{1}{2} \begin{pmatrix} 0 & 0 & 0 \\ 0 & 0 & 1 \\ 0 & 1 & 0 \end{pmatrix}, \quad t^7 = \frac{1}{2} \begin{pmatrix} 0 & 0 & 0 \\ 0 & 0 & -i \\ 0 & -i & 0 \end{pmatrix}, \quad t^8 = \frac{1}{2\sqrt{3}} \begin{pmatrix} 1 & 0 & 0 \\ 0 & 1 & 0 \\ 0 & 0 & -2 \end{pmatrix}\end{aligned}\quad (2.30)$$

206 and a Lagrangian defined as:

$$\begin{aligned}\mathcal{L}_{QCD} &= -\frac{1}{4}G_{\mu\nu}^a G^{a\mu\nu} + \bar{\psi}(i\gamma^\mu D_\mu)\psi \\ &= -\frac{1}{4}G_{\mu\nu}^a G^{a\mu\nu} + \bar{\psi}(i\gamma^\mu \partial_\mu - ig A_\mu^a t^a)\psi\end{aligned}\quad (2.31)$$

207 where  $t^a$  are the Gell-Mann matrices defined in equation 2.30 and the fields  $A_\mu^a$  are the eight  
 208 mediators of the QCD force, the *gluons*.

209 Like all non-abelian guage theories, it is asymptotically free. Thus, the strength of the cou-  
 210 pling constant,  $\alpha_s$ , decreases as the momentum-transfer,  $Q$  in interaction increases. This allows  
 211 the use of perturbation theory for high-momentum calculations, therefore allowing calculations  
 212 of hadronic-processes for experimental evaluation.

213 The idea of local gauge invariance was successful in describing the dynamics of QED and  
 214 QCD, which only contain massless gauge bosons. Theorists had long postulated that the weak  
 215 force was so weak because it was being facilitated by massive bosons, but adding a mass term  
 216 for a boson breaks the local gauge invariance. So, a tool was needed to reconcile the concept of  
 217 local gauge invariance, which works so well for the other forces, with the prospect of the weak  
 218 force being facilitated by massive gauge bosons.

## 219 2.4 The Higgs Mechanism in an Abelian Theory

220 In 1964 Peter Higgs introduced the idea that the gauge bosons can acquire their mass through  
 221 the breaking of an underlying symmetry [14]. In other words, the natural symmetry of the  
 222 Lagrangian describing a particular interaction could be different than the symmetry we observe  
 223 in nature. Consider an abelian example of complex scalar field theory, coupled to itself and to  
 224 an electromagnetic field [4].

$$\mathcal{L} = -\frac{1}{4}(F_{\mu\nu})^2 + |D_\mu\phi|^2 - V(\phi) \quad (2.32)$$

225 where  $D_\mu = \partial_\mu + ieA_\mu$ , is the familiar covariant derivative, and the Lagrangian is invariant  
 226 under the  $U(1)$  transformation as described earlier. The potential term,  $V(\phi)$  has the form

$$V(\phi) = -\mu^2\phi^*\phi + \frac{\lambda}{2}(\phi^*\phi)^2 \quad (2.33)$$

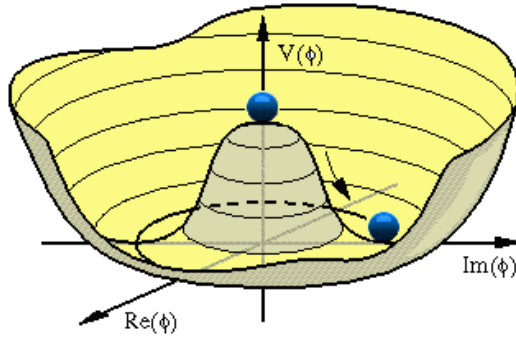


Figure 2.3: A visual representation of the Higgs potential

227 if  $\mu^2 > 0$  the shape of the potential no longer has a minimum at  $\langle\phi\rangle = 0$ . Figure 2.3 shows a plot  
 228 of the potential energy of  $\phi$  in terms of each of its components. The new minimum potential  
 229 energy occurs at:

$$\langle\phi\rangle = \phi_0 = \left(\frac{\mu^2}{\lambda}\right)^{1/2} \quad (2.34)$$

and while the field has a ground state at the zero potential point it is in an unstable equilibrium. Any quantum fluctuation about this point will take the field into the lower energy configuration with a ground state about the new minimum. When the Langrangian is expanded about 2.34, the field,  $\phi$  is rewritten as:

$$\phi(x) = \phi_0 + \frac{1}{\sqrt{2}}(\phi_1(x) + i\phi_2(x)) \quad (2.35)$$

the potential term,  $V(x)$ , then becomes:

$$V(x) = -\frac{1}{2\lambda}\mu^4 + \frac{1}{2} \cdot 2\mu^2\phi_1^2 + \mathcal{O}(\phi_i^3) \quad (2.36)$$

where we can notice that  $\phi_1$  has acquired a mass term with,  $m = \sqrt{2}\mu$ , while the scalar field  $\phi_2$  remains massless, and is known as the Goldstone boson. The covariant derivative is also transformed as:

$$|D_\mu\phi|^2 = \frac{1}{2}(\partial_\mu\phi_1)^2 + \frac{1}{2}(\partial_\mu\phi_2)^2 + \sqrt{2}e\phi_0 \cdot A_\mu\partial^\mu\phi_2 + e^2\phi_0^2A_\mu A^\mu + \dots \quad (2.37)$$

where cubic and quartic terms of  $A_\mu$ ,  $\phi_1$ , and  $\phi_2$  have been dropped. The important term is the last one, which can be interpreted as a mass term of the vector field,  $A_\mu$

$$\Delta\mathcal{L}_M = \frac{1}{2}m_A A_\mu A^\mu = e^2\phi_0^2 A_\mu A^\mu \quad (2.38)$$

where  $m_A = 2e^2\phi_0^2$ , has arisen from consequences of a non-zero vacuum expectation value of the  $\phi$  field. The remaining, massless Godlstone boson,  $\phi_2$  is not a physical particle, but rather a consequence of the choice of guage. This is illustrated when we can use the  $U(1)$  guage symmetry to rotate the field  $\phi(x)$  such that the field disappears.

$$\begin{aligned} \phi &\rightarrow \phi' = e^{i\alpha}(\phi_1 + \phi_2) \\ &= (\cos\alpha + i\sin\alpha)(\phi_1 + \phi_2) \\ &= (\phi_1 \cos\alpha - \phi_2 \sin\alpha) + i(\phi_1 \sin\alpha + \phi_2 \cos\alpha) \\ &= (\phi_1 - \phi_2 \tan\alpha) + i(\phi_1 \tan\alpha + \phi_2) \end{aligned} \quad (2.39)$$

Choosing  $\alpha = -\tan\phi_2/\phi_1$  will make  $\phi'$  a real quantity and elminate it's imaginary component,  $\phi'_2$ . The lagrangian can then be rewritten in terms of the rotated field  $\phi'$  and see that massless boson is indeed removed from the theory.

$$\begin{aligned}\mathcal{L} = & \frac{1}{2}(\partial_\mu\phi'_1)(\partial^\mu\phi'_1) - \frac{1}{2} \cdot 2\mu^2\phi'_1\phi'_1 \\ & - \frac{1}{4}(F^{\mu\nu}F_{\mu\nu}) + \frac{1}{2} \cdot e^2\phi_0^2A_\mu A^\nu \\ & + \phi_0e^2\phi'_1A_\mu A^\mu + \frac{1}{2}e^2\phi'^2A_\mu A^\mu + \mathcal{O}(\phi'^3)\dots\end{aligned}\quad (2.40)$$

247 The degree of freedom that  $\phi_2$  represents, is absorbed as a longitudinal polarization of the  
248  $A_{mu}$  field, a forbidden for massless gauge bosons, but necessary for massive bosons.

249 For this case of an abelian symmetry  $U(1)$ , it was shown that if a complex scalar field, which  
250 interacts with itself and another vector field, can gain a non-zero vacuum expectation value.  
251 The Lagrangian can be expanded about this new minimum, generating a mass term for the  
252 vector field. One of the degrees of freedom of the original complex scalar field is then absorbed  
253 as a longitudinal polarization state of the massive vector field.

## 254 2.5 The Higgs Mechanism in a non-Abelian Theory

255 Before describing the electroweak gauge theory of  $SU(2) \otimes U(1)$ , it will be helpful to see the effects  
256 of the Higgs mechanism for the non-Abelian group,  $SU(2)$  by itself. Consider an example  
257 of an  $SU(2)$  gauge field coupled to a scalar field that transforms like a real-valued vector under  
258  $SU(2)$  transformations [4]. The field  $\phi$  will have the form:

$$\phi = \begin{pmatrix} \phi_1 \\ \phi_2 \\ \phi_3 \end{pmatrix} \quad (2.41)$$

259 where the components,  $\phi_i$  are real-valued fields. The  $SU(2)$  transformation for this scalar field  
260 will also look like:

$$\phi \rightarrow e^{i\alpha^i T^i} \phi \quad (2.42)$$

261 where the matrices,  $T^i$  are defined as:

$$iT^1 = \begin{pmatrix} 0 & 0 & 0 \\ 0 & 0 & 1 \\ 0 & -1 & 0 \end{pmatrix}, \quad T^2 = \begin{pmatrix} 0 & 0 & -1 \\ 0 & 0 & 0 \\ 1 & 0 & 0 \end{pmatrix}, \quad T^3 = \begin{pmatrix} 0 & 1 & 0 \\ -1 & 0 & 0 \\ 0 & 0 & 0 \end{pmatrix} \quad (2.43)$$

262 The Lagrangian for this field will feature a Higgs potential term along with the previously  
263 mentioned  $SU(2)$  gauge fields,  $A_\mu^a$  coupled to the scalar field,  $\phi$ , and is given by:

$$\mathcal{L} = -\frac{1}{4}F_{\mu\nu}^a F^{a\mu\nu} + |D_\mu\phi|^2 + \mu^2\phi^*\phi - \frac{\lambda}{4}(\phi^*\phi)^2 \quad (2.44)$$

264 where  $F_{\mu\nu}^a$ , the field strength tensor is defined as:

$$F_{\mu\nu}^a = (\partial_\mu A_\nu^a - \partial_\nu A_\mu^a) + g\epsilon^{abc} A_\mu^b A_\nu^c \quad (2.45)$$

265 and the covariant derivative is defined as:

$$D_\mu = (\partial_\mu + igA_\mu^a T^a)\phi \quad (2.46)$$

266 Similarly to the Abelian case, the Higgs potential will induce a spontaneous symmetry breaking,  
267 and one of the components of the field  $\phi$  will gain a vacuum expectation value. After this  
268 breaking and expanding around the ground state potential, the field  $\phi$  will have the form:

$$\phi = \frac{1}{\sqrt{2}} \begin{pmatrix} 0 \\ 0 \\ v+h \end{pmatrix} \quad (2.47)$$

269 There has been no loss in generality in assuming this form since, similarly to the abelian case,  
270 we can use the gauge symmetry of  $SU(2)$  to rotate the field into this configuration. Goldstone's  
271 theorem tells us that we should expect two massive gague bosons corresponding to the  $T^1$ , and  
272  $T^2$  generators, while the  $T^3$  generator will correspond to a massless gauge boson, since  $\phi$  is still  
273 invariant under  $T^3$  transformations.

274 As in the Abelian case, the mass terms for the gauge bosons are generated from the covariant  
275 derivative term,  $|D_\mu\phi|^2$

$$\begin{aligned} D_\mu\phi &= \frac{1}{\sqrt{2}} \left( \partial_\mu + gA_\mu^1 \begin{pmatrix} 0 & 0 & 0 \\ 0 & 0 & 1 \\ 0 & -1 & 0 \end{pmatrix} + gA_\mu^2 \begin{pmatrix} 0 & 0 & -1 \\ 0 & 0 & 0 \\ 1 & 0 & 0 \end{pmatrix} + gA_\mu^3 \begin{pmatrix} 0 & 1 & 0 \\ -1 & 0 & 0 \\ 0 & 0 & 0 \end{pmatrix} \right) \begin{pmatrix} 0 \\ 0 \\ v+h \end{pmatrix} \\ &= \frac{1}{\sqrt{2}} \begin{pmatrix} 0 \\ 0 \\ \partial_\mu \end{pmatrix} + \frac{gA_\mu^1}{\sqrt{2}} \begin{pmatrix} 0 \\ v+h \\ 0 \end{pmatrix} - \frac{gA_\mu^2}{\sqrt{2}} \begin{pmatrix} v+h \\ 0 \\ 0 \end{pmatrix} \\ &= \frac{1}{\sqrt{2}} \begin{pmatrix} g(v+h)A_\mu^1 \\ g(v+h)A_\mu^2 \\ \partial_\mu h \end{pmatrix} \end{aligned} \quad (2.48)$$

276 Therefore

$$|D_\mu \phi|^2 = \frac{1}{2} \partial_\mu h \partial^\mu h + \frac{g^2 v^2}{2} ((A_\mu^1)^2 + (A_\mu^2)^2) + \frac{g^2}{2} (h^2 + 2hv) ((A_\mu^1)^2 + (A_\mu^2)^2) \quad (2.49)$$

This theory produces two massive bosons,  $A_\mu^1$  and  $A_\mu^2$ , both with mass,  $m_A = gv$ . These fields have  $h$ , and  $h^2$  couplings to the Higgs boson. The third gauge field,  $A_\mu^3$ , remains massless and is not coupled to the Higgs field. This model is beginning to resemble a description of electroweak physics, however, a third massive boson is necessary, as is a new gauge symmetry in order to generate it. That is the subject of the next section.

## 2.6 Glashow Weinberg Salam Theory

Glashow, Weinberg, and Salam published their theory unifying electromagnetic and weak forces in the 1960s [15] [16] [17]. It begins with the requirement of a  $SU(2)_L \otimes U(1)$  symmetry and incorporates the Higgs mechanism to give mass to the gauge bosons of the weak force. As described earlier, the  $U(1)$  symmetry requires introducing a vector field, which will be labeled  $B_\mu$ , and an interaction term, which is absorbed into the covariant derivative,  $D_\mu$ . The transformation will also be parameterized with a with a quantum number,  $Y$ , known as hypercharge. The  $SU(2)$  symmetry requires the introduction of three new vector fields, which will be labeled  $W_\mu^i, i = 1, 2, 3$ . The quantum number associated with this gauge group is known as isospin, and is determined by the  $T^3$  operator, acting on an  $SU(2)$  doublet on the third generator of the group. The  $SU(2) \otimes U(1)$  transformation,  $U(x)$ , will then be given by:

$$U(x) = e^{i\alpha^a(x)\tau^a} e^{iY\alpha(x)} \quad (2.50)$$

where  $\tau^a = \sigma^a/2$ , the Pauli matrices, 2.18. These gauge fields will be coupled, via the covariant derivative, to a doublet of complex scalar fields  $\phi$ , with hypercharge  $Y = +1/2$ . A Higgs potential will be added to generate the spontaneous symmetry breaking that will give mass to three of the gauge fields, and leave one massless. In order to preserve the  $SU(2)_L \otimes U(1)$  symmetry, the new covariant derivative will take the form:

$$D_\mu = (\partial_\mu - igW_\mu^a \tau^a - \frac{i}{2}g'B_\mu) \quad (2.51)$$

The subscript L on  $SU(2)_L$  refers to the experimental results that the weak force violates parity maximally, by only interacting with the left-handed chiral component of a field. Right versus left chirality is determined by whether the spin of a particle is aligned or anti-aligned with its direction of motion, and in general a particle is represented by a linear combination

of its right and left handed components. This idea was first proposed by Chen Ning Yang and Tsung-Dao Lee, in the 1950s. Their ideas were validated by the experimental discovery of parity violation in 1957, through the beta decays of Cobalt 60 atoms by C.S Wu. That same year, Yang and Lee were awarded the nobel prize for their insight [18]. In this model, then, the left-handed components of the particles participate in the weak interaction and are formed into doublets, while the right handed components are singlets, and will only interact with the electromagnetic field,  $B_\mu$ . The quantum numbers of the doublet will be given by +1/2 for the upper component of the  $SU(2)$  doublet, and -1/2 for the lower component. The fermion content of this theory is then given by:

$$\begin{pmatrix} \nu_L \\ e_L \end{pmatrix}, e_R \quad \begin{pmatrix} u_L \\ d_L \end{pmatrix}, u_R, d_R \quad (2.52)$$

where the right handed neutrino,  $\nu_R$  has been omitted, since it has zero charge, and isospin, and therefore does not participate in any of the interactions of this theory. The complete Lagrangian is given by a sum of free particle terms for massless bosons, fermions, and Higgs scalar fields; the Higgs potential; and a Yukawa coupling term between the fermions and the Higgs, which generates their masses.

$$\mathcal{L}_{GWS} = \mathcal{L}_{BosonKE} + \mathcal{L}_{Higgs} + \mathcal{L}_{FermionKE} + \mathcal{L}_{Yukawa} \quad (2.53)$$

The Higgs potential will have the form:

$$\mathcal{L}_{Higgs} = (D_\mu \phi)^\dagger (D^\mu \phi) + \mu^2 \phi^\dagger \phi - \lambda (\phi^\dagger \phi)^2 \quad (2.54)$$

The Higgs potential will break the symmetry of the Lagrangian when one of the four degrees of freedom in the complex scalar doublet,  $\phi$ , spontaneously acquires a vacuum expectation value. In this case, it will generate three massive gauge bosons, one massless gauge boson, and a massive scalar field. After gaining a vacuum expectation value, and expanding about this value, the scalar fields will have the form:

$$\langle \phi \rangle = \frac{1}{\sqrt{2}} \begin{pmatrix} 0 \\ v + h \end{pmatrix} \quad (2.55)$$

where no loss of generality has occurred since we are always able to rotate into this form through the appropriate gauge transformations, similar to what was described in the Abelian case. It should also be noted that this form is not invariant to any of the individual generators  $t^a$ , however  $\phi$  will be invariant to a combination of  $T^3 + Y$  generators. Per Goldstone's theorem, we

should expect this linear combination of fields to be the massless vector boson after symmetry breaking. The massless eigenstate will be the electromagnetic field,  $A_\mu \sim A_\mu^3 + B_\mu$ . The electric charge quantum number,  $Q$ , is then defined as

$$Q = T^3 + Y \quad (2.56)$$

<sup>321</sup> As before, the generation of the masses for the gauge bosons are generated by the interaction  
<sup>322</sup> of their fields with the Higgs field via the covariant derivative.

$$\begin{aligned} D_\mu \phi &= \frac{1}{\sqrt{2}} \left( \partial_\mu - \frac{ig}{2} A_\mu^1 \begin{pmatrix} 0 & 1 \\ 1 & 0 \end{pmatrix} - \frac{ig}{2} A_\mu^2 \begin{pmatrix} 0 & -i \\ i & 0 \end{pmatrix} - \frac{ig}{2} A_\mu^3 \begin{pmatrix} 1 & 0 \\ 0 & -1 \end{pmatrix} \right) \begin{pmatrix} 0 \\ v+h \end{pmatrix} \\ &= \frac{1}{\sqrt{2}} \left( \partial_\mu + i(\frac{1}{2}(v+h)(gA_\mu^3 - g'B_\mu)) \right) \end{aligned} \quad (2.57)$$

<sup>323</sup> Taking the dot product of this with its hermitian conjugate gives the  $|D_\mu \phi|^2$  term:

$$\begin{aligned} |D_\mu \phi|^2 &= \frac{1}{2} \partial_\mu h \partial^\mu h + \frac{1}{2} \frac{g^2 v^2}{4} ((A_\mu^1)^2 + (A_\mu^2)^2) + \frac{v^2}{4} (gA_\mu^3 - g'B_\mu)^2 \\ &\quad + \frac{1}{2} g^2 4(h^2 + 2vh)((A_\mu^1)^2 + (A_\mu^2)^2) + \frac{1}{2} \frac{1}{4}(h^2 + 2vh)(gA_\mu^3 - g'B_\mu) \end{aligned} \quad (2.58)$$

<sup>324</sup> From equation 2.58 we can identify three massive and one massless gauge bosons, corresponding  
<sup>325</sup> to the charged and neutral weak currents, and the electromagnetic current.

$$\begin{aligned} W_\mu^\pm &= \frac{1}{\sqrt{2}} (A_\mu^1 \mp iA_\mu^2) && \text{with mass } m_W = g \frac{v}{2}; \\ Z_\mu^0 &= \frac{1}{\sqrt{g^2 + g'^2}} (gW_\mu^3 - g'B_\mu) && \text{with mass } m_Z = \frac{v}{2} \sqrt{g^2 + g'^2}; \\ A_\mu &= \frac{1}{\sqrt{g^2 + g'^2}} (gW_\mu^3 + g'B_\mu) && \text{with mass } m_A = 0; \end{aligned} \quad (2.59)$$

<sup>326</sup> where the last field,  $A_\mu$  is absent from the covariant derivative term, but already identified as  
<sup>327</sup> the massless gauge boson of the theory due to its gauge invariance under a  $T^3 + Y$  rotation.  
<sup>328</sup> Using these definitions the covariant derivative has the following form:

$$\begin{aligned} D_\mu &= \partial_\mu - \frac{ig}{\sqrt{2}} (W^+ T^+ + W^- T^-) \\ &\quad - \frac{i}{\sqrt{g^2 + g'^2}} Z_\mu^0 (gT^3 - g'Y) - \frac{gg'}{\sqrt{g^2 + g'^2}} A_\mu (T^3 + Y) \end{aligned} \quad (2.60)$$

<sup>329</sup> where  $T^\pm = \frac{1}{2}(\sigma^1 \pm \sigma^2)$ . From this form, we can identify the fundamental electric charge,  $e$ , as

$$e = \frac{gg'}{\sqrt{g^2 + g'^2}} \quad (2.61)$$

<sup>330</sup> The similarity in the forms between  $Z_\mu^0$  and  $A_\mu$  suggest that their relationship can be ex-  
<sup>331</sup> pressed in a simpler form, as the rotation of underlying guage fields  $A_\mu^3$  and  $B_\mu$  through the  
<sup>332</sup> weak mixing angle,  $\theta_W$

$$\begin{pmatrix} Z_\mu^0 \\ A_\mu \end{pmatrix} = \begin{pmatrix} \cos \theta_W & -\sin \theta_W \\ \sin \theta_W & \cos \theta_W \end{pmatrix} \begin{pmatrix} A_\mu^3 \\ B_\mu \end{pmatrix} \quad (2.62)$$

<sup>333</sup> where  $\tan \theta_W = \frac{g'}{g}$ . Expanding 2.62, we have the definitions of the  $Z_\mu^0$  and  $A_\mu$  fields in terms of  
<sup>334</sup>  $\theta_W$

$$\begin{aligned} Z_\mu^0 &= A_\mu^3 \cos \theta_W - B_\mu \sin \theta_W \\ A_\mu &= A_\mu^3 \sin \theta_W + B_\mu \cos \theta_W \end{aligned} \quad (2.63)$$

<sup>335</sup> The weak mixing angle,  $\theta_W$ , also provides a simple relationship between the  $W_\mu^\pm$  and  $Z_\mu^0$  fields:

$$m_W = m_Z \cos \theta_W \quad (2.64)$$

<sup>336</sup> The covariant derivative,  $D_\mu$  is also rewritten in terms of the mass eingenstates of the gauge  
<sup>337</sup> fields

$$D_\mu = (\partial_\mu - \frac{ig}{\sqrt{2}}(W_\mu^+ + W_\mu^- T^-) - \frac{ig}{\cos \theta_W} Z_\mu^0(T_3 - \sin^2 \theta_W Q) - ieA_\mu Q) \quad (2.65)$$

<sup>338</sup> where  $g = e/\cos \theta_W$ . The square of the covariant derivative is then written as

$$\begin{aligned} |D_\mu|^2 &= \frac{1}{2}\partial_\mu h \partial^\mu h + \frac{1}{2}m_W^2 W_\mu^+ W^{\mu+} + \frac{1}{2}m_W^2 W_\mu^- W^{\mu-} + \frac{1}{2}m_Z^2 Z_\mu^0 Z^{\mu 0} \\ &\quad + \left(\frac{h^2}{v^2} + \frac{h}{v}\right)\left[\frac{1}{2}m_W^2(W_\mu^+ W^{\mu+} + W_\mu^- W^{\mu-}) + \frac{1}{2}m_Z^2 Z_\mu^0 Z^{\mu 0}\right] \end{aligned} \quad (2.66)$$

<sup>339</sup>

<sup>340</sup>

<sup>341</sup> With the form of the covariant derivative in place, the fermionic kinematic term of the  
<sup>342</sup> Lagrangian can be described. As mentioned earlier, the masses of the fermions in the model  
<sup>343</sup> will be generated by the Yukawa interaction term with the Higgs, so this term only involves the  
<sup>344</sup> covariant derivatives acting on the left-handed doublet and right-handed singlet states of this  
<sup>345</sup> model.

<sup>346</sup> The quantum number assignments for the leptons, which are chosen in order to reproduce the  
<sup>347</sup> known values of their electric charges, are shown in table 2.1. The values of these quantum

	$\nu_L$	$e_L$	$e_R$	$u_L$	$d_L$	$u_R$	$d_R$
Isospin	+1/2	-1/2	0	+1/2	-1/2	0	0
Hypercharge	-1/2	-1/2	-1	+1/6	1/3	2/3	-1/3
Electric Charge	0	-1	-1	2/3	-1/3	2/3	-1/3

Table 2.1: The quantum numbers Isospin and Hypercharge are assigned for each of the  $SU(2)$  and  $U(1)$  symmetries respectively

numbers enter into the covariant derivative via the  $Z_\mu^0$  term of equation 2.65. The fermionic kinetic energy term of the Lagrangian is given by:

$$\begin{aligned} \mathcal{L}_{Fermion} = & \bar{E}_L(i\gamma^\mu D_\mu)E_L + \bar{e}_R(i\gamma^\mu D_\mu)e_R \\ & \bar{Q}_L(i\gamma^\mu D_\mu)Q_L + \bar{u}_R(i\gamma^\mu D_\mu)u_R + \bar{d}_R(i\gamma^\mu D_\mu)d_R \end{aligned} \quad (2.67)$$

Expanding the covariant term for the left-handed electron shows its explicit coupling to the gauge boson fields.

$$\begin{aligned} \mathcal{L}_{E_L} = & \begin{pmatrix} \bar{\nu}_L & \bar{e}_L \end{pmatrix} \left( (i\gamma^\mu(\partial_\mu - \frac{ig}{\sqrt{2}}(W_\mu^+ T^+ + W_\mu^- T^-) - \frac{ig}{\cos\theta_W}Z_\mu^0(T^3 - \sin^2\theta_W Q) - ieA_\mu Q)) \right) \begin{pmatrix} \nu_L \\ e_L \end{pmatrix} \\ = & \bar{\nu}_L i\gamma^\mu \partial_\mu \nu_L + \bar{e}_L i\gamma^\mu \partial_\mu e_L + \frac{ig}{\sqrt{2}} W_\mu^+ \bar{\nu}_L \gamma^\mu e + \frac{ig}{\sqrt{2}} W_\mu^- \bar{e}_L \gamma^\mu \nu_L \\ & + \frac{ig}{\cos\theta_W} \bar{\nu}_L (1/2) \gamma^\mu \nu_L + \frac{ig}{\cos\theta_W} \bar{e}_L \gamma^\mu (-1/2 + \sin^2\theta_W (+1)) e_L + (ie) \bar{e}_L \gamma^\mu A_\mu (-1) \end{aligned} \quad (2.68)$$

All of the terms will be combined with the final, spontaneously broken GWS Lagranian at the end of this section.

The final term to discuss in the theory, before combing all of the results, is the Yukawa interaction term between the fermion fields and the Higgs. For the electron, this term takes the form:

$$\begin{aligned} \mathcal{L}_{Yukawa} = & -\lambda_e \bar{E}_L \cdot \phi e_R - \lambda_e E_L \cdot \phi \bar{e}_R \\ = & -\frac{\lambda_e}{\sqrt{2}} (v+h)(\bar{e}_L e_R + e_L \bar{e}_R) \\ = & -\frac{\lambda_e v}{\sqrt{2}} (\bar{e}_L e_R + e_L \bar{e}_R) - \frac{\lambda_e}{\sqrt{2}} (\bar{e}_L e_R + e_L \bar{e}_R) h \end{aligned} \quad (2.69)$$

where the mass of the electron is identified as  $m_e = \frac{\lambda_e v}{\sqrt{2}}$ . In order to generate the masses of the particles, each fermion has its own unique  $\lambda$  value. So while the Higgs mechanism is able to generate the masses in a way that preserves the underlying  $SU(2) \otimes U(1)$  symmetry, it does not explain the heirarchy of masses since each  $\lambda$  value is unique to each lepton. The second term in last equation of 2.69 is the coupling of the Higgs particle,  $h$ , to the fermions. The coupling is proportional to the mass of the particle. The largest of these is to the top quark,

<sup>363</sup> with  $m_t = 73.21 \pm 0.51 \pm 0.71 \text{GeV}$ .

<sup>364</sup> The Yukawa coupling for the quarks is necessarily modified when additional quarks besides  
<sup>365</sup> the  $u$  and  $d$  are added to the theory. This is because there can be additional coupling terms  
<sup>366</sup> that mix generations. This occurs when the mass eigenstate of the quarks is not the same as the  
<sup>367</sup> interaction eigenstate. The modification requires the expansion of the  $u_L$  and  $d_L$  components  
<sup>368</sup> into a vector of left handed quarks. If we let

$$u_L^i = (u_L, c_L, t_L), \quad d_L^i = (d_L, s_L, b_L) \quad (2.70)$$

<sup>369</sup> represent the up and down-type quarks in the original weak interaction basis, then the vectors,  
<sup>370</sup>  $u_L^i$  and  $d_L^i$ , can be defined as the diagonalized basis for the Higgs coupling. They are related  
<sup>371</sup> through a unitary transformation.

$$u_L^i = U_u^{ij} u_L^{j\prime}, \quad d_L^i = U_d^{ij} d_L^{j\prime} \quad (2.71)$$

<sup>372</sup> The interaction terms with the charged gauge boson currents must then be rewritten as

$$J_W^{\mu+} = \frac{1}{\sqrt{2}} \bar{u}_L^i \gamma^\mu d_L^i = \frac{1}{\sqrt{2}} \bar{u}_L^{i\prime} \gamma^\mu (U_u^\dagger U_d) d_L^{j\prime} = \frac{1}{\sqrt{2}} \bar{u}_L^{i\prime} \gamma^\mu V_{ij} d_L^{j\prime} \quad (2.72)$$

<sup>373</sup> where  $V_{ij}$  is the 3x3 Cabibbo-Kobayashi-Maskawa (CKM) matrix describing the mixing among  
<sup>374</sup> six quarks [19] [20]. It is an extension of the Glashow-Iliopoulos-Maiani mechanism, which  
<sup>375</sup> was a 2x2 matrix that predicted the existence of a fourth quark, the charm quark. The GIM  
<sup>376</sup> mechanism was an attempt to suppress flavor-changing-neutral currents, which occur at LO in  
<sup>377</sup> a three-quark model, but not in a four-quark model. The CKM matrix, however, was motivated  
<sup>378</sup> by an attempt to explain  $CP$  violation in the weak interaction. At the time of its publication,  
<sup>379</sup> the bottom and top quarks were not predicted. After these were discovered, they were awarded  
<sup>380</sup> the nobel prize in physics in 2008.

<sup>381</sup> At this point, all the pieces are ready to write down the GWS Lagrangian, after the  
<sup>382</sup> Higgs mechanism has spontaneously broken the  $SU(2) \otimes U(1)$  symmetry.

$$\begin{aligned} \mathcal{L}_{Unbroken} = & -\frac{1}{4} A_{\mu\nu}^a A^{\mu\nu a} - \frac{1}{4} F_{\mu\nu} F^{\mu\nu} \\ & + |D_\mu \phi|^2 + \mu^2 (\phi^\dagger \phi) - \lambda (\phi^\dagger \phi)^2 \\ & + \bar{E}_L (i\gamma^\mu D_\mu) E_L + \text{similar terms for } e_R, U_L, u_R, d_R \\ & - \lambda_e \bar{E}_L \cdot \phi e_R + h.c. + \text{similar terms for } e_R, U_L, u_R, d_R \end{aligned} \quad (2.73)$$

$$\begin{aligned}
\mathcal{L}_{GWS} = & -\frac{1}{4}(Z_{\mu\nu}^0)^2 - \frac{1}{2}(W_{\mu\nu}^+ W_{\mu\nu}^-) - \frac{1}{4}(F_{\mu\nu})^2 \\
& + ig \cos \theta_W ((W_\mu^- W_\nu^+ - W_\nu^- W_\mu^+) \partial^\mu Z^{0\nu} + W_{\mu\nu}^+ W^{-\mu} Z^{0\nu} + W_{\mu\nu}^- W^{+\mu} Z^{0\nu}) \\
& + ie ((W_\mu^- W_\nu^+ - W_\nu^- W_\mu^+) \partial^\mu A^\nu + W_{\mu\nu}^+ W^{-\mu} A^\nu - W_{\mu\nu}^- W^{+\mu} A^\nu) \\
& + g^2 \cos^2 \theta_W (W_\mu^+ W_\nu^- Z^{0\mu} Z^{0\nu} - W_\mu^+ W^{-\mu} Z_\nu^0 Z^{0\nu}) \\
& + g^2 (W_\mu^+ W_\mu^- A^\mu A^\nu - W_\mu^+ W^{-\mu} A_\nu A^\nu) \\
& + ge \cos \theta_W (W_\mu^+ W_\nu^- (Z^{0\mu} A_\nu + Z^{0\nu} A^\mu) - 2W_\mu^+ W^{-\mu} A^\nu) \\
& + \frac{1}{2}g^2 (W_\mu^+ W_\nu^-) (W^{+\mu} W^{-\nu} - W^{+\nu} W^{-\mu}) \\
& + \frac{1}{2}\partial_\mu h \partial^\nu h - v^2 \lambda h^2 + \frac{1}{2}m_W^2 W_\mu^+ W^{+\mu} + \frac{1}{2}m_W^2 W_\mu^- W^{-\mu} + \frac{1}{2}m_Z^2 Z_\mu^0 Z^{0\mu} \\
& + \left(\frac{h^2}{v^2} + \frac{h}{v}\right) \left(\frac{1}{2}m_W^2 (W_\mu^+ W^{+\mu} + W_\mu^- W^{-\mu}) + \frac{1}{2}m_Z^2 Z_\mu^0 Z^{0\mu}\right) - \lambda v h^3 - \frac{1}{4}\lambda h^4 \\
& + \bar{E}_L (i\gamma^\mu \partial_\mu) E_L + e_R^- (i\gamma^\mu \partial_\mu) e_R + \bar{Q}_L (i\gamma^\mu \partial_\mu) Q_L + u_R^- (i\gamma^\mu \partial_\mu) u_R + \bar{d}_R (i\gamma^\mu \partial_\mu) d_R \\
& + g(W_\mu^+ J_W^{\mu+} + W_\mu^- J_W^{\mu-} + Z_\mu^0 J_Z^\mu) + e A_\mu J_{EM}^\mu \\
& - \frac{\lambda_e v}{\sqrt{2}} (\bar{e}_L e_R + \bar{e}_R e_L) - \frac{\lambda_e h}{\sqrt{2}} (\bar{e}_L e_R + \bar{e}_R e_L) \\
& - \frac{\lambda_u v}{\sqrt{2}} (\bar{u}_L u_R + \bar{u}_R u_L) - \frac{\lambda_u h}{\sqrt{2}} (\bar{u}_L u_R + \bar{u}_R u_L) \\
& - \frac{\lambda_d v}{\sqrt{2}} (\bar{d}_L d_R + \bar{d}_R d_L) - \frac{\lambda_d h}{\sqrt{2}} (\bar{d}_L d_R + \bar{d}_R d_L)
\end{aligned} \tag{2.74}$$

where the currents of the electroweak interaction,  $J_W^{\mu+}$ ,  $J_W^{\mu-}$ ,  $J_Z^\mu$ ,  $J_A^\mu$  are defined as:

$$\begin{aligned}
J_W^{\mu+} &= \frac{1}{\sqrt{2}} (\bar{\nu}_L \gamma^\mu e_L + \bar{u}_L^i \gamma^\mu V_{ij} d_L^j) \\
J_W^{\mu-} &= \frac{1}{\sqrt{2}} (\bar{e}_L \gamma^\mu \nu_L + \bar{d}_L^i \gamma^\mu V_{ij} u_L^j) \\
J_Z^\mu &= \frac{1}{\cos \theta_W} (\bar{\nu}_L \gamma^\mu (+1/2) \nu_L + \bar{e}_L \gamma^\mu (-1/2 + \sin^2 \theta_W) e_L + \bar{e}_R \gamma^\mu \sin^2 \theta_W e_R \\
&\quad + \bar{u}_L \gamma^\mu (1/2 - 2/3 \sin^2 \theta_W) u_L + \bar{u}_R \gamma^\mu (-2/3 \sin^2 \theta_W) u_R \\
&\quad + \bar{d}_L \gamma^{mu} (-1/2 + 1/3 \sin^2 \theta_W) d_L + \bar{d}_R \gamma^\mu (1/3 \sin^2 \theta_W) d_R) \\
J_{EM}^\mu &= e_{L,R}^- \gamma^\mu (-1) e_{L,R} + u_{L,R}^- \gamma^\mu (2/3) u_{L,R} + d_{L,R}^- \gamma^\mu (-2/3) d_{L,R}
\end{aligned} \tag{2.75}$$

## 383 2.7 The Standard Model of Particle Physics

The Standard Model of particle physics, extends the GWS model by incorporating the QCD interaction between the quarks and gluons. The symmetry of this theory is that of:

$$SU(3)_C \otimes SU(2)_L \otimes U(1)_Y \tag{2.76}$$

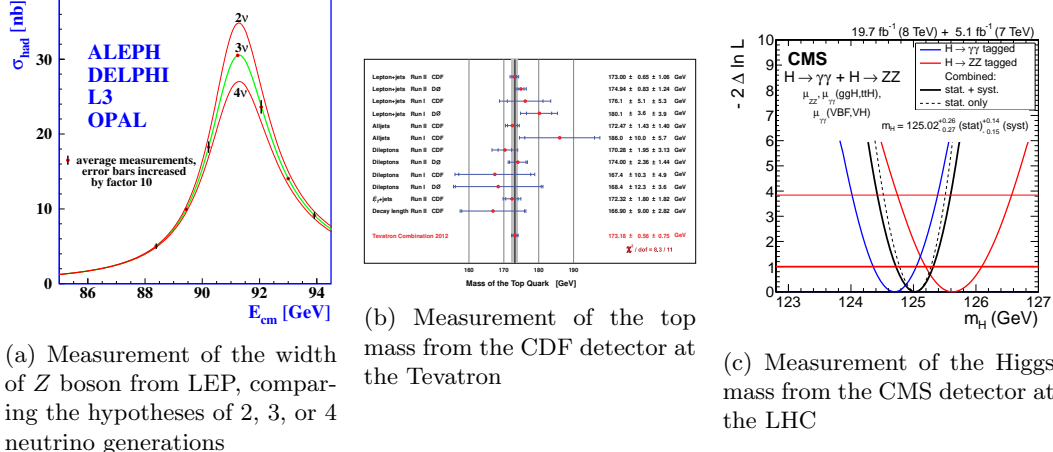


Figure 2.4: Experimental milestones of the Standard Model

<sup>384</sup> The Lagrangian of the model is given by

$$\mathcal{L}_{SM} = \mathcal{L}_{GWS} - \frac{1}{4} G_{\mu\nu}^a G^{a\mu\nu} + g_S C_\mu^a J_{QCD}^{a\mu} \quad (2.77)$$

<sup>385</sup> where the current for the QCD interaction,  $J_{QCD}^{a\mu}$  is defined as:

$$J_{QCD}^a = \bar{u}^i \gamma^\mu t^a u^i + \bar{d}^i \gamma^\mu t^a d^i \quad (2.78)$$

<sup>386</sup> where  $t^a$  are the Gell-Mann matrices defined in equation 2.30. The field strength tensor for the  
<sup>387</sup> eight gluon fields,  $G_{\mu\nu}^a$ , is defined as

$$G_{\mu\nu}^a = (\partial_\mu C_\nu^a - \partial_\nu C_\mu^a) - g_S f^{abc} C_\mu^b C_\nu^c \quad (2.79)$$

<sup>388</sup> The experimental evidence in favor of the SM is compelling. It has not only been able  
<sup>389</sup> to describe existing phenomenon to great precision, but has also predicted the existence of  
<sup>390</sup> new forms of matter and interactions among fundamental particles. The UA1 [21] [22] and  
<sup>391</sup> UA2 [23] [24] experiments at CERN, under the leadership of Carlo Rubbia, discovered the  
<sup>392</sup>  $W$  and  $Z$  bosons in 1983. The experiments observed a handful of events, in  $p\bar{b}$  collisions, at  
<sup>393</sup>  $\sqrt{s} = 540$  GeV, and were able to measure the masses to be  $M_W \sim 80$  GeV and  $M_Z \sim 95$  GeV.

<sup>394</sup> In the following years, from 1989-2000, the Large electron-positron (LEP) collider at CERN  
<sup>395</sup> conducted precision measurements of the Standard Model [25] [26]. Along with high-precision  
<sup>396</sup> measurements on the  $W, Z$  masses:

$$m_Z = 91.1875 \pm 0.0021 \text{ GeV} \quad (2.80)$$

$$m_W = 80.376 \pm 0.0033 \text{ GeV}$$

<sup>397</sup> the experiment was also able to put stringent limits on the existence of more than three families of

398 leptons and quarks by measuring the width of the  $Z$  boson. Figure 2.4(a) shows the comparison  
399 of two, three, and four family hypotheses to data.

400 Another milestone for the Standard Model occurred in 1995 when the CDF [27] and D0 experiments  
401 [28] at the Tevatron announced the observation of the top quark, with  $m_t \sim 176$  GeV,  
402 in  $p\bar{p}$  collisions at  $\sqrt{s} = 1.8$  TeV. Figure 2.4(c) shows a plot from 2012, the latest top quark  
403 mass measurements from CDF, which reports a  $m_t = 173.18 \pm 0.56 \pm 0.75$  GeV. It was the  
404 last quark predicted by the CKM matrix to be observed, and earned Makoto Kobayashi and  
405 Toshihide Maskawa the nobel prize in 2008 for their work extending the quark sector to three  
406 families and parameterizing their electroweak mixing.

407 Yet another milestone was reached in 2012, when the CMS and ATLAS detectors at CERN  
408 announced the observation of a new boson, with characteristics strikingly similar to the elusive  
409 Higgs boson of the SM. Figure 2.4(c) shows the latest measurement results on the mass from the  
410  $H \rightarrow \gamma\gamma$  and  $H \rightarrow ZZ$  channels, with a  $m_H = 125.02 \pm 0.27 \pm 0.15$ . One of the most important  
411 remaining goals is to measure the couplings of this new boson to all of the other particles in  
412 the Standard Model. Of particular interest is the coupling to the top-quark, since it offers the  
413 largest value of the Higgs Yukawa coupling to measure. This offers a test of the nature of the  
414 coupling, as well as a probe into deviations from its value.

## 415 2.8 Higgs Production in $pp$ Collisions at the LHC

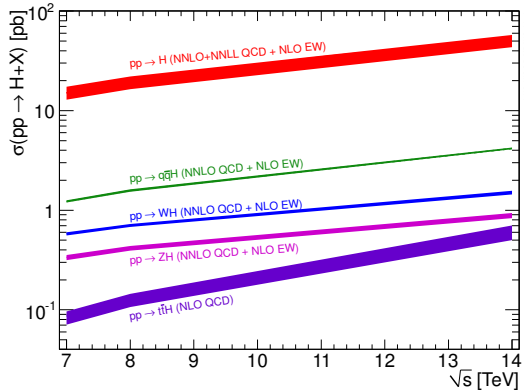


Figure 2.5: Higgs production cross-sections at the LHC, for 7–14 TeV  $pp$  collisions

416 The rest of the thesis will describe the search for Higgs boson production in proton-proton  
417 collisions at the LHC, so it will be useful to understand the production mechanisms for the Higgs  
418 in this scenario. At the LHC collision energies 7 – 14 TeV, there are four dominant production  
419 mechanisms that produce Higgs events: gluon-gluon fusion (ggf), vector-boson fusion (vbf),  
420 associated production with vector bosons (VH), and associated production with top-quark pairs  
421 (tth). Figure 2.5 shows the relative cross sections for each of these mechanisms.

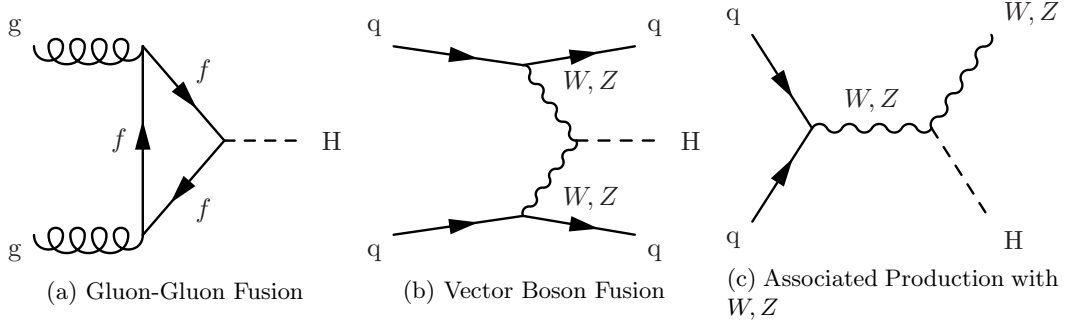


Figure 2.6: Feynman diagrams for the three largest Higgs production modes at the LHC

Gluon-gluon fusion, which proceeds via a heavy quark loop [29], is the dominant production mechanism at the LHC. The QCD radiative corrections to the total cross section have been computed at the next-to-leading order (NLO) and at the next-to-next-to-leading order (NNLO accuracy). The cross section for Higgs production at  $m_H = 125$  GeV and  $\sqrt{s} = 8$  TeV, the cross section is given as:

$$\sigma_{ggF} = 19.27 \pm \text{QCD Scale Unc.}^{+7.2\%}_{-7.8\%} \pm \text{PDF} + \alpha_S \text{ Unc.}^{+7.4\%}_{-6.9\%} \text{ pb}^{-1} \quad (2.81)$$

<sup>422</sup> Figure 2.6(a) shows a Feynman diagram for this process. The triangle loop contains all strongly  
<sup>423</sup> coupled fermions, which is dominated by the top-quark since the Yukawa coupling to the Higgs  
<sup>424</sup> is the largest.

Vector boson fusion proceeds through the fusion of  $W^+W^-$  or  $Z^0Z^0$  gauge bosons [29]. The characteristic signature of the production mode is the associated production of two quarks, typically at a low angle relative to the proton beam. This process has been calculated to NNLO for QCD and NLO for Electroweak corrections [29]. The cross section at  $m_H = 125$  GeV and  $\sqrt{s} = 8$  TeV is given as:

$$\sigma_{VBF} = 1.653 \pm \text{EW Unc.}^{+4.5\%}_{-4.5\%} \pm \text{QCD Scale Unc.}^{+0.2\%}_{-0.2\%} \pm \text{PDF} + \alpha_S \text{ Unc.}^{+2.6\%}_{-2.8\%} \text{ pb}^{-1} \quad (2.82)$$

<sup>425</sup> Figure 2.6(b) shows a Feynman diagram for VBF production. The large coupling to the  $W, Z$   
<sup>426</sup> bosons helps to make this the sub-dominant production mechanism at the LHC. However, the  
<sup>427</sup> gluon content of the proton at TeV energies is much larger than that of the valence quarks, thus  
<sup>428</sup> the relative suppression.

The third largest production mechanism for Higgs bosons at the LHC is through associated production with a  $W$  or  $Z$  boson [29]. It has been calculated to NNLO for QCD and NLO for Electroweak corrections. This process is also sometimes referred to as, Higgstrahlung, since it resembles the bremsstrahlung process of an electron radiating a photon. The higher order

electroweak corrections are similar to that of the Drell-Yan, so much of the technology to compute the cross-section can be borrowed from existing EW calculations. The cross section for  $m_H = 125 \text{ GeV}$  and  $\sqrt{s} = 8 \text{ TeV}$  is:

$$\begin{aligned}\sigma_{WH} &= 0.7046 \pm \text{QCD Scale Unc.}^{+1.0\%}_{-1.0\%} \pm \text{PDF+}\alpha_S\text{ Unc.}^{+2.3\%}_{-2.3\%} \text{ pb}^{-1} \\ \sigma_{ZH} &= 0.4153 \pm \text{QCD Scale Unc.}^{+3.1\%}_{-3.1\%} \pm \text{PDF+}\alpha_S\text{ Unc.}^{+2.5\%}_{-2.5\%} \text{ pb}^{-1}\end{aligned}\quad (2.83)$$

429 Figure 2.6(c) shows the Feynman diagram for VH production. This channel is most useful for  
430 identifying hadronic decays of the Higgs, since the associated gauge boson can decay to leptons,  
431 giving a strong kinematic handle over backgrounds that would normally overwhelm a similar  
432 search in the ggF channel.

## 433 2.9 $t\bar{t}H$ Production in $pp$ Collisions at the LHC

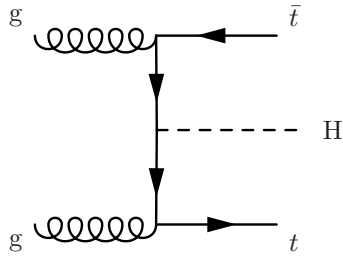


Figure 2.7: Feynman diagram for  $t\bar{t}H$  production

434 The  $t\bar{t}H$  production mode is the fourth largest production mode at the LHC [29]. This pro-  
435 duction mode has been calculated to NLO in QCD [30] [31] and has been studied recently with the  
436 state of the art NLO tools using the aMC@NLO [32] and POWHEG (PYTHIA+HERWIG) [33]  
437 frameworks. Studies have also been performed interfacing NLO QCD studies [34] with the  
438 Sherpa parton shower framework [35]. Additional studies on the effects of spin correlations with  
439 the aMC@NLO and Madspin framework have also been performed [36].

It has been found that the addition of NLO effects increases the cross-section relative to LO by  $\sim 20\%$ . The largest theoretical uncertainty comes from the variation of the renormalization and factorization scale, the QCD coupling  $\alpha_S$ , and the PDF uncertainty. The renormalization and factorization scales are set to  $\mu_R = \mu_F = (1/2)(m_T + m_T + m_H)$  and are varied by a factor of 2 to determine the cross-section's dependence on these parameters. Three different PDF sets, MSTW2008, CTEQ6.6, and NNPDF2.0 were used with the appropriate corresponding values of  $\alpha_S$  to determine the combined effect of varying PDF+ $\alpha_S$ . The cross section for  $m_H = 125 \text{ GeV}$

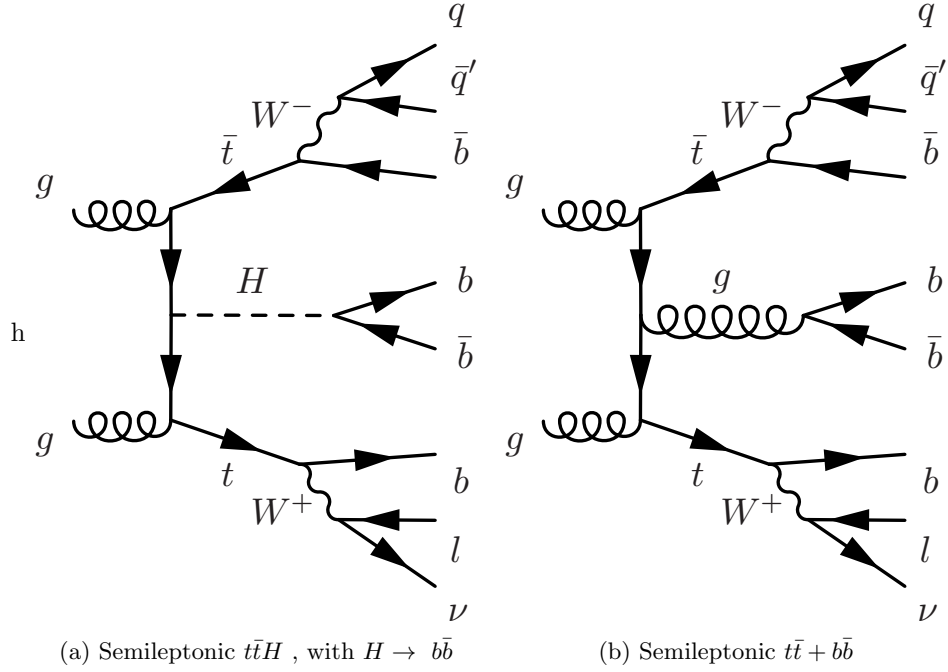


Figure 2.8: Feynman diagrams for the semileptonic  $t\bar{t}H$  process and its irreducible background,  $t\bar{t} + b\bar{b}$

and  $\sqrt{s} = 8$  TeV is given by:

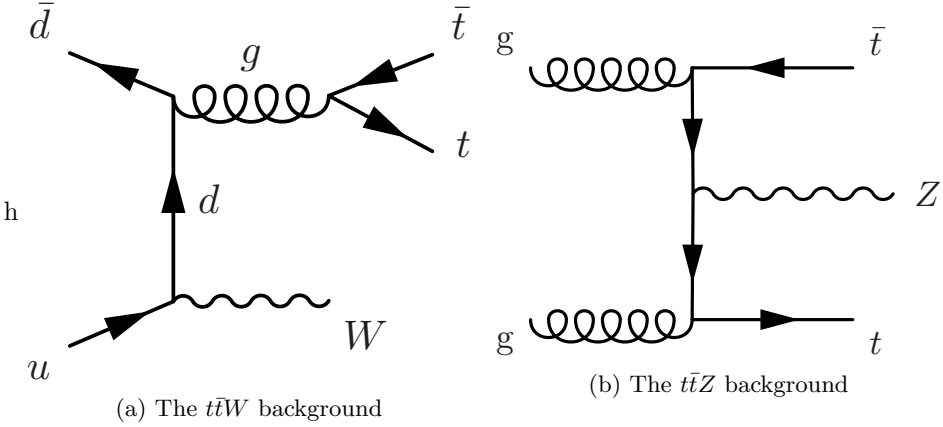
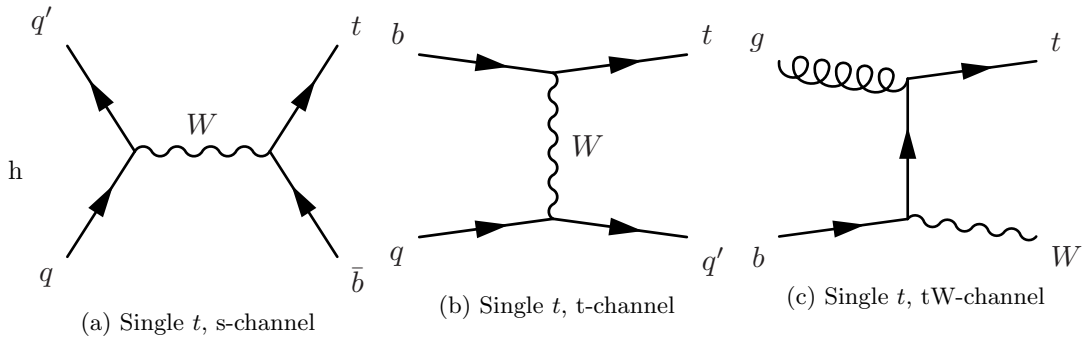
$$\sigma_{ttH} = 0.1293 \pm \text{QCD Scale Unc.}^{+3.8\%}_{-9.3\%} \pm \text{PDF} + \alpha_S \text{ Unc.}^{+8.1\%}_{-8.1\%} \text{ pb}^{-1} \quad (2.84)$$

440 A search for the Higgs in this production mode is additionally challenging due to this large  
441  $\sim 10\%$  error on the theoretical cross-section. Figure 2.7 shows a Feynman diagram for this  
442 process before the branching of the top-quarks or Higgs to final states.

443 When asking for the Higgs to decay to b-quark pairs, yet another complication arises when  
444 trying to identify which b-quarks came from a top decay or from a Higgs decay. For example, in  
445 the semileptonic decay of top quarks, there will be four b-quarks, and two light-flavor quarks in  
446 the final state. This means there are 15 (six choose four) possibilities to associate quarks to the  
447 top system. Although this is potentially constrained by b-tagging, and kinematic requirements  
448 (such as forming the top or  $W$  masses), the number of remaining possibilites smears out the  
449 resolution on peaking variables such as the invariant mass of b-quark pairs.

## 450 2.10 Background Processes to $t\bar{t}H$

451 The dominant background for  $t\bar{t}H$  production of top-quark pairs with additional ISR/FSR jets,  
452  $t\bar{t} + jets$ . The irreducible component of this background is comes when the extra radiation  
453 produces a final state with two additional b-quarks,  $t\bar{t} + b\bar{b}$ . Figure 2.8 compares the Feynman

Figure 2.9: Feynman diagrams for the  $t\bar{t}W$  and  $t\bar{t}Z$  background processesFigure 2.10: Feynman diagrams for the single  $t$  s,t, and  $tW$  background processes

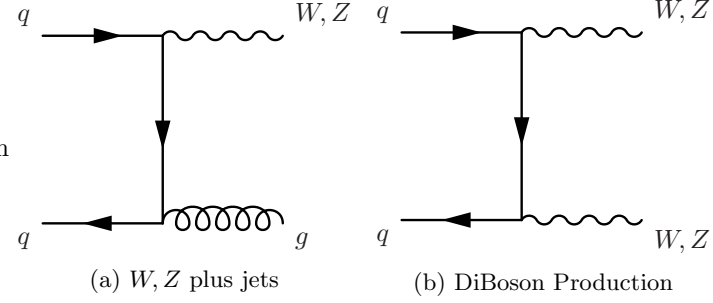
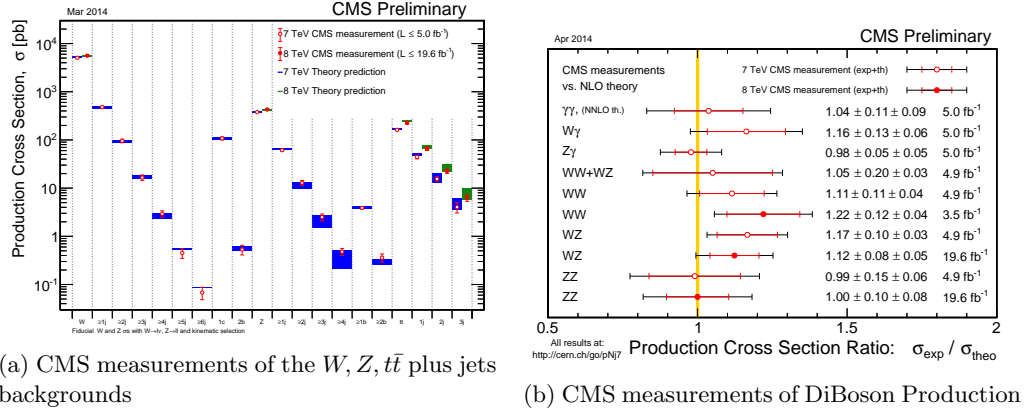
454 diagrams for the semileptonic decays of  $t\bar{t}H$  and  $t\bar{t} + b\bar{b}$ .

455 Additional difficulties come from the theoretical uncertainty on the  $t\bar{t} + b\bar{b}$  background [29].

456 The process has been calculated to NLO QCD in Sherpa [35] and OpenLoops [37] [38] [39]. It  
457 has been found that depending on selection cuts, and use of NLO PDF inputs, the difference  
458 between LO and NLO calculations on the cross section can be anywhere from 0.99% to 1.96%.

459 The light flavor component of the  $t\bar{t} + jets$  background also enters in the selection when any  
460 of the jets from the  $t\bar{t}$  system or extra radiation are misidentified as  $b$ -jets. The cross-section for  
461 the  $t\bar{t} + jets$  process is  $\sim 245 \text{ pb}^{-1}$ . This is a factor of 1800, so even if a  $b$ -tagging algorithm  
462 performs with a 1% mis-identification rate of light-jets, there will still be a large contribution  
463 from this process that will leave a very similar signature in the detector as  $t\bar{t}H$ .

464 The next largest background is the production of vector bosons in association with top-  
465 quark pairs,  $t\bar{t}W$  and  $t\bar{t}Z$ . Figure 2.9 shows Feynman diagrams from these two processes. They  
466 have cross-sections of  $\sigma_{ttW} = 0.249 \text{ pb}^{-1}$  and  $\sigma_{ttZ} = 0.208 \text{ pb}^{-1}$ , which are only a factor of  $\sim 2$   
467 greater than the  $t\bar{t}H$  process. These processes can enter the semileptonic  $t\bar{t}H$  selection by a  
468 semileptonic  $t\bar{t}$  decay, while the vector bosons decay to quarks, or through a hadronic  $t\bar{t}$  decay,  
469 while the vector bosons decay to quarks, and in the case of  $t\bar{t}Z$ , of the leptons is not identified  
470 in the reconstruction.

Figure 2.11: Feynman diagrams for the  $W, Z$  plus jets, and diBoson ( $WW, WZ, ZZ$ ) production.Figure 2.12: Measurements of  $t\bar{t}H$  backgrounds at CMS

Single top production is also an important background to consider in a search for  $t\bar{t}H$  production. Figure 2.10 shows Feynman diagrams for this process. It does not have as large of a contribution as the other backgrounds, since it requires additional radiation in order to have a similar final state jet multiplicity as  $t\bar{t}H$ . However, since a top-quark is still involved in the process, the final state kinematics of its decay products will be very similar. Single  $t$  production has a cross section of  $\sigma_t = 71.3 \text{ pb}^{-1}$ , while Single  $\bar{t}$  production has a cross section of  $\sigma_{\bar{t}} = 43.6 \text{ pb}^{-1}$ , due to charge asymmetry of the valence quarks of the proton

The last backgrounds to consider are the electroweak production of  $W$  and  $Z$  bosons in association with jets, as well as  $WW$ ,  $WZ$ , and  $ZZ$  pairs in association with jets. Figure ?? shows the Feynman diagrams for these processes, where the  $V$ , stands in for either  $W$  or  $Z$  bosons. For a semileptonic selection of  $t\bar{t}H$  events,  $Z$  plus jets events enter from a misidentification of one of the leptons from the  $Z$  boson decay. Extra FSR/ISR radiation is also to leave a similar signature in the signal region of a  $t\bar{t}H$  search, so it mainly contributes to control regions of the data.

All of these backgrounds have been measured at CMS. With the exception of a small degree of tension in the  $WW$  cross-section measurement, all backgrounds are in good agreement with Standard Model predictions. Figure 2.12(a) shows the results of CMS measurements on  $V+jets$  and  $t\bar{t} + jets$  backgrounds. Figure 2.12(b) shows the same, but for diBoson production.

## 489 2.11 Potential BSM Effects on $t\bar{t}H$ production

490 The phenomenological motivation for the existence of physics beyond the Standard Model come  
 491 from the observation of phenomenon or states of matter not described by the theory. Observations  
 492 of the cosmic microwave background from the Plank telescope have estimated that only  
 493  $\sim 5\%$  of the observable universe is composed of ordinary matter [40]. The remaining composition  
 494 is divided between Dark Matter ( $\sim 27\%$ , and  $\sim 68\%$  respectively). Evidence for Dark Matter  
 495 also comes from discrepancies between the observed rotational velocities of galaxies, and the  
 496 observed mass distributions, suggesting the presence of additional form of matter which does  
 497 not interact electromagnetically [41].

498 Additionally, in 1998, the Super-Kamiokande experiment proved that neutrinos oscillated  
 499 between flavors, implying indirectly that they also have mass [42]. This is something not de-  
 500 scribed in the Standard Model of physics. Due to their neutral charge, these particles are  
 501 extremely difficult to detect, so experiments have only been able to measure differences in the  
 502 mass squared between the three mass eigenstates. In 2005, the KamLAND experiment reported  
 503  $|\Delta m_{12}^2 = 0.000079 eV^2|$  [43]. In 2006, the MINOS experiment reported  $|\Delta m_{23} = 0.0027 eV^2|$  [44].

504 One of the largest theoretical problems with the Standard Model, comes the mechanism which  
 505 made it all possible- the Higgs. In equation 2.73 there are terms that couple the Higgs boson  
 506 to itself,  $-\lambda vh^3$ , and  $-\frac{1}{4}\lambda h^4$ . When computing NLO effects, these terms lead to a divergence  
 507 in the Higgs mass, when considering the effect of a loop of fermions on the Higgs propagator.  
 508 The corrections are of the form  $\Delta m_H = -\frac{\lambda_f^2}{8\pi^2} \Lambda_{UV}$ . Where  $\Lambda_{UV}$  is the high energy cut off for the  
 509 theory, which in the limit of a perfect theory, should extend to infinity. This is known as the  
 510 hierarchy problem.

511 Beyond the Standard Model physics is a term that describes extensions of the Standard  
 512 Model in order to describe the observed phenomenon. For the neutrino oscillations, a solution  
 513 similar to CKM matrix has been proposed, the PontecorvoMakiNakagawaSakata (PMNS) ma-  
 514 trix. This proposes that the mass eigenstates of the neutrino are linear combinations of the weak  
 515 eigenstates, allowing for the mixing of flavors. Current experiments now seek to measure the  
 516 free parameters of this matrix.

517 Both the dark matter and hierarchy problems suffer in the fact that there is no clear model,  
 518 such as the PMNS matrix, to provide a theoretical solution. Out of the plethora of theories that  
 519 attempt to solve these problems, supersymmetry (SUSY) is the most popular in the theoretical  
 520 and experimental community. It suggests that there is a broken symmetry between fermions  
 521 and bosons, and introduces a partner to each Standard Model particle with a spin quantum  
 522 number less 1/2 [45]. For the hierarchy problem, this provides a set of particles to cancel out the

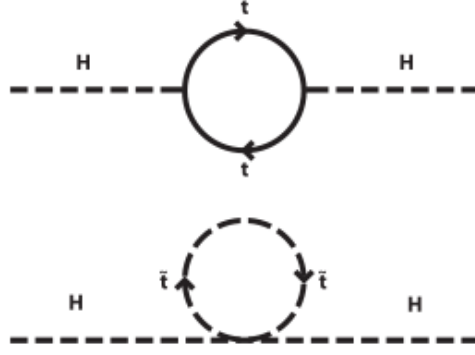


Figure 2.13: The cancellation of the divergent Higgs mass from a loop of top-quarks is cancelled by a loop of supersymmetric top-quarks, stop-quarks,

523 divergences in the NLO corrections to the Higgs mass. Figure 2.13 shows the Feynmann diagrams  
 524 for a supersymmetric top-quark, or stop quark, that would cancel the divergent contribution from  
 525 the Standard Model top quark. Depending on the specific form of the SUSY model, the stop  
 526 quarks can potentially couple directly or indirectly to the top-quark, producing them at a higer  
 527 rate during  $pp$  collisions. This would effect the number of observed events making it into the  
 528  $t\bar{t}H$  selection.

529 A number of extensions to the SM also involve introducing new top-like particles into the  
 530 theory. Vector-like quarks would be spin 1/2 particles that transform as triplets under the  $SU(3)$   
 531 color group and whose left and right-handed components have the same color and electroweak  
 532 quantum numbers [46]. These objects are common to several different types of models. Little  
 533 Higgs models [47] [48] [49], models with extra dimensions [50] [51], top-color models [52], and  
 534 composite Higgs models [53], include a vector-like top partner,  $t'$  that decays to a top-quark and  
 535 either a Higgs,  $W$ , or  $Z$  particle. Both  $t't'$  pair production and  $t't$  production would yield the  $t\bar{t}H$   
 536 final state, or at least one indistinguishable detector signature.  $t\bar{t}H$  search can provide indirect  
 537 limits on these models, by observing an excess or lack thereof of  $t\bar{t}H$  events, without having to  
 538 directly construct a  $t'$  resonance.

539 **Chapter 3**

540 **The Large Hadron Collider**



Figure 3.1: Aerial view of the LHC complex, spanning the French-Swiss border [1]

541 The Large Hadron Collider (LHC), is a superconducting, proton-proton, accelerator and  
542 collider operated by the European Center for Nuclear Research (CERN) laboratory in Geneva,  
543 Switzerland [54]. Figure 3.1 shows an aerial view of the LHC complex, with the main laboratory  
544 campus being labeled as CERN, with four of the detector experiments being labeled as ALICE,  
545 ATLAS, CMS, and LHCb. Three smaller experiments, not pictured, also use the LHC ring, and  
546 are TOTEM, LHCf, and MOeDAL. It was designed to elucidate the mechanism of electroweak  
547 symmetry breaking and explore TeV scale of particle physics. As such, it is required to produce  
548 a large number of high center-of-mass energy events. The high center-of-mass energy allows the  
549 creation of heavy particles, while a large luminosity allows for the creation of rare processes.  
550 The number of events produced at a collider is a product of the luminosity of the collider and

551 the total cross-section for the objects being collided.

$$N_{events} = L\sigma_{event} \quad (3.1)$$

552 The cross-section,  $\sigma_{event}$ , can be estimated from the theory of the Standard Model as described  
 553 in section 2.1 and validated by measurement at detectors, such as CMS, as shown in section 2.10.  
 554 The luminosity is a control of the experiment, and for Gaussian distributed beams, is given by  
 555 the equation:

$$L = \frac{N_b^2 n_b f_{rev} \gamma_r}{4\pi \epsilon_n \beta^*} F \quad (3.2)$$

556 The parameters of this equation and their value for the LHC is as follows:

- 557 •  $N_b$  - Number of particles per bunch, squared since there are two beams. The mechanism  
 558 of achieving such high energies is based in Radio-Frequency (RF) cavity technology, which  
 559 clusters the protons together into packets, which are all accelerated and collided together.  
 560 For the LHC,  $N_b = 1.15 \times 10^{11}$ .
  - 561 •  $n_b$  - Number of bunches per beam. The maximum design for the LHC allows for  $n_b = 2808$   
 562 bunches, however in practice, lower number of bunches have been run with in order to  
 563 create more time between bunch crossings.
  - 564 •  $f_{rev}$  - Revolution frequency of the protons in the LHC ring. This is determined by ring  
 565 circumference, and for the LHC,  $f_{rev} = 11.2$  kHz.
  - 566 •  $\gamma_r$  - This is the relativistic gamma-factor, determined by the speed, and thus the center of  
 567 mass energy of the collisions.
  - 568 •  $\epsilon_n$  - This is the normalized transverse emittance of the beam, which describes the RMS  
 569 spread of the beam in its transverse plane. For the LHC  $\epsilon_n = 3.75 \mu\text{m}$ .
  - 570 •  $\beta^*$  - Is the minimum of the  $\beta$  function, which is defined as the square of the transverse  
 571 beamsize divided by  $\epsilon_n$ . It is minimized at interaction regions, where the beams are being  
 572 squeezed into the smallest region possible, to maximize the probability of protons colliding  
 573 during each bunch crossing. For the LHC,  $\beta^* = 0.55$
  - 574 •  $F$  - This is the efficiency for having the two beams head-on, and is determined by the  
 575 crossing angle at which the two counter-rotating beams meet each other.
- 576 The LHC is designed to deliver a maximum luminosity of  $L = 10^{34} \text{ cm}^{-2}\text{s}^{-1}$  to the CMS and ATLAS  
 577 experiments, with a maximum center-of-mass energy of  $\sqrt{s} = 14$  TeV.

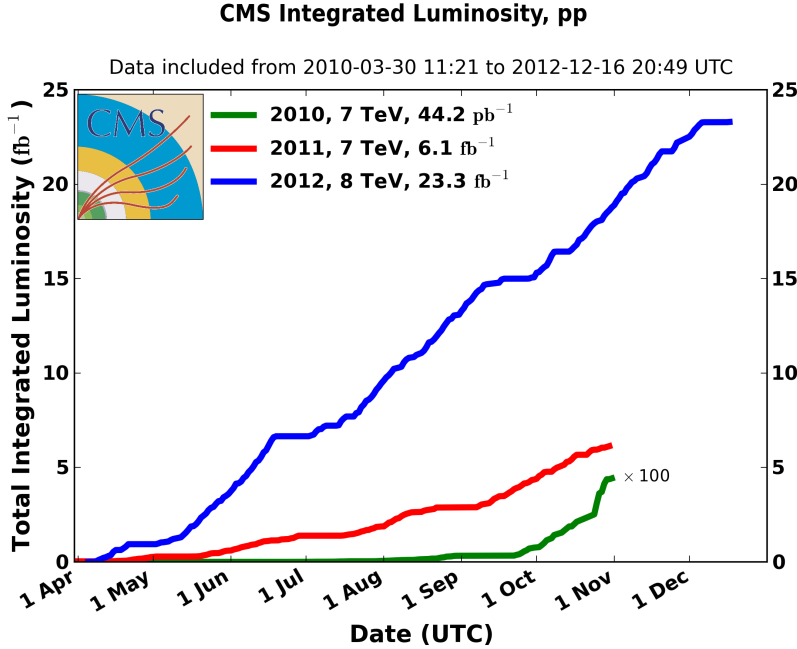


Figure 3.2: Integrated Luminosity delivered to the CMS experiment from 2010-12

578 In 2010-11, the LHC ran at center-of-mass energy,  $\sqrt{s} = 7 \text{ TeV}$  and delivered  $\sim 6 \text{ fb}^{-1}$  of  
 579 data to the CMS experiment. In 2012, it ran at  $\sqrt{s} = 8 \text{ TeV}$  and collected  $\sim 23 \text{ fb}^{-1}$ . Figure 3.2  
 580 shows a diagram of the luminosity collected as a function of time for each year running.

581 The next sections will describe the LHC accelerator complex, the chain of events leading  
 582 up to collisions of protons at the LHC, and the associated technologies that allow for the con-  
 583 trol and operation of the high-energy, high-luminosity beams that allow the CMS and ATLAS  
 584 experiments to search for heavy particles and rare-processes.

### 585 3.1 The LHC Accelerator Complex

586 The main LHC ring is a 26.7 km tunnel, that is 45 m to 170 m underneath the surface of the  
 587 earth, with 1.4% slope towards Lake Leman. It extends accross the French-Swiss border, into  
 588 the French coutnryside. The tunnel was originally constructed between 1984 and 1989 for the  
 589 Large Electron Positron (LEP) experiment that is famous for it's precision mesaurements of  
 590 several Standard Model parameters [54]. The choice to build the ring underground was driven  
 591 by real estate costs, but the underground setting also provides natural radiation shielding from  
 592 the beamline and greatly reduces the impact of cosmic radiation on the detectors.

593 The LHC also utilizes the existing accelerator complex from the LEP experiment, which is  
 594 shown in figure 3.3. The complex is composed a series of increasingly powerful accelerators that  
 595 gradually increase the energy of the protons.

596 Protons are initially accelerated by the Linac2 linear accelerator up to 50 MeV [55] [56]. A

## The LHC injection complex

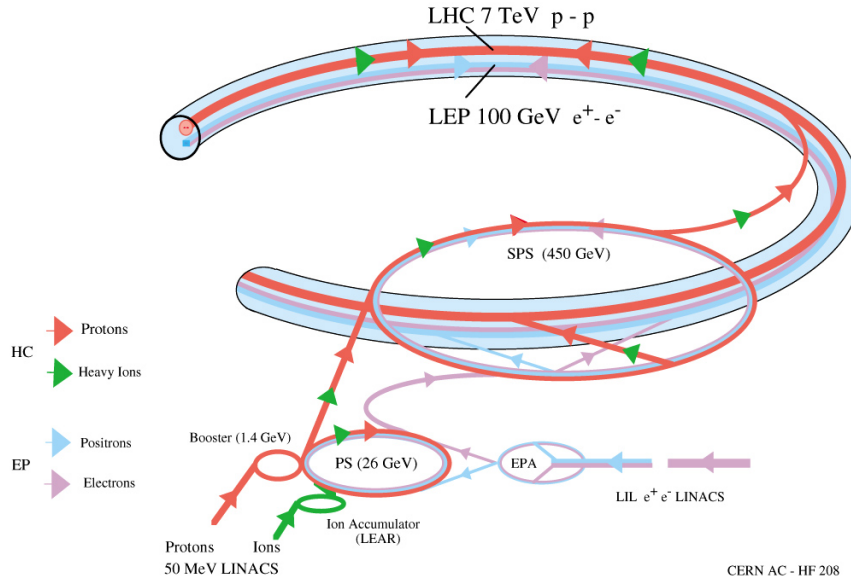


Figure 3.3: The LHC accelerator complex, taking protons from a bottle of Hydrogen at the Linac2, all the way to the LHC ring

bottle of Hydrogen is attached to a duoplasmatron source. This device ionizes the Hydrogen, and creates a 300 mA beam of protons, through a high-voltage anode, and a geometry designed to focus and collimate the beam as it leaves the device. Figure 3.4(a) shows a schematic for this device, showing the gas input on the left, and proton beam leaving to the right. Figure 3.4(b) shows the actual device used in the Linac2 at CERN. The proton beam then enters the Radio-Frequency Quadropole (RFQ) system, which accelerates and bunches the protons up to 750 keV. The RFQ is a waveguide with four flanges, which have been machined with a sinusoidal modulation in the longitudinal direction, which creates an standing electric wave in this direction, accelerating the protons. Figure 3.4(c) shows a schematic of this modulation, and figure 3.4(d) is a close-up image of this modulation in an actual RFQ. The last stage of acceleration is provided by three Alvarez tanks. Each Alvarez tank holds a series of elctrically isolated cylinders, known as drift tubes, coaxial with the main tank, with gaps in between them. An alternating electric field is present in the gaps, and space between each drift tube and the walls of the tank. Protons passing through the center of the drift tubes feel no electric field, but the gaps are located such that, a proton will always see an accelerating field in the gap, and are thus receive a boost of energy from each gap as it traverses the length of the three tanks. Figure 3.4(e) shows an image of the inside of an Alvaez tank, and figure 3.4(f) shows the tanks at the Linac2 at CERN. The final product is a 180 mA, 50 MeV proton beam, which is steered to the Proton Synchotron Booster for the next stage of acceleration.

The Proton Synchotron Booster (PS booster) complex accelerates the protons up to 1.4

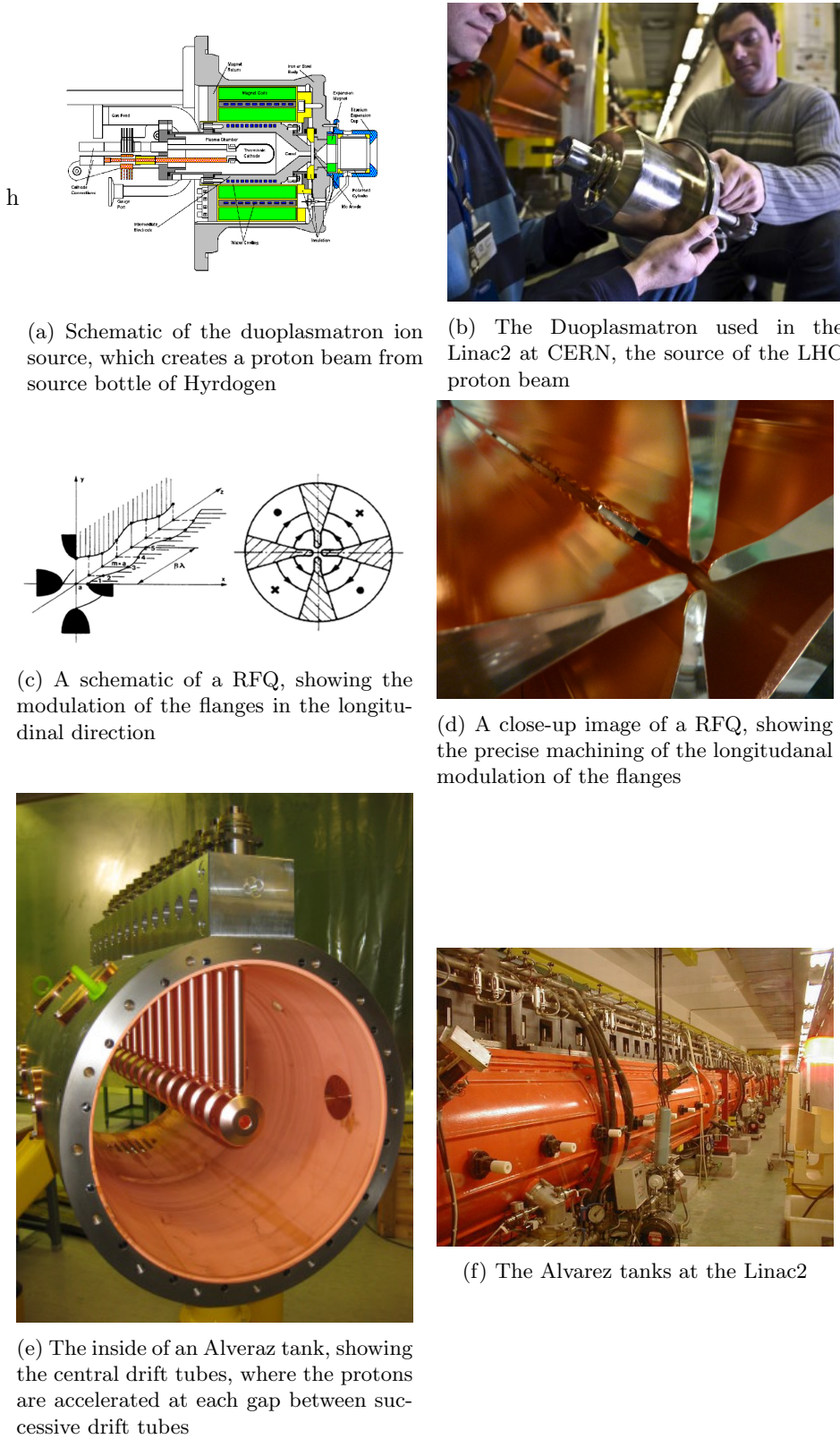


Figure 3.4: Features of the Linac2, the first stage of acceleration in the LHC injection chain

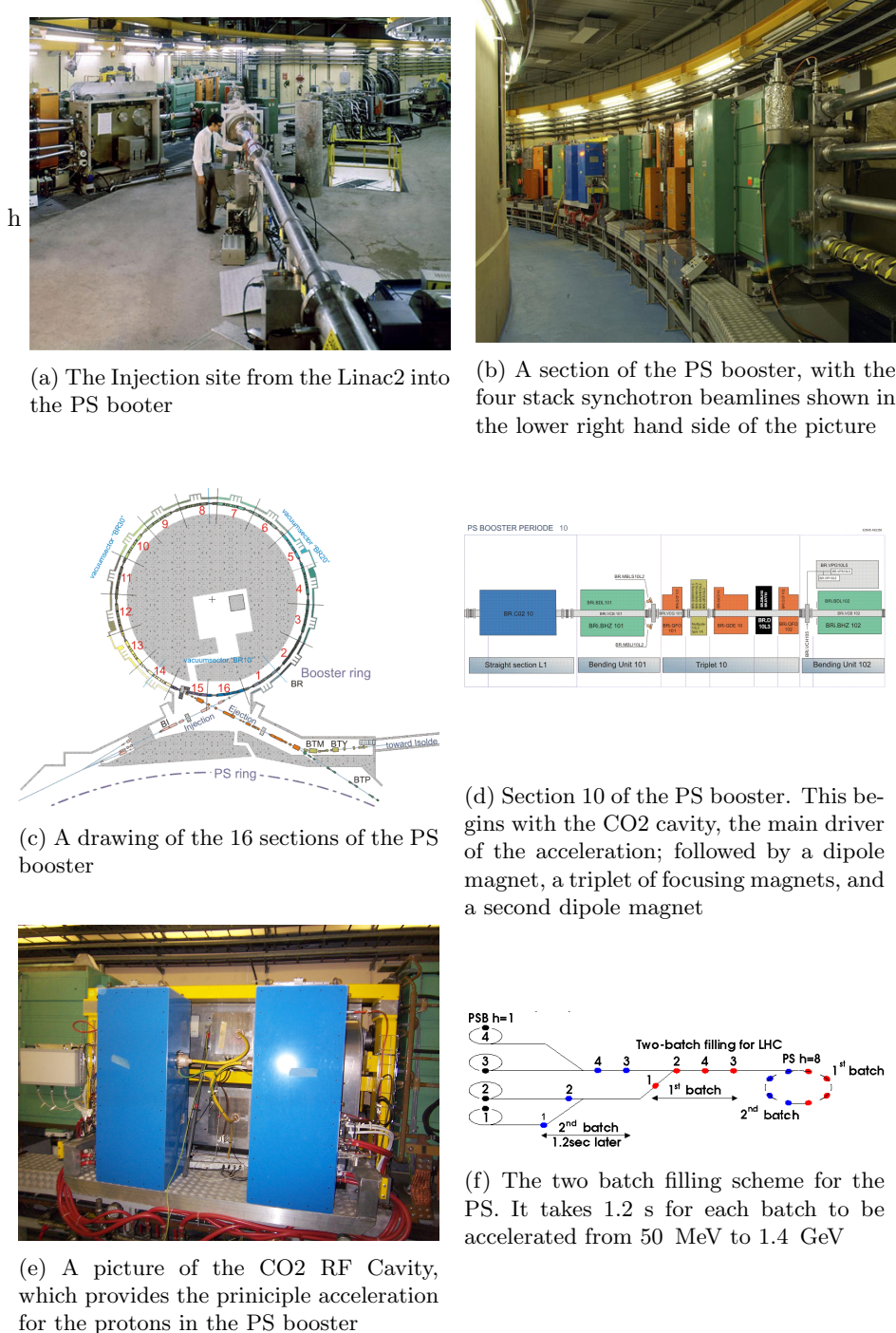


Figure 3.5: Features of the PS booster, the second stage of the LHC injection chain

617 GeV [55]. The complex takes the proton beam from the Linac2 and splits the beam into four  
 618 separate, synchrotrons, stacked on top of one another. Figure 3.5(a) shows the injection site of  
 619 the proton beam from the Linac2 into the PS booster. The right side of figure 3.5(b) shows the  
 620 four synchotron beam pipes stacked vertically on top one another. The splitting of the beam is  
 621 done in order to reduce the effect of the space charge of the proton beam, which would increase  
 622 the transverse emmitance beyond a tolerable degree. The PS booster uses thirty-two 0.87 T  
 623 dipole magnets to bend the beams, and fourty-eight quadrupoles to focus the beam as it makes  
 624 its way around each of the 50 m diameter rings. Each magnet is composed of a vertical stack  
 625 of four magnets, one for each of the synchotrons, and share a common yoke, allowing one power  
 626 supply to provide the current to all of them in series [57]. The booster is divided into 16 arcs, as  
 627 shown in figure 3.5(c). Each arc contains a bending dipole, 3 focusing quadrupoles, and a second  
 628 bending dipole, followed by a straight section containing beam diagnostic, injection and ejection  
 629 systems, and in three sections, the Radio-Frequency (RF) cavities, which is the mechanism of  
 630 accelerating the beam [58]. Figure 3.5(d) shows the layout of the tenth arc, which also contains  
 631 one of the RF cavities in the first section.

632 An RF cavity is a specially shaped, hollow conductor, that the beam passes through [59].  
 633 The shape of the cavity determines the resonant frequency and harmonics (integer multiples of  
 634 the fundamental frequency), of the standing electromagnetic fields that result when the cavity  
 635 is driven by an alternating voltage source. The idea is to choose a resonant frequency such  
 636 that the proton will always experience a positive electric field, and thus an acceleration, each  
 637 time it passes through the RF cavity. This means that the revolution frequency of the proton  
 638 must be equal to the fundamental frequency or harmonic of the RF cavity,  $f_{RF} = n \times f_{rev}$ , with  
 639  $n = 1, 2, 3, \dots$ . Eventually, the proton is accelerated up to an equilibrium speed and will enter the  
 640 cavity just as the standing electric field is alternating through it's zero point. If arrives too early  
 641 for this (moving too fast), then it will experience a negative electric force, a deceleration, which  
 642 will eventually bring it back to the equilibrium revolution frequency, where it experiences zero  
 643 net force. A diffuse beam of protons will be bunched into groups of protons through this effect  
 644 as well, as the faster protons in the beams are decelerated, and the slower ones accelerated,  
 645 until they all reach the same equilibrium revolution frequency. Driving the RF cavity with a  
 646 harmonic,  $n$ , of the proton's revolution speed will thus create  $n$  bunches of protons. Each one of  
 647 the potential  $n$  bunch positions is referred to as a bucket. In the case where a proton has to be  
 648 accelerated through a wide range of energies, the frequency of the cavity must also increase to  
 649 maintain synchronization with the proton revolution frequency.

650 Three types of RF cavities are used to accelerate the beam during each revolution. The first  
 651 of the three types of RF cavities is the CO<sub>2</sub>, with frequency range of 0.6 to 2.0 MHz and is used

652 to drive the  $h = 1$  harmonic of the synchrotron, and is pictured in figure 3.5(e). The second  
 653 type of cavity is the CO4 chamber, with a frequency range of 1.2 to 3.9 MHz, and drives the  
 654  $h = 2$  mode of the synchrotron. This second mode is capable of splitting the beam and creating  
 655 two separate bunch structures. However, for LHC running, only one bunch is used, and is driven  
 656 primarily by the  $h = 1$  mode. The  $h = 2$  mode is supplemental and is used to shape the beam.  
 657 A third type of RF cavity, CO16, has a frequency range of 5 to 16 MHz, and is used to control  
 658 the longitudinal shape of a bunch during acceleration. The beam leaves the PS booster and enters  
 659 the PS in a two-batch filling scheme, taking only 1.2 s to accelerate a second batch of protons  
 660 from 50 MeV to 1.4 GeV. This second batch enters just as the first batch has traveled to the  
 661 opposite side of the PS ring. A schematic of this process is shown in figure 3.5(f). To achieve  
 662 the 25 ns bunch spacing design of the LHC, only 6 bunches of proton beam need to be delivered  
 663 to PS. This is achieved by either using a 4+2 or 3+3 filling scheme, in terms of the number of  
 664 proton bunches derived from the four possible synchotrons.

665 The next stage is the Proton Synchrotron (PS), which will boost the protons up to 25  
 666 GeV [55]. The layout is shown in figure 3.6(a). The ring has a circumference of 628 m, and  
 667 uses 100 dipole magnets and 177 higher-order focusing magnets, to steer the beam around the  
 668 ring. Figure 3.6(b) shows a picture of one of the dipole magnets used at the PS. In addition  
 669 to providing acceleration up to 25 GeV, the PS forms the basis of the bunch structure that is  
 670 eventually used in the LHC. The  $h = 7$  harmonic is used to capture the 6 bunches of protons  
 671 delivered from the PS booster, leaving a gap in the place of a seventh bunch. The beam is then  
 672 split into three, by using three different RF cavities tuned to the  $h = 7, 14, 21$  modes of the PS.  
 673 Figure 3.6(c) shows a simulation of a proton bunch being divided into three over the course of  
 674 25 ms. The  $h = 21$  mode is then used to accelerate the protons to from 1.4 to 25 GeV using the  
 675 20 MHz RF cavity. Each bunch is then split twice, using the  $h = 21, 42, 84$  synchroton modes,  
 676 to create 72 bunches, spaced 25 ns apart, with a 320 ns gap for the 12 unused buckets of the  
 677  $h = 84$  harmonic. This process is simulated in figure 3.6(d), over the course of 125 ms. The 320  
 678 ns gap is created to account for the rise time of the kicker magnet, which ejects the beam out of  
 679 the PS into the SPS. The entire splitting process is summarized in figure 3.6(e). For the case of  
 680 50 ns bunch spacing, the final stage of splitting is not performed, and the  $h = 21, 42$  modes are  
 681 used to split the beam. Finally, in order to fit the bunches into the 200 MHz RF acceleration  
 682 scheme of the SPS, the bunch length must be compressed from 11 ns to 4 ns. This is achieved  
 683 by rotating the beam in the energy vs time phase space by sequential increases in voltage to  
 684 the 40 MHz  $h = 84$  mode, followed by an increase to the 80 MHz  $h = 168$  mode. Figure 3.6(f)  
 685 shows the result of this rotation - a distortion free ellipse with a smaller 4 ns spread, but a larger  
 686 spread in the energy spectrum of the proton beam.

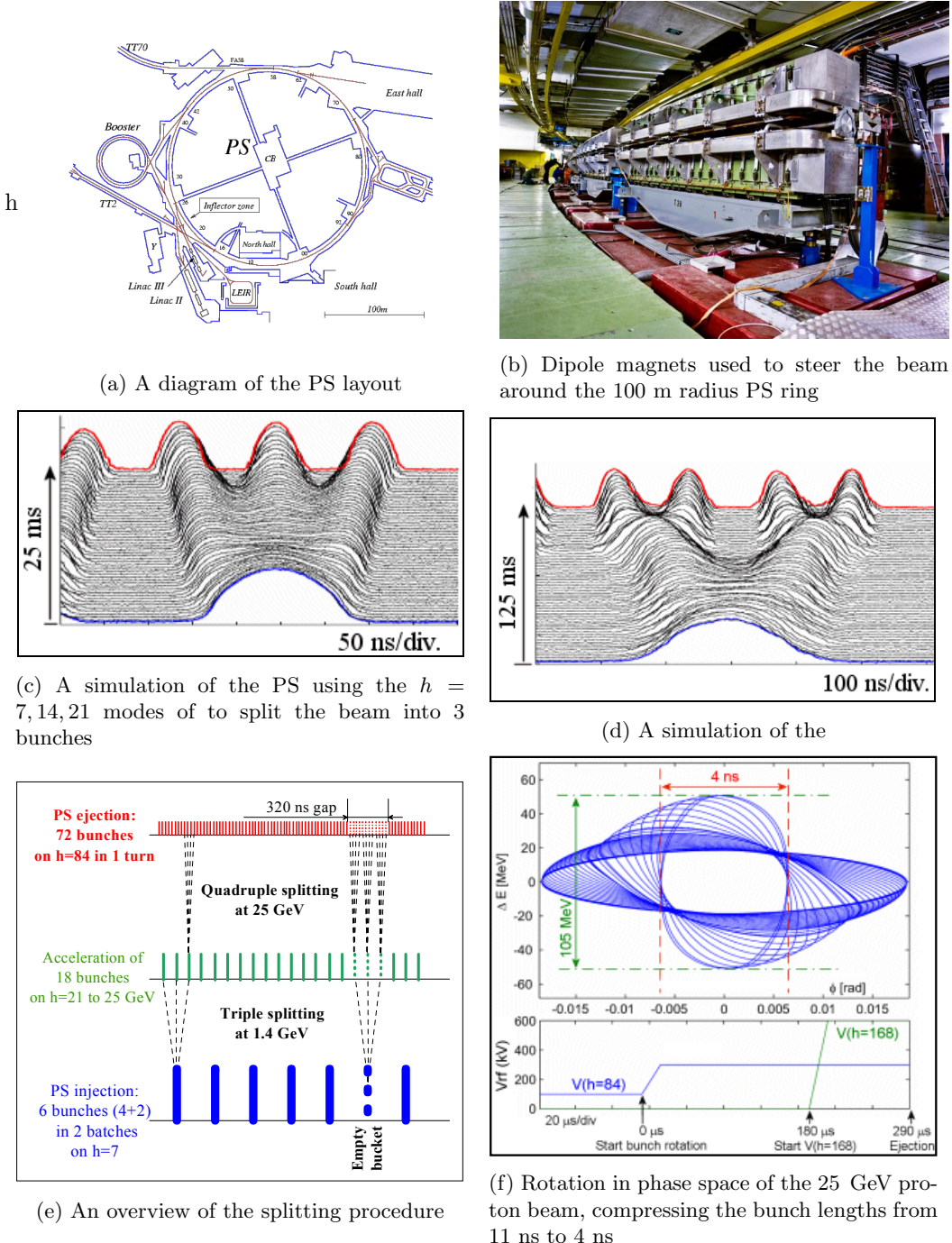


Figure 3.6: Features of the PS, the third stage of the LHC injection chain

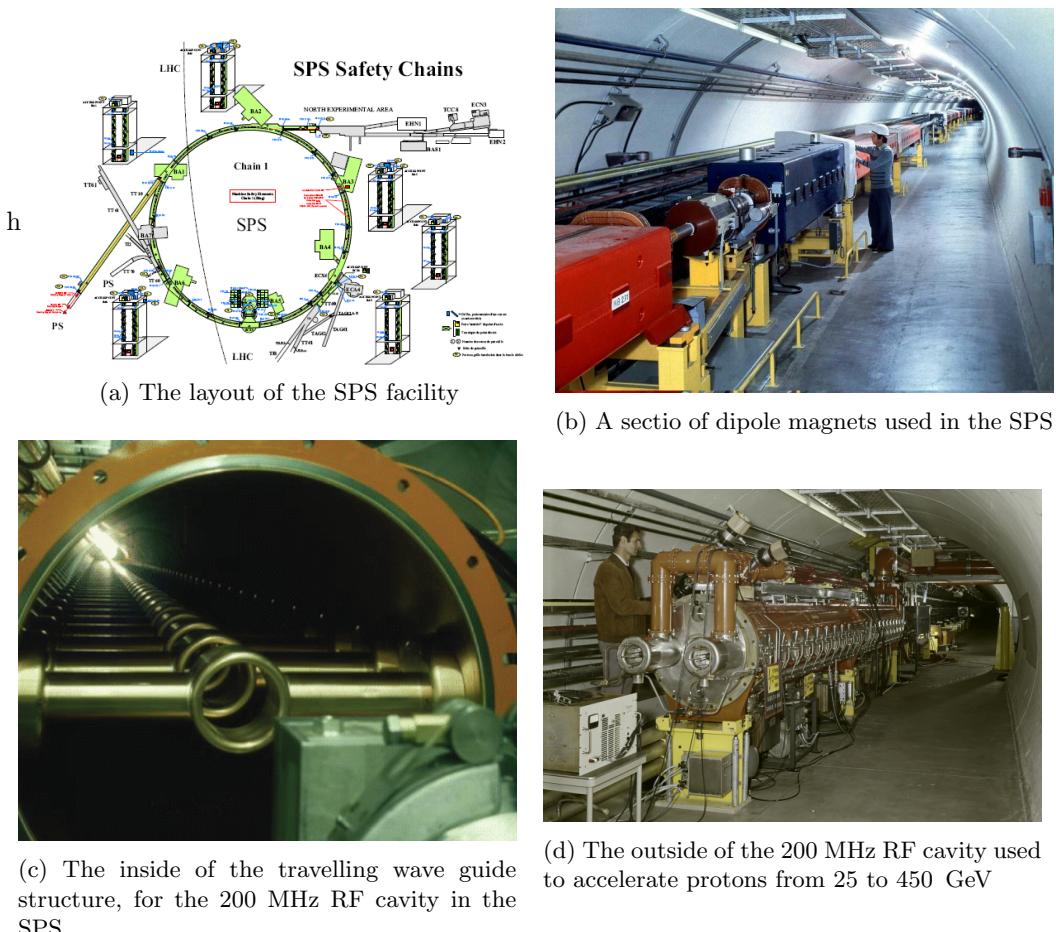


Figure 3.7: Features of the SPS, the fourth and final stage of the LHC injection chain

687 Next, the protons arrive at the Super Proton Synchotron (SPS), where they will be acceler-  
 688 erated to 450 GeV. The SPS is the last stage of acceleration before the protons are injected  
 689 into the LHC. The layout is show in figure 3.7(a). It has a circumference of 7 km, and steers  
 690 the proton beam with 744 dipole magnets, with 573 higher-order focusing magnets [60]. Figure  
 691 3.7(b) shows one of the dipole mangets in the SPS tunnel. Like all the other synchrotrons in  
 692 the injection chain, the acceleration is provided by RF cavities. A 200 MHz system of RF cavi-  
 693 ties capture and fill the SPS by using 2-4 batches of 72 bunch proton beams from the PS [55].  
 694 Although the relative change in frequency is small, the large degree of acceleration necessitates  
 695 the use of a tunable RF cavity. The 200 MHz system has 2 sections of 4 travelling wave cavities  
 696 in series, and another 2 sections of 5 cavities in series. Figure 3.7(c) shows the insde of this  
 697 structure, which uses drift tubes to accelerate protons in the gaps between tubes, with horzion-  
 698 tally mounted bars, spaced 374 mm [61] apart, determining the periodicity of the resonant RF  
 699 field that builds up inside. The outside of the structure is shown in figure 3.7(d). An additional  
 700 800 MHz system is used to control the transverse emmitance. It is also used to stabalize the  
 701 beam-line and prevent coupled-bunch instabilities [55].

702 Finally, protons are injected into the LHC ring in one clockwise, and another counter-  
 703 clockwise rotating beams. In order to work in the limited space of the existing LEP tunnel,  
 704 the two beams are contained within a single meachanical and cryostate structure, with a dual-  
 705 bore design for each of the beams. Here, each proton beam is accelerated to their final energy of  
 706 7 TeV, moving at 99.999991% the speed of light, before they meet head on, producing 14 TeV  
 707 center-of-mass collisions.

708 The LHC ring itslef is divided into eight octants, with eight straight sections that are located  
 709 in front and behind each of the eight collision points, where the beams are made to cross and  
 710 collide, as shown in figure 3.8. These crossings are known as interaction regions (IRs). Four  
 711 of these points are currently being used by experiments. TOTEM has detectors on either side  
 712 of the CMS experiment at one interaction region, known as point 5 (P5). LHCf has detectors  
 713 on either side of ATLAS at point 1 (P1). MOeDAL has detectors near LHCb at point 8 (P8)  
 714 and the ALICE detector is located at point 2 (P2). The following sections will cover the RF,  
 715 magnet, cryogen, and vaccuum technologies used in the LHC ring.

## 716 3.2 LHC Magnets

717 Several types of magnets are used in order to properly circulate and focus the proton beam as  
 718 it makes its way around the 26.7 km long tunnel. A complete list of all types, can be found in  
 719 the technical design report [62], as well as through CERN's outreach web resources [63]. This

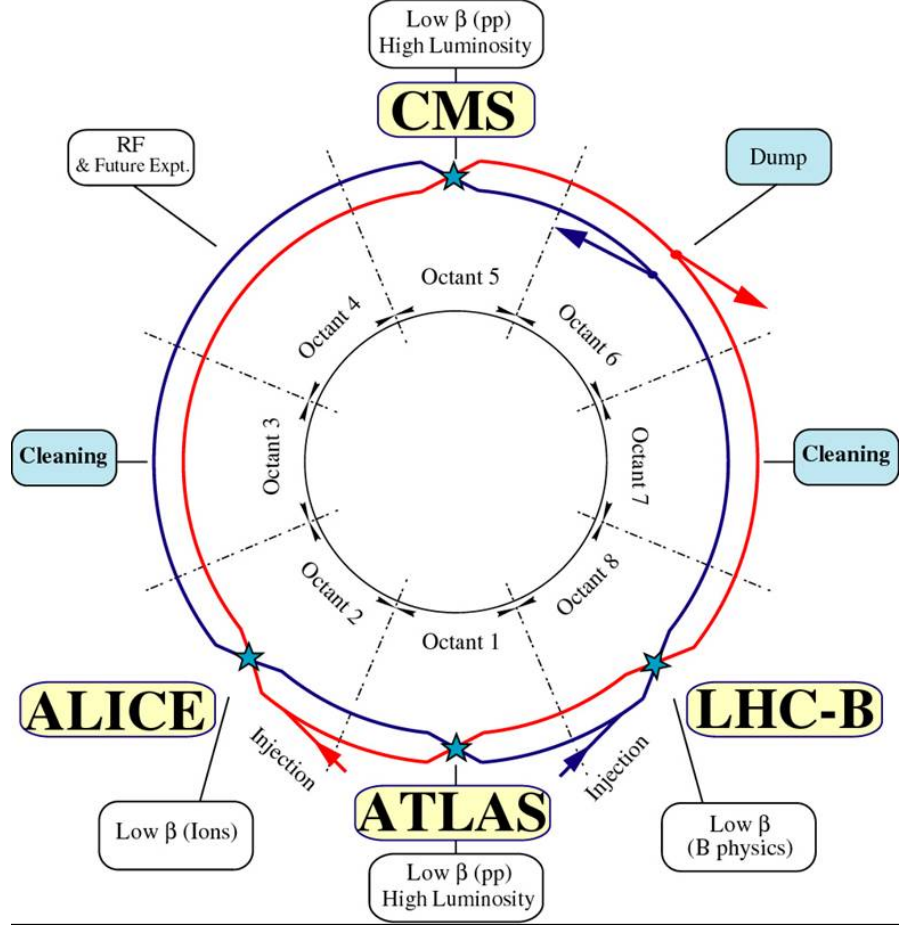


Figure 3.8: The LHC ring is divided into eight octants

section will give an overview of the a few of the critical subsystems: the septum and kicker magnets used for injection from the SPS, the dipole magnets used for bending the beam around the circumference of the ring, and the higher-order-pole magnets that are used for focusing the beam.

The injection and extraction of proton beams from one synchrotron to another involves three types of magnets, septums, kickers, and bumpers. Septum magnets contain a partition, or a septum, that provides a boundary between a high magnetic field region and a near-zero magnetic field region and are operated in DC or a slow-pulsed mode [64]. In case of injecting a beam of protons into a synchrotron, the target beampipe of the synchrotron passes through the low-field region, so the trajectory is unaffected by the high-field region, which bends the injection beam towards the synchrotron aligning it horizontally, with the target beam. The kicker magnet, is a fast-pulsed magnet and provides the timing selection in order to make a final bend vertical bend into the synchrotron orbit, and into the correct basket of the synchrotron bunch train [65]. Finally, bumper magnets make small bends to the beam and align it with the injection site. Figure 3.9 shows a schematic for this process, where a transfer line brings protons to a septum, which bends the beam to a kicker, which makes the final corrections to match the synchrotron

## Single-turn injection

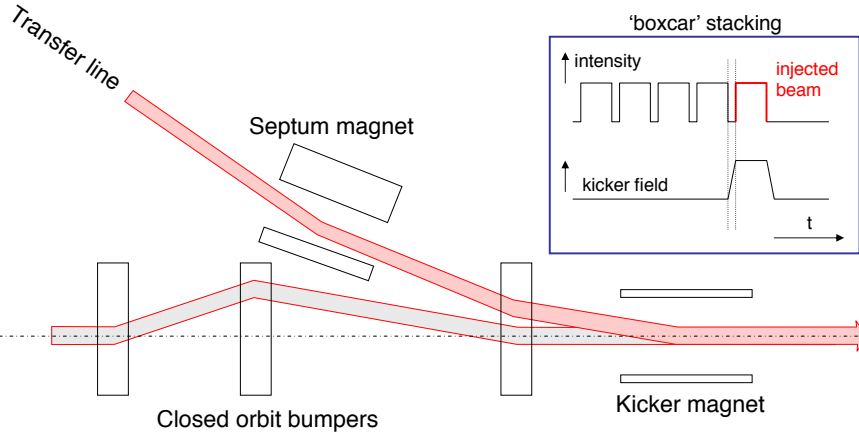


Figure 3.9: The single turn injection scheme. A septum magnet makes the initial alignment. The kicker magnet times the injection and makes the final alignment. Bumper magnets align the LHC beam with the injected beam.

736 orbit. For extraction, the kicker magnet quickly displaces a portion of the beam, which is steered  
 737 away by the septum, while the original beam passes through its low-field region unaffected.

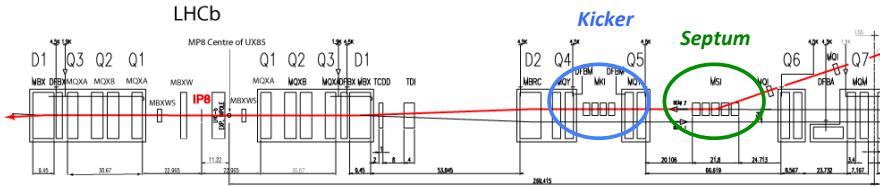


Figure 3.10: Layout of Interaction Region 8, where one proton beam is injected into the LHC ring. A transfer line from the SPS brings a proton in from the right. In green, a septum magnet aligns the beam horizontally with the LHC. In blue, a kicker magnet makes the final vertical alignment into the LHC, and is timed to fill one of the 400 MHz buckets of the RF capture system

738 At the LHC, beam is injected at Interaction Regions (IR) 2 and 8 [54]. Two transfer lines  
 739 bring the beam extracted from the SPS to  $\sim 150$  m of the LHC ring. Five Labertson-type septum  
 740 magnets, of field strength  $\sim 1$  T, are used to deflect each of the transfer line beams 12 mrad  
 741 to align the transfer beam horizontally with the LHC orbit. Then, four  $\sim 0.12$  T MKI kicker  
 742 magnets quickly deflect the beam 0.85 mrad to close the orbit with the LHC ring. Figure 3.10  
 743 shows the layout of the injection point at IR 8. The green circle encloses the septum structure,  
 744 which provides the horizontal alignment, and the blue encloses the kicker structure, which makes  
 745 the final vertical alignment and synchronizes the injection of the beam into the LHC. The rise  
 746 time for the field provided by the kicker magnets in the LHC and SPS determine the final bunch  
 747 structure of the LHC. Figure 3.11 extends figure 3.6(e) showing how the rise times of the kickers  
 748 that inject, or eject beam create gaps in the bunch structure of the LHC. The initial filling of the  
 749 PS with 6 batches of protons from the PSB, leaves one initial bucket unused in the PS. After

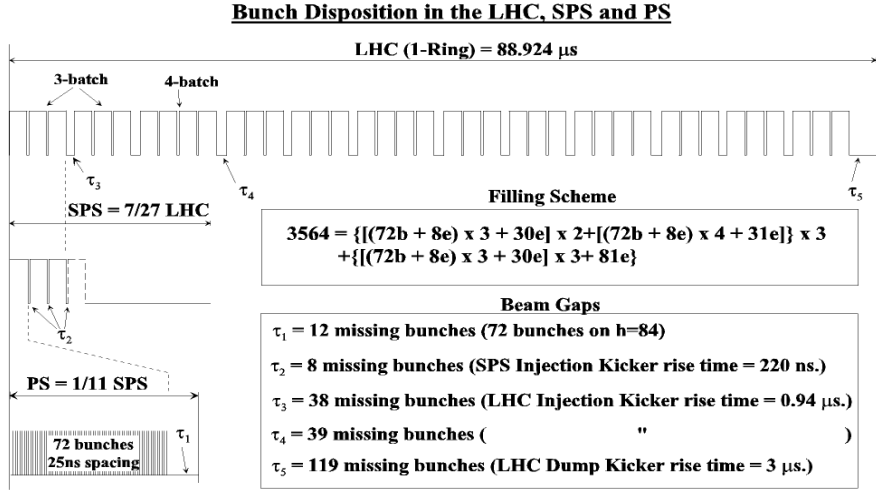


Figure 3.11: The initial filling of 6 batches of protons from the PSB to the PS, leaves 12 empty buckets in the PS bunch structure. The rise time of the SPS magnet creates an additional gap in the SPS bunch structure. Additional gaps emerge due to the rise time of the LHC injection and dumping kicker magnets

750 the splitting of the beam into the 25 ns bunches, there 12 empty buckets at the of the PS bunch  
 751 train. The SPS is filled with three to four of these trains, leaving an additional 8 25 ns buckets  
 752 unfilled due to the 220 ns rise time of the SPS kicker magnet. These three to four trains are  
 753 then injected into the LHC, where there are 38 or 39 bunch gaps due to the LHC injector 0.94  
 754  $\mu$ s rise time. At the end of a full LHC orbit, 119 buckets are left empty to allow for the rise time  
 755 of the beam dumping kicker magnet, used to remove beam from the LHC.

756 Once the beam is injected, the curved path around the circumference of the LHC is main-  
 757 tained via 1232 superconducting dipole magnets. The superconducting material niobium-titanium,  
 758 NbTi, is cooled to 1.9 K in order to produce the 8.33 T field. Figure 3.12(a) shows a cross-section  
 759 view of one of the LHC dipoles. The dual-bore design of the beam-pipe is enclosed by an iron  
 760 yoke, that serves as the cold mass to maintain the superconducting temperature, and provides  
 761 a 195 mm gap between each beam. A close up picture of the non-magnetic collar and supercon-  
 762 ducting coils are shown in figure 3.12(b). A simulation of the magnet in figure 3.12(c) shows the  
 763 homogenous, vertical magnetic field produced in the center of the coil. Diagram 3.12(d) shows  
 764 an exaggerated view of the 2812 m radius curvature of each dipole. However, since each dipole  
 765 is only  $\sim 14$  m in length, this curvature is hardly noticeable, as shown in a photo of an actual  
 766 dipole magnet in a staging area at CERN, awaiting installation in figure ??(e).

767 Quadrupole, septupole, octupole, and other multipole magnets are used to focus a single  
 768 beam, as well as squeeze the two beams together. There are 392 quadrupole magnets on the  
 769 LHC ring, each controlling the height and width of the beam. Figure 3.13(a) shows a schematic  
 770 of a dual-bore quadrupole magnet, and figure 3.13(b) shows an actual quadrupole in a staging  
 771 area before installation. Quadrupole magnets use four sets of coils to create a magnetic field that

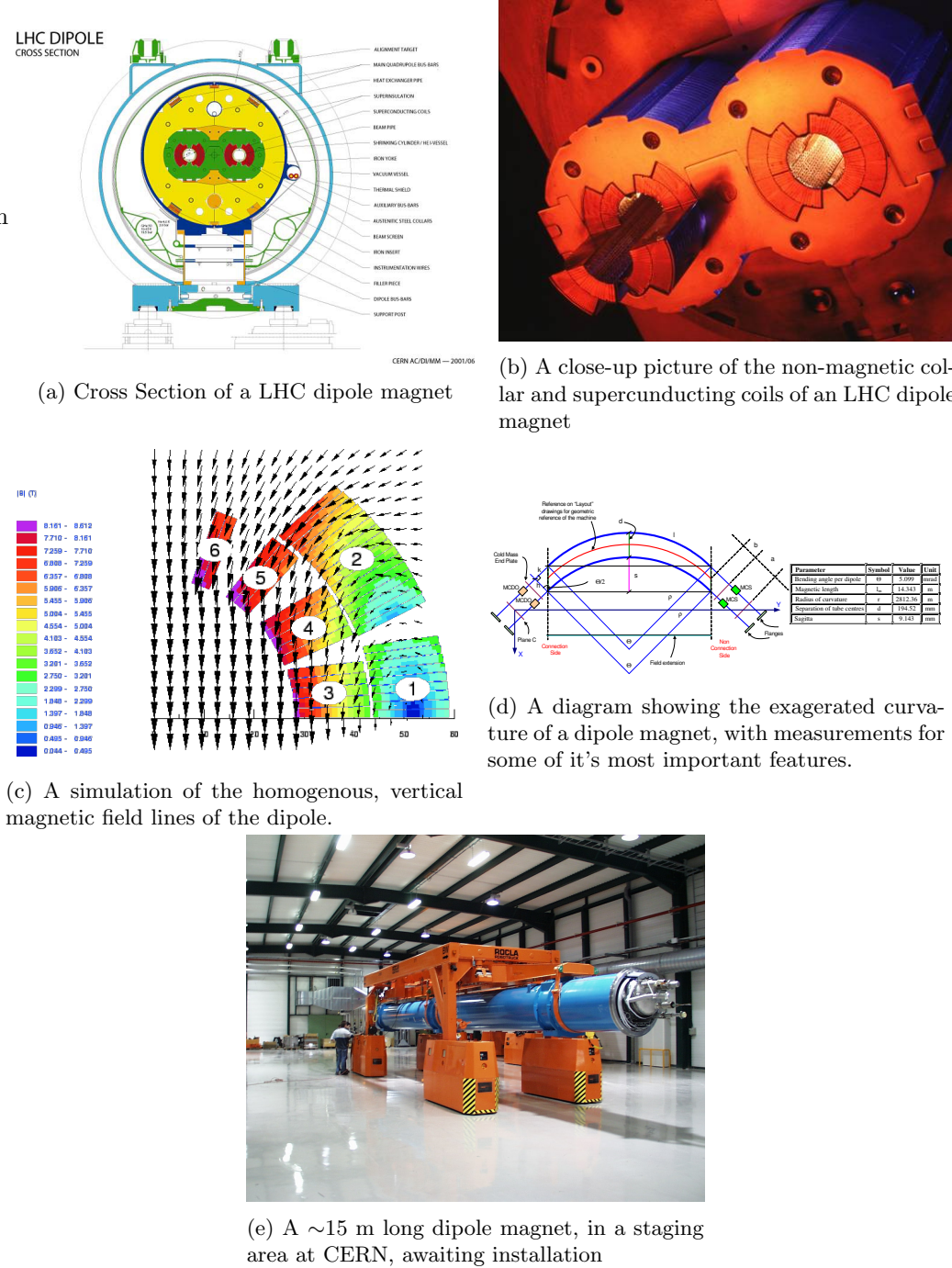
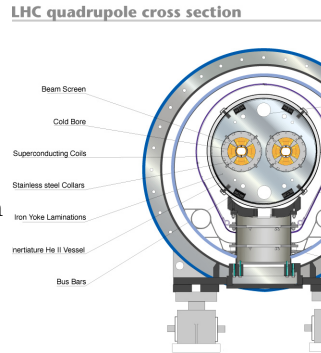


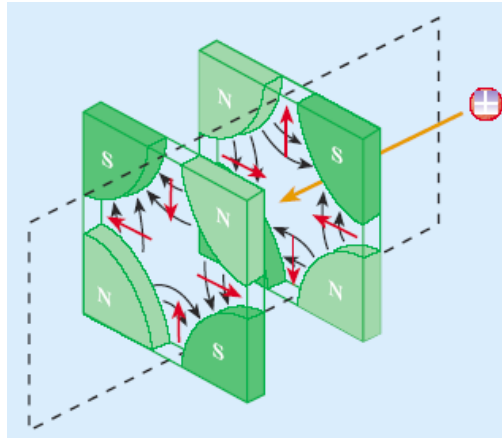
Figure 3.12: Features of the dipole magnets used in the LHC



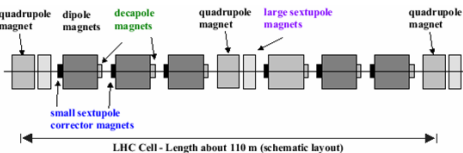
(a) Cross Section of a LHC quadrupole magnet



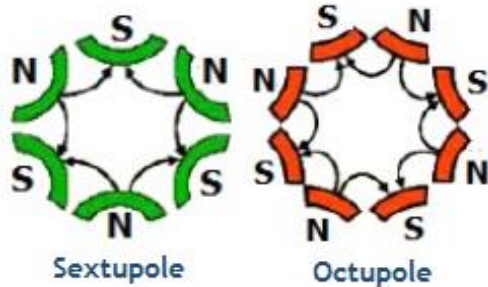
(b) A dual-bore quadrupole magnet, in a staging aread prior to installation



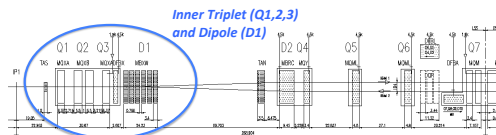
(c) A quadrupole magnet can provide focusing either in the horizontal or vertical direction



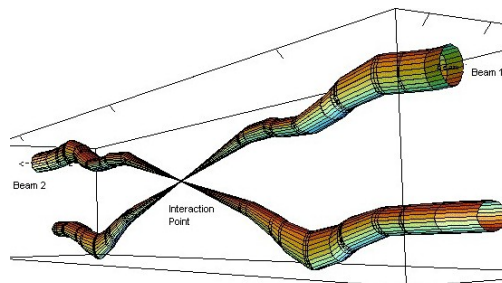
(e) A typical 110m long magnetic cell at the LHC featuring several types of multipole magnets



(d) Multipole fields from a sextupole and an octupole magnet



(f) Schematic of the Inner triplet structure that brings the two separate beams together in the interaction region



(g) A simulation of two beams being squeezed together by the inner triplet.

Figure 3.13: Features of the dipole magnets used in the LHC

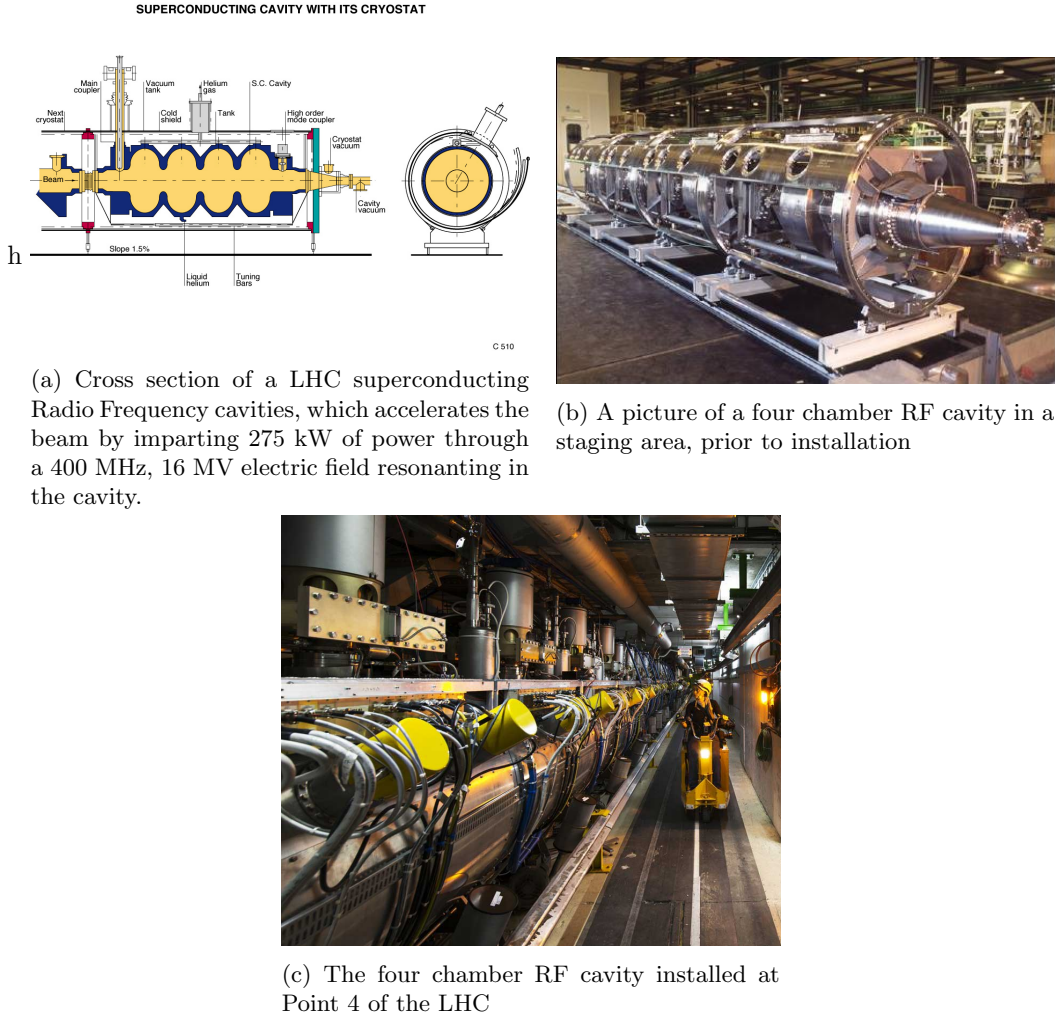


Figure 3.14: Features of the 400 MHz superconducting RF system used in the LHC

either squeezes the beam horizontally or vertically, as shown in figure 3.13(c). Finer corrections to the beam shape are made with the multipole magnets, since they are able to compress the beam from more than two axes. Figure 3.13(d) shows the fields lines of a sextupole and octupole magnet. A typical cell of magnets, 110 m long, in the LHC beamline is shown in a diagram in figure 3.13(e), where the dipole, quadrupole and higher order magnet work in series to confine the protons to the LHC ring. Finally, a set of single bore magnets, known as an inner triplet, bring the two beams together into an interaction region. Figure 3.13(f) shows the arrangement of magnets that squeeze the beam together, while figure 3.13(g) shows a simulation of the beams being brought together to collide in the interaction region.

### 3.3 LHC RF Technology

The LHC uses a 400 MHz superconducting RF cavity system to capture and accelerate the beam from 450 GeV to 7 TeV [54]. Two independent system are used to provide 8 MV of RF voltage

at injection at 16 MV during equilibrium at 7 TeV and deliver 275 kW of power to each beam. This is provided by 16 niobium sputtered cavities, housed in 4.5 K refrigeration units, known as cryomodules, at Point 4 of the LHC octant. The superconducting material covering the inside of the cavity has near-zero resistivity, which dissipates much less power and has a much narrower resonance width, or Q-factor, than a cavity made from normally conducting material. Figure 3.14(a) shows a schematic of a four cavity cryomodule. The beam pipe passes through the center of each chamber and longitudinal (left to right in the diagram) electric fields accelerate the protons each time they circulate the LHC ring. Figure 3.14(b) shows an actual four cavity module in a staging area prior to installation. In this picture, the resonance cavities are concealed underneath the cylindrical housing of the vacuum tank and cryostat. Figure 3.14(??) is a picture of the module installed at Point 4. The thin cylindrical structures extending off the top is the LHe intake valve and quench system. The thicker cylindrical structures are the waveguides that couple the cavities to the source of the electric field, the klystrons.

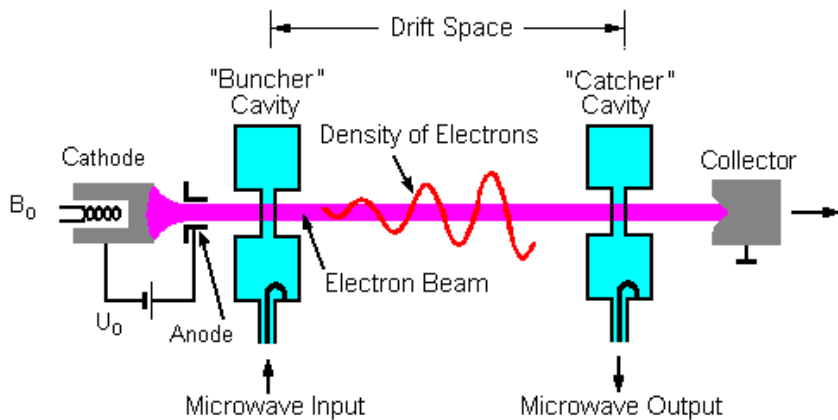


Figure 3.15: A klystron uses a weak RF signal coupled to a resonance cavity to bunch an electron beam, which in turn creates an amplified RF signal as it passes through a second resonance cavity tuned to the same frequency.

A Klystron is the source of RF power that builds up as a resonance in the cavities that accelerate the protons. Figure 3.15 shows a diagram of the basic operating principle. The device uses an anode to accelerate the thermionic emission of electrons off of a cathode material into one or more bunching cavities tuned to the frequency the device is designed to produce. This cavity is driven with a weak RF source, that groups electrons into bunches. Just as discussed for protons earlier, when electrons arrive at the entrance of the cavity at just the right time, it will experience the zero-point of the oscillation of the resonating electric field. If it arrives early or late, it is accelerated or decelerated and thus bringing it closer to its neighbors, and increasing the density of the beam. After passing through multiple chambers, the tightly bunched electrons enter a catcher cavity tuned to the same resonance frequency. As the electrons pass through at

807 this resonance frequency, standing electric waves are excited and quickly build up in the catcher  
 808 cavity. The electron beam is thus used to amplify the original RF signal in the catcher cavity,  
 809 which is then transported via waveguide to power the RF cavity used to accelerate the proton  
 810 beamline.

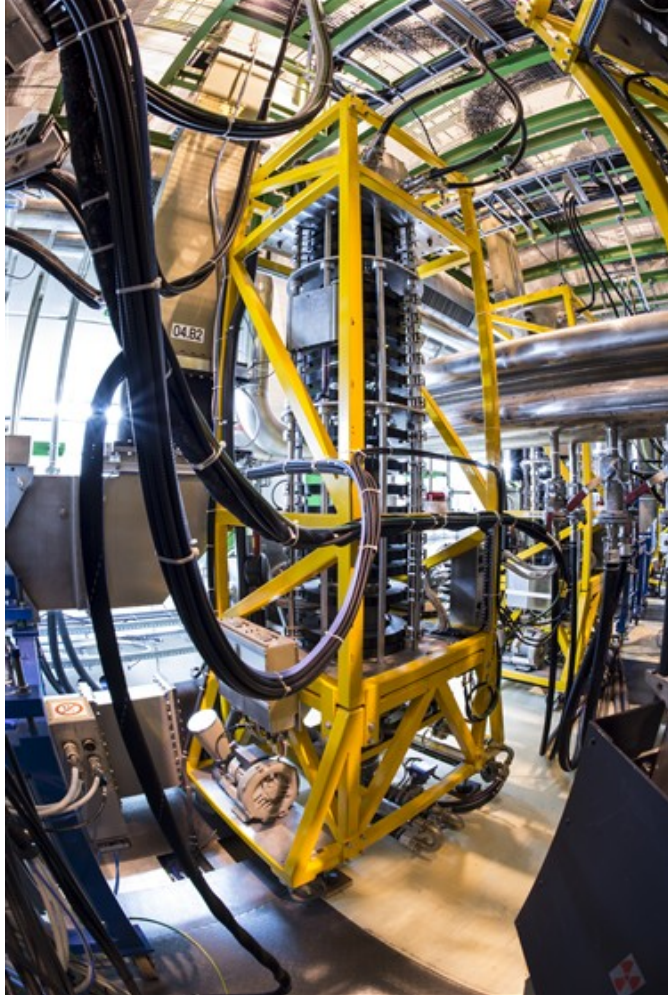


Figure 3.16: One of sixteen 300 kW, 400 MHz klystrons that power the superconducting RF cavities that accelerate the proton beam.

811 At the LHC, 16 400 MHz, 300 kW kylstrons, work together to provide 4800 kW of power  
 812 to the superconducting RF cavities [54]. They are also located at Point 4, in the UX45 service  
 813 cavern adjacent to the RF cavities, about 6 m below the beamline. An average of 22 m of  
 814 waveguide is used to transport the power generated by the klystrons to the RF cavities. Figure  
 815 3.16 shows a klystron installed at the LHC, and like most modern klystrons, it also utilizes a  
 816 multi-bunching chamber design.

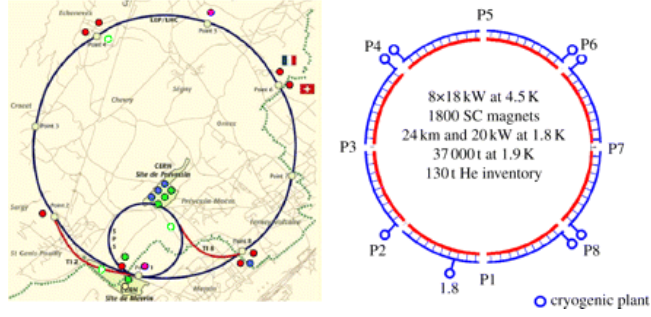


Figure 3.17: Layout of the five cryogenic islands, which are home to the eight facilities that provide liquid helium to the LHC



(a) The compressor station for the 4.5 K refrigeration system

(b) The 4.5 K refrigeration system cold box, containing heat exchanging fins and turbines to cool the He

Figure 3.18: Features of the 4.5 K refrigeration system

## 3.4 The LHC Cryogen System

The LHC is the largest cryogenic system in the world [66], as its operating temperature is 1.8 K, in order to produce the high-magnetic fields needed by the dipole magnets. Additionally, the acceleration mechanism, the RF cavities, are also superconducting, and must be cooled to 4.5 K. Over 120 tons of Helium are used as the cryogenic medium, since once it is cooled below 2.17 K, it becomes a superfluid, a phase of matter with a high thermal conductivity, making it ideal for refrigeration. Cryogenic and auxiliary equipment are concentrated into 5 cryogenic islands at Points 1,2,4,6, and 8 [54]. As shown in figure 3.17, Point 4,6, and 8 house two facilities each, making a total of eight, one for each octant of the LHC arc.

At each cryogenic plant, He is cooled to 80 K by circulating it through refrigeration equipment with liquid nitrogen in the heat exchangers[66]. Next, the He is brought to 4.5 K with refrigerators recovered from the LEP experiment [67]. The He gas is first compressed and allowed to expand, where it is cooled by losing energy through mechanical turbo-expanders that run at up to 140,000 rpm on helium-gas bearings. Figure 3.18(a). The He is then liquified after passing through a vacuum sealed box containing heat exchangers and more turbo-expanders [68].

832 The compressor for this system is pictured in figure 3.18(b). Finally, the liquified He is brought  
 833 to 1.8 K with a refrigeration unit that uses a cold compression train to decrease the saturation  
 834 pressure, and thus temperature as well.

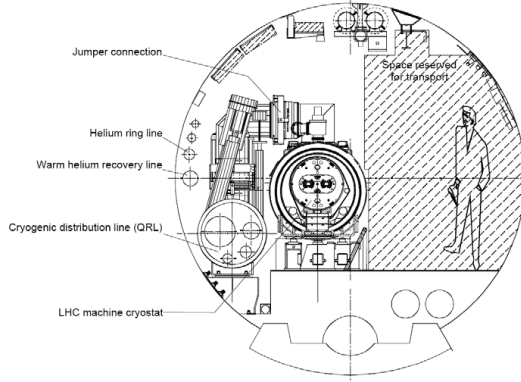


Figure 3.19: Cross section schematic of the cryogenic distribution system in the LHC tunnel

835 In the LHC tunnel, a cryogenic distribution line runs parallel to the machine [67]. It consists  
 836 of eight 3.2 km long cryostats, that contain the equipment to supply and recover helium with  
 837 temperatures ranging from 4 K to 75 K. A total of 310 service modules, are used to control the  
 838 system and provide safety mechanisms against pressure buildup and magnet quenching. Figure  
 839 shows a cross section of the cryogen distribution system in the tunnel.

### 840 3.5 The LHC Vacuum System

841 The LHC is also the largest operational vacuum system in the world and is capable of achieving  
 842 pressures lower than outer space [69]. Three different types of vacuum systems are used: one for  
 843 insulating the helium distribution lines, another for insulating the dipole magnets, and a final  
 844 ultra-high vacuum system for the beam pipe [54].

845 The vacuum systems for insulating the helium distribution and dipoles involves some 104 km  
 846 of piping an over 250,000 welding joints [69]. Pressure here is required to be kept at  $10^{-1}$  mbar,  
 847 but at cryogenic temperatures, pressures tend to equalize at a much lower level, to  $10^{-6}$  mbar  
 848 ( $\sim 10^{-9}$  atm) [54].

849 The most stringent requirements come on the vacuum of the beam-pipe. The beam must  
 850 minimize the number of interactions it has with any particles outside of the interaction region.  
 851 A pressure of  $10^{-10}$  to  $10^{-11}$  mbar are maintained in the 54 km of beampipe [69]. Weeks of  
 852 cryogenic pumping, eventually condenses gas trapped in the beampipe into a liquid that can be  
 853 absorbed by the walls of the beampipe. The inside beampipe is also coated with a thin layer

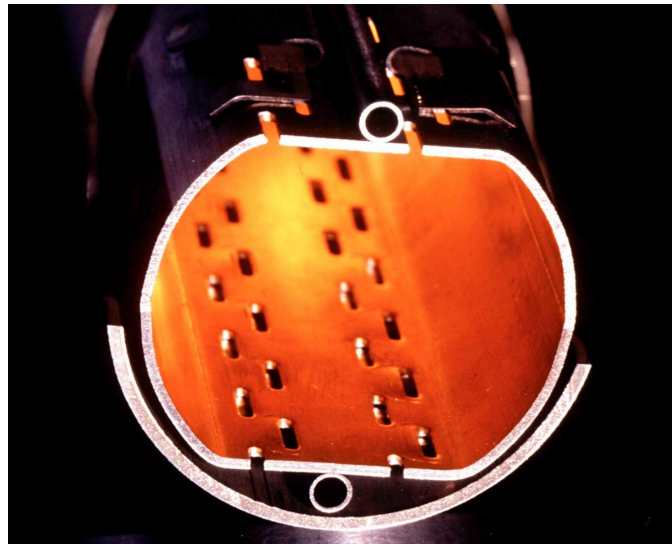


Figure 3.20: Beam screen for the LHC, with slits to allow for easy pumping of residual gas molecules in the beampipe.

of a special substance developed at CERN, a titanium-zirconium-vanadium alloy, which absorbs residual particles when heated. 780 ion pumps are used to remove the noble gases and methane, which do not interact with the substance, which acts as its own distributed pumping system. Room-temperature sections of the beampipe are also heated to  $300^{\text{deg}}$  to be baked-out from the outside. This is done to periodically remove any material which may have settled and become trapped. Additionally, the beam-pipe is designed with a racetrack shape, which optimises the available aperture while leaving space for the cooling tubes, as shown in figure 3.20. Slits also allow for gas molecules to be easily pumped out from inside its volume.

862 **Chapter 4**

863 **The Compact Muon Solenoid**

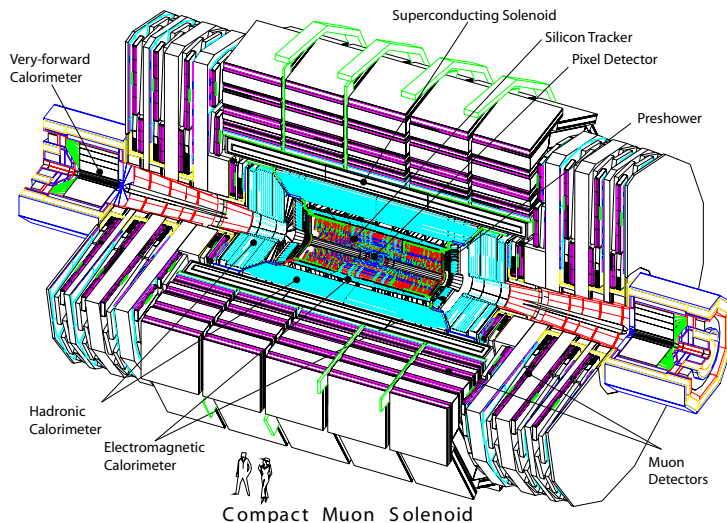


Figure 4.1: A cutaway diagram of the CMS detector. Two humans are present at the bottom of the image to provide scale.

864 The Compact Muon Solenoid (CMS) experiment is a general-purpose particle detector ca-  
865 pable of performing a wide range of physics measurements at the TeV energy scale. It provides  
866 hermetic,  $4\pi$ , coverage surrounding the interaction region on Point 5 of the LHC octant, and  
867 is capable of identifying and reconstructing charged and neutral hadrons, photons, electrons,  
868 and muons directly. Tau leptons, are measured indirectly through a careful reconstruction of  
869 its decay products. The hermetic coverage allows the detection of neutrinos by measuring a  
870 momentum imbalance in a given collision. The detector is assembled in five sections and weights  
871 over 14,000 tons. The "Compact" part of the experiment's name comes from its relativley small  
872 volume for a modern particle detector, with length of 28.7 m and a diameter of 15.0 m. Ironi-  
873 cally, this is as tall as most 4-5 story buildings and weights as much as  $\sim$ 7000 cars. Figure 4.1  
874 shows a cutaway drawing of the CMS detector.

A right-handed coordinate system is used to measure particle positions within the detector. The origin is centered at the nominal interaction point with the  $\hat{x}$  direction pointed towards the center of the LHC ring, the  $\hat{y}$  direction towards the sky, and the  $\hat{z}$  direction pointed counter-clockwise along the LHC ring towards Point 2 and the ALICE experiment. In the much more natural polar coordinates,  $\hat{r}$ , points radially outward from the interaction point, the azimuthal angle  $\hat{\phi}$  is measured as the angle relative to the  $\hat{x}$  axis, and the polar angle,  $\hat{\theta}$ , is measured as the angle relative to the  $\hat{z}$  axis. An important lorentz invariant position variable is the rapidity,  $y$ , and its approximation in terms of the polar angle, the pseudorapidity,  $\eta$ :

$$\begin{aligned} y &= \frac{1}{2} \ln \left( \frac{E + p_z c}{E - p_z c} \right) \\ \eta &= -\ln \left( \tan \frac{\theta}{2} \right) \end{aligned} \quad (4.1)$$

The psuedorapidity is useful since it is an approximately lorentz invariant version of polar angle, which allows for a more intuitive understanding of the distribution of particles when boosting into different measurement reference frames. The component of the momentum transverse to the beamline,  $p_T$  is the most common form of measuring the momentum, and is defined as  $p_T = |p| \cos \phi$ .

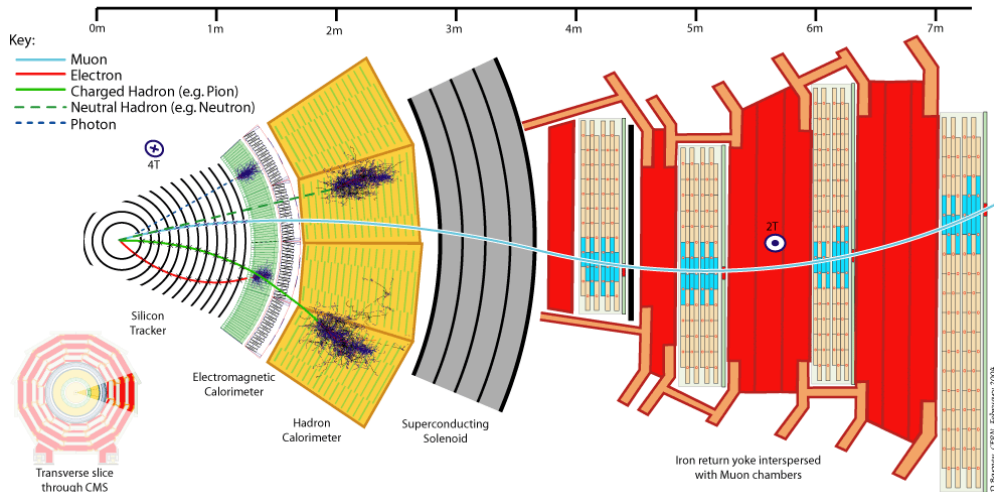


Figure 4.2: A slice of the CMS detector showing how various particles interact and deposit energy. The trajectory of charged particles is measured in the tracker; electrons and photons deposit most of their energy in the ECAL; charged and neutral hadrons deposit most of their energy in the HCAL; the muon chambers measures the trajectory of muons or long-lived charged particles

CMS is composed of a system of sub-detectors, each specialized in measuring a certain type or characteristic of a particle. They are arranged approximately as concentric cylinders of increasing radius, wrapped around the interaction region of the  $pp$  collisions and an analogy is often made between the layers of subdetectors being similar to the layers of an onion. The closest sub-

detector to the interaction region is the tracker system. It is an all silicon pixel and strip detector, with a high precision position resolution, which is used to identify the trajectory of charged particles close to the primary vertex of a collision. The Electromagnetic Calorimeter (ECAL) is the next layer, and is used to absorb energy of electromagnetically interacting particles. It uses lead-tungstate ( $\text{PbWO}_4$ ) crystals which act as both the absorbing and scintilating medium for energy deposited by charged particles and photons as they pass through this sub-detector. The Hadronic Calorimeter (HCAL) uses brass and steel tiles to absorb energy and induce hadronic interactions, while a plastic scintillator material layered between the absorber tiles samples the energy of hadrons. The tracker, ECAL, and HCAL systems are all contained in the bore of the 3.8 T solenoid from the CMS namesake. This device bends the trajectory of charged particles as they traverse the detector, and the curvature of this bend is used to obtain information on the charge and momentum of the measured particle. The muon system sits outside of the solenoid structure, and uses three types of detection systems: drift tubes (DTs), resistive strip chambers (RPCs) and cathode strip chambers (CSCs), which provide excellent timing and position resolution. The return yoke structure of the magnet also provides the mechanical support for the muon chambers. Figure 4.2 shows a slice of the CMS experiment showing how various particles interact and traverse the different sub-detector regions, as described above.

At center-of-mass energy of  $\sqrt{s} = 14 \text{ TeV}$ , the expected event rate is approximately  $10^9$  events/second. This is too much information to store and analyze, and is mainly dominated by Standard Model QCD multi-jet production, a background for searches for new particles or physics. An online event selection, or trigger, must be used to reduce this rate to a manageable 100 events/second. This is achieved through a combination of hardware, firmware, and software that provides a rough reconstruction of events in near real-time, and makes a decision about whether it meets a minimum set of criteria to be used in an analysis.

## 4.1 The Tracker

The innermost sub-detector is an all silicon pixel and strip tracker designed to provide precise and efficient measurement of the trajectories of charged particles and reconstruction secondary vertices necessary for identification of  $b$ -jets and  $\tau$  leptons.

At peak LHC design luminosity of  $10^{34} \text{ cm}^{-2} \text{ s}^{-1}$ , and bunch spacing of 25 ns, there will be  $\sim 1000$  particles from 20 overlapping  $pp$  collisions for each bunch crossing. This corresponds to a hit rate density of  $1 \text{ MHz/mm}^2$  at a radius of 4 cm,  $60 \text{ kHz/mm}^2$  at 22 cm, and  $3 \text{ kHz/mm}^2$  at 115 cm from the beam line. This large particle flux will also cause intense radiation damage to detector components. These conditions necessitate the use of radiation-hard silicon, with a high-

925 granularity to create a low occupancy for each detector element, which are read out by fast  
 926 electronics. Additional mitigation of the effects of radiation damage is taken by cooling and  
 927 operating the entire detector to  $-10^{\circ}$  C in order to maintain a signal to noise ratio of 10:1 for  
 928 the sensors. After 10 years of running, it is anticipated that this will need to decrease to  $-27^{\circ}$  in  
 929 order to compensate for the accumulated damage.

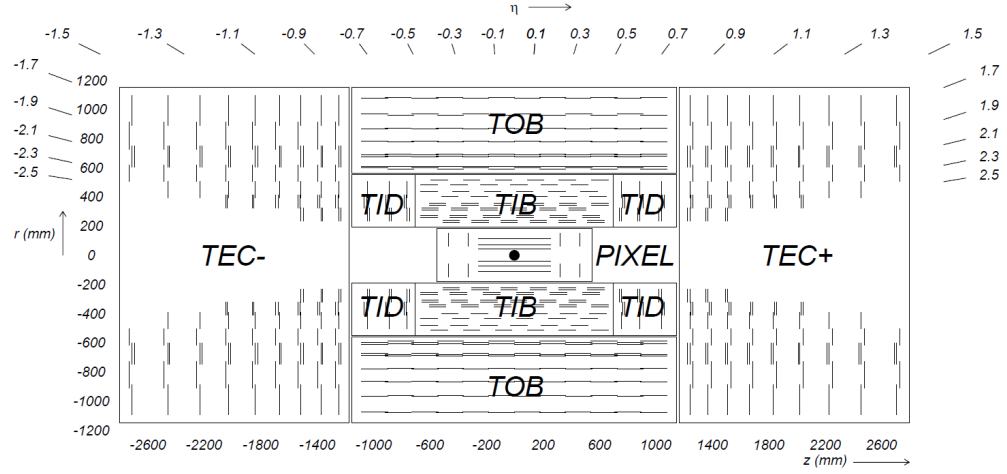


Figure 4.3: A side view of the tracker. The pixel detector is the innermost sub-system, with three concentric rings of detectors in the barrel, and two in the endcap. The tracker inner barrel (TIB) is a silicon strip detector, with four concentric rings. The tracker inner disks (TID) are three layers deep. The tracker outer barrel (TOB) is six concentric rings and the tracker end caps (TEC) are nine layers deep.

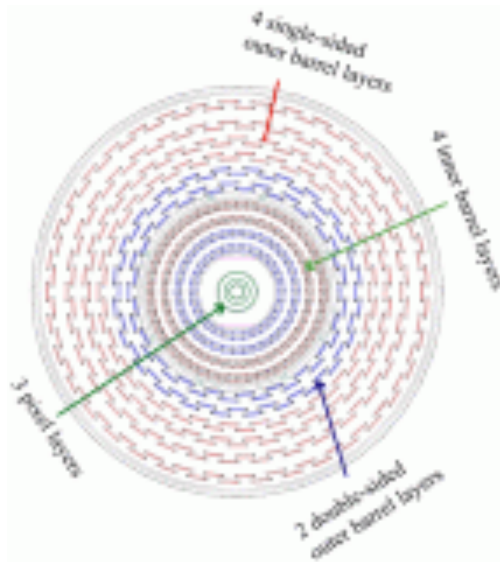


Figure 4.4: A head-on view of the beamline and barrel components of the tracker.

930 The tracker has a cylindrical shape that surrounds the interaction region, with a length of  
 931 5.8 m and a diameter of 2.5 m. The large particle flux close to the beamline requires the use  
 932 of a pixel detector sub-system in the innermost region, from radius 4.4 cm to 10.2 cm from  
 933 the beamline. The particle flux drops off sufficiently at larger radii to use silicon strip detectors,

arranged into four different sub-systems: the tracker inner barrel (TIB), tracker inner disks (TID), tracker outer barrel (TOB) and tracker end caps (TEC), which extend to a radius of 1.2 m from the beamline. Figure 4.3 shows a side view of the tracker layout and figure 4.4 shows a view down the beamline of the barrel sections. The tracker has a total acceptance of  $|\eta| < 2.5$ .

There are competing factors for the radial length of the tracker. More layers allow for more samples of a particle's trajectory, giving a higher spatial precision, but more material means photons and hadrons are more likely to decay, and create a shower of particles that would better measured through the absorption of energy via calorimeters. The depth of the tracker varies from 0.4 to 1.8 radiation lengths, resulting in small degradation of the ECAL performance, since approximately half the photons will be converted to  $e^+e^-$  pairs.

#### 4.1.1 The Silicon Pixel Detector

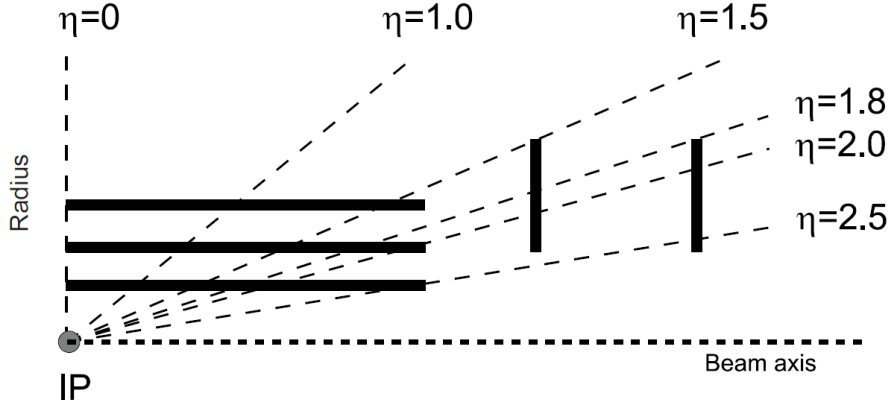


Figure 4.5: The three barrel and two disk layers of the silicon pixel tracker provide coverage of  $|\eta| < 2.5$

The pixel detector consists of 66 million  $100 \times 150 \mu\text{m}$  pixels, arranged in three concentric cylindrical layers of radius of 4.4, 7.3, and 10.2 cm from the beam line and two disc layers on either side of the barrel detectors. Figure 4.5 shows the eta coverage of the detector out to  $|\eta| < 2.5$ .

The sensor technology uses a  $n$ -on- $n$  concept, where a high-dose  $n$ -implant is introduced onto a  $n$ -substrate with large resistance. A  $p - n$  junction is made by the placement of a  $p$ -type semiconductor on the back side of the substrate. When a charged particle passes through the face of the substrate, between the  $p - n$  junction, it liberates electrons from the silicon atoms, creating electron-hole pairs. The  $p$ -side has a voltage bias of 150 V in the barrel, and 300 V in the disks, that sweeps the pair apart, creating a current. Pixels are isolated from one another using a moderated  $p$ -spray in the barrel region, and open  $p$ -stops in the disks in order to create an additional  $p - n$  structure that acts like a diode to limit current flow between pixels. The 3.7 T

957 magnetic field of the CMS solenoid also induces a Lorentz drift of the current in the  $\hat{\phi}$  direction.  
 958 This results in the current produced in one pixel being shared among multiple neighboring pixels.  
 959 The charge collected by each of the multiple pixels are read-out, using an interpolation between  
 960 pixels, resulting in a  $15\text{-}20 \mu\text{m}$  spatial resolution on the trajectory of the charged particle - much  
 961 smaller than the size of an individual pixel. In order to induce this effect in the disks (where the  
 962 pixels are orientated perpendicular to the barrel), the pixels are angled  $20^\circ$  in the  $\hat{y}$  direction.

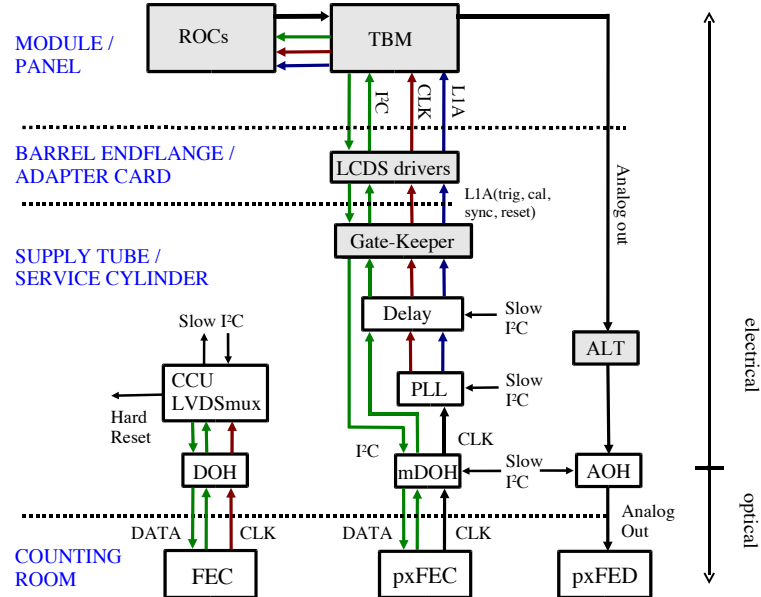


Figure 4.6: The readout electronics chain for the pixel detector

963 The current created by the charged particle is collected by a readout chip (ROC) that is  
 964 soldered with a bump bond type connection to the pixel. The ROC is a custom ASIC chip,  
 965 that processes the signals for a grid of  $52\times 80$  pixels. It provides amplification, buffering, and  
 966 zero suppression (threshold) of the charge from each pixel. Depending on the layer, 8-16 ROCs  
 967 in the barrel, and 21-24 ROCs in the disks are connected and read-out by a single token bit  
 968 manager (TBM) chip. This chip communicates information from the sensors to the trigger  
 969 system, which is used to determine whether a given event is stored as data for analysis later.  
 970 The pixel front end controller (pxFEC) interfaces with the ROC and TBM and provides central  
 971 clocking and communicates to the CMS data acquisition system. The pixel front end digitizer  
 972 (pxFED) converts the analog signals from the ROC and TBMs. A total of 40 pxFED (32 in the  
 973 barrel and 8 in the disks) modules are used to read-out the entire pixel detector, and figure 4.6  
 974 shows a schematic of the pixel read-out chain.

975 The resolution of the pixel detector was measured in 2012 with  $\sqrt{s} = 8 \text{ TeV}$   $pp$  collision. The  
 976 residual distance between the hit position recorded by a pixel, and an interpolated track that

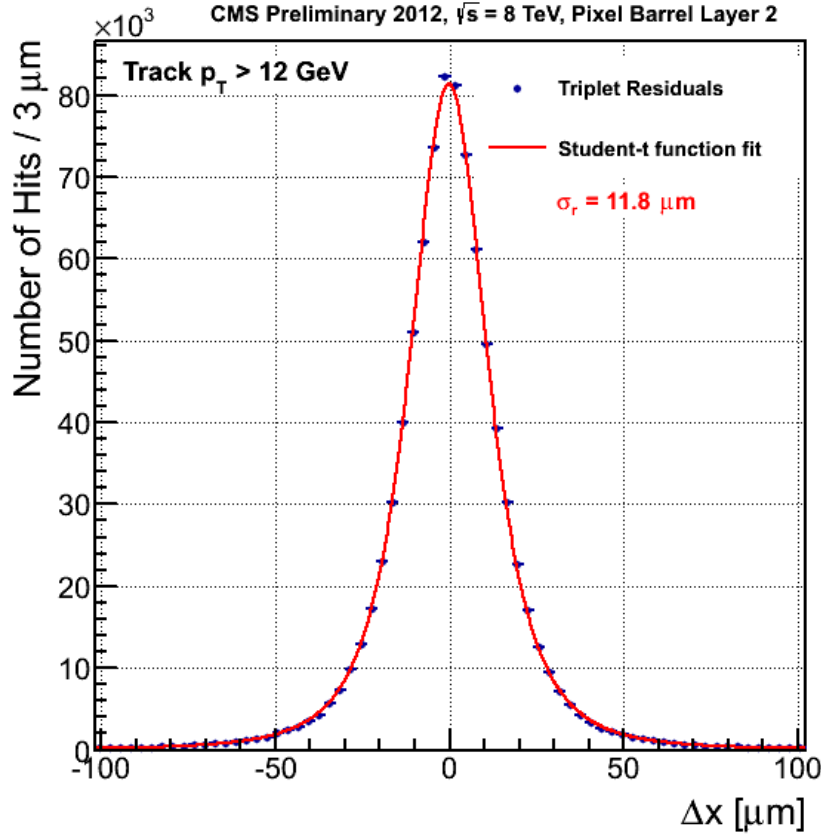


Figure 4.7: In 2012  $pp$  collisions at  $\sqrt{s} = 8$  TeV, the pixel detector performed with a resolution of  $11.8 \mu\text{m}$ . The above is a plot of the residual difference between a pixel and the results of a fit to a particle track.

977 uses that hit is plotted and fit with a student-t function in figure 4.7. For tracks with  $p_{\text{T}} > 12$   
 978 GeV, the pixel detector was found to have a spatial resolution of  $11.8 \mu\text{m}$ .

### 979 4.1.2 The Silicon Strip Detector

980 As shown in figure 4.3, the silicon strip tracking system has four components: the tracker inner  
 981 barrel (TIB), tracker inner disks (TID), tracker outer barrel (TOB) and tracker end caps (TEC).  
 982 A total of 15,148 detector modules are distributed among these systems, each with either one  
 983  $320 \mu\text{m}$  thick sensor, or two  $500 \mu\text{m}$  thick sensors, making 24,244 sensors with an active area of  
 984  $198 \text{ m}^2$  of silicon. A model with two sensors is shown in figure 4.8. Each sensor has either 512  
 985 or 768 strips since they are read out by two multiplexed 128-channel front end chips, making it  
 986 possible to only read out sensors in groups of 256. Each strip has a pitch that varies between 80  
 987 and  $200 \mu\text{m}$  and lengths that vary between 10 and 25 cm. All in all, 9.3 million strips are used  
 988 in the silicon tracker.

989 The TIB and TID provide radial coverage from 20 to 55 cm. The TIB has four barrel layers,  
 990 with  $80 \mu\text{m}$  pitch strips on the first two layers, and  $120 \mu\text{m}$  strips on the outer two, giving a single

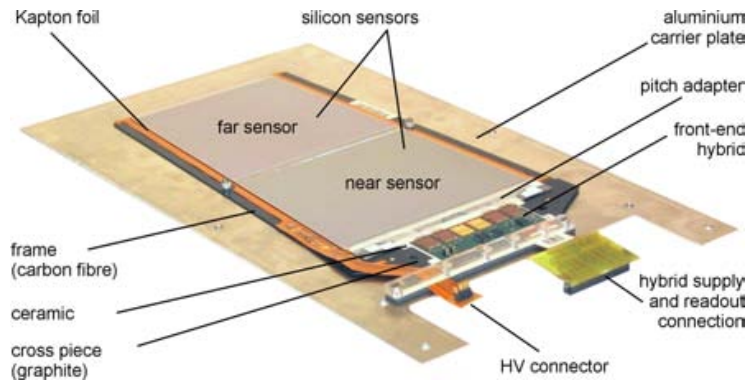


Figure 4.8: A silicon strip module, with two  $500 \mu\text{m}$  thick sensors.

point resolution of 23 and  $35 \mu\text{m}$  respectively. The strip pitch varies between 100 and  $141 \mu\text{m}$  in the three discs of the TID. The TOB surrounds the TIB/TID and is composed of six barrel layers that extend the tracker radius to 116 cm. It is composed of  $500 \mu\text{m}$  thick strip sensors, with pitches of  $183 \mu\text{m}$  in the first four layers and  $122 \mu\text{m}$  in the outer two layers. It provides 6 measurement points of the particle trajectory with a single point resolution of 53 (35)  $\mu\text{m}$  in the first four (last two) layers. Each TEC is made of 9 discs, each with 7 rings of strip detectors. The inner four rings of each disk use the single,  $320 \mu\text{m}$  thick strip modules, while the outer three rings use the double,  $520 \mu\text{m}$  thick strip modules. The average pitch varies between 97 to  $184 \mu\text{m}$  in each of the rings. In the first two layers of the TIB, the first two rings of the TID, the first two layers of the TOB, and rings 1, 2, and 5 in each disk of the TEC contain modules mounted back-to-back, with an angle of 100 mrad between them to provide a two-dimensional measurement of a particle's trajectory.

Each of the strips is a single sided  $p$ -on- $n$  type silicon sensor manufactured on 6 inch wafers, with a base material of  $n$  doped silicon. The front side of the wafer is implanted with a  $p^+$  type semiconductor. A uniform  $n^+$  implantation on the back forms the ohmic contact to 500 V. This forms a  $pn$  junction and when a charged particle passes through the face of the wafer, atoms in the junction are ionized and the 500 V potential difference creates a current out of the resulting electron/hole pairs. This current is collected and processed through the read-out system.

A custom integrated circuit, the APV25, is used to amplify, shape, and buffer the signals produced from the silicon strips. It has 128 read-out channels, and samples the detector signals at the 40 MHz, suitable for the 25 ns collisions. It is able to store data for up to 4  $\mu\text{s}$  to account for trigger latency. Two APV25 chips are linked with fiber optics to the Front End Driver

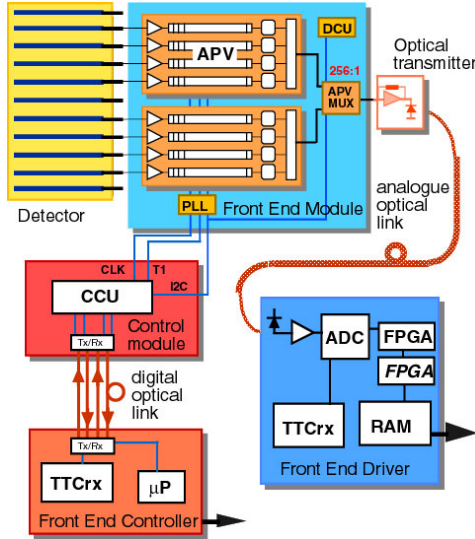


Figure 4.9: Schematic of the readout sequence of the silicon strip detector.

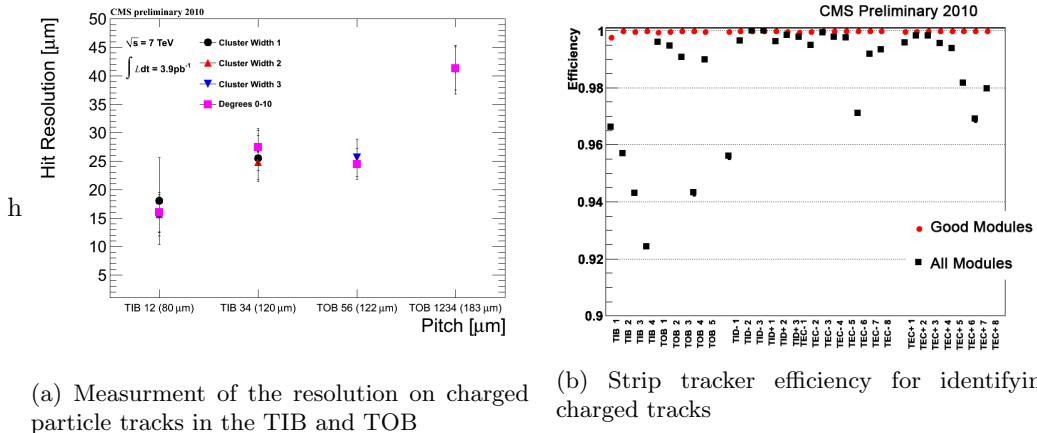


Figure 4.10: Measurements of the performance of the silicon strip track using  $pp$  collisions from 2011 at  $\sqrt{s} = 7 \text{ TeV}$

1013 (FED) system. Each FED receives data from 94 optical fibers, and digitizes them in parallel.

1014 The Front End Controller (FEC) transmits clock, trigger, and control data to the APV25s. The  
1015 entire readout chain is shown in figure 4.9.

1016 In 2011, the strip efficiency and resolution were measured from data in center-of-mass energy,  
1017  $\sqrt{s} = 7 \text{ TeV}$   $pp$  collisions. Figure 4.10(a) shows the resolution varying between  $15\text{--}40 \mu\text{m}$  for the  
1018 TIB and TOB detectors. Figure 4.10(b) shows the efficiency for reconstructing tracks with the  
1019 strip tracker, which is well above 99% when only considering operational modules.

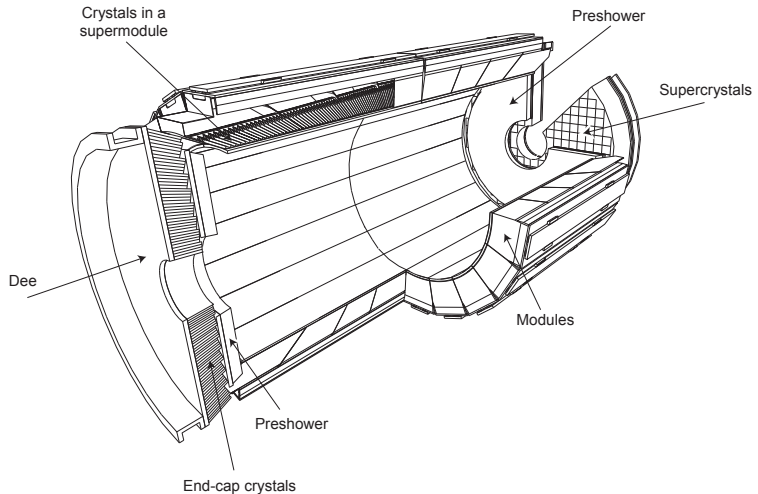


Figure 4.11: Layout of the ECAL sub-detector

## 1020 4.2 The Electromagnetic Calorimeter

1021 The Electromagnetic Calorimeter (ECAL) surrounds the inner tracker with 61,200 high density  
 1022 lead tungstate ( $\text{PbWO}_4$ ) crystals in the central barrel section, and 7,324 crystals in each of  
 1023 the two endcaps. The crystals have a fast response, provide fine granularity, and are radiation  
 1024 resistant, making them ideal for the LHC environment and the physics goal of observing the  
 1025 Standard Model Higgs boson decay to two high energy photons. The primary background for  
 1026 this process comes from neutral pions decaying to two photons, which is especially difficult when  
 1027 the photons are close together and can potentially be reconstructed as a single high-energy  
 1028 photon. This occurs most frequently in the endcaps, so an additional detector, the preshower,  
 1029 provides additional spatial resolution with silicon microstrip detectors, similar to those in the  
 1030 tracker. Figure 4.11 shows the layout of the ECAL.

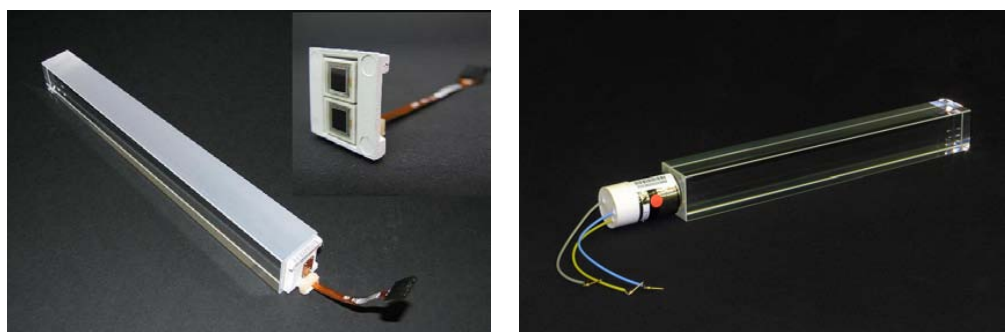


Figure 4.12: Typical Lead Tungstate crystal, with APD attached to the rear face in the left frame, and a VPT attached in the right frame.

1031 Lead tungstate is an ideal material for electromagnetic calorimetry. Figure 4.12 shows a  
 1032 typical crystal, with photomultipliers attached to the rear faces, which will be discussed later.

1033 The material has a high density,  $8.28 \text{ g/cm}^3$ , giving it a large electromagnetic cross-section,  
 1034 making it much more likely for a particle traversing the crystal to interact with one of the atoms  
 1035 in its structure. When a particle interacts with the crystal, it does so by depositing energy into  
 1036 its atoms, which excite the electrons that are bound to it. The atoms then relax by emitting  
 1037 photons, in a process known as scintillation and the  $\text{PbWO}_4$  crystals release 80% of their light  
 1038 in the 25 ns LHC bunch crossing time. This light is collected by photomultipliers attached to  
 1039 the rear face of the crystal and converted into an electrical signal. Read-out electronics amplify,  
 1040 digitize, and buffer the signal until it can be stored as data or discarded.

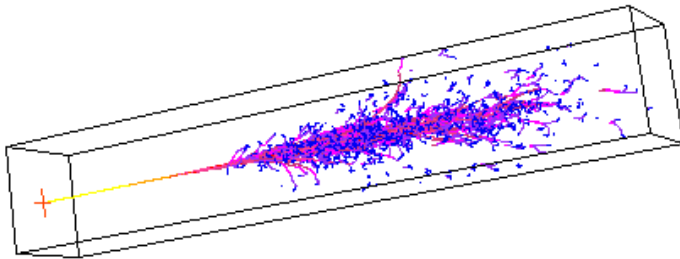


Figure 4.13: A simulation of the evolution of a electromagnetic shower being initiated by an electron entering the center of the front face.

1041 As a charged particle or photon begins to deposit energy, it begins a decay chain into many  
 1042 lower energy photons and electrons, known as an electromagnetic shower. Electrons, being  
 1043 bent by the CMS magnetic field, and multiple scattering off of the  $\text{PbWO}_4$  crystals, create  
 1044 bremsstrahlung photon radiation. Since the intensity of bremsstrahlung is inversely proportional  
 1045 to the mass of the particle squared, particles heavier than electrons such as muons and hadrons  
 1046 do not leave a large signature in the ECAL. Photons convert to  $e^+e^-$  pairs, which in turn create  
 1047 additional bremsstrahlung. The crystals have a short radiation length,  $X_0=0.89\text{cm}$ , which is the  
 1048 distance it takes an electron to deposit  $1/e$  of its energy through bremsstrahlung, and  $7/9$  of  
 1049 the mean free path of a high energy photon before it converts to an  $e^+e^-$  pair. A corollary  
 1050 of the crystal's short radiation length is its small Moliere radius,  $2.2\text{cm}$ , which is the radius of  
 1051 a cylinder that encloses 90% of the electromagnetic shower's energy deposition. A typical  
 1052 crystal has a front face that is  $22\times 22 \text{ mm}^2$ , a rear face of  $26\times 26 \text{ mm}^2$ , and a length of  $230 \text{ mm}$ ,  
 1053 or  $25.8 X_0$  radiation lengths. This means that a relatively small grid of crystals can be used to  
 1054 fully collect the energy deposited by a high energy electron or photon. As previously mentioned,  
 1055 heavier charged particles will not bremsstrahlung as much as electrons, and will travel through  
 1056 the entire ECAL, depositing only a moderate fraction of their energy in the crystals. Figure 4.13  
 1057 shows a simulation of an electromagnetic shower produced by an electron entering the front face  
 1058 of a crystal.



Figure 4.14: A module of 500 crystals (25 crystals wide by 20 crystal tall).

1059     The barrel of ECAL (EB) covers a pseudorapidity range of  $|\eta| < 1.479$  with 61,200 crystals  
 1060    at a radius 1.29 m from the beam-line. The crystals are positioned in a quasi-projective geometry,  
 1061    such that their axes make a  $3^\circ$  angle with respect to the vector pointing to the nominal interaction  
 1062    point. This ensures that particles will not pass through the cracks and spaces between crystals,  
 1063    and are forced to interact with a portion of the ECAL. Crystals are assembled in groups of  
 1064    400 or 500 into modules, as shown in figure 4.14 . Four of these modules are assembled into a  
 1065    supermodule contain 1700 crystals, and 36 supermodules make up the barrel region.

1066     The crystals in the EB are read out by Avalanche Photo-Diode (APD) photomultipliers,  
 1067    shown in the left frame of figure 4.12. The APDs were manufactured by Hamamatsu and are a  
 1068    bulk *n*-type silicon material, with a *p*-type implanted on its surface to form a *pn*-junction. The  
 1069    operation principle is similar to that of tracker. When scintillation light from the lead tungstate  
 1070    crystals enters the face of the APD, it creates electron-hole pairs in the intrinsic region between  
 1071    the *p* implantation and the *n* bulk material. The APD is biased with 45 V, which creates a  
 1072    current from the electron-hole pairs and is the signal that a particle has created scintillation in  
 1073    the crystal. The APD provides a gain of 50 and has a quantum efficiency of 75%. Both the  
 1074    APDs and the PbWO<sub>4</sub> exhibit a strong temperature dependence, so the entire system is kept at  
 1075    18° C with a water-based cooling system distributed throughout the barrel and end-caps.

1076     The ECAL readout electronics are designed to read-out a  $5 \times 5$  array of crystals, known as a  
 1077    trigger tower, in the EB, and a single supercrystal in the EE. Each trigger or tower or supercrystal  
 1078    consists of 5 Very Front End (VFE) boards, each connected to 5 APDs (VPTs), one Front End  
 1079    (FE) board, two (EB) or six (EE) Gigabit Optical Hybrids (GOHs), one Low Voltage Regulator  
 1080    (LVR) and a motherboard. Once triggered, the APD (or VPT in the EE) is sampled 10 times, at

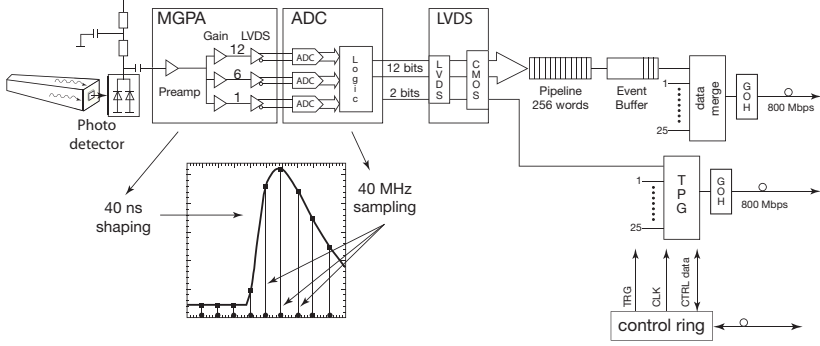


Figure 4.15: Schematic of the On-Detector Readout for the ECAL

1081 a 40 MHz sampling rate, and amplified by a multi-gain amplifier (MGPA), with nominal gains  
 1082 of 1, 6, and 12 contained on the VFE. These digitized samples are sent to the FE, where they  
 1083 are buffered until receiving a Level-1 trigger, where they are sent to the off-detector elcectronics  
 1084 Data Concentrator Card (DCC) via the GOHs. Figure 4.15 shows a schematic of the on-detector  
 1085 read-out.

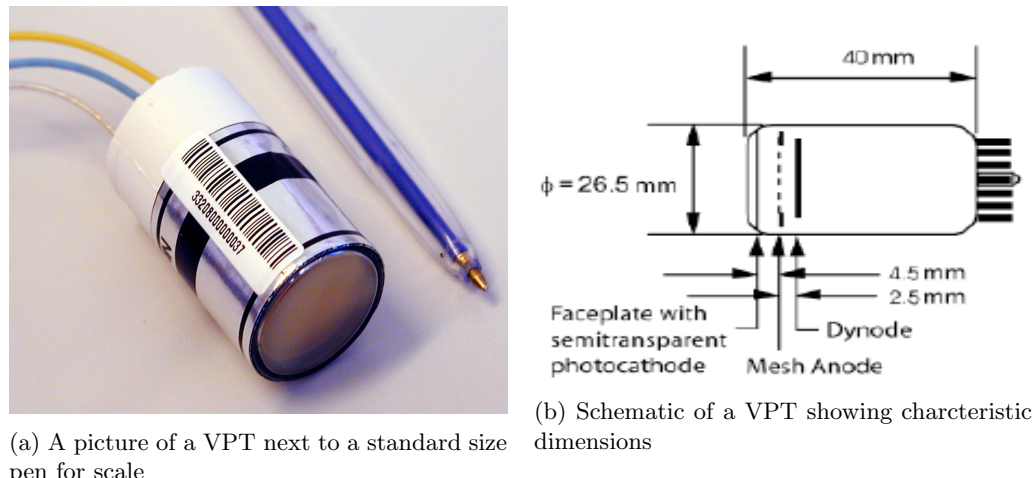
1086 In the barrel, the  $5 \times 5$  trigger towers are divided in the 5 strips in the  $\hat{\phi}$  direction. The energy  
 1087 deposits in these strips is summed by the FE cards and define the transvere energy of the tower.  
 1088 In the endcaps, supercrystals are divided into groups of five contiguous crystals of variable shape,  
 1089 known as psuedo-strips. The energy of these strips is performed by the FE, and the off-detector  
 1090 electronics use these to compute the transvere energy deposition.

1091 The preshower detector sits in front of the ECAL end-caps and provides coverage from  
 1092  $1.653 < |\eta| < 2.6$ . It is a two-layer sampling calorimeter. Lead radiators initiate electromagnetic  
 1093 showers from electrons and photons, and silicon strips are placed behind them to measure trajec-  
 1094 tories and deposited energy of passing particles. The total thickness is 20cm, which corresponds  
 1095 to a 2 raidation lengths in the first layer, and another radiation length in the second layer. 95%  
 1096 of photons are converted to  $e^+e^-$  pairs after the first layer. Each silicon sensor is composed of  
 1097 31 strips, with thickness of  $320 \mu\text{m}$  and are 1.9 mm in pitch. A front-end ASIC performs pre-  
 1098 amplification, shaping, voltage sampling, and communicates informaiton to the trigger system  
 1099 to determine if data is stored or discarded. The structure is formed into Dees, and two Dees  
 1100 form a disk with a hole for the beam-line to pass through.

1101 Behind the preshower is the ECAL end-cap (EE). It covers the psuedorapidity range of  
 1102  $1.479 < |\eta| < 3.0$ , and sits a longitudinal distance of 315.4 cm from the nominal interaction point.  
 1103 Crystals are grouped into  $5 \times 5$  modules known as supercrystals (SCs). Like the preshower, each  
 1104 endcap is divided into two sections, Dees, which form a disk with an inner bore for the beam  
 1105 line to pass through, as shown in figure 4.16. Each Dee holds 3,662 crystals, which are divided



Figure 4.16: A section of the ECAL end-cap, a Dee. Two Dees form a disk with an inner bore for the beam-line to pass through. 5x5 modules, or supercrystals, are mounted in preparation for installation at CMS



(a) A picture of a VPT next to a standard size pen for scale

(b) Schematic of a VPT showing characteristic dimensions

Figure 4.17: Vacuum Photo-Triode devices used in the ECAL end-caps (EE)

<sub>1106</sub> into 138 supercrysals, and 18 special partial-supercrystals for the inner and outer sections of the  
<sub>1107</sub> Dee.

#### <sub>1108</sub> 4.2.1 Vacuum Photo-Triodes

<sub>1109</sub> The photomultier used to readout the lead tungstate crystals in the EE is the Vaccum Photo-  
<sub>1110</sub> Triode (VPT), shown in the right frame of figure 4.17(a). Each device is 26.5mm in diameter  
<sub>1111</sub> and 40mm in lenth as shown in figure 4.17(b). It is a gain stage device. Photons from the  
<sub>1112</sub> lead tungstate scintilation light enter the front face of the VPT and liberate electrons from the  
<sub>1113</sub> grounded bialkali photocathode (SbKCs) via the photoelectron effect. The cathode material  
<sub>1114</sub> has a quantum efficiency of  $\sim 20 - 25\%$ . The photo-electrons are accelerated towards the mesh

1115 anode grid, which is held at 800 V. Approximately half the photo-electrons pass through the  
 1116 mesh and encounter a dynode plate held at 600 V. Electrons either collide with the dynode,  
 1117 liberating secondary electrons from the collision, or are turned around by the 200 V differenc  
 1118 between anode and dynode. Electrons are thus constantly accelerated towards the anode, and  
 1119 create secondary electrons as they collide with the anode. The process repeats with the secondary  
 1120 electrons, creating an avalanche of charge near the anode. As these charges eventually recombine  
 1121 with the anode over the course of a few nanoseconds, the voltage of anode drops, signaling the  
 1122 device has detected a photon from the PbWO<sub>4</sub> crystals.

1123 The performance of the VPT is degraded over time by two effects associated with exposure  
 1124 to the scintillation light from the crystals. The first is loss of the vacuum inside the tube.  
 1125 Molecules from the air become ionized by the large voltages and the positive ions are accelerated  
 1126 towards the photo-cathode, which is damaged through the resulting collision. The second effect  
 1127 is the gradual depletion of photo-electrons from the bialkali cathode material. The result is a  
 1128 decrease in the current, and thus signal, produced by the anode. Both of these effects can be  
 1129 effectively modeled as the sum of two falling exponential functions. The University of Virginia  
 1130 has studied the performance of VPTs with respect to their light exposure rates over the course  
 1131 of several years in order to characterize the device's response and long-term behavior.

#### 1132 4.2.2 Test Rig at UVa

1133 The University of Virginia (UVa) has continuously monitored four production VPTs operated  
 1134 at 800 V anode and 600 V dynode, in a 3.8 T field, at 15° to the tube axis, with photocath-  
 1135 ode currents of approximately 10 nA. This was done to simulate light exposure from the lead  
 1136 tungstate crystals in the forward regions of the ECAL end-caps, as well as provide an accelerated  
 1137 simulation of photocurrents that would be experienced in the larger eta regions. As described  
 1138 above, the light exposure is theorized to be the most significant cause of the loss of response  
 1139 in the VPT, known as burn-in. The amount of light that the device has been exposed to is  
 1140 measured in terms of the total number amount of charge liberated from the cathode, measured  
 1141 from the cathode current draw, and is known as the integrated charge. By operating at such  
 1142 high photocurrents, UVa is able to probe this burn-in effect in an attempt to understand the  
 1143 long term behaviour of the VPT response to light.

1144 The University of Virginia is well suited to test these devices, since it operates a 3.8 T  
 1145 solenoid magnet, with a sufficiently large inner bore to accommodate a rig containing five (5)  
 1146 VPTs, LEDs, LED driving hardware, and amplifying equipment. The magnet itself was built  
 1147 by Oxford instruments and has an inner bore diameter of 0.4 m and an outer bore diameter of  
 1148 1.5 m. The inner bore is 0.13 m in height from the ground, and the magnet has a length of 1.5m

1149 along its z-axis, which is perpendicular to the normal of the floor.

1150 The VPTs were supplied with high voltage (800 V anode, 600 V cathode) from a CAEN  
1151 High Voltage supply. This manufacturer also provides high voltage supplies for the VPTs used  
1152 in CMS. They are preferable due to their stability, programmable user interface, and capacity  
1153 to drive multiple VPTs simultaneously. A voltage separation between anode and cathode much  
1154 larger than this is not recommended due to its potential do damage the device.

1155 The VPTs were pulsed with blue and orange LEDs at rates of 10 kHz, and 20 kHz, to capture  
1156 the same features (frequency and rate) that light from the lead tungstate crystals would produce  
1157 while collisions were occurring in the detector. The driving circuits are the same as those used in  
1158 the LED system in the end-caps at point 5 (the location of CMS at CERN), with the exception  
1159 that the current limiting resistors are larger. They are Dallas Semiconductor DS1040Z-D70  
1160 Programmable One-Shot Pulse Generators. The TTL signals from the FPGA serve as a trigger  
1161 for a Dallas Semiconductor pulse generator chip on the board that generates a 30 nSec pulse, so  
1162 there is no overlap in pulses generated by the VPT. The pulsing was also run in an on/off cycle  
1163 of 16 hrs on, 8 hrs off to be consistent with the LHC beam fill cycle.

1164 The LED pulsing and data acquisition was automated via a PXI unit manufactured by Na-  
1165 tional Instruments, which contains a FPGA card, a digital oscilloscope, and computer running  
1166 Windows XP. The FPGA card was programmed with LabVIEW software which controlled LED  
1167 pulse rate, low voltage power, and measurements of VPT signals. The data acquisition was  
1168 triggered by means of a PIN diode placed next to the VPT. This served the dual purpose of in-  
1169 dependent data triggering and also provided the means to correct fluctuations in the illumination  
1170 provided by the LEDs.

1171 The current from the VPTs anode and cathode are ultimately routed to the PXI Crates  
1172 switches, and then on to the crates DMM or oscilloscope via a preliminary amplification stage.  
1173 The VPTs anode is connected directly to a Stephenson amplifier, which connects to a high-  
1174 frequency switch. The PIN diode signal passes unmodified to that same high-frequency switch.  
1175 The cathode signal cables connect to a distribution box near the PXI Crate. The distribution  
1176 box then routes their signals to the terminal block on a low-frequency switch. All of these signals  
1177 leave the rig over BNC cables before terminating at or adjacent to the PXI Crate. Figure 4.18  
1178 highlights different components of the test stand at UVa.

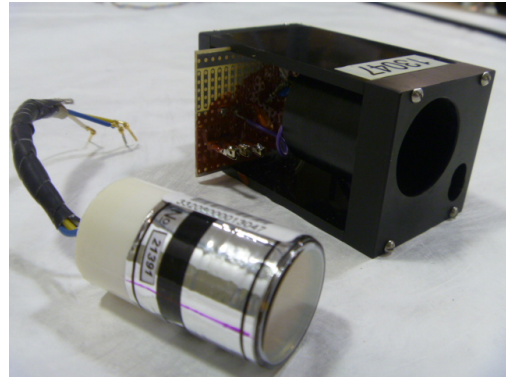
### 1179 4.2.3 Results of UVa Tests

1180 The University of Virginia rig ran three sets of 5 VPTs for approximately 30 wks each in a  
1181 3.8 T magnetic field under high light conditions from blue and orange frequencies to simulate  
1182 a large light yield found in large eta regions of the end-cap. The large photocurrents allowed

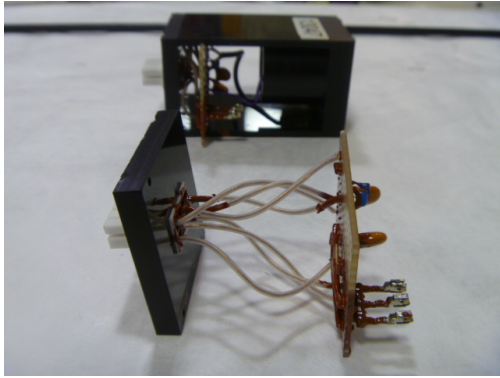


h

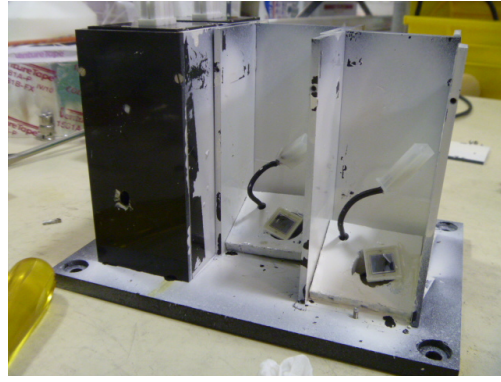
(a) The 3.8 T superconducting solenoid magnet used at UVa to study VPT performance



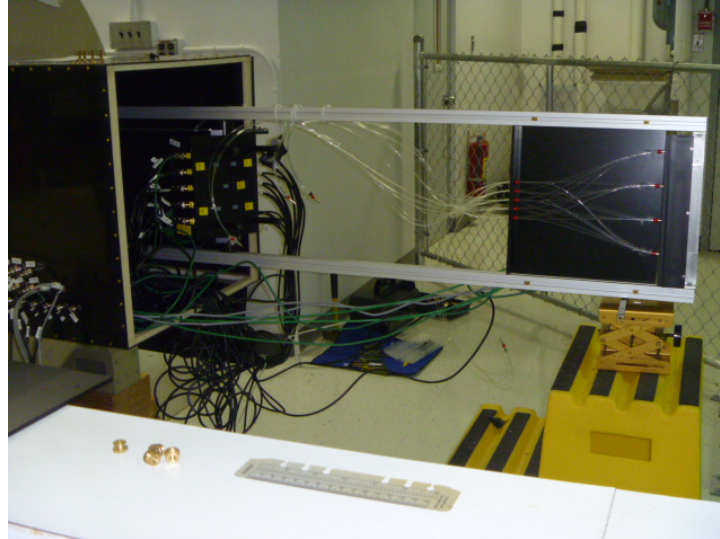
(b) A VPT before being installed in the rig and the housing that provides mechanical support and high voltage connections



(c) The housing for the VPT also provides simple HV filtering to provide stable power to the device



(d) The structure which holds 5 vpts in their housing. A PIN diode is used to measure the LED light and make corrections for fluctuations in brightness



(e) The VPT rig in maintenance position outside of the bore of magnet (during operation the rail is inserted into the bore such that the vpt housing is at the center). Fiber optics feed from the left into the VPT and amplifier housing.

Figure 4.18: Features of the UVa VPT test stand

the collection of an integrated charge of  $\sim 48$  mC for the largest gain VPT, and  $\sim 16$  mC for the other three. All VPTs were characterized by an initial steep decline followed by a plateau region, which was fit with a double exponential function of the form

$$f(x) = A + B \exp(Cx) + D \exp(Ex) \quad (4.2)$$

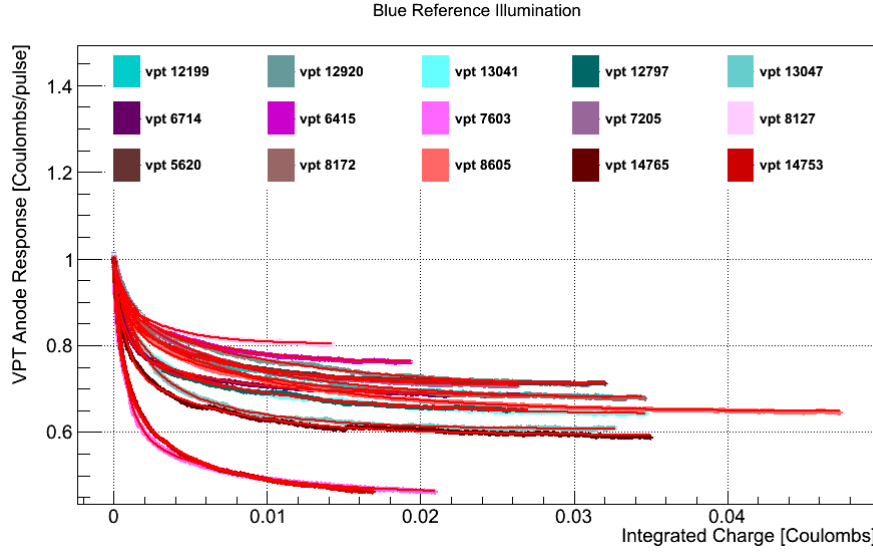


Figure 4.19: 3 runs of 5 VPTs, exposed to blue LED light, and fit to a sum of two exponentials.

Table 4.1: Fit Results for VPT Conditioning Studies at U.Va. and Brunel, Blue Reference LED

RIE Number	% Drop	$\chi^2/NDF$	Pedestal	Fast exp Amplitude	Fast exp $\tau$	Slow exp Amplitude	Slow exp $\tau$
12199	30.1	1.20e+00	1.51e-09	3.42e-10	-8.84e-04	3.85e-10	-1.00e-02
12920	27.0	7.27e-01	1.72e-09	3.16e-10	-1.16e-03	4.03e-10	-1.05e-02
13041	33.5	8.46e-01	1.09e-09	3.43e-10	-1.20e-03	2.46e-10	-9.31e-03
12797	33.6	1.07e+00	6.39e-10	2.18e-10	-9.72e-04	1.31e-10	-9.87e-03
13047	38.1	1.06e+00	5.48e-10	1.98e-10	-1.40e-03	1.49e-10	-6.19e-03
6714	29.3	8.37e-01	1.55e-09	4.10e-10	-6.66e-04	2.48e-10	-6.11e-03
6415	23.6	1.28e-01	1.19e-09	1.54e-10	-6.55e-04	2.20e-10	-5.16e-03
7603	50.3	3.25e+00	1.44e-09	1.02e-09	-8.22e-04	4.87e-10	-6.72e-03
7205	29.4	4.53e-01	1.41e-09	2.14e-10	-5.68e-04	3.94e-10	-5.96e-03
8127	19.6	1.97e-01	1.71e-09	1.82e-10	-3.12e-04	2.35e-10	-3.30e-03
5620	27.4	4.57e+00	1.68e-09	2.85e-10	-5.20e-04	3.68e-10	-6.19e-03
8172	30.3	8.75e+00	8.32e-10	1.52e-10	-1.06e-03	2.27e-10	-6.87e-03
8605	32.1	6.94e+00	1.36e-09	3.33e-10	-8.97e-04	3.94e-10	-1.03e-02
14765	38.9	2.78e+01	3.47e-10	1.37e-10	-7.46e-04	9.24e-11	-6.77e-03
14753	52.9	2.53e+01	1.19e-09	7.45e-10	-5.86e-04	6.10e-10	-4.77e-03
Average	31.0	4.62e+00	1.17e-09	2.94e-10	-1.09e-03	1.66e-10	-3.07e-01

where A is a pedestal parameter, B is the amplitude of the fastest dropping exponential, C is the time constant of the fast dropping exponential, D is the amplitude of the slow dropping exponential, and E is the time constant of the fast exponential. The summary of the fit parameters for blue LED light is shown in table 4.1 and the summary of fit parameters for the orange LED light is shown in table 4.2. Plots of the VPT anode response versus integrated charge, and

the associated fit for each of the devices is shown in figure 4.19 for blue LED exposure and in figure 4.20 for orange LED exposure. Based on these findings, it can be concluded that the VPT "burn-in" eventually reaches a plateau at about  $\sim 70\%$  for blue LED exposure and  $\sim 50\%$  for orange LED exposure.

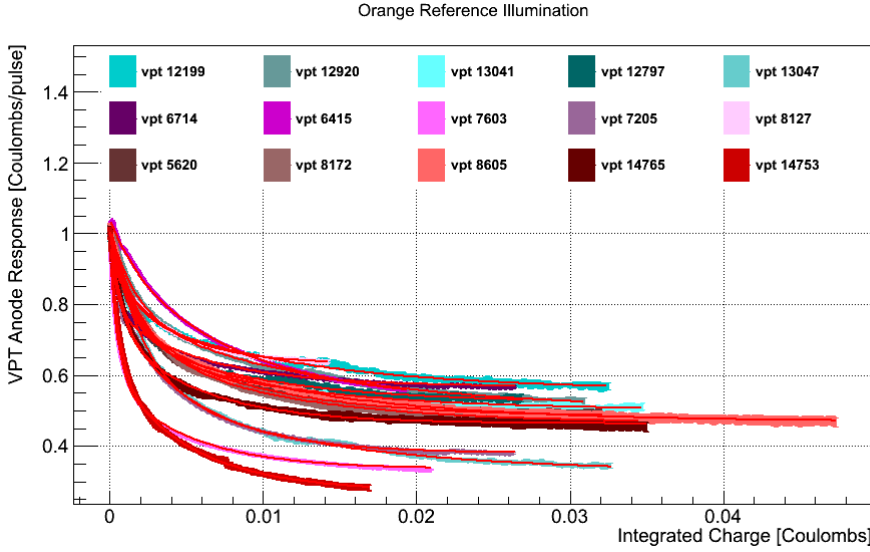


Figure 4.20: 3 runs of 5 VPTs, exposed to orange LED light, and fit to a sum of two exponentials.

Table 4.2: Fit Results for VPT Conditioning Studies at U.Va., Orange LED

RIE Number	% Drop	$\chi^2/NDF$	Pedestal	Fast exp Amplitude	Fast exp $\tau$	Slow exp Amplitude	Slow exp $\tau$
12199	41.9	6.23e-01	4.23e-10	1.79e-10	-1.10e-03	1.76e-10	-1.10e-02
12920	45.3	1.84e-01	6.73e-10	3.24e-10	-1.67e-03	3.72e-10	-1.26e-02
13041	48.3	7.42e-01	2.75e-10	1.81e-10	-1.63e-03	1.04e-10	-1.02e-02
12797	46.4	5.05e-01	2.05e-10	1.14e-10	-1.23e-03	7.87e-11	-8.77e-03
13047	63.0	1.09e+00	1.34e-10	1.73e-10	-2.18e-03	1.07e-10	-1.16e-02
6714	43.4	1.43e+01	7.73e-10	3.29e-10	-4.49e-04	2.84e-10	-6.11e-03
6415	46.5	2.34e+01	4.41e-10	8.75e-11	-1.80e-03	3.47e-10	-7.95e-03
7603	64.8	3.20e+01	3.01e-10	3.42e-10	-5.42e-04	2.24e-10	-5.04e-03
7205	63.2	6.52e+01	1.94e-10	1.29e-10	-4.49e-04	2.16e-10	-5.13e-03
8127	39.4	2.24e+01	7.09e-10	1.54e-10	-2.08e-04	3.10e-10	-3.75e-03
5620	50.3	2.30e-01	4.07e-10	2.13e-10	-1.16e-03	2.37e-10	-7.79e-03
8172	51.7	1.56e-01	4.01e-10	2.73e-10	-1.91e-03	2.08e-10	-9.48e-03
8605	49.6	1.83e-01	2.39e-10	1.46e-10	-1.45e-03	1.33e-10	-1.12e-02
14765	53.3	3.08e-01	2.07e-10	1.27e-10	-8.55e-04	1.17e-10	-5.66e-03
14753	72.2	2.22e-01	1.94e-10	2.76e-10	-6.01e-04	2.47e-10	-5.06e-03
Average	52.0	1.08e+01	3.72e-10	2.03e-10	-1.15e-03	2.11e-10	-8.10e-03

### 4.3 The Hadronic Calorimeter

The Hadronic Calorimeter (HCAL) is divided into four sub-systems: the barrel (HB), the endcap (HE), the outer calorimeter (HO), and the forward calorimeter (HF). It is especially important for measuring hadronic jets and neutrinos by measuring an imbalance in energy trans-

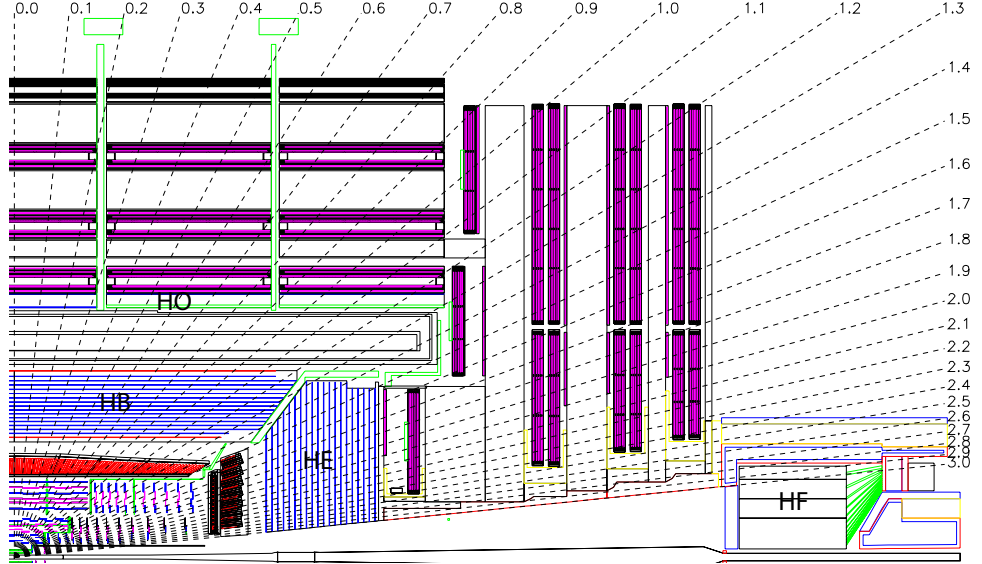


Figure 4.21: Longitudinal cross-section of the HCAL with the four sub-systems labeled

verse to the beamline. It provides coverage from  $|\eta| < 3$  from the HB, HE, and HO, and the HF extends the coverage out to  $|\eta| < 5.2$ . A diagram of the longitudinal cross section is shown in figure 4.21.

The barrel section of the HCAL, the HB, is divided into two sections longitudinally, each with 18 identical azimuthal wedges wrapped around the beamline. Each wedge has four azimuthal sections, with the center two sections aligned and each edge piece angled and staggered in a configuration that creates no projective dead material for the full radial extent of the HCAL. Figure 4.22 shows a closeup photograph of four wedges, where optical fibers are layed out accross the seam that joins the staggered edge layers to the two aligned center layers, and blue lines highlight the four azimuthal divisions for a single wedge.

The HB is a sampling calorimeter, with each azimuthal section composed of 14 alternating layers of brass absorber plates, and layers plastic scintillator tiles, with steel plates on the top and bottom layers for structural support. Each quarter-barrel section of scintillator has 16  $\eta$  divisions, giving a segmentation of  $(\Delta\eta, \Delta\phi) = (0.087, 0.087)$ . The brass absorber plates are C26000/Cartridge Brass. The material was chosen since the absorber material could not be distorted or bend under the stress of its own weight for at least 15 years of experimental running. Much of the material was purchased, but over a million Russian WW2 brass shell casings, designed to withstand the stresses of travel aboard 1940s Navy vessels, were melted down and processed into absorber tiles. Figure 4.24 shows members of the Russian Navy posing with some of the shells.

When a hadron passes through a wedge, the brass and steel plates absorb energy and ini-



Figure 4.22: Closeup of the HCAL barrel section. The center section of each of the 18 wedges are labeled, optical cables lay accross the joint of the center and staggered edge sections of each wedge. The blue lines show the apporximate azimuthal division of the wedge.

tiates the decay of the hadron into a number of lighter particles. These particles pass through the scintillator layer, which absorb energy from the interactions or collisions with the passing particles. The electrons of the scintillator become excited and relax by emitting a number of photons in the blue-violet range of the visible spectrum proportional to the amount of energy absorbed by the scintillator. These photons are abosrbed by wavelength shifting fibers (WSFs), which re-emit the light in the green part of the visible spectrum. The WSFs are spliced into four clear fiber optical cables. These fibers transport the light from each of the layers to an optical de-coding unit (ODU), which arranges the fibers into readout towers. A hydrid photodiode (HPD) converts this light into electric signals and is digitized by an ADC contained on the front-end elctronics. The HPD is a photo-cathode, which converts light to electrons via the photoelectric effect, that sits above a silicon diode that amplifies the signal of the cathode. The HPD provides a gain of 2000 to the light signals received from the scintialator trays. The on-detector electronics communicate to the HCAL trigger/readout (HTR) boards, which communicate with the trigger system to decide whether the store the event as data or discard it.

The brass absorbing material has a nuclear interaction length, or the length necesary to reduce the number of charged particles in a hadron shower by  $1/e$ , of 16.42 cm, and a radiation length of 1.49 cm. This means that te HB will be able to contain a large part of most hadron showers produced at LHC energies, but a portion will still pass through the entire radial distance. The outer barrel layer, HO is designed to measure the remnants of the hadron shower. It sits



Figure 4.23: Over 1 million Russian shells of military artillery were re-processed in the construction of the HCAL

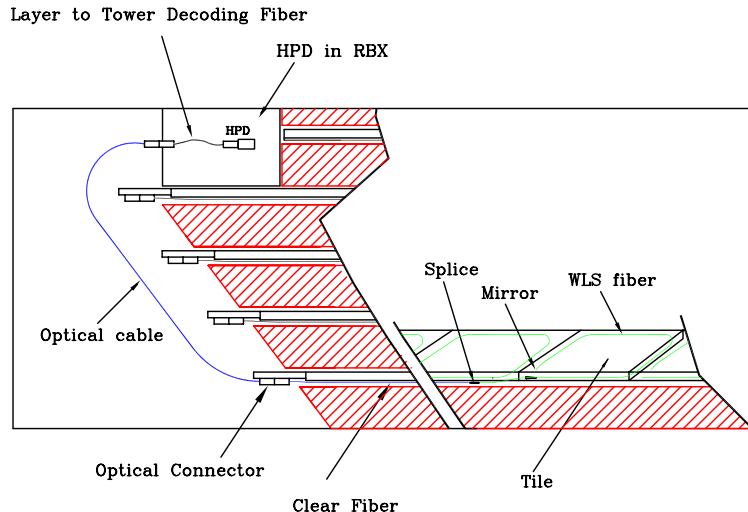


Figure 4.24: Optical readout chain of the HCAL scintilllator tiles

1239 outside of the solenoid magnet, using it as an absorber layer  $1.4/\sin \theta$  interaction lengths. It  
 1240 consists of 5 sections along the z-axis, which form rings around the beamline. Each ring is a layer  
 1241 of scintillator tiles at radial distance of 4.07m, except for the center ring. Since it corresponds  
 1242 to the  $\eta = 0$  ring, there is a minimum amount of absorber material in front of it. The central  
 1243 ring is thus two layers of scintillator at radial distances 3.82 and 4.07 m, which sit on either  
 1244 side of a 19.5cm thick piece of iron absorber.

1245 The endcap system, the HE, provide a substantial portion of the total  $\eta$  coverage, from  
 1246  $1.3 < |\eta| < 3.0$ , and contains  $\sim 1/3$  of the final state particles in a collision. Like the HB, it is  
 1247 a sampling calorimeter with alternating layers of brass and plastic. The demand for radiation  
 1248 hardness, and the need for a non-magnetic material, lead to the same choice of C26000 cartridge

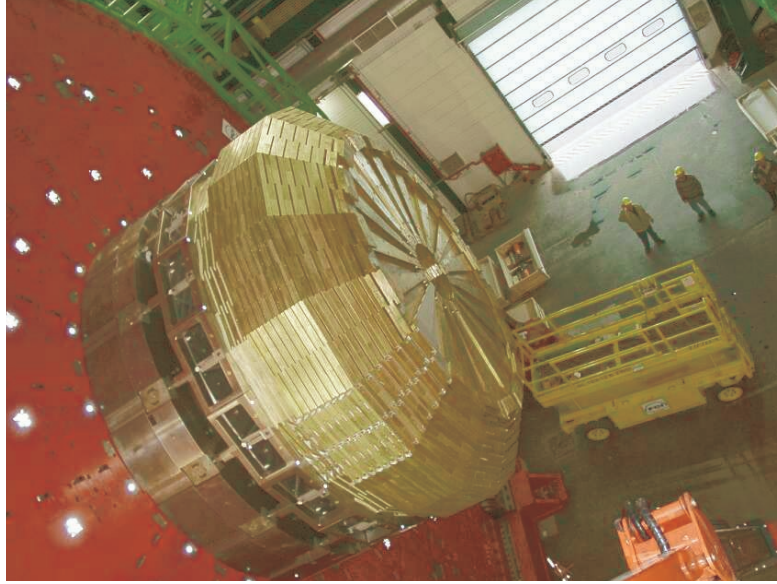


Figure 4.25: HCAL endcap, 18 azimuthal divisions of alternating layers of brass and plastic scintillator.

<sub>1249</sub> brass found in the HB. It is also divided into 18 azimuthal wedges, and 16  $\eta$  divisions, giving  
<sub>1250</sub> it the same  $(\Delta\eta, \Delta\phi) = (0.087, 0.087)$  segmentation. Figure 4.25 shows an image of a partially  
<sub>1251</sub> assembled endcap before being installed.

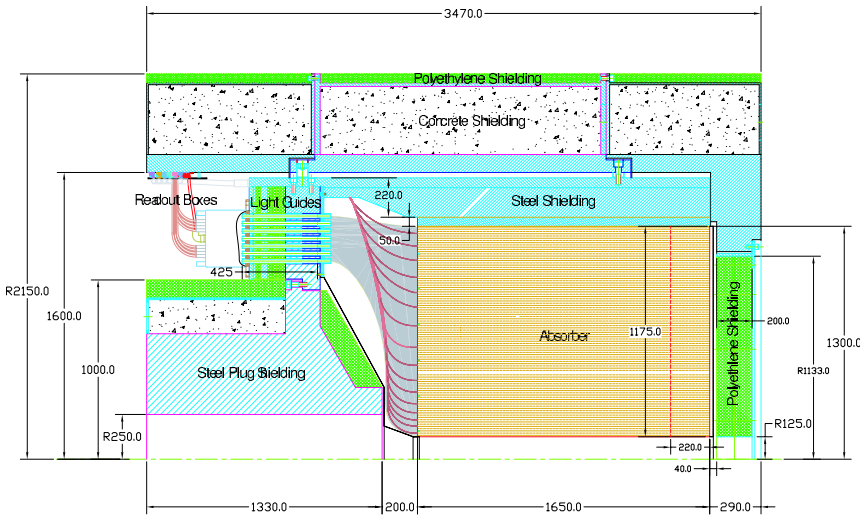


Figure 4.26: Longitudinal cross-section of the HCAL forward calorimetry, the HF

<sub>1252</sub> The forward calorimetry, HF, extends the HCAL coverage from  $3.0 < |\eta| < 5.0$ , and neces-  
<sub>1253</sub> sarily must sit in the region of the detector with the largest particle fluxes and thus radiation  
<sub>1254</sub> exposure. The HF is a cylindrical steel structure with an inner bore 12.5 cm from the beam line,  
<sub>1255</sub> and a outer radius of 130.0 cm. It sits 11.2 m away from the nominal interaction point in the

1256  $\hat{z}$  direction. Like the HE, it has 18 azimuthal divisions on either side of the interaction point.  
1257 Relativistic particles that move through the steel generate Cherenkov light, which is collected  
1258 by radiation hard quartz fibers, which transport the light to HPDs which are readout in the  
1259 manner as described above. Since the detection mechanism is Cherenkov light, this sub-system  
1260 is primarily sensitive to the electromagnetic component of the hadronic shower. Figure 4.26 shows  
1261 a cross-sectional view of the HF detector.

## 1262 4.4 Muon Chambers

1263 In  $pp$  collisions, muons are only created through electroweak or exotic physics processes, making  
1264 the detection of this particle an invaluable tool for reducing the large hadronic backgrounds  
1265 produced at the LHC. The muon chambers, positioned furthest from the beamline, sit behind  
1266 the ECAL and HCAL detectors, which absorb almost all of the hadronic activity from a collision.  
1267 They operate in a relatively low flux environment, allowing for robust measurement of their  
1268 kinematics, making it an excellent trigger system. One of the most important discovery channels  
1269 for the Higgs boson, involved the decay of the Higgs into two  $Z$  bosons, which decay to two pairs  
1270 of muons. Only 25 events were needed for a statistically significant observation in that channel,  
1271 since the backgrounds had been reduced to only 5 expected events and the muons had provided  
1272 high resolution on the invariant mass of the Higgs.

1273 The muon chambers are composed of three types of gaseous detector technology: drift tubes  
1274 (DTs), cathode strip chambers (CSCs), and resistive plate chambers (RPCs). In the muon barrel  
1275 system (MB), where the magnetic field is uniform DTs provide  $\eta$  coverage, for  $|\eta| < 1.4$ , and  
1276 are supplemented by a system of RPCs that provide an independent trigger source and faster  
1277 timing resolution. In the muon endcap system (ME), where the magnetic field would degrade  
1278 the performance of DTs, a system of CSCs and RPCs provide  $\eta$  coverage from  $1.4 < |\eta| < 2.4$ .

1279 The DTs are located in the MB system, which is divided into 5 longitudinal, cylindrical  
1280 sections around the beamline, known as wheels. In each wheel there are 4 concentric layers of  
1281 drift tube stations, one on either side of the magnet return yoke, and two interspersed inside of  
1282 it. Each wheel is divided into two 12 azimuthal sectors, making 48 stations in the barrel, as shown  
1283 in figure 4.27. Each station on the first three (fourth) layers contain 3(2) superlayers, where  
1284 each superlayer is made of a stack of 4 layers of rectangular drift cells, which are staggered  
1285 by half a cell each. Two of the superlayers are oriented such that they are parallel to the  
1286 beam, measuring the muon in the  $r - \phi$  plane. The first three layers contain a third superlayer,  
1287 orientated perpendicular to the beam, measuring a  $z$  component of the muon trajectory. Each  
1288 drift cell is a hollow  $13 \times 42$  mm tube, with a relatively thick 1.5mm wall to provide isolation

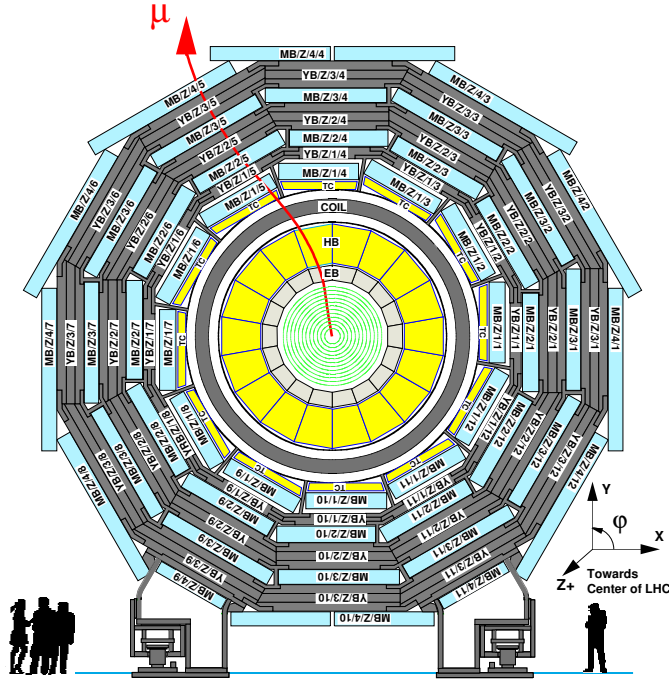


Figure 4.27: Longitudinal cross-section of one of the 5 wheels of the muon system. Drift tubes are placed in 4 concentric layers, with 2 being placed inside the return yoke of the magnet, and 12 azimuthal divisions.

1289 between adjacent cells. Each cell is filled with a mixture of 85% argon + 15% CO<sub>2</sub> gas mixture,  
 1290 and contains an anode wire that is held at 3600 V that runs down the axis of the cell. The walls  
 1291 of the cell are held at 1800 V or -1200 V depending on the wall. When a muon passes through the  
 1292 chamber, it's charge ionizes molecules of the CO<sub>2</sub> gas, causing the electrons to drift towards the  
 1293 anode wire, and the CO<sub>2</sub> ions drift towards the wall. As the electrons approach the anode, they  
 1294 are accelerated and liberate secondary elctrons from other CO<sub>2</sub> molecules, creating an avalanche  
 1295 of electrons near the wire, resulting in a drop in voltage as they are collected. The voltage drop  
 1296 is read out by front end electronics as a signal that a muon has passed through the chamber.  
 1297 The Argon gas quenches the avalanche reaction, and the maximum drift time for electrons in  
 1298 the gas is 380 ns. This long time scale necessitates the use of an addtional, fast-timing system,  
 1299 the RPCs. Figure 4.28 shows a cross-section view of a drift cell, including electric field lines  
 1300 produced by the potential difference between the anode wire and the walls of the drift cell.

1301 The reisistive place chambers (RPCs) are the fast timing system chosen to supplement the  
 1302 DTs in the barrel, and the CSCs in the endcaps. In the barrel, they are adhered to the top and  
 1303 bottom of the first two layers of drift stations. In the outer two layers, they are only adhered  
 1304 to the bottom of each station. Figure 4.29(a) shows the layout of the barrel RPC system. The  
 1305 muon endcap system is composed of three disks on either side of the intreraction point, and is  
 1306 shown in figure 4.29(b). RPCs are mounted on the back of the CSC stations of the innermost

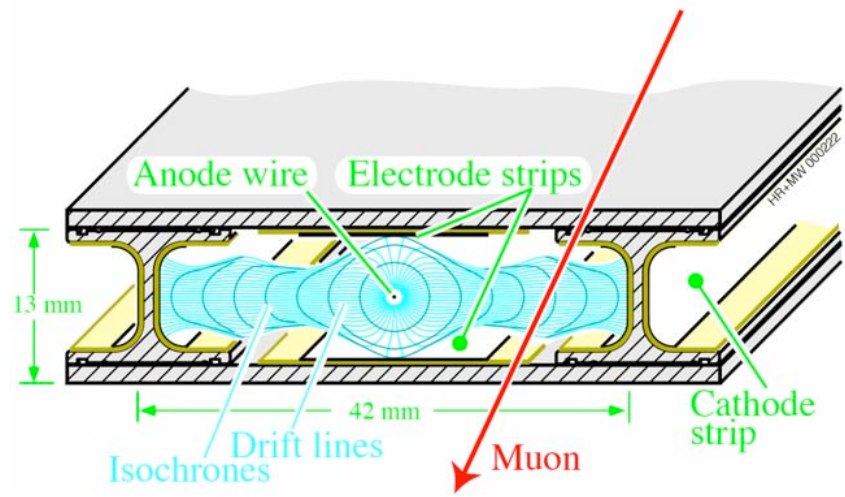
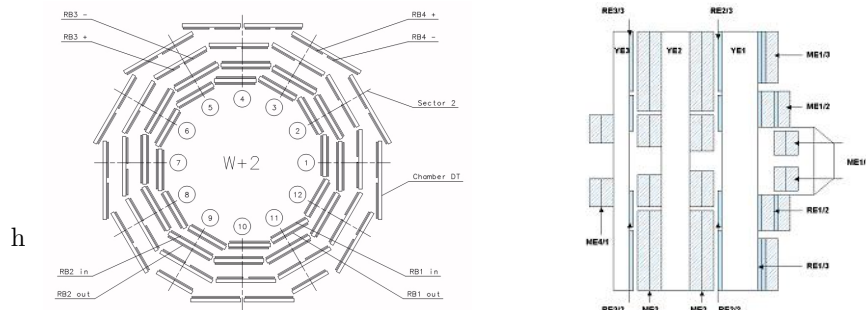


Figure 4.28: A cross-section view of a drift cell. The anode wire is held at 3600 V, creating a potential difference with the walls. Electric field lines are shown in blue.

and outermost disks, and on the front of the CSC for the middle disk. Each RPC consists of two plates of high resistance material, one held at a positive voltage, the anode, and the other held at a negative voltage, the cathode. The volume between the plates is filled with a gas similar to the drift tubes. When a muon passes between the plates, it ionizes the gas molecules, and the electrons are accelerated towards the positive plate, creating an avalanche of secondary electrons that combine with the positive plate creating a voltage drop that is read out as a signal. The timing resolution achieved from the RPCs is less than the 25 ns LHC bunch crossing, supplementing the spatial resolution provided by the DTs in the barrel, and the CSCs



(a) A longitudinal cross-section of the muon barrel RPC system. RPCs are attached to the top and bottom of the first two layers of drift stations, and to the bottom of the outer two layers

(b) Cross-section of muon endcap system. It is composed of three disks, with RPCs mounted on the back of CSC system on the first and last disks, and on the front of the CSC in the middle disk

Figure 4.29: RPC layout for the barrel and endcaps

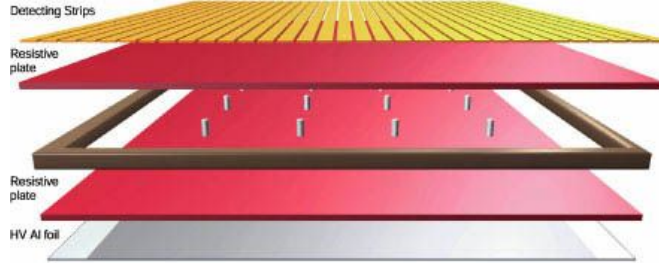


Figure 4.30: Exploded diagram of an RPC

1315 in the endcap.

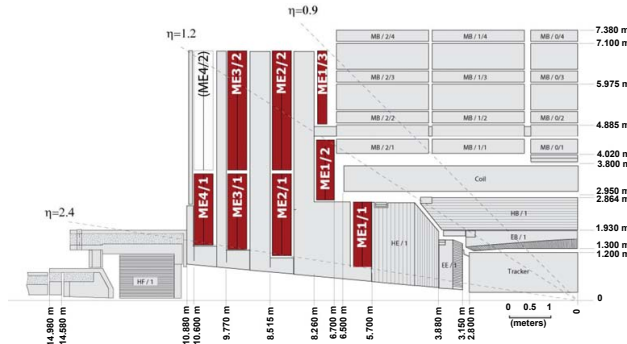


Figure 4.31: Cross-section of one quarter of the muon endcap system, with the 4 disks of CSC systems shown in red

1316 In addition to RPCs, the muon endcap (ME) system, uses cathode strip chambers (CSCs)  
1317 to provide additional spatial resolution on muons. Each endcap has 4 layers of CSCs, with a  
1318 trapezoidal shape, with 468 cathode strip chambers distributed on each. Three groups of 72  
1319 are located on the inner disk, a group of 36 and a group of 72 in the second and third disk, and  
1320 a group of 36 in the outer disk. Figure 4.32 shows the layout of a quarter section of the CSC  
1321 system in the ME. A CSC station consists of 6 layers of gas chambers, where each chamber is  
1322 an array of anode wires, held at a positive voltage, arranged perpendicular to cathode strips,  
1323 held at negative voltage. The volume of the chamber is filled with a gas that is 40% Argon,  
1324 50% CO<sub>2</sub>, and 10% CF<sub>4</sub>. When a muon passes through the volume, the gas is ionized, and now,  
1325 since the anode and cathode strips are perpendicular, when the electrons and gas ions combine  
1326 with the anode and cathode respectively, a 2-D measurement of the muon's position is recorded.  
1327 Figure 4.32 shows a diagram of a CSC chamber with 7 layers to create the 6 gas chambers.

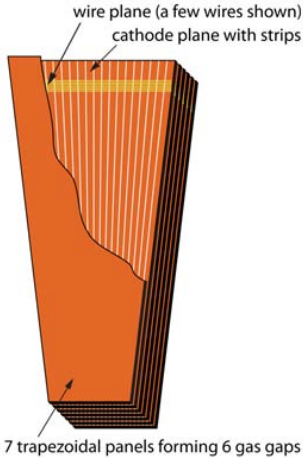


Figure 4.32: A CSC station with 7 layers, making 6 gas chambers. Cathode strips are shown in yellow, perpendicular to the vertical anode wires in orange.

## 1328 4.5 Data Collection Overview

1329 The LHC is designed to deliver protons at 40 MHz, corresponding to a bunch crossing every 25 ns.  
1330 The majority of the interactions will be glancing, low-energy collisions, which do little to reveal  
1331 new phenomenon, and would be impossible to store for analysis. A trigger system is designed to  
1332 select interesting events with a large potential of revealing new physics. The rate is reduced in  
1333 two steps through the Level-1 (L1) trigger, and the High-Level Trigger (HLT). The L1 trigger is  
1334 composed of programmable electronics and hardware that buffers the data and perform simple  
1335 calculations on tracks and calorimeter energy deposits to determine whether an event should be  
1336 kept for analysis. This reduces the event rate from 40 MHz to 10 kHz. The HLT is a computer  
1337 farm of  $\sim$ 1000 computer processors, that perform a more sophisticated reconstruction of the  
1338 tracks and energy deposits, as well as more complicated calculations between reconstructed  
1339 objects. This stage reduces the rate to a much more manageable 100 Hz.

1340 The L1 trigger is composed of local, regional, and global components. The process of deter-  
1341 mining whether to accept or reject the event begins by calculating Trigger Primitive Generators  
1342 (TPGs) based on calorimeter energy deposits, and tracks in the muon chambers. The entire  
1343 process has a latency time of  $3.2 \mu\text{s}$ , which corresponds to the length of the LHC abort gap.  
1344 Sufficiently large data buffers allow the storage of all the events processed during a bunch train,  
1345 meaning that CMS is capable of running with zero dead time due to detector readout latency.

1346 In the ECAL a trigger tower consists of a  $5 \times 5$  array of crystals. Front-end electronics on the  
1347 crystals receive ADC counts on the amplitudes of the photomultipliers, and uses information  
1348 encoded in the electronics to convert this sum to the transverse energy,  $E_T$  deposited in the  
1349 crystals. The EB TPG also encodes information about the distribution of energy, and thus the

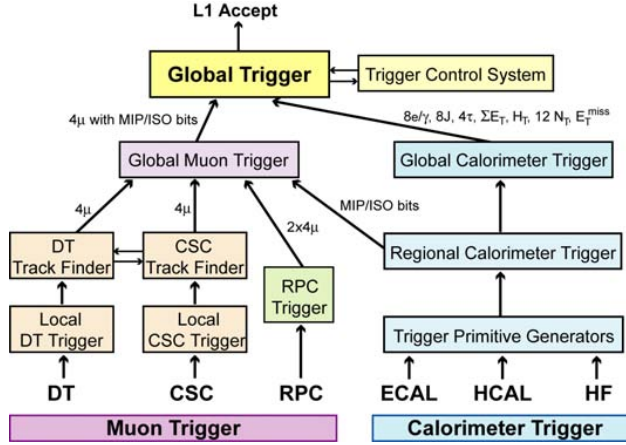
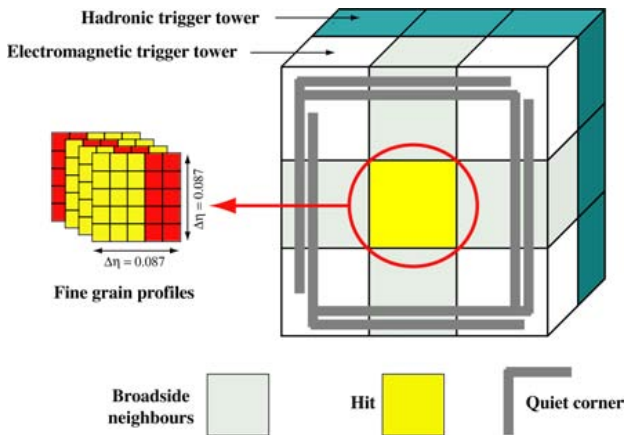


Figure 4.33: A block diagram of the L1 trigger

shower shape in the  $5 \times 5$  array, which is used to veto anomalous signals. In the HCAL, a trigger tower consists of one of the 16 azimuthal wedges, with segmentation  $(\Delta\eta, \Delta\phi) = (0.087, 0.087)$ , in the barrel and endcap. Similarly to the ECAL, front-end electronics digitize the signal from the HCAL HPDs, and convert the ADC counts into sums of transverse energy. These calorimeter TPGs are sent to a Regional Calorimeter Trigger (RCT) that is composed of a  $4 \times 4$  array of trigger towers, with the exception of the HF, which is formed by a single trigger tower.

Figure 4.34: A schematic of the  $e/\gamma$  trigger algorithm

The RCT determines electron and photon candidates from the calorimeter sums. The  $e/\gamma$  trigger searches for the highest energy trigger tower in the ECAL. Within that trigger tower, it checks that the EM shower is contained in a  $2 \times 5$  array of crystals and that the ratio of ECAL to HCAL energies is less than 5%. It is considered an isolated electron if all eight of its nearest neighbors pass these requirements, and a corner of five neighbors has energy below a threshold requirement. It is considered a non-isolated electron if only the second highest  $E_T$

1362 broadside neighbor trigger tower passes these criteria. Up to four isolated, and four non-isolated  
 1363  $e/\gamma$  candidates per RCT are passed to the Global Calorimeter Trigger (GCT).

1364 The GCT determines jets, total transverse energy, missing transverse energy, jet counts, and  
 1365  $H_T$  (scalar sum of transverse momentum), in addition to the highest rank isolated and non-  
 1366 isolated *egamma* candidates. Jets are found in a clustering algorithm that looks for large energy  
 1367 deposits in  $2 \times 12$  cells of  $\phi$  or  $\eta$  that span  $40^\circ$  and half the detector in each of coordinates. Up  
 1368 to four jets, and four tau jets from the HCAL and four jets from the HF are forwarded to the  
 1369 Global Trigger (GT).

1370 The non-calorimeter based triggers are based on measurements of the DTs, CSCs, and RPCs  
 1371 in the muon drift chambers. The barrel DTs look for hit patterns among neighboring tubes  
 1372 in successive layers, and fits a track segments in the  $\eta$  and  $\phi$  coordinates. The endcap CSCs  
 1373 provide 3-dimensional track segments and are combined with the DTs to form tracks that are  
 1374 passed to the Global Muon Trigger (GMT). The RPCs provide an independent set of tracks and  
 1375 timing hits to the GMT. Each bunch crossing the GMTs receive up to four muon candidates  
 1376 in the barrel RPCs, four from the barrel DTs, four from the endcap RPCs, and four from the  
 1377 endcap CSCs. The GMT records the candidate's  $p_T$ , charge,  $\eta$ , and  $\phi$  position, as well as a  
 1378 quality code related to the fit of the track to the hit positions of the detector. The GMT sends  
 1379 then sends these muon candidates to the GT.

1380 The Global Trigger can execute up to 128 trigger algorithms in parallel to analyze the  $p_T$ ,  
 1381 charge,  $\eta$ , and  $\phi$  position, and associated quality codes for muons, electrons, photons, jets, and  
 1382 missing transverse energy. Most algorithms compare single object characteristics to thresholds  
 1383 to determine if they pass minimally interesting criteria. If any of the algorithms return a passing  
 1384 decision, the L1 trigger issues an accept statement that allows the data stored in buffers to be  
 1385 readout by the CMS Data Acquisition (DAQ) system.

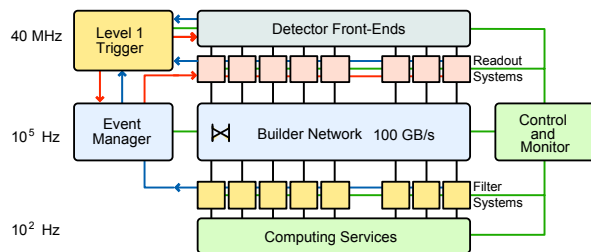


Figure 4.35: Layout of the CMS DAQ

The CMS DAQ collects information from 626 subdetector Front End Drivers (FEDs), which extract the buffered information from the various front-end systems, upon the arrival of a L1 trigger accept. An event builder algorithm assembles the fragments from the various sub-systems into a single coherent event, and transmits the information to the HLT computing farms. Figure 4.35 shows a schematic of the DAQ system.

The HLT computer farm performs the final reduction of data rate, from 100kHz from the L1 to 100Hz. The computer farm performs basic consistency checks to ensure the quality of the data, then performs calculations based on topology of the HLT path. Typically, a more sophisticated reconstruction of an object takes place, and kinematic cuts are applied to the object or in relationship to other objects in the event. Each HLT path forms its own data set, thus creating single muon, single electron, electron+jets, etc. type datasets. The unpacked detector information read by the DAQ is composed of ADC counts for each readout channel, TPGs, and the L1 decision. This is known as the RAW dataset. Reconstructed physics objects are stored RECO data tier, and finally an analysis object data (AOD) tier is created containing only information about the reconstructed objects without having to store detector information. This last format requires the least amount of data per event for storage, and contains the reconstructed physics objects, such as electrons, muons, jets, etc. which are used to search for new physics phenomena.

1404 **Chapter 5**

1405 **Particle Reconstruction at CMS**

1406 Charged and neutral hadrons in the form of jets, missing transverse energy (MET), photons,  
1407 electrons, muons, and tau leptons are reconstructed at CMS using the particle flow event-  
1408 reconstruction algorithm [70]. The algorithm is based on a three step process of identifying  
1409 charged particle tracks using the muon chambers and silicontracker, identifying clusters of energy  
1410 in the ECAL and HCAL, and linking the tracks to the calorimeter clusters. The calorimeter  
1411 energy deposits were calibrated with test beam sources, data from cosmic rays and beam dumps,  
1412 and finally from collision data. The algorithm constructs muons by fitting the tracks formed  
1413 between the muon chambers, pixel and silicon trackers. Electrons have tracks from the pixel and  
1414 silicon tracker matched to the ECAL, with a minimum energy deposited in the HCAL. Jets are  
1415 formed from tracks, ECAL, and HCAL clusters falling with a conical angle. The identification  
1416 of one, three, or larger odd number of tracks, and the majoriy of the energy contained in a small  
1417 cone size, allows a jet to be tagged as a hadronically decaying tau lepton. Additional algorithms  
1418 are also used to identify a jet as coming from the decay of a b-quark, primarily by looking for  
1419 secondary vertices in the pixel and silicon tracker.

1420 **5.1 Iterative Tracking**

1421 Since approximately two-thirds of the energy of a jet is carried by charged hadrons, the tracker is  
1422 the cornerstone of the particle-flow algorithm [70]. The path of a charged particle in a magnetic  
1423 field follows a helical pattern, described by 5 parameters. The extraction of these requires  
1424 three 3-dimensional measurements of the particle, or two 3-dimensional measurements and a  
1425 constraint on the origin [71]. The pixel detector is ideal for this since each pixel provides a 3-  
1426 dimensional measurment of the particle's location. Track reconstruction is the process of using  
1427 hits in the pixel and silicon detector elements to estimate the momentum and trajectory of the

1428 charged particle responsible for the hit [71]. The tracking software at CMS is known as the  
1429 Combinatorial Track Finder (CTF), which is based on producing tracks over multiple iterations  
1430 of the reconstruction sequence, removing the tracks with the largest  $p_T$  closest to the interaction  
1431 region first, reducing the combinatorial complexity over each iteration.

1432 Each iteration begins by identifying a seed for the particle tracks, which is a minimum  
1433 combination of pixel or silicon tracker hits that is used as an initial estimate of the trajectory  
1434 of the particle [71]. Then, tracks are found by applying the Kalman filter [72]. This method  
1435 is based on applying a small gaussian uncertainty to the location of the seed hits, fitting an  
1436 intial track to these hits, then looking for additional hits that fall within the error of the initial  
1437 estimate, deeper in the tracker. These hits are added to the fit with their own uncertainties,  
1438 and the fit is re-calculated, each time attempting to minimize the mean-square estimation of the  
1439 error. The 5 helical trajectory parameters are extracted, and tracks with poor fits are discarded.

1440 A total a six iterations is used, each with a different starting seed or kinematic requirement  
1441 on the  $p_T$  of the tack, as well as the transverse and longitudinal distance from the reconstructed  
1442 vertex [72]. The first iteration is seeded by three hits in the pixel detector. The second, is seeded  
1443 by two hits in the pixel detector and a pixel vertex, which is form when at least four pixel tracks  
1444 point back to a common origin. The third iteration is seeded once again by three hits in the  
1445 pixel detector, except with a looser minimum  $p_T$  cut. The fourth iteration uses seeds from any  
1446 three hits in the pixel detector or silicon tracker, with at least one hit coming from the pixel  
1447 detector. In the fifth iteration seeds are formed from the inner two rings of the TIB, TID, and  
1448 TEC. The final iteration begins with seeds from the first two rings of the TOB and the fifth ring  
1449 of the TEC.

## 1450 5.2 Calorimeter Clustering

1451 The clustering algorithm is used to detector the energy and director of stable, neutral particles  
1452 such as photons and neutral hadrons [70]. It also seperates the energy contributions from the  
1453 netural and charged hadrons, and provides an aditional energy measurement for charged hadrons  
1454 with very low or high  $p_T$  tracks, both cases that degrade the energy resolution. Finally, the  
1455 clustering algorith properly accounts for bremmstrahlung energy losses from electrons. The  
1456 algorithm is performed independently for the ECAL barrel, ECAL endcaps, HCAL barrel, and  
1457 HCAL endcaps. In the HF, no clustering algorithms are used, as each cell is used as its own  
1458 cluster in an event.

1459 The clustering alorithm begins by identifying "cluster seeds", which are the highest  $p_T$  cells  
1460 above a defined energy threshold [70]. Then, "topological clusters" are formed by grouping

1461 adjacent cells together with energy above 80 MeV in the ECAL barrel, 300 MeV in the ECAL  
 1462 endcaps, and 800 MeV in the HCAL. As a new cell is added, the total cluster energy and  
 1463 position is updated until no new cells are able to be added. Each cluster seed thus gives rise  
 1464 to a "particle-flow cluster". Each of these clusters is used as a candidate to be associated with  
 1465 tracks during the third stage of the algorithm, the linking step.

### 1466 5.3 Calorimeter Energy Calibration

1467 One of the most critical steps in reconstructing particles is the calorimeter energy calibration,  
 1468 which is the conversion of calorimeter scintillator light and photodetector current to the energy  
 1469 deposited in the calorimeter by the particle traversing it. This is done by exposing the crystals  
 1470 to particles of a known energy, using large samples of cosmic ray muons, by measuring minimum-  
 1471 bias events assuming a  $\phi$  symmetry, the of  $\pi^0$  and  $\eta^0$  meson resonances decaying into photons,  
 1472 and  $W$  and  $Z$  bosons into electrons.

1473 Before installation at P5, the ECAL and HCAL were pre-calibrated using test beam. In  
 1474 2006, the ECAL was exposed to an electron beam with energies between 15 and 250 GeV [73]  
 1475 at CERN. Additionally, intercalibrations between crystals were performed with 90 and 120 GeV  
 1476 beams. Also at CERN in 2006, the HCAL was calibrated, prior to installation using a beam of  
 1477 50 GeV pions [74].

1478 Once both calorimeters were installed, the detectors were calibrated with cosmic ray muon  
 1479 events in 2007 with the CMS magnet de-energized during the CRUZET (Cosmic RUn at ZErO  
 1480 Tesla) data taking campaign, and again with the CMS field on in 2008 during the CRAFT  
 1481 (Cosmic Run At Four Tesla) campaign. Shortly after the CRAFT campaign, the LHC delivered  
 1482 450 GeV proton beams to collimator targets upstream of the CMS detector, creating accelerator  
 1483 muons that are additionally used to calibrate the detector response. The ECAL energy  
 1484 resolution was improved from 7.6% to 6.3%, and in the barrel, the intercalibrations from the  
 1485 test beam were validated at a 2% level of agreement [75]. The HCAL energy calibration resulted  
 1486 in 5% energy resolution in the HB, 10% in the HE, 12% in the HF, and 5% in the HE[76].

1487 After an initial set of data collection three independent calibration methods are combined to  
 1488 determine the absolute energy scale and intercalibration coefficients for the crystals [?]. The first  
 1489 method uses a large amount of data collected from minimum-bias trigger events, events which  
 1490 are dominated by glancing collisions and QCD jet production. The processes that contribute  
 1491 to these events have final state particles symmetrically distributed in the  $\phi$  coordinate. By  
 1492 grouping the crystals into rings of  $\eta$ , and the response of each crystal can be determined and  
 1493 modified such that it matches the average crystal response in that  $\eta$  ring, with the uncertainty on

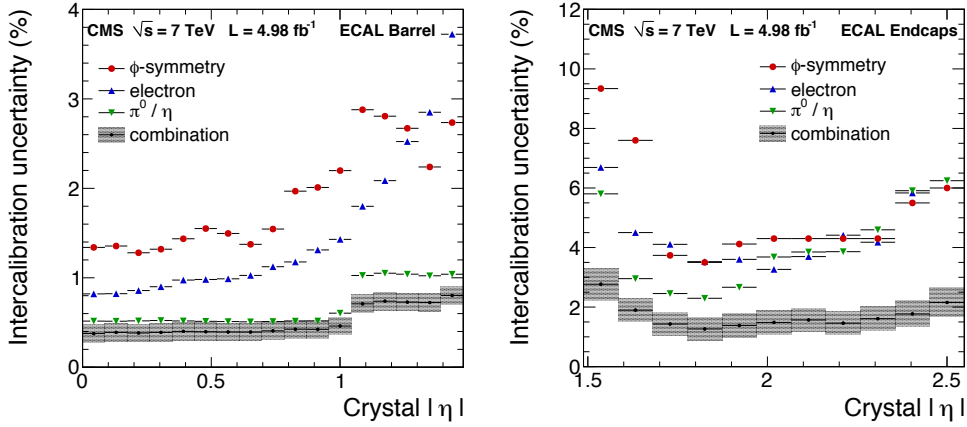


Figure 5.1: Results of the uncertainty on the ECAL intercalibration coefficients for the barrel (left) and endcaps (right)

the average representing the uncertainty on the intercalibration coefficient. The second method involves reconstructing the resonances of the  $\pi^0$  and  $\eta^0$  mesons decaying to two photons and relying on the high-precision measurements from other experiments to determine the exact mass of the resonance. Events near the resonance of these two particles are once again divided into rings of  $\eta$ , and averaged over the  $\phi$  coordinate. Decays of the  $Z$  boson and electron pair is also used to determine the absolute scale (ADC counts/GeV) of the crystals, once again relying on the higher-precision measurements of previous experiments for the location of the mass peak. Finally, comparisons between the energy measured in the tracker and that measured in the ECAL are made from  $W$  and  $Z$  boson decays to electrons. Figure 5.1 shows the results of combining all three methods, to determine the uncertainty of the intercalibration coefficients.

The ECAL also has a strong dependence on the rate of instantaneous luminosity that the crystals are exposed to. It is therefore necessary to perform additional crystal calibrations as a function of time during a run of data collection. Blue and orange LED light, and blue laser light is fed through a network of optical fibers to each crystal. A known amount of light is injected and the crystal response is measured. Figure 5.2 shows a plot of the crystal response versus time. Rings of  $\eta$  are formed and crystals within the same  $\eta$  ring are used to calculate an average response, as is done in the intercalibration procedures described above.

The performance of the HCAL calibration to the 50 GeV pion beam is validated by comparing energy measurements in the tracker to energy deposits in the HCAL [77]. Since neutral hadrons contribute approximately 10% of the energy contained in a jet, it is necessary to recalibrate the measured energy in the HCAL using simulated events where the true hadronic energy is known. The equation for the total calorimeter energy is given by:

$$E_{\text{calib}} = a + b(E, \eta)E_{\text{ECAL}} + c(E, \eta)E_{\text{HCAL}} \quad (5.1)$$

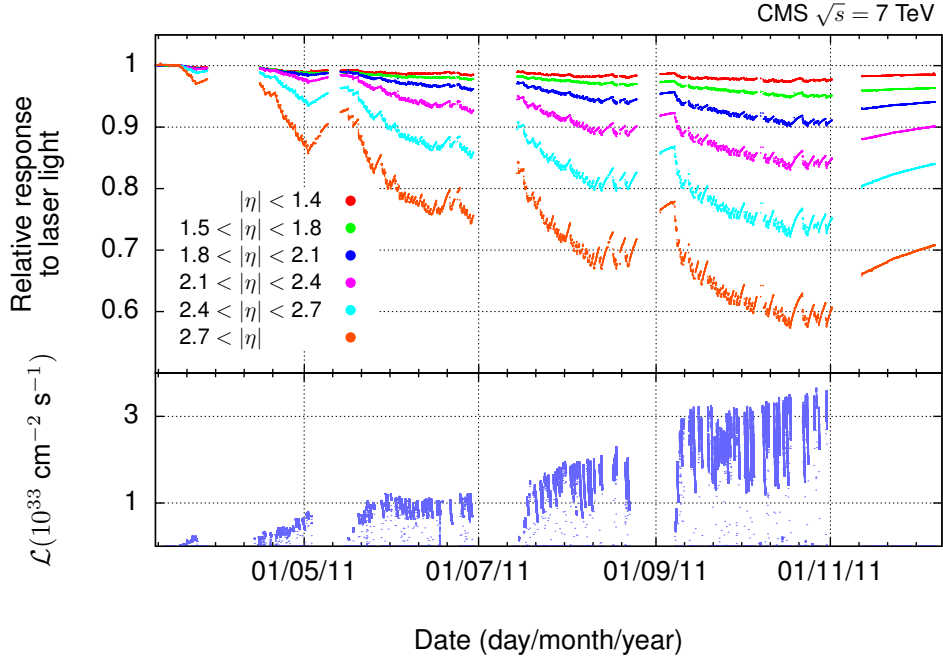


Figure 5.2: Instantaneous luminosity response to the crystals as measured by the laser and LED system. Additional crystal calibration constants are derived to normalize the crystal response over the range of collected data

1516 The coefficients, a, b, and c are determined through a  $\chi^2$  minimization procedure over each bin  
 1517 of energy, minimizing the difference between the reconstructed and true energies and solving for  
 1518 the parameters a, b, and c. Figure 5.3 shows the resulting HCAL energy resolution as a function  
 1519 of energy, and the values of the coefficients a, b, and c.

## 1520 5.4 Linking

1521 Once clusters are formed in the ECAL and HCAL barrels and endcaps, they are associated with  
 1522 nearby tracks in the pixel and silicon tracker in the phase of the particle-flow algorithm known  
 1523 as linking [70]. Single particles are formed out of the tracks and calorimeter clusters without  
 1524 double counting contributions from different detectors, forming "blocks" of linked elements. Due  
 1525 to the high granularity of each sub-detector, blocks of two-four elements are typical.

1526 The linking procedure between pixel and silicon strip tracks and the calorimeter deposits  
 1527 occurs in three steps: extrapolating the track to the ECAL preshower (PS); then to the ECAL  
 1528 to a depth corresponding to the maximum longitudinal shower profile; and finally to the HCAL  
 1529 to a depth corresponding to one interaction length. A track is then linked to a cluster if it  
 1530 falls within the cluster boundaries. One HCAL cluster may be associated to many tracks, but  
 1531 each track can only be associated with a single cluster, determined as the track with the shortest

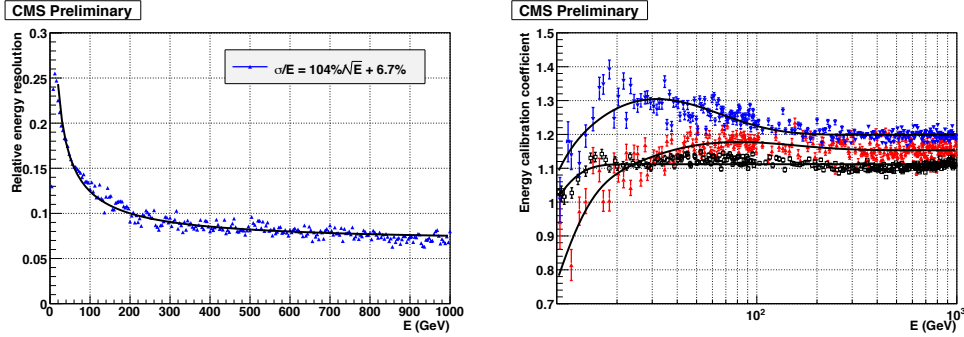


Figure 5.3: Results of using a  $\chi^2$  minimization procedure to estimate the neutral hadron energy contribution in the HCAL using simulated events

distance. For the ECAL, one track may be associated with many energy clusters, since they may have originated from hadronic shower fluctuations, so links to tracks should be preserved to avoid double counting the hadron energy. In order to account for the bremmstrahlung energy losses of electrons, tangent lines to the tracks are linked to the ECAL. If this extrapolated, tangent track falls within the ECAL cluster boundaries, it becomes a candidate for a bremmstrahlung photon from an electron. Since the ECAL has a finer granularity than the HCAL, clusters of the ECAL are linked to HCAL clusters if an ECAL cluster falls within the boundary of the HCAL cluster. Finally, linking between the muon chambers and the inner tracker occurs via a  $\chi^2$  fit to a muon trajectory that would traverse the entire detector.

## 5.5 Physics Object Reconstruction

Once tracks have been formed from the muon chambers, pixel, and silicon tracker detectors and linked to clusters in the ECAL and HCAL, particles can be reconstructed. The process begins by reconstructing muons, then electrons and photons, finishing with charged and neutral hadrons. The charged and neutral hadrons are then clustered together to make jets, which can be tagged as  $\tau$  or  $b$ -jets. After each object is formed, the tracks and calorimeter energy depositions associated with it are removed from the collection of blocks that are used to form the particle-flow candidates, ensuring that no double counting of energy contributions is taking place.

### 5.5.1 Muon Reconstruction

The reconstruction of physics objects in the particle-flow algorithm begins by identifying muons [70]. The algorithm begins by identifying tracks in the pixel and silicon strip detectors that have been linked to tracks in the muon chambers, and fit with a muon trajectory with a minimum  $\chi^2$ . Additionally, it is required that muon track that is fit with both muon chambers, pixel,

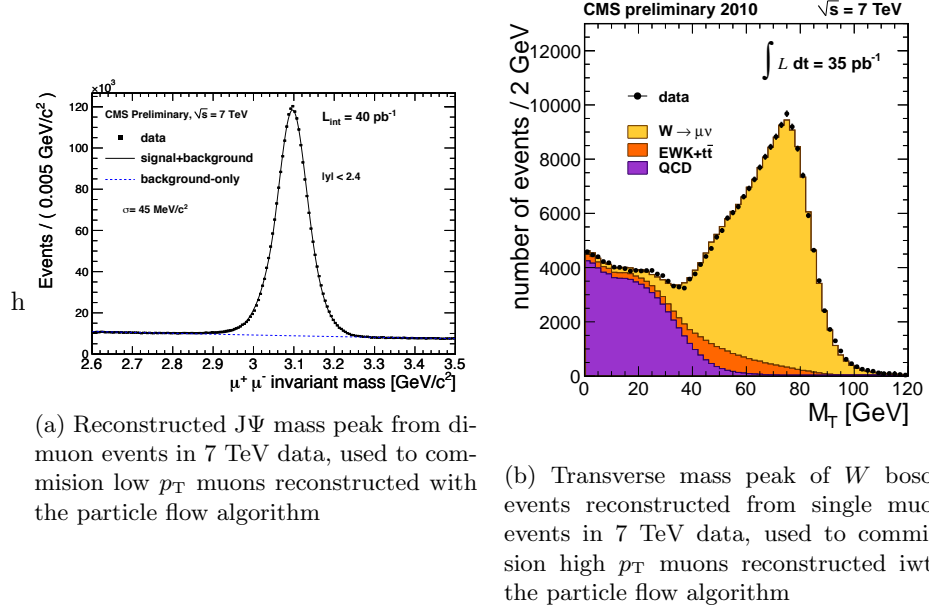


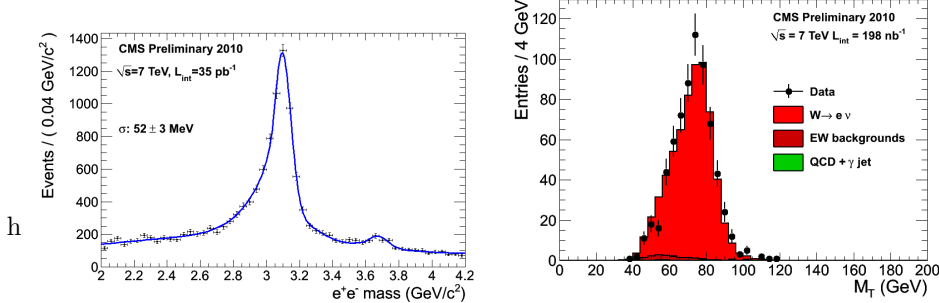
Figure 5.4: Muon validation plots for the particle-flow reconstruction

and silicon tracker information is compatible within 3 sigma, to a track fit with the pixel and silicon tracker information alone. When the "particle-flow" muon is removed from the collection of candidate blocks, the muon tracks, and based on studies from the CRAFT data run, 3 (0.5)  $\text{GeV} \pm 100\%$  is removed from the HCAL (ECAL) cells that the muon traverses.

In 2010, 7 TeV data was collected [78] in order to commission the reconstruction of muons. The  $J/\Psi$  resonance at 3.1 GeV provides a large number of low  $p_T$  di-muon pairs. Figure 5.4(a) shows the reconstructed  $J/\Psi$  mass with  $40 \text{ pb}^{-1}$  of data. High  $p_T$  muons are commissioned by reconstructing the  $W$  boson mass. Figure 5.4(b) shows the results the first  $35 \text{ pb}^{-1}$  of 7 TeV data.

### 5.5.2 Electron Reconstruction

The next stage in particle-reconstruction is the identification of electrons [70]. Electrons leave hits in the tracker and deposits most of its energy into the ECAL, with the clustering widest in the  $\phi$  direction due to brehmmstralung. Electron tracks tend to be shorter and lose energy in the tracker due to bremsmstrahlung, a highly non-linear process, that the Kalman fitter used in the track identification phase is not optimized for. These tracks are re-fit using the Guassian Sum Filter (GSF) algorithm [79]. This algorithm accounts for the change in trajectory of the electron due to bremmstrahlung, extending the linking to ECAL clusters in the  $\phi$  direction. Blocks that have GSF tracks linked to ECAL clusters, including clusters identified as bremmstrahlung photons, and additionally linked to a HCAL cluster with a much smaller energy deposition than in the ECAL are then identified as a "particle-flow electron".



(a) Reconstructed  $J/\Psi$  mass peak from di-electron events in 7 TeV data, used to commission low  $p_T$  electrons reconstructed with the particle flow algorithm

(b) Transverse mass peak of  $W$  boson events reconstructed from single electron events in 7 TeV data, used to commission high  $p_T$  electrons reconstructed with the particle flow algorithm

Figure 5.5: Electron validation plots for the particle-flow reconstruction

Similarly to the muons, the electron identification from the particle-flow algorithm was commissioned using 7 TeV data collected in 2010. Low  $p_T$  electrons were commissioned from the  $J/\Psi$  mass peak, shown in figure 5.5(a) and high  $p_T$  electrons were commissioned from  $W$  boson decays, shown in figure 5.5(b).

### 5.5.3 Charged Hadron Reconstruction

Charged hadrons are reconstructed next in the particle flow algorithm [70]. Tracks linked to both ECAL and HCAL energy deposits give rise to "particle-flow charged hadrons" if calorimeter energy is compatible measured from the curvature of the tracks in the pixel and silicon detector. A fit is then performed between all of the tracks and the HCAL energy clusters to determine an optimally measured momentum. In the case where there is only one track, this fit reduces to a weighted average between the track and HCAL energy clusters.

### 5.5.4 Photon and Neutral Hadron Reconstruction

The next step in the algorithm is to identify ECAL and HCAL energy clusters that aren't linked to tracks or clusters that are linked to tracks, but have a much larger energy measurement. In the latter case, blocks are kept if the excess energy in the calorimeter clusters is larger than the energy resolution of the calorimeter. In both cases, if the total energy excess in the HCAL is larger than the energy measured in the ECAL, than a "particle-flow photon" is created using the energy in the ECAL and the remaining HCAL energy forms a "particle-flow neutral hadron", with calibrations performed in the manner described in section 5.3. In the case where the ECAL energy is larger than the HCAL energy, both cluster energies form a particle-flow photon. This is justified the observation that, in jets, the neutral component of the hadronic energy only deposits

1595 3% of the total jet energy in the ECAL, compared to 25% of the jet energy from photons.

### 1596 5.5.5 Jet Reconstruction

1597 After the formation of photons, charged and neutral hadrons, jets can be formed by clustering  
 1598 groups of these objects together based on their momentum weighted, spatial separation from one  
 1599 another. This clustering procedure is performed with the anti- $k_T$  algorithm [80]. The momentum  
 1600 weighted spatial operation function between two particles,  $i$  and  $j$ , is defined as:

$$d_{ij} = \min\left(\frac{1}{p_{iT}^2}, \frac{1}{p_{jT}^2}\right) \frac{\Delta_{ij}^2}{R^2} \quad (5.2)$$

1601 where  $\Delta_{ij}^2 = (y_i - y_j)^2 + (\phi_i - \phi_j)^2$  and  $y_{i,j}$  is the rapidity, and  $\phi$  is the azimuthal angle in  
 1602 the CMS detector.  $R$  is the distance parameter, which is a user-defined quantity for the  
 1603 algorithm.

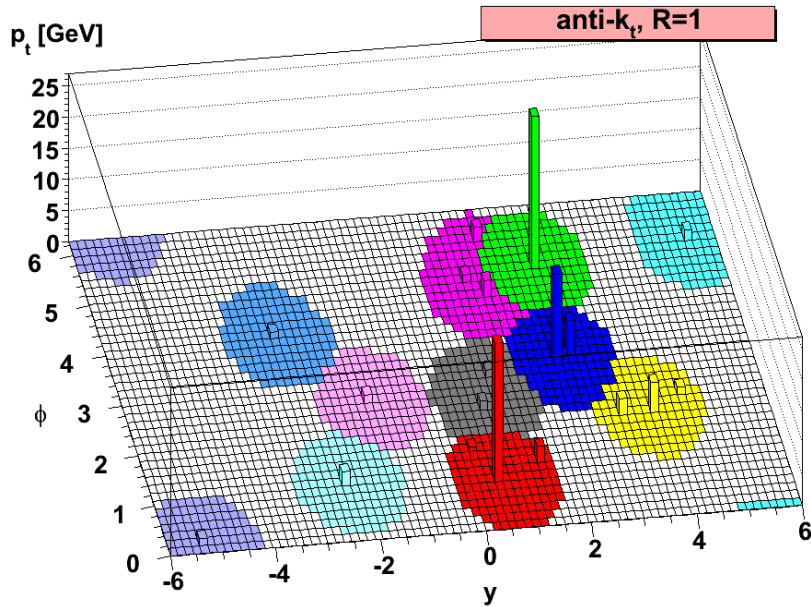


Figure 5.6: The anti- $k_T$  jet clustering algorithm with distance parameter  $R=1.0$

1604 The algorithm proceeds by looping over all of the particle-flow candidate objects that have  
 1605 been formed and calculates the quantity  $d_{ij}$ , and combines the two objects with smallest value,  
 1606 into a single object. The process is repeated until the smallest value,  $d_{ij}$  has a value  $d_{ij} > \frac{1}{p_{Ti}^2}$  for  
 1607 all remaining pairs. The parameter,  $d_{ij}$ , will be larger for two small  $p_T$  objects, when compared  
 1608 to a pair of equally separated high  $p_T$  objects. Thus, softer particles will cluster around  
 1609 harder objects before clustering amongst themselves. No hard particles are present, within the  
 1610 distance parameter, then the object will accumulate soft particles in a circle of radius  $R$ . The  
 1611 tendency is to produce circular jets, but in the case where a soft  $p_T$  cluster intersects with a hard

$p_T$  cluster, objects the  $1/p_T^2$  weighting will tend to favor clustering around the harder  $p_T$  object. Figure 5.6 shows an example of the results of an anti- $\text{kt}$  algorithm with distance parameter  $R = 1.0$ , in the azimuthal-rapidity coordinate system. An example of the preferential grouping around harder  $p_T$  objects can be seen at  $\phi = 5, y = 2$ .

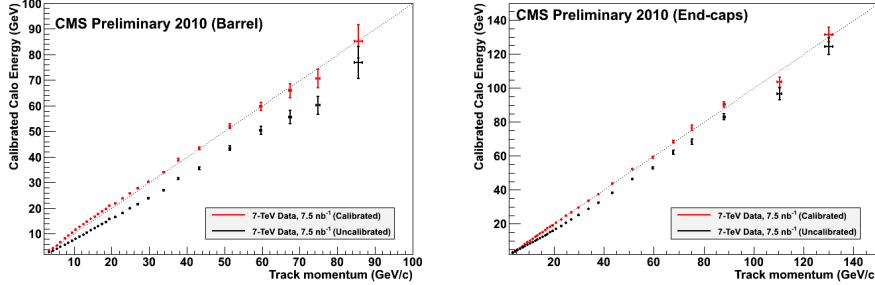


Figure 5.7: Commissioning of the particle-flow algorithm on jets, involved comparing the energy measured from charged hadron tracks, to energy measured in calorimeter clusters linked to the tracks

In 2010, the particle-flow algorithm for jet reconstruction was commissioned with 7 TeV data [81]. The calibration procedure involved selecting charged hadrons from tracks in the pixel and silicon strip detector, and comparing the energy measured there to the energy measured in the calorimeter. After calibration, the measurements between tracker and calorimeter agree within error bars up to 100 GeV, as shown in figure 5.7.

## Hadronic Tau Reconstruction

Tau leptons are unstable particles which decay via a weak interaction to lighter particles. If it decays hadronically via a  $W$  boson to two quarks, the tau lepton can be reconstructed analyzing the resulting jets that are clustered by the anti- $\text{kt}$  algorithm. Tau jets are characterized by the number of charged hadrons produced in the decay. Since charge must be conserved, this results in one charged hadron being produced  $\sim 85\%$  of the time, known as a "one-pronged" decay, and three charged hadrons being produced  $\sim 15\%$  of the time, known as a "three-pronged" decay. Thus, a tau jet is identified as a jet with only 1 or 3 tracks associated with the calorimeter cluster. Additionally, the jets from hadronic tau decays tend to have their energy more collimated than jets produced from quarks or gluons. Jets are clustered twice, using two different distance-parameters. The ratio of energies of the smaller to the larger of the distance parameters jets is used to determine how collimated a jet is. If the ratio is within a given threshold, determined by the analyst in terms of the reconstruction efficiency and fake rate, the jet is tagged as a hadronic tau jet.

1635 **b-Tagging**

1636 Jet that originate from  $b$ -quarks have unique characteristics that allow them to be distinguished  
1637 from jets originating from other quarks or gluons. This identification process is known as  $b$ -tagging.  
1638 Several algorithms exist to identify  $b$ -jets, since there are many kinematic variables  
1639 that distinguish them from other jets. Due to the heavier nature of the  $b$ -quark,  $b$ -jets have a  
1640 larger transverse momentum compared to lighter-flavour quarks. Since it belongs to the third  
1641 quark generation, it is much more likely to find a non-prompt lepton embedded in the jet. Muons  
1642 are especially useful to tag  $b$ -jets since the information they leave in the tracker can be used to easily  
1643 identify if it came from prompt decay or not.

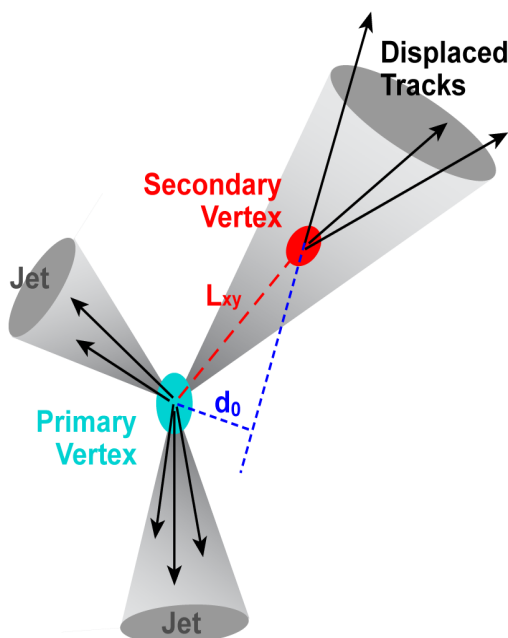


Figure 5.8: A  $b$ -meson will travel a distance  $L_{xy}$  before decaying and creating a secondary vertex. The impact parameter,  $d_0$  measures the longitudinal displacement of the two vertices

1644 The most important characteristic of the  $b$ -quark is its relatively long lifetime compared to  
1645 lighter-flavour quarks. The consequence is that a  $b$ -meson will travel a very small, but observable  
1646 distance within the tracker before it decays, forming a secondary vertex. The distance and  
1647 uncertainty measured on the distance between the primary and secondary vertex is then used as  
1648 discriminating variables to tag  $b$ -jets. Figure 5.8 shows a cartoon of a  $b$ -jet creating a secondary  
1649 vertex after traveling some distance from the primary vertex.

1650 **5.5.6 Missing Transverse Energy Reconstruction**

1651 CMS has a hermetic design to ensure that all particles produced in a collision would pass through  
1652 the detector. Only long-lived, neutral particles avoid detection, such as neutrinos in the standard

<sup>1653</sup> model. Many BSM theories, such as SUSY, are also characterized by stable, neutral particles.  
<sup>1654</sup> These particles can only be detected by measuring a momentum imbalance after measuring all  
<sup>1655</sup> of the particles in the event.

<sup>1656</sup> The missing transverse energy (MET),  $\cancel{E}_T$ , is the vector sum of all of particle-flow candidates  
<sup>1657</sup> reconstructed in the event. It is defined as

$$\cancel{E}_T = \left| - \sum_{i=1}^{nPF} \vec{p}_{Ti} \right| \quad (5.3)$$

<sup>1658</sup> where  $nPF$  is the number of particle-flow candidates in the event, and  $\vec{p}_{Ti}$  is the vector sum of  
<sup>1659</sup> their transverse momentum.

<sup>1660</sup> The particle-flow algorithm for reconstructing MET was commissioned in 2010 with 7 TeV data  
<sup>1661</sup> [81]. Minimum-bias collisions and QCD multi-jet production are processes that produce no real  
<sup>1662</sup> MET. Therefore, a sample of these events were collected, allowing for the algorithm to be tuned  
<sup>1663</sup> and calibrated.

# 1664 Chapter 6

## 1665 Analysis I: The first $5.08 \text{ fb}^{-1}$ of 1666 8 TeV data

1667 The search for  $t\bar{t}H$  production begins by identifying  $pp$  collisions consistent with the production  
1668 of a top quark pair with additional  $b$  jets. Top quarks decay  $\sim 100\%$  of the time to a bottom  
1669 quark and a  $W$  boson, and the  $W$  boson can decay either into a charged lepton and a neutrino  
1670 or into a pair of quarks. Since there are two  $W$  bosons in the event, the decays of the  $W$   
1671 bosons determine the specific top pair signatures recorded in the detector. The decay of the two  
1672  $W$  bosons define the categorizations of  $t\bar{t}$ -like events as either all-hadronic, in the case of zero  
1673 charged leptons; semi-leptonic, in the case of one charged lepton; and di-leptonic in the case of  
1674 two charged leptons. the detector. This analysis describes the Lepton+Jets (LJ) channel, where  
1675 one of the  $W$  bosons has decayed to an electron or a muon and the corresponding neutrino,  
1676 while the other  $W$  boson decays into two quarks. To compensate for the low production rate,  
1677 the analysis is optimized to search for the Higgs boson decaying to a  $b$ -quark pair. The final  
1678 state is then  $l\nu qqbbbb$ , where  $l$  refers to either an electron or a muon. In the case of an ideal  
1679 reconstruction of the event, the LJ signal events contains six jets, four of which are  $b$ -tagged.  
1680 However, to accommodate jets lost to detector acceptance and merging between separate partons,  
1681 and the  $b$ -tagging efficiency, events with four or more jets and two or more  $b$ -tags are included  
1682 in the signal region.

1683 The largest background contribution is  $t\bar{t}+\text{jets}$  production. This process can be decomposed  
1684 in terms of the flavour of the extra jets produced in the event. For this analysis, the inclusive  
1685  $t\bar{t}\text{jets}$  process is broken into three sub-processes:  $t\bar{t}+$  light flavor jets where one or more of the  
1686 jets is mistagged,  $t\bar{t} + c\bar{c}$  and  $t\bar{t} + b\bar{b}$ . Smaller background contributions come from  $W+\text{jets}$ ,  
1687  $Z+\text{jets}$ , single top quark, diboson, and  $t\bar{t} + W/Z$  production.

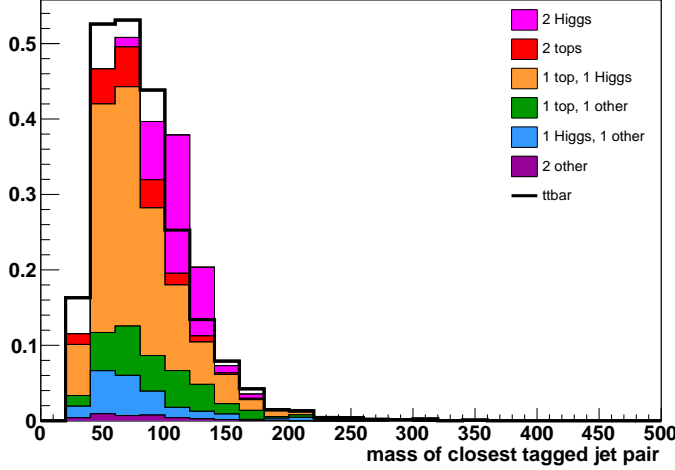


Figure 6.1: This figure shows the breakdown of jet-to-parton assignments for the two jets with the minimum  $\Delta R$  separation in the event for events with greater or equal 4  $b$ -tagged jets.

In other Higgs searches involving the decay to two  $b$ -quarks, the most powerful discriminating variable is the invariant mass of the  $b\bar{b}$  pair, which has a peak at the mass of the Higgs. However, for  $t\bar{t}H$  production, with a final state of four  $b$ -quarks, the combinatorics of selecting the quarks coming from the Higgs, instead of the  $t\bar{t}$  system, prevents the reconstruction of a clear resonant peak, as shown in figure 6.1. This results in an additional loss of mass resolution, or smearing, on the  $b\bar{b}$  invariant mass spectrum.

Although there is poor resolution on the Higgs boson resonance in the  $b$ -quark dijet mass spectrum, there are a number of kinematic variables that can be used to discriminate between the  $t\bar{t}+j$  background and the  $t\bar{t}H$  signal. For example, the recoil of the Higgs off of the  $t\bar{t}$  system, the decay products of the top quarks from the  $t\bar{t}H$  signal will have, on average, a slightly larger component of momentum transverse to the beam-line. Additionally, the larger number of authentic  $b$ -jets in  $t\bar{t}H$  events can be exploited through the likelihood value returned by a  $b$ -tagging algorithm for all of the jets in the event. By themselves, none of these variables provide a large degree of discriminating power to separate the  $t\bar{t}H$  signal from the large, and kinematically similar background. Therefore, the discriminating power of several variables is combined using a multivariate analysis technique (MVA), which is used to set upper limits on  $t\bar{t}H$  production in the data set.

The following sections will describe the analysis that was carried out on the first  $5\text{ fb}^{-1}$  of data collected by the CMS detector. This includes definitions of the simulated samples used to estimate the expected backgrounds in data, the event selection used to isolate the  $t\bar{t}H$  signal, the application of MVA techniques, evaluation of systematic uncertainties, and upper limit setting on the production rate of  $t\bar{t}H$ .

## 6.1 Data and Simulated Samples

*pp* collision data is collected by the CMS detector, as described in previous chapters. The signal and background signatures are estimated using Monte Carlo simulation techniques. The simulation involves the combination of the most current theoretical and empirical information about the interactions of the known particles. The simulation of an event is decomposed into a sequence of calculations and each signal and background process is calculated separately. Information about Monte Carlo event simulation techniques is taken from reference [82].

The first stage of event simulation for a given signal or background process is to calculate the probability that some set initial state particles with a certain momentum will create a final state of particles with a certain momentum. For example, in the case of the  $t\bar{t}H$  signal, this is the probability that two protons travelling towards each other along the z-axis (beam-line), each with a given energy and momentum, will produce a top quark pair and a Higgs boson, each with some momentum vector,  $\hat{p}_t, \hat{p}_{\bar{t}}, \hat{p}_H$ , which points into the hermetic CMS detector. As discussed in section 2.1, this probability is calculated by examining the lagrangian of the theory describing the process and calculating its scattering amplitude, to some order in perturbation theory, using the Feynman rules derived from the lagrangian. The scattering amplitude is a multi-dimensional probability function, which depends on the initial and final state momentum of the particles in the process. Thus, given some initial state momentum,  $p_i$ , it tells you the probability to produce a final state particle with momentum  $p_f$ . It is understandable that the scattering amplitude is often referred to as a matrix element, since given a vector of initial state particles with a certain momentum, the scattering amplitude would be a matrix, whose elements would give the probability of creating the vector of final state particles.

Since protons are composite objects, when they collide, it is their quarks or gluons which are actually interacting. The momentum distribution of each of the valence quarks, the gluons, and the sea quarks, which account for quantum fluctuations that temporarily create all other quark flavours inside the proton, is described by a Parton Distribution Function (PDF). The PDF describes what fraction of the proton's momentum is distributed among each of its constituents. Due to the large strength of the QCD interactions that bind the quarks together, the PDF cannot be calculated perturbatively from QCD. It has been measured empirically, and is composed of the results of several experiments over the past decades.

Event generator algorithms are computer programs that, given a lagrangian of particle theory, will calculate the matrix element for a given process. Then, the generator is provided with values of the momentum of the initial state particles. For protons, this would be the beam energy of the LHC. To assign momentum values to the constituent quarks or gluons that actually participate in the interaction, random values are sampled from the probability distributions described by

1745 a PDF that is provided to the algorithm. Given a choice of momentum for the input particles,  
1746 a value and direction of the momentum for each of the final state particles is sampled from  
1747 the probability function provided by the calculated the matrix element (ME). The process of  
1748 randomly sampling a probability function, in order to conduct a calculation, is known as a Monte  
1749 Carlo sampling technique.

1750 In the case where final state particles are quarks or gluons, also known as partons, an ad-  
1751 ditional calculation is necessary to create the physical hadron states. First, the decay sequence  
1752 of each parton is calculated until the decay products reach a user defined value, known as the  
1753 hadronization scale. This decay sequence is referred to as the parton shower (PS), since each  
1754 parton creates a multitude, or a shower, of additional partons. Once the parton shower is cal-  
1755 culated, each of the colored partons are transformed into color-singlet primary hadrons, which  
1756 themselves decay, and form secondary hadrons. This process, known as hadronization, results in  
1757 a collimated spray of hadrons, each with a component of momentum along the original parton's  
1758 direction. These hadrons are clustered together and referred to as a hadron jet.

1759 Once the hadronization is completed, the next stage of the event generation is to simulate the  
1760 response of the CMS detector when this process occurs at the interaction point where the LHC  
1761 beams are made to collide. The Geant 4 detector simulation framework is used to create a model  
1762 of each and every detector element, electronic readout, and mechanical support structures that  
1763 make compose CMS. Geant 4 is also about to describe how energy is deposited into the different  
1764 types of material as a particle passes through each detector element, simulating the response  
1765 each element to presence of a particle in the detector. The digitization and signal acquisition of  
1766 the electronics that read-out the detector elements is also simulated.

1767 The final stage the generation of an event is the reconstruction of the simulated detector  
1768 signals into physics objects. This process is described in detail in the previous chapter. It  
1769 proceeds with simulated, instead of real detector signals.

1770 The entire event simulation, reconstruction, and subsequent analysis is implemented in a  
1771 software framework that is known as CMS Software (CMSSW).

### 1772 6.1.1 Data Samples

1773 The results presented here are based on the first  $5.08\text{ fb}^{-1}$  of the 2012 CMS dataset. Data-sets  
1774 are collected through HLT triggers and stored offline for analysis. Table 7.1 lists the datasets  
1775 used for this analysis, which is composed of two runs of data collection triggered on the presence  
1776 of one muon or electron in an event. The luminosities are quoted from a calculation performed  
1777 with minimum-bias events measured with the HF detector and have been determined to have a  
1778 2.2% uncertainty.

Dataset	Run Range	Integrated Luminosity
/SingleMu/Run2012A-PromptReco-v1/AOD	190645–193621	0.87 fb <sup>-1</sup>
/SingleMu/Run2012B-PromptReco-v1/AOD	193834–196531	4.21 fb <sup>-1</sup>
<b>Total SingleMu</b>	<b>190645–196531</b>	<b>5.08 fb<sup>-1</sup></b>
/SingleElectron/Run2012A-PromptReco-v1/AOD	190645–193621	0.87 pb <sup>-1</sup>
/SingleElectron/Run2012B-PromptReco-v1/AOD	193834–196531	4.21 pb <sup>-1</sup>
<b>Total SingleElectron</b>	<b>190645–196531</b>	<b>5.08 fb<sup>-1</sup></b>

Table 6.1: The datasets analyzed for this analysis.

### 1779 6.1.2 Signal Samples

1780 The  $t\bar{t}H$  signal is modeled using the Pythia Monte Carlo generator. Signal events were generated  
 1781 privately using the same conditions and configuration as the "Summer" MC campaign, which  
 1782 generated the background samples used in this analysis and is a central effort by a dedicated  
 1783 team of collaborators within the CMS experiment. The samples and associated cross sections  
 1784 used are listed in Table 7.2.

Mass	Dataset	Cross Sect.
110 GeV/c <sup>2</sup>	/TTH_HToAll_M_110_8TeV_FastSim_pythia6/lannon-TTH_HToAll_M_110_8TeV _FastSim_pythia6-dff75535147f54d9d70123289019ff88/USER	0.1887 pb
115 GeV/c <sup>2</sup>	/TTH_HToAll_M_115_8TeV_FastSim_pythia6/lannonTTH_HToAll_M_115_8TeV _FastSim_pythia6f8fb6149649333009ec8462da200312d/USER	0.1663 pb
120 GeV/c <sup>2</sup>	/TTH_HToAll_M_120_8TeV_FastSim_pythia6/puighTTH_HToAll_M_120_8TeV _FastSim_pythia695111b4e2be5b1aa536a508d15d97f92/USER	0.1470 pb
122.5 GeV/c <sup>2</sup>	/TTH_HToAll_M_122p5_8TeV_FastSim_pythia6/slaunwhj- TTH_HToAll_M_122p5_8TeV_FastSim_pythia61e2fdcc9a937df208692b27cb39e0444/USER	0.1383 pb
125 GeV/c <sup>2</sup>	/TTH_HToAll_M_125_8TeV_FastSim_pythia6/lwmingTTH_HToAll_M_125_8TeV _FastSim_pythia6191b19832235558f2b51f7486e9bfa14/USER	0.1302 pb
127.5 GeV/c <sup>2</sup>	/TTH_HToAll_M_127p5_8TeV_FastSim_pythia6_crabv2/jgwoodTTH_HToAll _M_127p5_8TeV_FastSim_pythia6_crabv28cc2ab68d00e069563cff89a5be0e271/USER	0.1227 pb
130 GeV/c <sup>2</sup>	/TTH_HToAll_M_130_8TeV_FastSim_pythia6/neuTTH_HToAll_M_130_8TeV _FastSim_pythia65052c957a6363e9b1d5c2be444ffc86d/USER	0.1157 pb
135 GeV/c <sup>2</sup>	/TTH_HToAll_M_135_8TeV_FastSim_pythia6/lwmingTTH_HToAll_M_135_8TeV _FastSim_pythia6c8734ad98f674743d713309ea4b6ad34/USER	0.1031 pb
140 GeV/c <sup>2</sup>	/TTH_HToAll_M_140_8TeV_FastSim_pythia6/lwmingTTH_HToAll_M_140_8TeV _FastSim_pythia6cf0b11a8bdd755ec1ec3d7a35c9a88be/USER	0.09207 pb

Table 6.2: List of signal MC datasets and cross sections used to determine the SM expectation.

### 1785 6.1.3 Background Samples

1786 In order to estimate the rate and kinematic behavior of the backgrounds, this analysis primarily  
 1787 uses Monte Carlo (MC) samples from the "Summer12" MC campaign. Most of the samples are  
 1788 generated either with the Madgraph tree-level matrix element generator matched to Pythia for  
 1789 the parton shower, or with the NLO generator Powheg combined with Pythia. These samples  
 1790 are reconstructed with the same CMSSW version as the data samples listed above. Table 7.3  
 1791 lists the background MC samples and associated cross sections.

Sample	Dataset	Cross Sect.
$t\bar{t}$ +jets	/TTJets_MassiveBinDECAY_TuneZ2star_8TeVmadgraph-tauola/Summer12PU_S6_START52_V9v1/AODSIM	225.197 pb
$t\bar{t} + W$	/TTWJets_8TeVmadgraph/Summer12PU_S7_START52_V9v1/AODSIM	0.249 pb
$t\bar{t} + Z$	/TTZJets_8TeVmadgraph_v2/Summer12PU_S7_START52_V9-v1/AODSIM	0.208 pb
$W$ +jets	/WJetsToLNu_TuneZ2Star_8TeVmadgraphtarball/Summer12-PU_S7_START52_V9v1/AODSIM	36257.2 pb
$Z/\gamma^*$ + jets $M_{\ell\ell} > 50 \text{ GeV}/c^2$	/DYJetsToLL_M50_TuneZ2Star_8TeVmadgraphtarball/Summer12-PU_S7_START52_V9v2/AODSIM	3503.17 pb
$10 \text{ GeV}/c^2 < M_{\ell\ell} < 50 \text{ GeV}/c^2$	/DYJetsToLL_M10To50filter_8TeVmadgraph/Summer12-PU_S7_START52_V9v1/AODSIM	860 pb
Single $t$ schannel	/T_schannel_TuneZ2star_8TeVpowhegtauola/Summer12-PU_S7_START52_V9v1/AODSIM	3.79 pb
$t$ channel	/T_tchannel_TuneZ2star_8TeVpowhegtauola/Summer12-PU_S7_START52_V9v1/AODSIM	56.4 pb
$tW$	/T_tWchannelDR_TuneZ2star_8TeVpowhegtauola/Summer12-PU_S7_START52_V9v1/AODSIM	11.1 pb
Single $\bar{t}$ schannel	/Tbar_schannel_TuneZ2star_8TeVpowhegtauola/Summer12-PU_S7_START52_V9v1/AODSIM	1.76 pb
$t$ channel	/Tbar_tchannel_TuneZ2star_8TeVpowhegtauola/Summer12-PU_S7_START52_V9v1/AODSIM	30.7 pb
$tW$	/Tbar_tWchannelDR_TuneZ2star_8TeVpowhegtauola/Summer12-PU_S7_START52_V9v1/AODSIM	11.1 pb
$WW$	/WW_TuneZ2star_8TeV_pythia6_tauola/Summer12-PU_S7_START52_V9v1/AODSIM	54.8 pb
$WZ$	/WZ_TuneZ2star_8TeV_pythia6_tauola/Summer12PU_S7_START52_V9-v1/AODSIM	32.3 pb
$ZZ$	/ZZ_TuneZ2star_8TeV_pythia6_tauola/Summer12PU_S7_START52_V9-v1/AODSIM	7.7 pb

Table 6.3: List of background MC datasets and cross sections used for normalization.

### 6.1.4 MC pileup reweighting

During 2012 data collection, the LHC provided increasingly large instantaneous luminosities to the CMS experiment. Consequently, the average number of overlapping events reconstructed in single detector readout window has also increased. When these overlapping events, known as pileup events, occur within the same bunch crossing, which as referred to as "in-time" pileout. Alternatively, "out-of-time" pileup, comes from energy deposits in the detector from previous bunch crossings and from very early arrivals of particles from the forthcoming bunch crossing. Pileup events can affect many aspects of the reconstruction of a more interesting event, such as the degradation of lepton isolation and jet energy resolution. The simulated samples used in the analysis must also have the same distribution of pileup events as what was measured in the data.

During the generation of the simulated samples used in the analysis, the average amount of expected pileup was unknown. Events were thus simulated with a conservatively large estimate of the pileup distribution, so that if the measured data revealed a smaller average value, the simulation could be reweighted to match the data. For the simulation, number of interactions is a user defined value added to every generated event. For the data, the number of pileup interactions for each unit of time depends on the instantaneous luminosity for each bunch pair

and the total inelastic cross section,  $\sigma_{inelastic}$ , of the proton. The value of  $\sigma_{inelastic} = 69.4$  mb was found to describe the data well. To estimate the effect of the systematic uncertainty of this choice, the value was varied by  $\pm 7\%$ .

To gauge the accuracy of the calibration of the pileup distribution used in the simulated samples, a comparison of the number of reconstructed vertices between data and the simulated  $t\bar{t}$  MC sample is shown in figure 7.1. The unweighted MC distribution is shown in blue, the reweighted distribution in red, and the measured data in black points. After reweighting, there is a good level of agreement between the data and MC distributions.

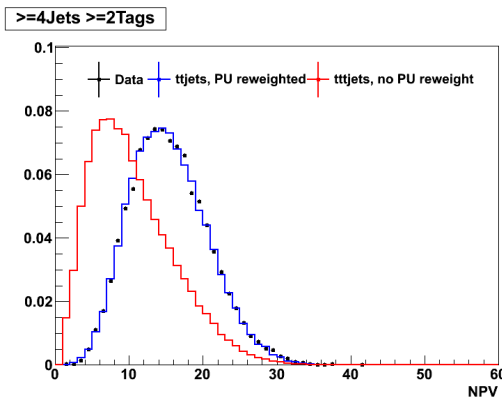


Figure 6.2: Comparison of number of reconstructed vertices for data (black) and the  $t\bar{t}$  MC sample before (blue) and after (red) pileup reweighting. After pileup reweighting, the MC matches the data well.

### 6.1.5 Additional Pileup Corrections

Studies comparing the Monte Carlo simulations to observed data revealed that the jet  $p_T$  spectra was not well modeled. Many sources of this discrepancy were investigated, but the clearest correlations arises when the 8 TeV data events are divided into three categories according to their amount of pileup:

• Low PU, number of primary vertices  $\leq 10$

• Medium PU, number of primary vertices from 11 to 15

• High PU, number of primary vertices  $\geq 16$

The modeling of jet  $p_T$  was worse for events with a larger number of pileup events overlapping in the detector. The same effect was present for the majority of the jets in the event, evidenced by the discrepancy in the  $H_T$  distribution, shown in figure 6.3, where  $H_T$  is defined as the scalar sum of the transverse momentum for reconstructed jets in the event:

$$H_T = \sum_i^j p_T^i \quad (6.1)$$

The effect makes the data have a softer  $p_T$  spectrum than the simulations. The same effect was observed in 7 TeV data as well. It was present, even after employing several sophisticated reconstruction techniques designed to mitigate pileup effects. These techniques included the removal of charged hadrons in the particle-flow algorithm, not associated with the primary vertex and re-weighting the simulated samples to match the pileup distribution measured in the data.

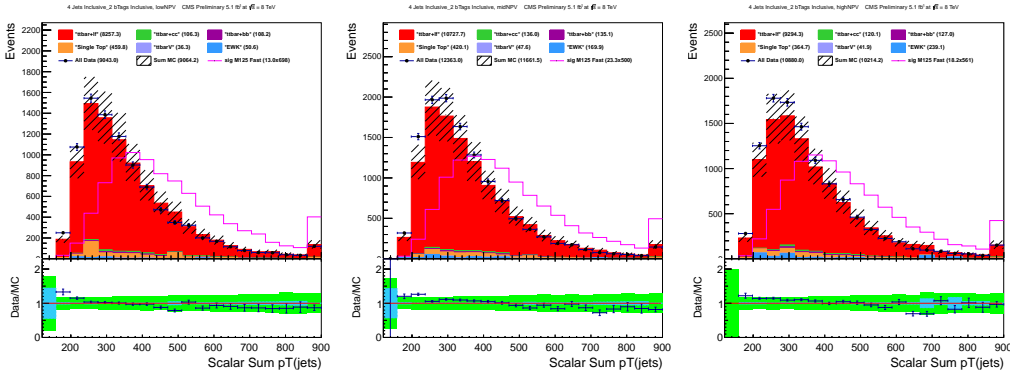


Figure 6.3:  $H_T$  distribution for 8 TeV lepton plus jet events with  $\geq 4$  jets and  $\geq 2$  tags shown for different amounts of pileup. The left-hand plot shows low pileup, the middle plot shows medium pileup, and the right-hand plot shows high pileup.

Although the exact underlying cause of the jet mis-modelling effect was not able to be identified, the magnitude of the effect seemed to be related to the number of pileup events. As such, an additional correction factor is needed to account for the remaining difference in pileup effects between data and Monte Carlo. The correction factor was calculated from data that was dominated by background events, with a single lepton,  $\geq 4$  jets, and  $\geq 2$  tags. The expected signal-to-background ratio in this sample is 0.002, which is low enough that the correction factor will not be biased by signal events. The correction factor is based on the  $H_T$  distribution for data and Monte Carlo for Low pileup (PU), Medium PU, and High PU events. The correction factor is the bin-by-bin ratio of the data and the Monte Carlo  $H_T$  distributions in each PU category. By preparing a separate correction factor for each PU category smaller adjustments were made to well-modeled Low PU events and larger adjustments to the poorly modeled High PU events.  $H_T$  shows the same mis-modelling as each of the jet  $p_T$ s and it effects all of the jet  $p_T$ s. This makes it a natural choice for a correction factor.

In order to evaluate the systematic shape uncertainty introduced by the correction factor, the uncorrected simulated distributions are used as  $-1\sigma$  systematic uncertainty and the  $+1\sigma$  uncertainty is determined by doubling the correction factor. The factor of two for the  $+1\sigma$  variation is motivated by the desire to provide a large enough systematic uncertainty to cover

any possible over-correction of the simulations. This is a reasonable choice because it creates a deviation that is the same size as the original observed difference between data and simulations.

The correction factor and uncertainty improved the agreement between data and Monte Carlo. Figure 6.4 compares the  $H_T$  distributions before and after reweighting. The data-to-MC ratio plots are the clearest indicators of the improvement from the correction factor. Before the correction, the  $H_T$  ratio plot forms a line with a slope. After the correction the slope is gone.

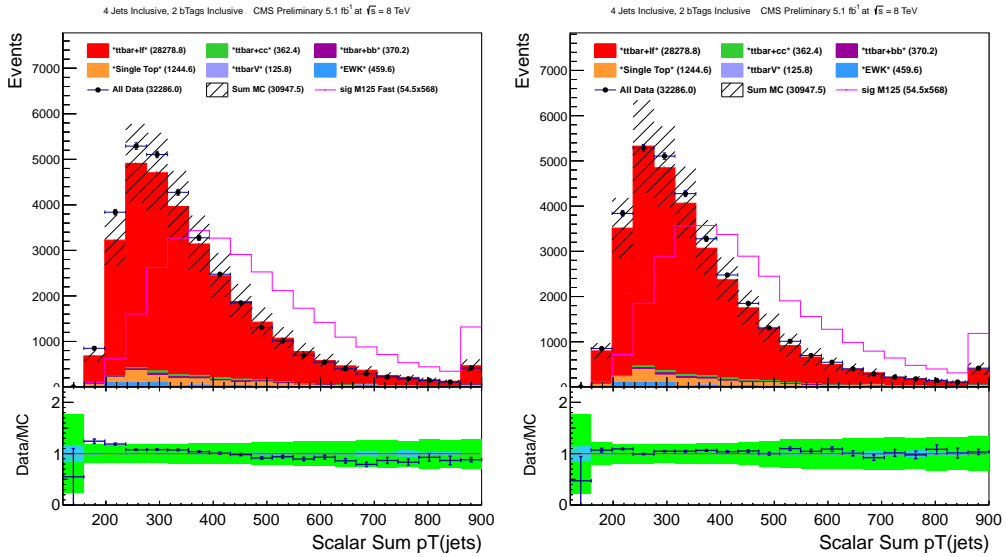


Figure 6.4:  $H_T$  distribution for 8 TeV lepton plus jet events with  $\geq 4$  jets and  $\geq 2$  tags. The left-hand plot shows the distribution before correction. The right-hand plot shows the distribution after correction. Note that the ratio in the right-hand plot is flatter than the left-hand plot.

## 6.2 Event Selection

This section defines the common physics objects and event selection requirements. Leptons are classified into two categories, tight and loose, defined for muons in section 6.2.3 and for electrons in 6.2.4. For this analysis, exactly one tight muon or exactly one tight electron is required and events with any additional loose leptons are rejected.

### 6.2.1 Event cleaning

For data and MC events, certain cuts are applied to remove events that are either non-physical or that come from non-collision events, such as instrumental noise or beam backgrounds. In the data, every event is required to pass the following filters:

- CSC tight beam halo filter - Secondary particles are produced in showers which are initiated by collisions of the beam with residual gas inside the LHC vacuum chamber or by interactions of the particles with a large transverse emmitance with limiting apertures.

- HBHE noise filter with isolated noise rejection - this filters spurious signals from the HCAL barrel and endcap subdetectors which are not associated with particles measured in a collision event.
- HCAL laser filter - ensures that data is not taken simultaneous with the laser calibration system
- ECAL dead cell trigger primitive (TP) filter - removes dead or noisy ECAL cells from being used in the reconstruction, these compose  $< 1\%$  of the total crystals in the ECAL
- Tracking failure - designed to catch events with too few tracks
- Noisy SCs in EE - new filter from the ECAL Detector Performance Group (PDG), and validated by the MET Physics Object Group (POG)

which are described in [83].

Additionally, beam scraping events are filtered based on the fraction of good tracks. At least 25% of tracks are required to be of high purity. Finally, every data event must contain at least one primary vertex (PV) that passes the following selection:

- The number of degrees of freedom used to find the PV must be larger than 4,
- The absolute value of the  $z$ -coordinate of the PV must be smaller than 24 cm,
- The absolute value of the  $\rho$ -coordinate of the PV must be smaller than 2 cm,
- The PV must not be identified as fake.

### 6.2.2 Trigger

Each data and MC event is required to pass one of the triggers in Table 6.4, which are a subset of the total number of SingleMu and SingleEle HLT triggers available. Muon+jet events must pass the SingleMu trigger, while electron+jet events must pass the SingleEle trigger.

Dataset	Trigger Name
SingleMu	HLT_IsoMu24_eta2p1_v*
SingleEle	HLT_Ele27_WP80_v*

Table 6.4: List of lepton+jets triggers

### 6.2.3 Muon Selection

In this analysis, muons are selected from the set of "particle-flow" muon objects that have been reconstructed in the event. Muons are classified into two categories: tight and loose, according

1893 to the quality of their reconstruction. This is ensured by applying the selection cuts shown in  
1894 Table 6.5. The cuts are defined as follows:

- 1895 •  $p_T$  - the component of the momentum transverse to the beam-line.
- 1896 • PFRelIso - this is the quantity known as relative isolation, computed by the particle flow  
1897 algorithm. It is a ratio of the energy deposits remaining in the calorimeter and tracker,  
1898 after the contribution from the muon has been removed, in a cone size  $\Delta R = 0.3$ , around  
1899 the muon track.
- 1900 •  $|\eta|$  - the absolute value of the pseudorapidity of the muon
- 1901 • ID - This refers to whether the muon was reconstructed with a  $\chi^2$  fit to the tracks from  
1902 the tracker only (tracker muon), the tracker and the muon chambers (global muon), or if  
1903 the particle was reconstructed from the particle-flow algorithm (PFmuon)
- 1904 •  $N_{layers}(\text{tracker})$  - the number of layers in the tracker with hits used in the muon track  
1905 reconstruction
- 1906 •  $X^2$  of track fit - the reduced  $\chi^2$  (raw  $\chi^2$ /Number of Degrees of Freedom in the fit), typically  
1907 a value of 1 indicates the fit describes the data well
- 1908 •  $N_{layers}(\text{pixel})$  - the number of layers in the inner pixel detector with hits used in the muon  
1909 track reconstruction
- 1910 •  $N_{segments}(\mu)$  - the number of segments in the muon chambers used to reconstruct the  
1911 muon tracks
- 1912 •  $|d0(\text{BS})|$  - the absolute value of the transverse distance of the extrapolated muon track to  
1913 the primary vertex, as calculated from the beam spot (BS)
- 1914 •  $|dZ(\text{BS})|$  - the absolute value of the longitudinal distance of the extrapolated muon track  
1915 to the primary vertex

#### 1916 6.2.4 Electron Selection

1917 Electrons are selected from the set of "particle-flow electron" objects reconstructed in the event.  
1918 Similarly to muons, electrons are classified into two categories: tight and loose, according to the  
1919 quality of their reconstruction. The selection cuts are shown in Table 6.6. The definitions  
1920 are identical to the ones provided in section 6.2.3. Additional variables not described are:

- 1921 •  $E_T$  - the transverse energy of the electron, which due to its relatively light mass, is approx-  
1922 imately equal to its  $p_T$

Cuts	Tight $\mu$	Loose $\mu$
$p_T$	$>30 \text{ GeV}/c$	$>10 \text{ GeV}/c$
PFRelIso(0.4)	0.12	<0.2
$ \eta $	<2.1	<2.5
ID	Global Muon	Global Muon or Tracker Muon
ID	PFMuon	PFmuon
$N_{\text{layers}}(\text{tracker})$	>5	
$X^2$ of track fit	<10	
$N_{\text{layers}}(\text{pixel})$	>0	
$N_{\text{segments}}(\mu)$	>1	
$ d0(\text{BS}) $	<0.2 cm	
$ dZ(\text{BS}) $	<0.5 cm	

Table 6.5: Tight and loose muon definition

- ID - electron ID is passed on a multivariate analysis (MVA) technique, which provides a discriminant value to separate fake from real electrons, and is trained with events that are required to pass a HLT trigger (mvaTrigV0), or not (mvaNonTrigV0). The "passConversionVeto" ID ensures that the electron has not been reconstructed from a photon which has converted to an electron positron pair

Cuts	Tight $e$	Loose $e$
$E_T$	$>30 \text{ GeV}/c^2$	$>15 \text{ GeV}/c^2$
PFRelIso(0.3)	<0.1	<0.2
$ \eta $	<2.5	<2.5
ID	MVA ID("mvaTrigV0") >0.0	MVA ID("mvaNonTrigV0") >0.0
ID	passConversionVeto	passConversionVeto
$ d0(BS) $	<0.02 cm	
$ dZ(PV) $	<1 cm	

Table 6.6: Tight and loose muon definition

### 6.2.5 Lepton selection and trigger efficiencies

The cumulative reconstruction efficiency of id+isolation+trigger has been calculated from data, as a function of pT and eta, as shown in figure 6.5 for electrons and muons. In order to reproduce the same response in the simulations as found in data, an event-by-event scale factor is applied to correct for this difference in efficiency.

The efficiency in data was measured by selected events with two tight muons, or two tight electrons with an invariant mass in a range between 70 and 130 GeV. This is centered on the  $Z$  boson resonance, and ensures that the selected leptons are authentic. The two leptons are additionally required to have opposite charge, which is measured by the direction of the curvature of their tracks in the magnetic field. A "tag" lepton is selected if has  $p_T > 30 \text{ GeV}$ , and passes the appropriate muon or electron trigger. The second lepton, the "probe" lepton, since selected as a pair coming from a  $Z$  boson, should be identical to the tag lepton, and thus should be identically reconstructed. The efficiency is then the ratio of the number events where both tag and probe leptons pass the  $p_T$  and trigger requirements over the number of events where only

1942 the tag lepton passes the  $p_T$  and trigger requirements. This study is repeated in bins of  $p_T$  and  
 1943  $\eta$  to remove any kinematic dependence on lepton efficiency.

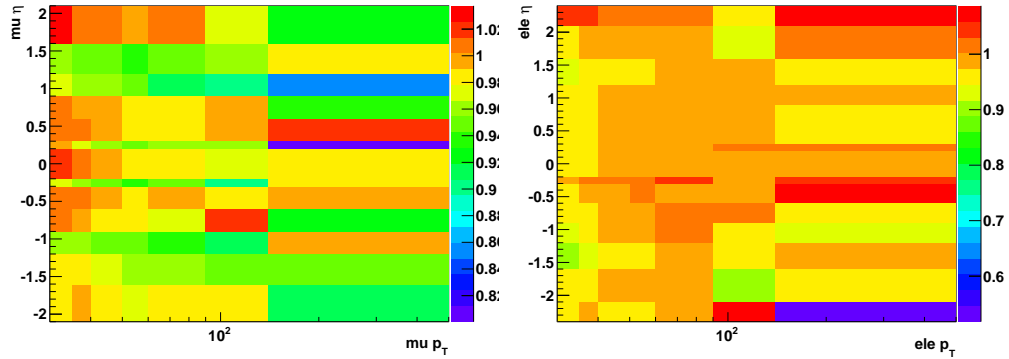


Figure 6.5: Muon and electron ID, isolation selection and trigger efficiency scale factors in bins of  $p_T$  and  $\eta$ .

1944 The combined ID, isolation, and trigger scale factor uncertainty is evaluated by looking at the  
 1945 variation of the scale factor as a function of parameters besides  $p_T$  and  $\eta$ , such as pileup and  $b$ -tag  
 1946 scale factor reweighting. A flat uncertainty of 4% covers the variations that are observed, and is  
 1947 thus adopted as a conservative estimate of the uncertainty on the combined lepton reconstruction  
 1948 efficiency.

### 1949 6.2.6 Jet selection

1950 As described in the previous chapter, jets are reconstructed with the anti-KT clustering algo-  
 1951 rithm [80], with a distance parameter of 0.5, starting from the set of objects reconstructed  
 1952 by the particle flow algorithm [70]. Non-isolated leptons, not associated with the decay of a  
 1953  $W$  boson, are allowed to be clustered into the jets. The selection cuts defining our jets can be  
 1954 found in Table 6.7. The cuts use the following variables to ensure the reconstruction of authentic  
 1955 hadronic jets:

- 1956 •  $p_T$  - component of the momentum transverse to the beam-line
- 1957 •  $\eta$  - the pseudorapidity of the reconstructed jet
- 1958 • CEF - Charged Electromagnetic Fraction: the ratio of charged particles to the total number  
 1959 of particles in the jet
- 1960 • NHF - Neutral Hadron Fraction: the ratio of neutral particles to the total number of  
 1961 particles in the jet
- 1962 • NEF - Neutral Electromagnetic Fraction: the ratio of photons to the total number of  
 1963 particles in the jet

- CHF - Charged Hadron Fraction: the ratio of charged hadrons to the total number of particles in the jet
- NCH - Number of Charged Hadrons: raw charged hadron multiplicity
- $N_{\text{constituents}}$  - Number of constituents, which can be charged and neutral hadrons, as well as non-prompt photons and leptons.

Cuts	Jet
$p_T$	$>30\text{ GeV}/c$
$ \eta $	$<2.4$
CEF, NHF, NEF	$<0.99$
CHF, NCH	$>0$
$N_{\text{constituents}}$	$>1$

Table 6.7: Jet definition

Additional correction factors are required such that the measured energy of the jet correctly reproduces the energy of the initial parton. This is done in four stages. The L1 Charged Hadron Subtraction (CHS) correction, is implemented in the particle-flow algorithm, and involves subtracting the energy contributions from charged hadrons that are not associated with the jet from the energy cluster. The next stage, L2 correction is a relative correction to make the measured jet response flat in  $\eta$ . The third stage, L3, is an absolute correction to the measured  $p_T$  of a jet in order to match the simulated jet  $p_T$  created using generator level input and a similar jet clustering algorithm. The L2 and L3 corrections are calculated using Monte Carlo, and thus an fourth correction factor, the L2L3 residual correction is applied that fixes the discrepancies between Monte Carlo and data. The correction factors are described in reference [84], and are derived from 2011 7 TeV data, with a selection of dijet events near the  $Z$ -boson mass peak. A "tag-and-probe" procedure similar to the lepton scale factors is applied to jets to determine the kinematic dependence ( $p_T$  and  $\eta$ ) of the detector in both simulations and data. Additionally, a scale factor is needed to adjust for the difference in jet energy resolution as measured in data and predicted in simulation. Table 6.8 gives the scale factors, and uncertainties, as derived from dijet events [84] as a function of  $\eta$  only, since no significant  $p_T$  dependence was observed.

$ \eta $	Data/MC Ratio (factor +stat. +syst.- syst.)
0.00-0.5	$1.052 \pm 0.012 + 0.062 - 0.061$
0.51-1.1	$1.057 \pm 0.012 + 0.056 - 0.055$
1.11-1.7	$1.096 \pm 0.017 + 0.063 - 0.062$
1.72-2.3	$1.134 \pm 0.035 + 0.087 - 0.085$
2.35-3.0	$1.288 \pm 0.127 + 0.155 - 0.153$

Table 6.8: Jet Energy Resolution (JER) scale factors

1985 **6.2.7 *b*-tagging selection**

1986 The algorithm used to perform *b*-tagging in this analysis is the combined secondary vertex (CSV)  
 1987 algorithm [85]. It relies on the superior ability of the inner tracker to reconstruct secondary  
 1988 vertices, which are the characteristic signature of *b*-quark decays. Tracks are selected if they  
 1989 meet the following requirements:

- 1990 • At least 8 hits in the pixel and silicon tracker, with at least 2 hits in the pixel detector  
 1991 • tracks must have  $p_T > 1$  GeV  
 1992 •  $\chi^2/\text{NDF}$  of the fitted track  $< 10$   
 1993 •  $|d_0|$  - transverse impact parameter  $< 2\text{mm}$ , since *b*-quarks will on average travel 0.45 mm  
 1994 in the detector before decaying

1995 Additionally, the following cuts are required:

- 1996 • The transverse distance between the primary and secondary vertices,  $L_T$ , is between 100  
 1997  $\mu\text{m}$  and 2.5 cm  
 1998 • The ratio of  $L_T$  and the uncertainty on its measurement,  $L_T/\sigma_{L_T} < 3$   
 1999 • The invariant mass formed by adding the four-vectors of all the tracks forming the sec-  
 2000 ondary vertex  $< 6.5$  GeV  
 2001 • The invariant mass falls outside a window near 50 MeV, corresponding to the  $K_S^0$  resonance

2002 Secondary vertices are decomposed into three categories. If a secondary vertex is found meeting  
 2003 the above criteria, it is a "reco vertex". If no secondary vertex is found meeting all the above  
 2004 criteria, the event can be classified as a "psuedo vertex" if more than two tracks have a signed  
 2005 transverse impact parameter significance, relative to the primary vertex, greater than 2. "No  
 2006 vertex" is found if neither of the prior two classification criteria can be met.

2007 For each of the vertex categories, a set of variables is used to create a single discriminating  
 2008 variable, using a likelihood ratio technique. The following input variables are used:

- 2009 • The invariant mass of the charged particles associated with the secondary vertex  
 2010 • The multiplicity of charged tracks associated with the primary vertex  
 2011 • The distance between the primary and secondary vertex in the transverse plane, divided  
 2012 by its error (only used in reco vertex category)  
 2013 • The psuedorapidities of the charged particle tracks associated with the secondary vertices

- The track impact parameter significance of the highest  $p_T$  track with invariant mass larger than the charm quark threshold, 1.5 GeV.

The likelihood function is split to separate between the charm and light-flavour backgrounds and is defined as:

$$\mathcal{L}^{b,c,q} = f^{b,c,q}(\alpha) \times \prod_i f_{\alpha}^{b,c,q}(x_i) \quad (6.2)$$

where  $\alpha = 1,2,3$ , denotes the different vertex categories,  $x_i$  are the individual variables,  $q$  stands for the light flavour quarks, while  $b$  and  $c$  stand for the bottom and charm quarks respectively.  $f^{b,c,q}(\alpha)$  is the probability for a quark flavour  $b, c$ , or  $q$ , to fall into category  $\alpha$ .  $f_{\alpha}^{b,c,q}(x_i)$  is the probability density function of the variable  $x_i$  in category  $\alpha$  for quark flavour  $b, c$ , or  $q$ . The combined discriminant is defined as

$$d = f_{BG}(c) \times \frac{\mathcal{L}^b}{\mathcal{L}^c + \mathcal{L}^b} + f_{BG}(q) \times \frac{\mathcal{L}^b}{\mathcal{L}^q + \mathcal{L}^b} \quad (6.3)$$

where  $f_{BG}(c)$ , and  $f_{BG}(q)$  are the a-priori probabilities for the content of charm and light flavour quarks in non-b jets.

A jet is considered  $b$ -tagged if the CSV discriminant is greater than 0.679, which is the medium working point defined by the BTAG Physics Object Group (POG) [86], defined in order to produce a light-flavour mistag rate at  $\sim 1\%$ , with the reconstruction efficiency for real b-jets at  $\sim 70\%$ .

Additionally, it is necessary to account for differences in the measured efficiency for  $b$ -tagging jets between data and simulation [87]. An event weight scale factor is used to correct the MC  $b$ -tagging efficiency ( $SF_{tag} = \epsilon_{tag}^{data} / \epsilon_{tag}^{MC}$ ). The scale factor is measured for three different cuts, or working points, on the CSV discriminant value, and it is binned in terms of the  $p_T$  and  $\eta$  and flavour of the jet.

In addition to providing jet flavour identification for event classification, the discriminant value of the algorithm will be used to separate between  $t\bar{t}H$  signal and  $t\bar{t} + jets$  background. Therefore, a correction value for the efficiency difference between data and MC over the whole range of discriminator values is needed, not just for three working points. This procedure was developed in the context of the search for the standard model Higgs boson produced in association with a W or Z boson, with the Higgs decaying to bottom quarks [88].

For each of the three operating points and for each of the data/MC SFs, an equivalent cut on the CSV value is determined,  $CSV_{equiv}$ , such that

$$\epsilon_{CSV > CSV_{orig}}^{data} = SF_{CSV > CSV_{orig}} \cdot \epsilon_{CSV > CSV_{orig}}^{MC} = \epsilon_{CSV > CSV_{equiv}}^{MC} \quad (6.4)$$

2042 where the SFs are measured in data and the MC efficiency measurements are calculated for each  
 2043 sample.

2044 In order to correct or "reshape" the CSV discriminator output values, a function is applied to  
 2045 the MC to produce a corrected CSV value:  $CSV_{\text{corr}} = f(CSV_{\text{orig}})$ . Given that there are three  $b$ -  
 2046 tag efficiency measurements, there are three pairs of  $(CSV_{\text{orig}}, CSV_{\text{equiv}})$ . The reshaping function  
 2047 must satisfy  $f(CSV_{\text{equiv}}) = CSV_{\text{orig}}$  for each of the operating points and for the upper and lower  
 2048 values of the CSV discriminant to make sure those values do not change (e.g.,  $CSV = 0.0$  and  
 2049  $CSV = 1.0$ ). The whole range of CSV discriminant values is found by linearly interpolating  
 2050 between these five points (the three working points, and upper and lower limit of the discriminant  
 2051 range).

### 2052 6.2.8 Lepton + Jets Selection

2053 The final Lepton+Jets (LJ) selection is finally carried out by requiring that events have exactly  
 2054 one tight lepton ( $e$  or  $\mu$ ), and at least four jets. Events with any additional loose or tight leptons  
 2055 are vetoed so this analysis can later be combined with a diLepton final state, without double  
 2056 counting events. Additionally, each event must have at least three jets with  $p_T > 40 \text{ GeV}/c$ .

2057 Events are further categorized by the reconstructed jet, and  $b$ -tagged jet multiplicities as  
 2058 follows:

2059 •  $\geq 6$  jets,  $==2$   $b$ -tags: At least 6 jets, 2 of which are  $b$ -tagged

2060 •  $==4$  jets,  $==3$   $b$ -tags: Exactly 4 jets, 3 of which are  $b$ -tagged

2061 •  $==5$  jets,  $==3$   $b$ -tags: Exactly 5 jets, 3 of which are  $b$ -tagged

2062 •  $\geq 6$  jets,  $==3$   $b$ -tags: At least 6 jets, 3 of which are  $b$ -tagged

2063 •  $==4$  jets,  $==4$   $b$ -tags: Exactly 4 jets, 4 of which are  $b$ -tagged

2064 •  $==5$  jets,  $==4$   $b$ -tags: Exactly 5 jets, 4 of which are  $b$ -tagged

2065 •  $\geq 6$  jets,  $\geq 4$   $b$ -tags: At least 6 jets, with at least 4 of which are  $b$ -tagged

2066 Events with either 4 or 5 jets, where 2 of those jets are  $b$ -tagged, make up two categories,  
 2067 which are used only as a control region to validate comparisons between collected data and  
 2068 simulations. The number of  $t\bar{t}H$  events increases with the number of jets and tags because the  
 2069 largest branching fraction is  $H$  to  $b\bar{b}$ . Data to monte carlo comparisons of the jet and  $b$ -tag  
 2070 multiplicities are shown in figure 6.6. The event yields for the  $\mu$ +jets and  $e$ +jets channels are  
 2071 shown in tables 6.11 and 6.10 respectively.

Table 6.9: Expected event yields in  $5\text{ fb}^{-1}$  for signal and backgrounds in the  $\mu+\text{jets}$  channel.

	$\geq 6$ jets 2 tags	4 jets 3 tags	5 jets 3 tags	$\geq 6$ jets 3 tags	4 jets 4 tags	5 jets $\geq 4$ tags	$\geq 6$ jets $\geq 4$ tags
$t\bar{t}H(125)$	$6.1 \pm 1.1$	$2.1 \pm 1.9$	$3.2 \pm 2.7$	$3.6 \pm 3.3$	$0.3 \pm 0.3$	$0.8 \pm 0.9$	$1.3 \pm 1.4$
$t\bar{t}+1\text{f}$	$1750 \pm 480$	$680 \pm 150$	$460 \pm 110$	$270 \pm 84$	$9.5 \pm 3.2$	$13.0 \pm 4.2$	$20.6 \pm 7.8$
$t\bar{t} + b\bar{b}$	$34 \pm 19$	$21 \pm 12$	$24 \pm 14$	$17.3 \pm 10.0$	$1.5 \pm 1.1$	$5.1 \pm 3.2$	$8.6 \pm 5.6$
$t\bar{t} + c\bar{c}$	$29.5 \pm 8.7$	$10.0 \pm 2.9$	$13.2 \pm 3.9$	$11.1 \pm 3.5$	$0.2 \pm 0.2$	$0.2 \pm 0.1$	$1.1 \pm 0.8$
$t\bar{t}V$	$18.7 \pm 3.9$	$2.3 \pm 0.6$	$3.3 \pm 0.8$	$4.1 \pm 1.1$	$0.1 \pm 0.0$	$0.4 \pm 0.2$	$0.8 \pm 0.2$
Single $t$	$42.6 \pm 9.8$	$25.8 \pm 6.0$	$14.3 \pm 3.8$	$4.3 \pm 1.3$	$0.2 \pm 0.3$	$1.6 \pm 1.8$	$0.7 \pm 0.5$
$V+\text{jets}$	$39 \pm 32$	$1.0 \pm 0.9$	$0.0 \pm 0.0$	$0.0 \pm 0.0$	$0.0 \pm 0.0$	$0.0 \pm 0.0$	$0.0 \pm 0.0$
Diboson	$0.6 \pm 0.2$	$0.9 \pm 0.4$	$0.3 \pm 0.1$	$0.1 \pm 0.1$	$0.0 \pm 0.0$	$0.0 \pm 0.0$	$0.0 \pm 0.0$
Total bkg	$1910 \pm 500$	$740 \pm 160$	$520 \pm 120$	$307 \pm 90$	$11.4 \pm 3.8$	$20.3 \pm 6.1$	$32 \pm 11$
Data	$1780$	$861$	$585$	$362$	$15$	$32$	$37$

Table 6.10: Expected event yields in  $5\text{ fb}^{-1}$  for signal and backgrounds in the  $e+\text{jets}$  channel.

	$\geq 6$ jets 2 tags	4 jets 3 tags	5 jets 3 tags	$\geq 6$ jets 3 tags	4 jets 4 tags	5 jets $\geq 4$ tags	$\geq 6$ jets $\geq 4$ tags
$t\bar{t}H(125)$	$5.6 \pm 1.0$	$1.8 \pm 1.2$	$2.9 \pm 1.8$	$3.2 \pm 2.1$	$0.3 \pm 0.2$	$0.7 \pm 0.6$	$1.2 \pm 1.0$
$t\bar{t}+1\text{f}$	$1720 \pm 470$	$640 \pm 140$	$410 \pm 94$	$293 \pm 85$	$8.6 \pm 2.9$	$14.5 \pm 5.2$	$20.7 \pm 7.8$
$t\bar{t} + b\bar{b}$	$27 \pm 15$	$14.3 \pm 7.9$	$19 \pm 11$	$18 \pm 10$	$1.0 \pm 1.0$	$3.3 \pm 2.6$	$6.7 \pm 4.3$
$t\bar{t} + c\bar{c}$	$32.8 \pm 9.4$	$9.6 \pm 2.9$	$11.8 \pm 3.5$	$14.8 \pm 4.8$	$0.4 \pm 0.3$	$0.6 \pm 0.6$	$2.6 \pm 1.4$
$t\bar{t}V$	$17.0 \pm 3.6$	$2.1 \pm 0.6$	$2.8 \pm 0.7$	$4.5 \pm 1.1$	$0.0 \pm 0.0$	$0.3 \pm 0.1$	$0.6 \pm 0.2$
Single $t$	$35.9 \pm 8.9$	$30.5 \pm 6.4$	$11.3 \pm 3.4$	$6.0 \pm 2.0$	$0.1 \pm 0.3$	$1.4 \pm 1.2$	$0.4 \pm 0.4$
$V+\text{jets}$	$14 \pm 14$	$4.8 \pm 5.8$	$0.8 \pm 0.9$	$0.0 \pm 0.0$	$0.0 \pm 0.0$	$0.0 \pm 0.0$	$0.0 \pm 0.0$
Diboson	$0.7 \pm 0.3$	$1.0 \pm 0.3$	$0.2 \pm 0.1$	$0.1 \pm 0.0$	$0.0 \pm 0.0$	$0.0 \pm 0.0$	$0.0 \pm 0.0$
Total bkg	$1850 \pm 490$	$700 \pm 150$	$460 \pm 110$	$336 \pm 93$	$10.1 \pm 3.2$	$20.2 \pm 6.6$	$31 \pm 11$
Data	$1723$	$785$	$531$	$324$	$13$	$24$	$37$

Table 6.11: Expected event yields in  $5 \text{ fb}^{-1}$  for signal and backgrounds in the  $\mu+\text{jets}$  channel.

	$\geq 6$ jets 2 tags	$4$ jets 3 tags	$5$ jets 3 tags	$\geq 6$ jets 3 tags	$4$ jets $\geq 4$ tags	$5$ jets $\geq 4$ tags	$\geq 6$ jets $\geq 4$ tags
$t\bar{t}H(125)$	$11.7 \pm 1.9$	$3.9 \pm 1.9$	$6.1 \pm 3.1$	$6.9 \pm 3.5$	$0.6 \pm 0.3$	$1.5 \pm 0.8$	$2.5 \pm 1.3$
$t\bar{t}+1\text{f}$	$3460 \pm 940$	$1320 \pm 280$	$870 \pm 210$	$570 \pm 170$	$18.0 \pm 5.1$	$27.6 \pm 8.6$	$41 \pm 15$
$t\bar{t} + b\bar{b}$	$61 \pm 34$	$35 \pm 19$	$43 \pm 24$	$35 \pm 20$	$2.5 \pm 1.7$	$8.4 \pm 5.4$	$15.4 \pm 9.4$
$t\bar{t} + c\bar{c}$	$62 \pm 17$	$19.6 \pm 5.2$	$25.0 \pm 6.9$	$25.9 \pm 7.7$	$0.6 \pm 0.4$	$0.8 \pm 0.9$	$3.7 \pm 1.8$
$t\bar{t}V$	$35.7 \pm 7.5$	$4.5 \pm 1.1$	$6.1 \pm 1.4$	$8.6 \pm 2.1$	$0.1 \pm 0.1$	$0.7 \pm 0.2$	$1.5 \pm 0.4$
Single $t$	$79 \pm 18$	$56 \pm 11$	$25.6 \pm 6.3$	$10.3 \pm 2.9$	$0.3 \pm 0.6$	$3.1 \pm 2.2$	$1.0 \pm 0.6$
$V+\text{jets}$	$53 \pm 40$	$5.9 \pm 5.9$	$0.8 \pm 0.9$	$0.0 \pm 0.0$	$0.0 \pm 0.0$	$0.0 \pm 0.0$	$0.0 \pm 0.0$
Diboson	$1.2 \pm 0.4$	$1.8 \pm 0.6$	$0.5 \pm 0.2$	$0.2 \pm 0.1$	$0.0 \pm 0.0$	$0.0 \pm 0.0$	$0.0 \pm 0.0$
Total bkg	$3760 \pm 980$	$1440 \pm 300$	$970 \pm 230$	$650 \pm 190$	$21.5 \pm 6.1$	$41 \pm 12$	$63 \pm 21$
Data	$3503$	$1646$	$1116$	$686$	$28$	$56$	$74$

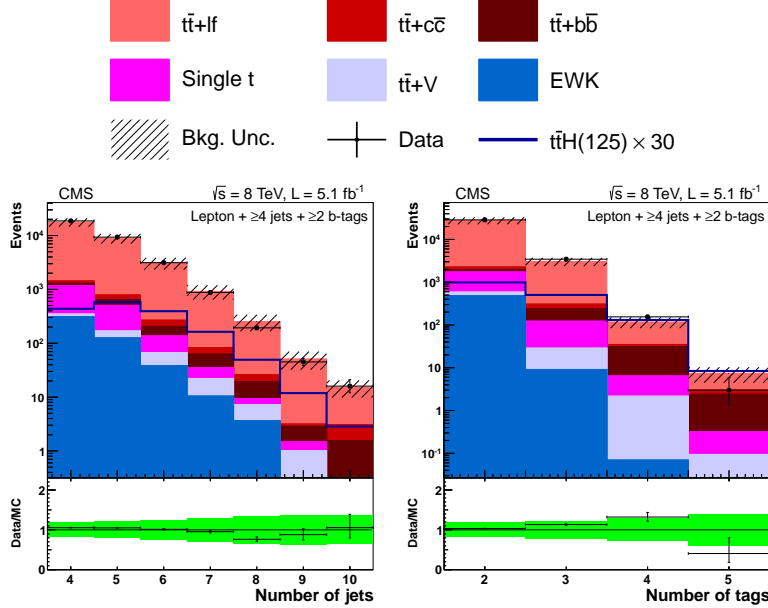


Figure 6.6: Number of jets (left) and number of b-tagged jets (right) in data and simulation for events with  $\geq 4$  jets +  $\geq 2$  b-tags in the lepton+jets channel at 8 TeV. The background is normalized to the SM expectation; the uncertainty band (shown as a hatched band in the stack plot and a green band in the ratio plot) includes statistical and systematic uncertainties that affect both the rate and shape of the background distributions. The  $t\bar{t}H$  signal ( $m_H = 125\text{ GeV}/c^2$ ) is normalized to  $30 \times$  SM expectation.

### 2072 6.3 Multivariate Analysis

2073 As discussed in the chapter introduction, no single variable offers sufficient discriminating power,  
 2074 to separate the  $t\bar{t}H$  signal from the  $t\bar{t} + \text{jets}$  background. Instead, the combined power of several  
 2075 input variables is utilized through a multivariate analysis (MVA) technique. For this analysis, the  
 2076 MVA algorithm chosen from the sub-class of artificial neural network (ANN) algorithms, known  
 2077 as multi-layer perceptrons (MLPs). The specific algorithm is the Clermont-Ferrand Multi-Layer  
 2078 Perceptron Artificial Neural Network (CFMlpANN). It was first developed at the Universite  
 2079 Blaise Pascal in Clermont-Ferrand, for the ALEPH experiment at the LEP collider to search for  
 2080 the Standard Model Higgs and has also been utilized by the BABAR experiment to search for  
 2081 rare  $B$  meson decays [89]. It has been implemented in the ROOT TMVA framework, available  
 2082 in all CMSSW releases. A CFMlpANN is trained for each jet-tag category listed in section 6.2.8.  
 2083 A total of 10 input variables is used in each category, with the exception of the  $\geq 6$  jets,  $\geq 4$   
 2084  $b$ -tags category, where the full reconstruction of the  $t\bar{t}H$  system is possible, features an additional  
 2085 variable that is the invariant mass of the di-jet system of  $b$ -jets selected by a  $\chi^2$  minimization  
 2086 algorithm.

2087 **6.3.1 Artificial Neural Network Overview**

2088 An artificial neural network (ANN), most generally speaking, is any collection of interconnected,  
2089 simulated "neurons" which produce a certain response to a set of input variables [89]. A simu-  
2090 lated neuron, is some independent function, which takes several input variables, performs a  
2091 mathematical operation, and passes the result to one or more other neurons. In the most gen-  
2092 eral case, a set of  $n$  input variables, connected to a single output, will produce on the order  
2093  $n^2$  connections. For case of using the network to discriminate between signal from background  
2094 (a yes or no answer on whether an event is signal-like), the ANN is mapping an  $n$ -dimensional  
2095 space onto a one-dimensional space.

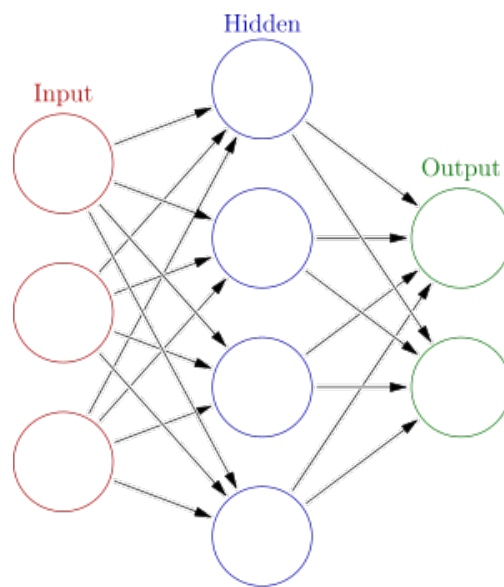


Figure 6.7: A simple example of a MLP type ANN, with one layer of input neurons that make connections to a hidden layer, which is connected to the output layer

2096 The multi-layer perceptron (MLP) is a specific type of arrangement of neurons. Any number  
2097 of neurons are arranged into a single layer, and connections to other neurons are only made if  
2098 they are arranged in a successive layer [89]. This is known as feed-forward network, and a simple  
2099 example with one input layer, one hidden layer, and one output layer is shown in figure 6.7.  
2100 This limits the complexity of the connections formed by the neurons and allows for simplified  
2101 calculations.

2102 This analysis uses an architecture that consists of two hidden layers, with  $N$  and  $N - 1$   
2103 variables respectively, where  $N$  is the number of input variables for the given jet/tag category.  
2104 An example diagram is shown in figure 6.8. The output of the CFMlpANN algorithm is one-  
2105 dimensional discriminant with range from 0 to 1, for background-like and signal-like events.  
2106 Each neuron response is based on an activation function  $A(\alpha)$ , and a synapse response,  $\alpha$ .

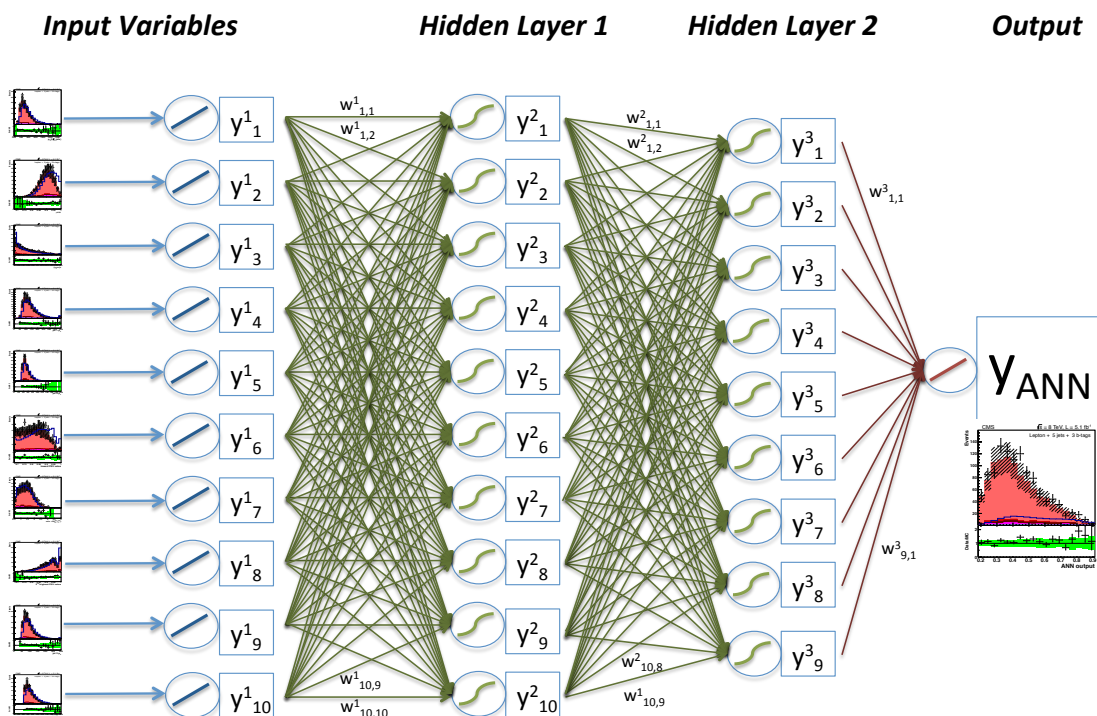


Figure 6.8: The CFMlpANN architecture used in this analysis features two hidden layers, and 10 input variables for each jet/tag category (11 variables for the  $\geq 6$ jets,  $\geq 4b$ -tags category)

<sup>2107</sup> In this case, a sigmoid function is used as the activation function:

$$A(\alpha) = \frac{1}{1 + e^{-x}} \quad (6.5)$$

<sup>2108</sup> and the synapse response is a simple weighted sum:

$$\alpha = w_{0j}^{(l)} + \sum_{i=1}^n y_i^{(l)} w_{ij}^{(l)} \quad (6.6)$$

<sup>2109</sup> The entire CFMlpANN response is then

$$y_{ANN} = \sum_{k=1}^{n-1} y_k^{(3)} w_{k1}^{(3)} = \sum_{k=1}^{n-1} A \left( \sum_{j=1}^n y_j^{(2)} w_{jk}^{(2)} \right) w_{k1}^{(3)} = \sum_{k=1}^{n-1} A \left( \sum_{j=1}^n A \left( \sum_{i=1}^n x_i w_{ij}^{(1)} \right) w_{jk}^{(2)} \right) w_{k1}^{(3)} \quad (6.7)$$

<sup>2110</sup> where  $n$  is the number of input variables for that jet tag category and  $A$  is the sigmoid function  
<sup>2111</sup> described in equation 6.5.

<sup>2112</sup> The CFMlpANN is trained with  $t\bar{t}H$  signal events and inclusive  $t\bar{t} + jets$  background events  
<sup>2113</sup> in order to optimize the weights  $w_{ij}^{(l)}$  that are used for each neuron connection such that the  
<sup>2114</sup> output,  $y_{ANN}$  is closest to 1 for signal-like events, and closest to 0 for background-like events.  
<sup>2115</sup> This process involves sending the CFMlpANN an event from a known source (either signal or  
<sup>2116</sup> background), calculating the response,  $y_{ANN}$ , and computing an error function associated with  
<sup>2117</sup> the answer, given by:

$$E(x_1, \dots, x_N | w) = \sum_{a=1}^N E_a(x_a | w) = \sum_{a=1}^N \frac{1}{2} (y_{ANN} - \hat{y}_a) \quad (6.8)$$

<sup>2118</sup> where  $\hat{y}_a$  is the correct response (either 0 or 1), knowing that the event was either signal or  
<sup>2119</sup> background, and  $N$  is the number of events used to train the CFMlpANN. The optimized set  
<sup>2120</sup> of weights is the set that minimizes this error function. This is done by the method of steepest  
<sup>2121</sup> descent, where a random set of weights is moved a small distance in the direction that gives the  
<sup>2122</sup> largest change in minimizing the error function.

$$w^{t+1} = w^t - \eta \nabla_w E \quad (6.9)$$

<sup>2123</sup> where  $\nabla_w$  is the direction that reduces the error function the most, and  $\eta$  is a parameter that  
<sup>2124</sup> determines how large of an adjustment is made. After the weights are adjusted, the CFMlpANN  
<sup>2125</sup> makes another iteration over the training events, re-calculating the CFMlpANN output for each  
<sup>2126</sup> event and the error function. For this analysis a total of 2000 iterations were used to train the  
<sup>2127</sup> CFMlpANN.

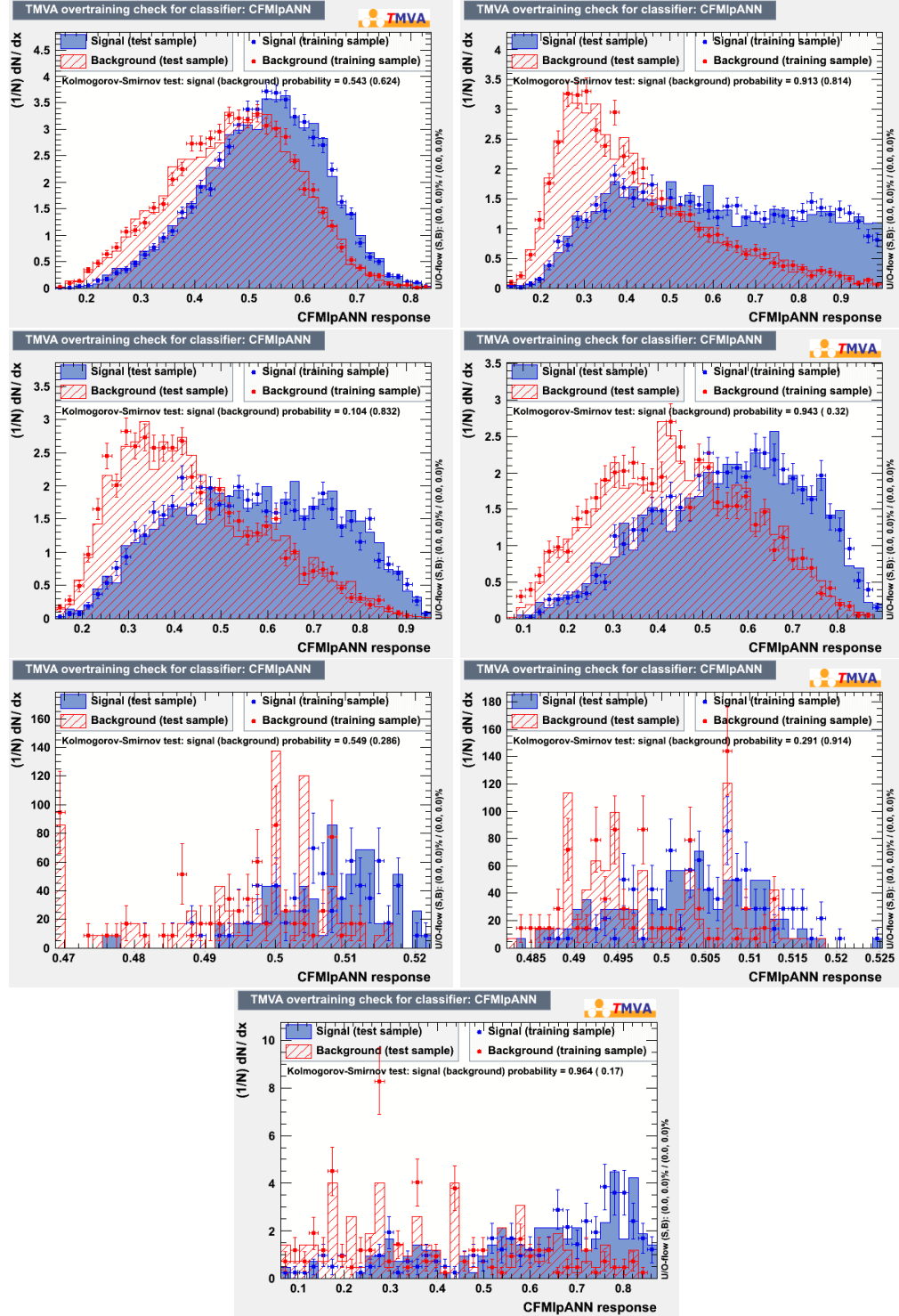


Figure 6.9: Comparisons of the testing and training samples used to optimize the CFMlpANN weights for each jet/tag category

2128 It is possible to bias the CFMlpANN response, by overtraining it. This is the case where the  
 2129 weights are over-adjusted to correctly classify events in the training sample. If overtrained, small  
 2130 fluctuations in the input variable distributions of authentic signal events can lead to incorrect  
 2131 classification of the signal events when the CFMlpANN attempts to classify the data. To avoid  
 2132 this, half of the simulated events for  $t\bar{t}H$  signal and  $t\bar{t}+jets$  background are used during training.  
 2133 After training, the other half are used to test the response of the algorithm. If properly trained,  
 2134 the testing and training samples should have identical CFMlpANN responses. The figure of  
 2135 merit used to assess this is the Kolmogorov-Smirnov test, which computes the probability that  
 2136 two distributions have been sampled from the same underlying probability distribution. The  
 2137 results of the training and testing for each of the jet/tag categories is shown in figure 6.9. No  
 2138 signs of overtraining are observed.

### 2139 6.3.2 MVA Input Variables, Data to Monte Carlo Comparisons

2140 As mentioned in the previous section, each jet/tag category has been trained with its own  
 2141 CFMlpANN. Each category uses ten input variables, except for the  $\geq 6j$ ,  $\geq 4t$  category, which  
 2142 uses eleven. A total of 24 unique input variables are used in the 7 different jet/tag categories  
 2143 and are listed in table 6.12. The most discriminating variable for each category is denoted by  
 2144 a  $\star$ . The inputs are selected from a ranked list based on initial separation between signal  
 2145 and background. The separation of the individual variables is evaluated using a separation  
 2146 benchmark  $\langle S^2 \rangle$  [89] defined as follows:

$$\langle S^2 \rangle = \frac{1}{2} \int \frac{(\hat{y}_S(y) - \hat{y}_B(y))^2}{\hat{y}_S(y) + \hat{y}_B(y)} dy, \quad (6.10)$$

2147 where  $y$  is the input variable, and  $\hat{y}_S$  and  $\hat{y}_B$  are the signal and background probability density  
 2148 functions for that input variable in the signal and background samples, respectively. The maxi-  
 2149 mum number of input variables used in each category is limited by the statistics in the simulated  
 2150 samples used for the CFMlpANN training. The number of variables per category is determined  
 2151 by reducing the number of variables until the minimum number of variables needed to maintain  
 2152 roughly the same ANN performance is reached. In this case, 10 input variables yields stable and  
 2153 approximately identical performance to using 15, while using 5 variables degraded discrimination  
 2154 power significantly.

2155 The input variables used in the CFMlpANN can be broken down into several classes. The  
 2156 first is related to jet, and multi-object kinematics. The  $b$ -jets produced by the Higgs boson tend  
 2157 to have a harder  $p_T$  spectrum compared to  $b$ -jets produced from gluon radiation. Additionally,  
 2158 the recoil of the Higgs off of the top-system produces small differences in the  $p_T$  and invariant

Table 6.12: The ANN inputs for the nine jet-tag categories in the 8 TeV  $t\bar{t}H$  analysis in the lepton+jets and dilepton channels. The choice of inputs is optimized for each category. Definitions of the variables are given in the text. The best input variable for each jet-tag category is denoted by  $\star$ .

Jets Tags	Lepton+Jets						
	$\geq 6$ 2	4 3	5 3	$\geq 6$ 3	4 4	5 $\geq 4$	$\geq 6$ $\geq 4$
Jet 1 $p_T$		✓	✓		✓		
Jet 2 $p_T$		✓	✓				
Jet 3 $p_T$	✓	✓	✓			✓	
Jet 4 $p_T$	✓	✓	✓			✓	
$p_T(\ell, E_T^{\text{miss}}, \text{jets})$		★	✓		✓	✓	
$M(\ell, E_T^{\text{miss}}, \text{jets})$	✓	✓		✓	✓		✓
Average $M((j_m^{\text{untag}}, j_n^{\text{untag}}))$	✓			✓			
$M((j_m^{\text{tag}}, j_n^{\text{tag}})_{\text{closest}})$							✓
$M((j_m^{\text{tag}}, j_n^{\text{tag}})_{\text{best}})$							✓
Average $\Delta R(j_m^{\text{tag}}, j_n^{\text{tag}})$				✓	✓	✓	✓
Minimum $\Delta R(j_m^{\text{tag}}, j_n^{\text{tag}})$			✓				
$\Delta R(\ell, j_{\text{closest}})$						✓	✓
Sphericity	✓			✓			✓
Aplanarity	✓				✓		
$H_0$	✓						
$H_1$	✓				✓		
$H_2$				✓			✓
$H_3$	★			✓			✓
$\mu^{\text{CSV}}$	✓	✓	★	★	★	★	★
$(\sigma_n^{\text{CSV}})^2$	✓	✓	✓	✓	✓	✓	
Highest CSV value							✓
2 <sup>nd</sup> -highest CSV value	✓	✓	✓	✓	✓	✓	✓
Lowest CSV value	✓	✓	✓	✓	✓	✓	✓

2159 mass of the reconstructed  $t\bar{t} + jets$  system.

- 2160 • Jet 1  $p_T$  - the highest value of transverse jet momentum in the event
- 2161 • Jet 2  $p_T$  - the second highest value of transverse jet momentum in the event
- 2162 • Jet 3  $p_T$  - the third highest value of transverse jet momentum in the event
- 2163 • Jet 4  $p_T$  - the fourth highest value of transverse jet momentum in the event
- 2164 •  $p_T(\ell, E_T^{\text{miss}}, \text{jets})$  - the transverse momentum of the four-vector formed by summing the
- 2165    four-vectors of the lepton, MET, and all selected jets in the event
- 2166 •  $M(\ell, E_T^{\text{miss}}, \text{jets})$  - the invariant mass of the four-vector formed by summing the four-vectors
- 2167    of the lepton, MET, and all selected jets in the event
- 2168 • Average  $M((j_m^{\text{untag}}, j_n^{\text{untag}}))$  - the average di-Jet mass formed by all combinations of jets
- 2169    that have not been  $b$ -tagged in the event
- 2170 •  $M((j_m^{\text{tag}}, j_n^{\text{tag}})_{\text{closest}})$  - the invariant di-Jet mass of the two  $b$ -tagged jets that are closest to
- 2171    one another in the detector

- 2172     •  $M((j_m^{\text{tag}}, j_n^{\text{tag}})_{\text{best}})$  - the invariant mass constructed from the two tagged jets least likely  
 2173       to be a part of the  $t\bar{t}$  system as determined by a minimum  $\chi^2$  search among all the  
 2174       jet, lepton, and  $E_T^{\text{miss}}$  combinations in the event, using the  $W$  boson and top masses as  
 2175       kinematic constraints.

2176     The next class of input variables describe the angular relationship between reconstructed  
 2177     objects in the event. These are event shape variables. Production of a relatively massive ob-  
 2178     ject, in addition to top quarks, such as the Higgs, tends to make  $t\bar{t}H$  events more spherically  
 2179     distributed in the detected, while the background events are more collimated. Variables in this  
 2180     class include angular correlations, like the opening angle between the tagged jets

- 2181     • Average  $\Delta R(j_m^{\text{tag}}, j_n^{\text{tag}})$  - the average  $\Delta R$  spatial separation between all combinations of  
 2182        $b$ -tagged jets in the event
- 2183     • Minimum  $\Delta R(j_m^{\text{tag}}, j_n^{\text{tag}})$  - the smallest value of  $\Delta R$  measured between a pair of  $b$ -tagged  
 2184       jets
- 2185     •  $\Delta R(\ell, j_{\text{closest}})$  - the  $\Delta R$  spatial separation of the lepton and the closest reconstructed jet
- 2186     • Sphericity - Event shape variable equal to  $\frac{3}{2}(\lambda_2 + \lambda_3)$ , where  $\lambda_2$  and  $\lambda_3$  are the second and  
 2187       third eigenvalues of the sphericity tensor as described in[90]
- 2188     • Aplanarity - Event shape variable equal to  $\frac{3}{2}(\lambda_3)$ , where  $\lambda_3$  is the third eigenvalue of the  
 2189       sphericity tensor as described in
- 2190     •  $H_0$  - the zeroth Fox-Wolfram moment [91]
- 2191     •  $H_1$  - the first Fox-Wolfram moment
- 2192     •  $H_2$  - the second Fox-Wolfram moment
- 2193     •  $H_3$  - the third Fox-Wolfram moment

2194     where  $\Delta R = \sqrt{\Delta\eta^2 + \Delta\phi^2}$ . The sphericity tensor is given by the equation:

$$S^{a,b} = \frac{\sum_i p_i^a p_i^b}{\sum_i |\hat{p}_i|^2} \quad (6.11)$$

2195     where  $a, b = x, y, z$  coordinates. This tensor is diagonalized, and solved for its eigenvalues,  
 2196     which are used to compute the sphericity and aplanarity variables. The Fox-Wolfram moments  
 2197     are defined are momentum weighted spherical harmonics, defined as:

$$H_\ell = \sum_{i,j=1}^{N_{\text{jets}}} \frac{|\hat{p}_i||\hat{p}_j|}{|\hat{p}|_{tot}^2} P_\ell(\cos \Omega_{ij}) \quad (6.12)$$

2198 where  $P_\ell(\cos \Omega_{ij})$  is the  $\ell^{th}$  spherical harmonic, with polar angle calculated between jets i and j.

2199 The final class of variables is based on the discriminant output from the b-tagging algorithm.

2200 For many of the categories, the average  $b$ -tag discriminant of all of the jets in the event tends to

2201 be the most powerful single variable. This is due to the high multiplicity of authentic  $b$ -jets in

2202 a  $t\bar{t}H$  event.

2203 •  $\mu^{\text{CSV}}$  - the average value of the output of the CSV algorithm for all selected jets in the  
2204 event.

2205 •  $(\sigma_n^{\text{CSV}})^2$  - the variance of the average value of the output of the CSV algorithm for all  
2206 selected jets in the event.

2207 • Highest CSV value - the highest value of the CSV discriminant for any selected jet in the  
2208 event

2209 •  $2^{nd}$ -highest CSV value - the second highest value of the CSV discriminant for any selected  
2210 jet in the event

2211 • Lowest CSV value - the lowest value of the CSV discriminant for any selected jet in the  
2212 event

2213 The modeling of the input variables is compared against data for each of the jet/tag diagrams

2214 in the the following figures:

2215 •  $\geq 6$  jets, ==2  $b$ -tags: Figure 6.10, and Figure 6.11

2216 • ==4 jets, ==3  $b$ -tags: Figure 6.12, and Figure 6.13

2217 • ==5 jets, ==3  $b$ -tags: Figure 6.14, and Figure 6.15

2218 •  $\geq 6$  jets, ==3  $b$ -tags: Figure 6.16, and Figure 6.17

2219 • ==4 jets, ==4  $b$ -tags: Figure 6.18, and Figure 6.19

2220 • ==5 jets, ==4  $b$ -tags: Figure 6.20, and Figure 6.21

2221 •  $\geq 6$  jets,  $\geq 4$   $b$ -tags: Figure 6.22, and Figure 6.23

2222 Below each histogram is a ratio of the yields for data over the simulated sample prediction. The

2223 green band is the total uncertainty estimated for the simulation, and the error bars on the points

2224 are determined by the statistical error on the data collected.

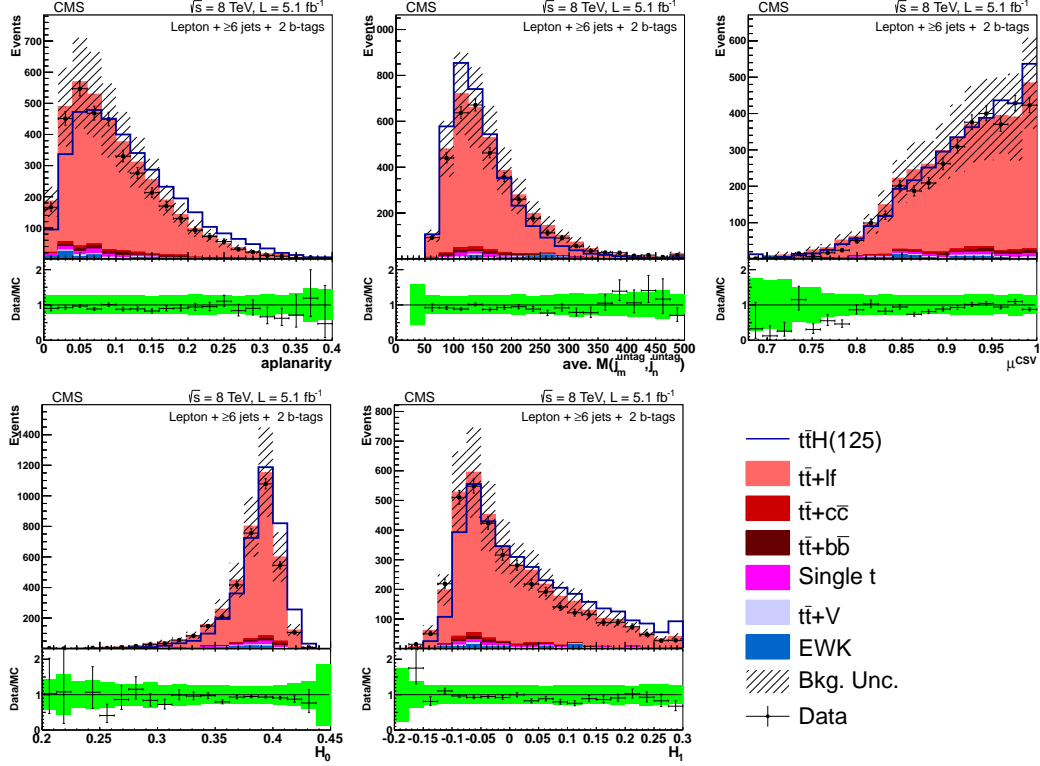


Figure 6.10: Lepton + jets data/MC comparison for the  $\geq 6$  jets + 2 tag category. The uncertainty band includes statistical and systematic uncertainties that affect both the rate and shape of the background distributions.

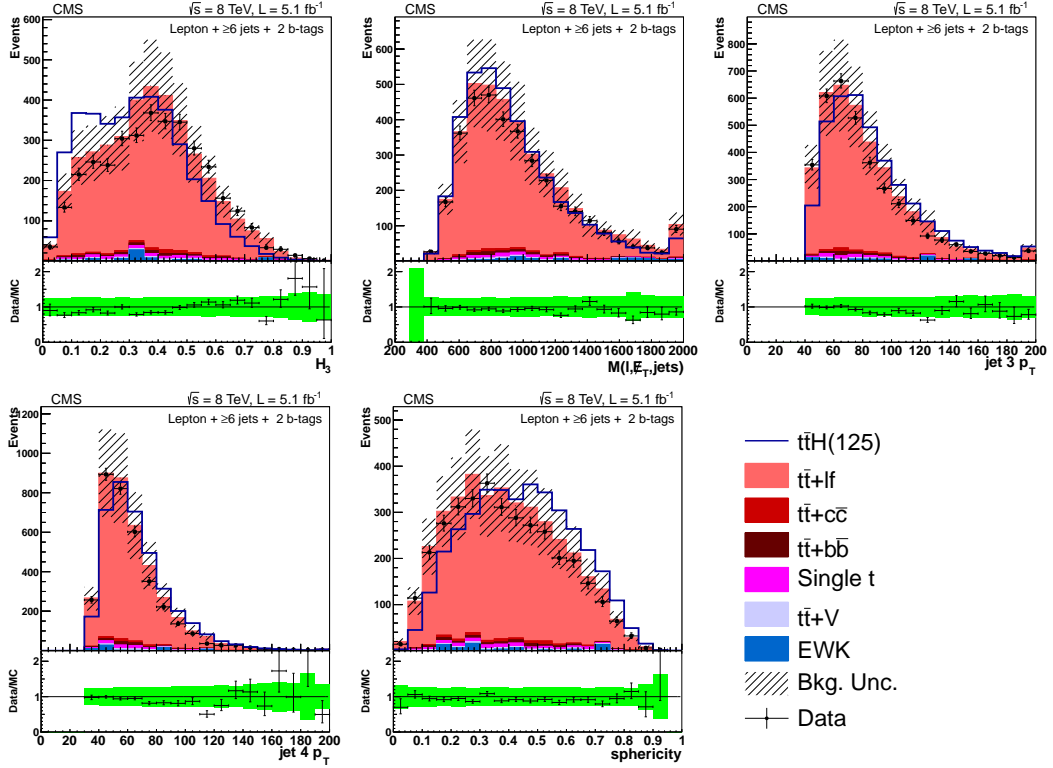


Figure 6.11: Lepton + jets data/MC comparison for the  $\geq 6$  jets + 2 tag category. The uncertainty band includes statistical and systematic uncertainties that affect both the rate and shape of the background distributions.

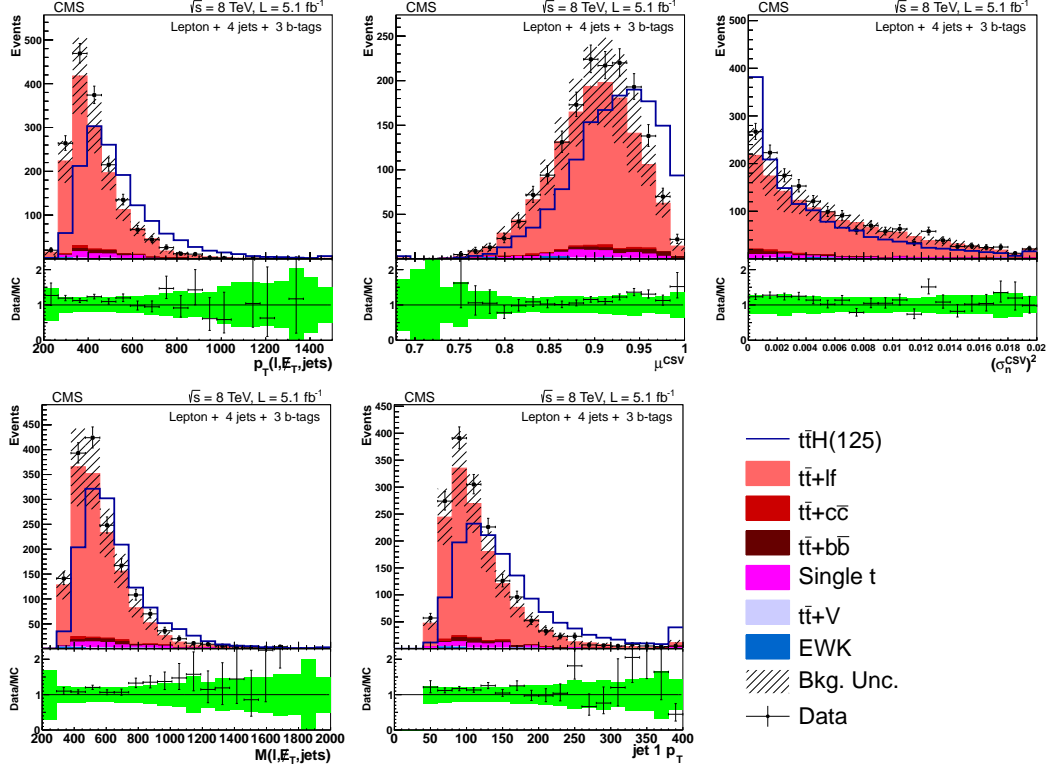


Figure 6.12: Lepton + jets data/MC comparison for the 4 jets + 3 tag category. The uncertainty band includes statistical and systematic uncertainties that affect both the rate and shape of the background distributions.

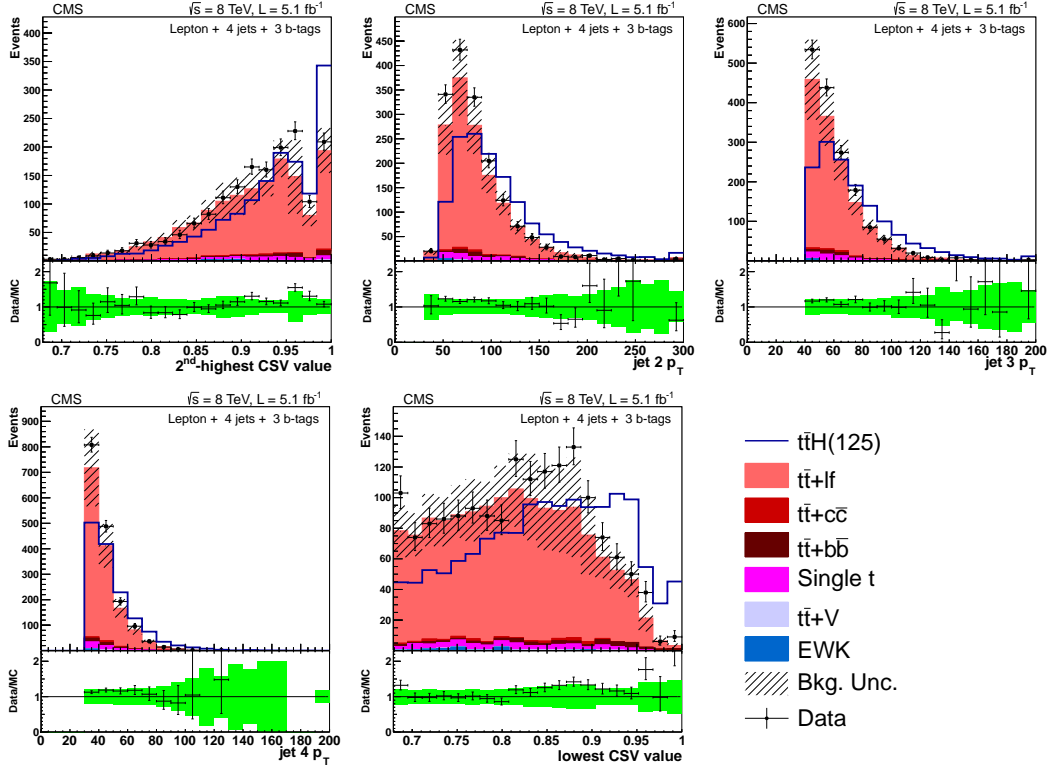


Figure 6.13: Lepton + jets data/MC comparison for the 4 jets + 3 tag category. The uncertainty band includes statistical and systematic uncertainties that affect both the rate and shape of the background distributions.

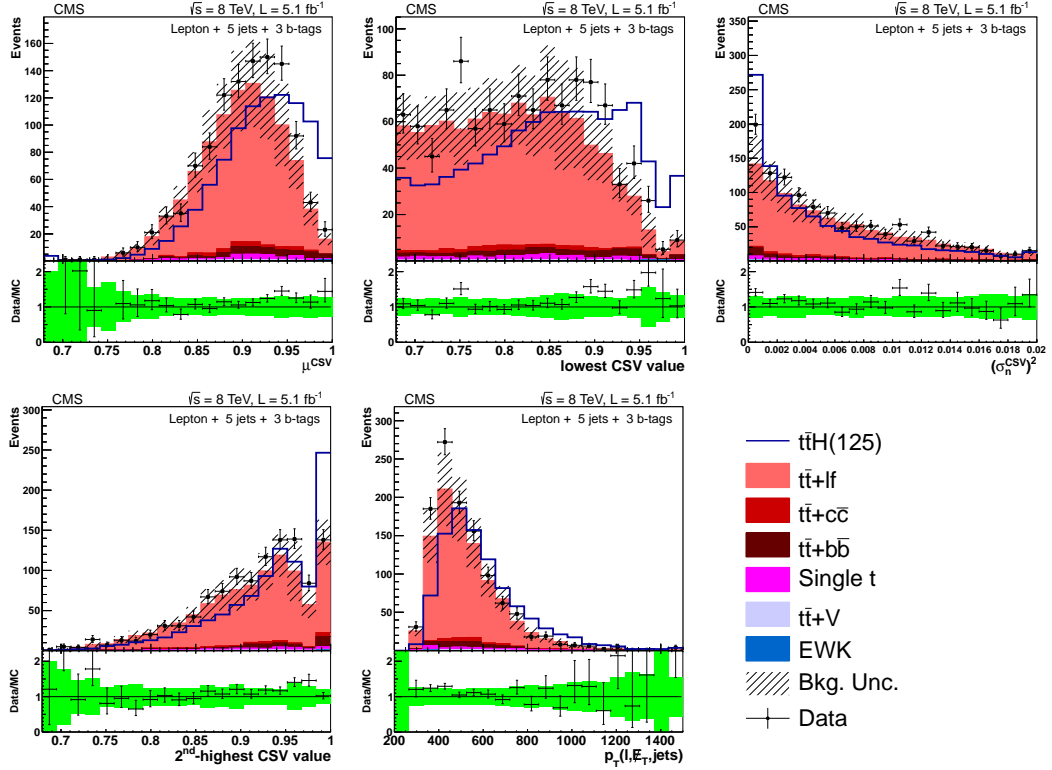


Figure 6.14: Distributions of the five ANN input variables with rankings 1 through 5, in terms of separation, for the 5 jets + 3 b-tags category of the lepton+jets channel at 8 TeV. Definitions of the variables are given in the text. The background is normalized to the SM expectation; the uncertainty band (shown as a hatched band in the stack plot and a green band in the ratio plot) includes statistical and systematic uncertainties that affect both the rate and shape of the background distributions. The  $t\bar{t}H$  signal ( $m_H = 125 \text{ GeV}/c^2$ ) is normalized to the total background yield, for easier comparison of the shapes.

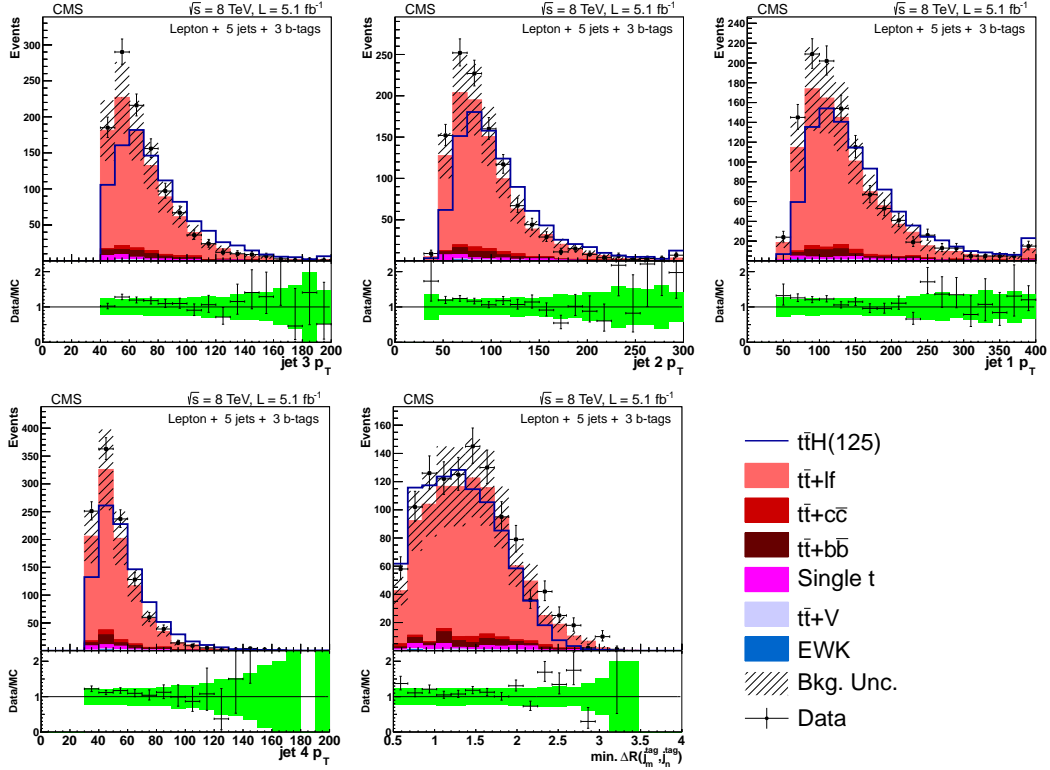


Figure 6.15: Distributions of the five ANN input variables with rankings 6 through 10, in terms of separation, for the 5 jets + 3 b-tags category of the lepton+jets channel at 8 TeV. Definitions of the variables are given in the text. The background is normalized to the SM expectation; the uncertainty band (shown as a hatched band in the stack plot and a green band in the ratio plot) includes statistical and systematic uncertainties that affect both the rate and shape of the background distributions. The  $t\bar{t}H$  signal ( $m_H = 125 \text{ GeV}/c^2$ ) is normalized to the total background yield, for easier comparison of the shapes.

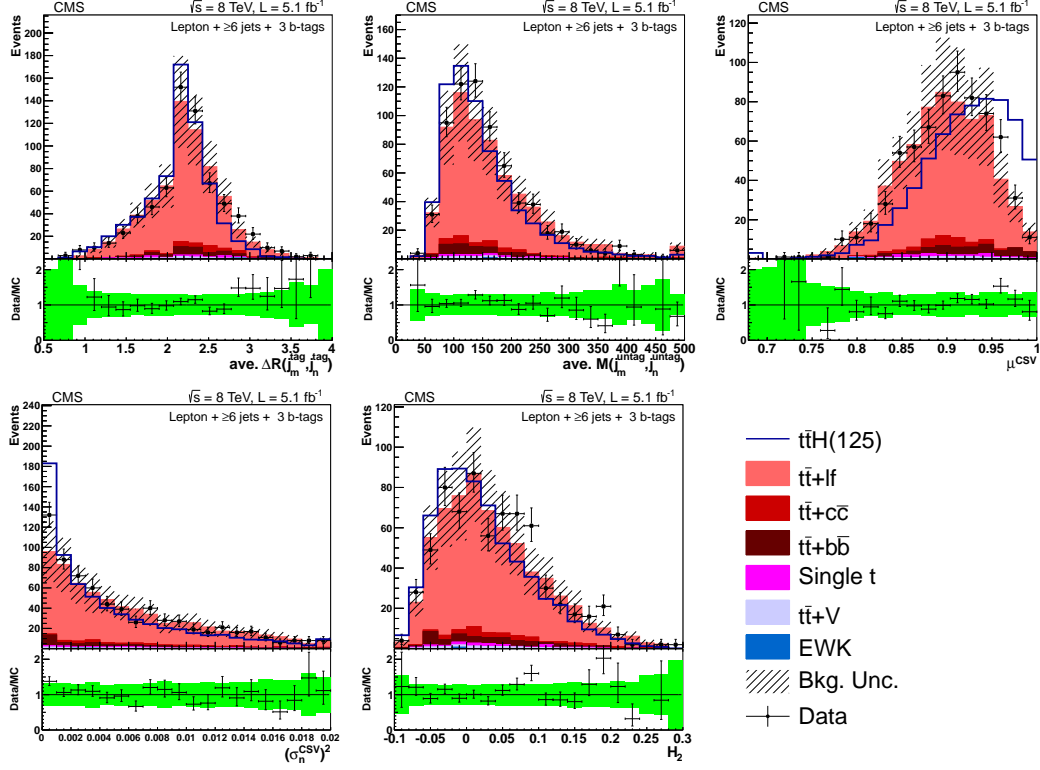


Figure 6.16: Lepton + jets data/MC comparison for the  $\geq 6$  jets + 3 tag category. The uncertainty band includes statistical and systematic uncertainties that affect both the rate and shape of the background distributions.

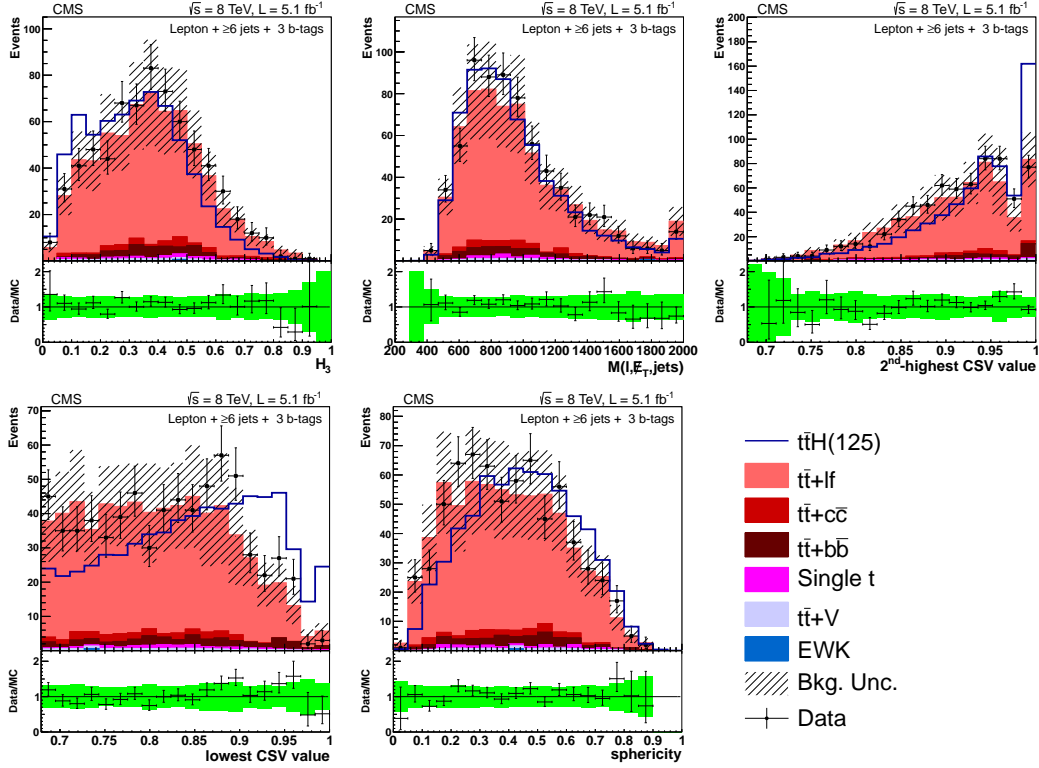


Figure 6.17: Lepton + jets data/MC comparison for the  $\geq 6$  jets + 3 tag category. The uncertainty band includes statistical and systematic uncertainties that affect both the rate and shape of the background distributions.

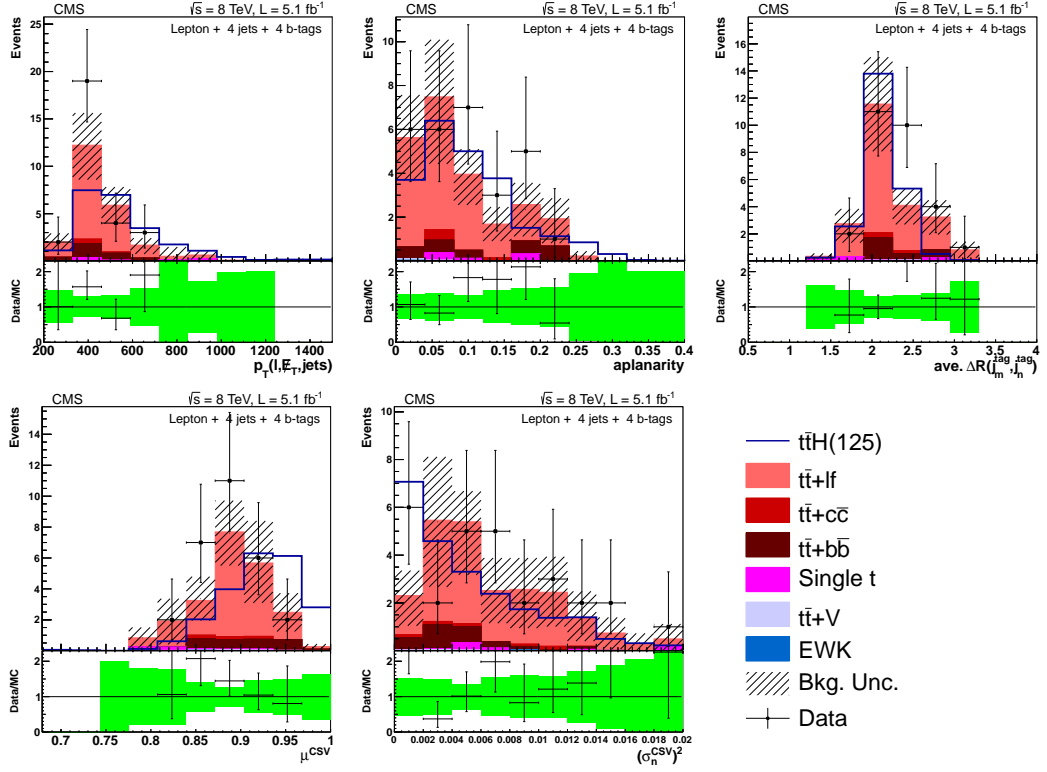


Figure 6.18: Lepton + jets data/MC comparison for the 4 jets + 4 tag category. The uncertainty band includes statistical and systematic uncertainties that affect both the rate and shape of the background distributions.

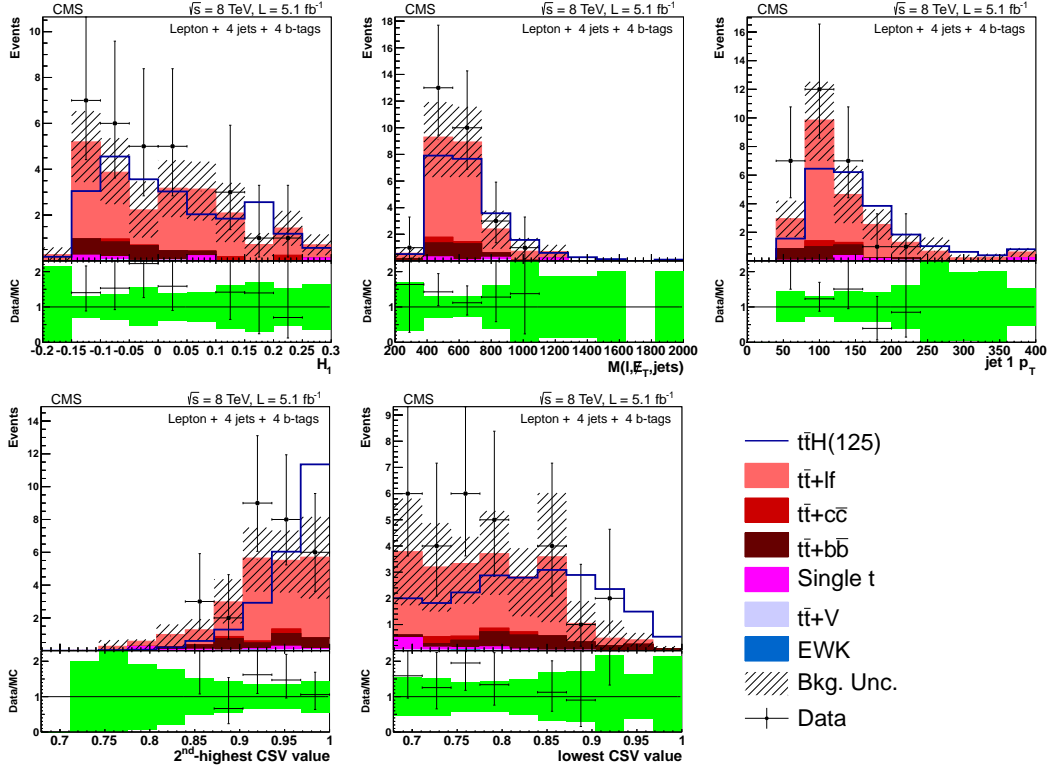


Figure 6.19: Lepton + jets data/MC comparison for the 4 jets + 4 tag category. The uncertainty band includes statistical and systematic uncertainties that affect both the rate and shape of the background distributions.

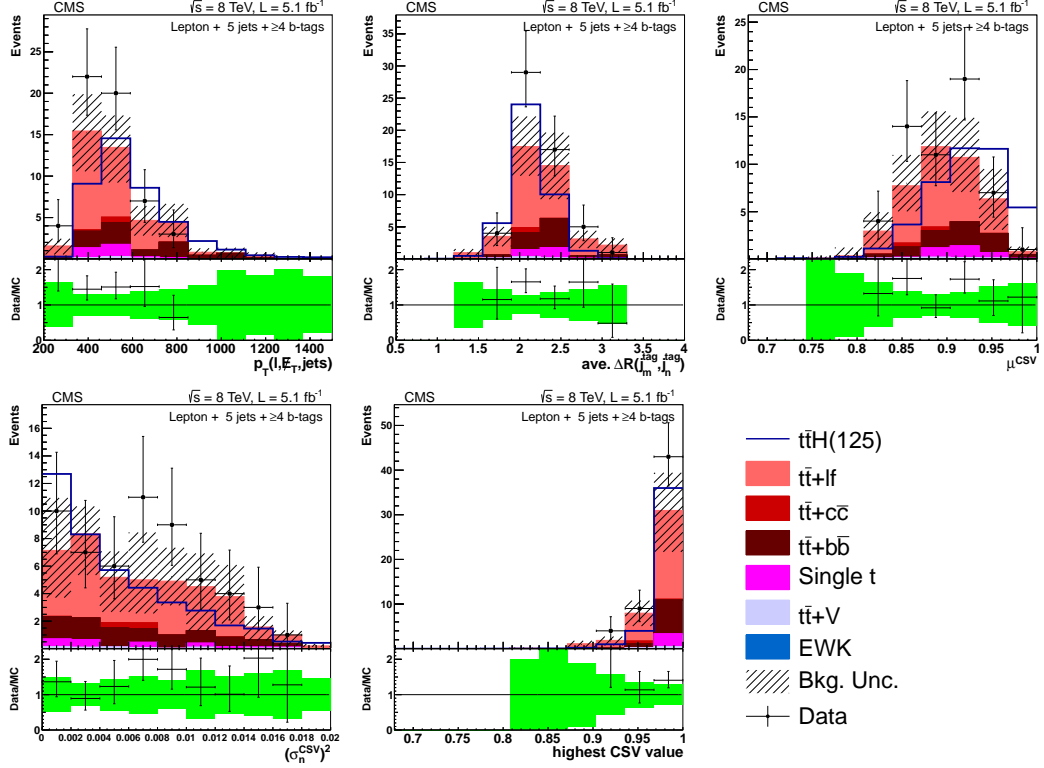


Figure 6.20: Lepton + jets data/MC comparison for the 5 jets + 4 tag category. The uncertainty band includes statistical and systematic uncertainties that affect both the rate and shape of the background distributions.

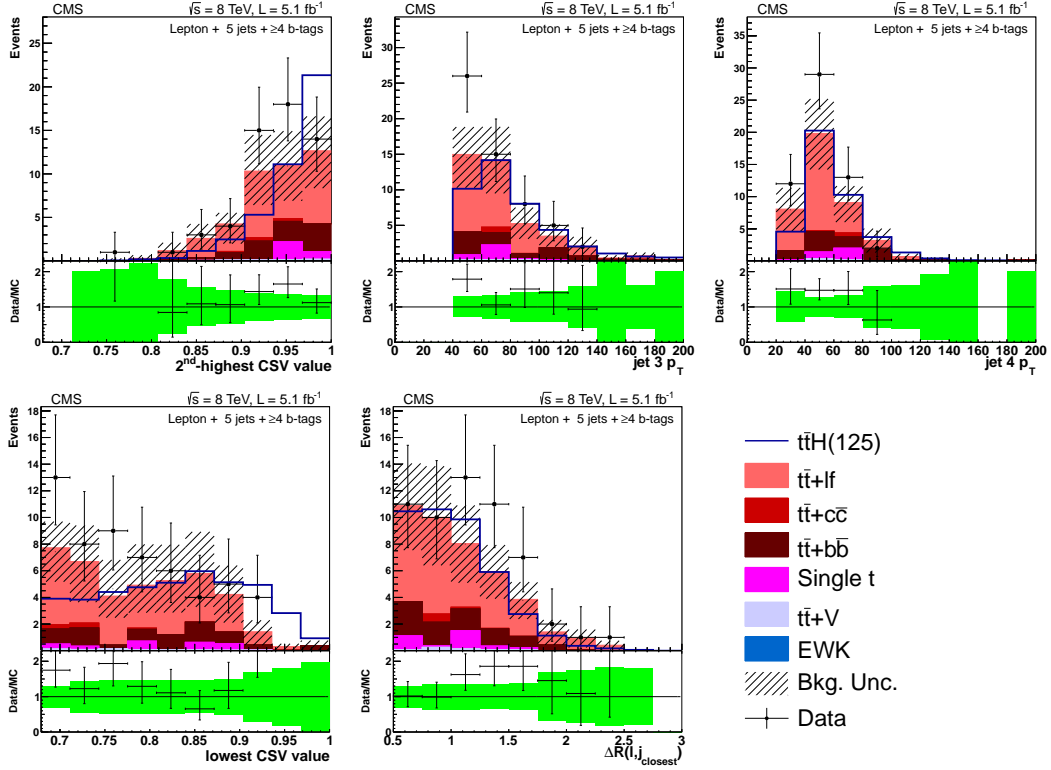


Figure 6.21: Lepton + jets data/MC comparison for the 5 jets + 4 tag category. The uncertainty band includes statistical and systematic uncertainties that affect both the rate and shape of the background distributions.

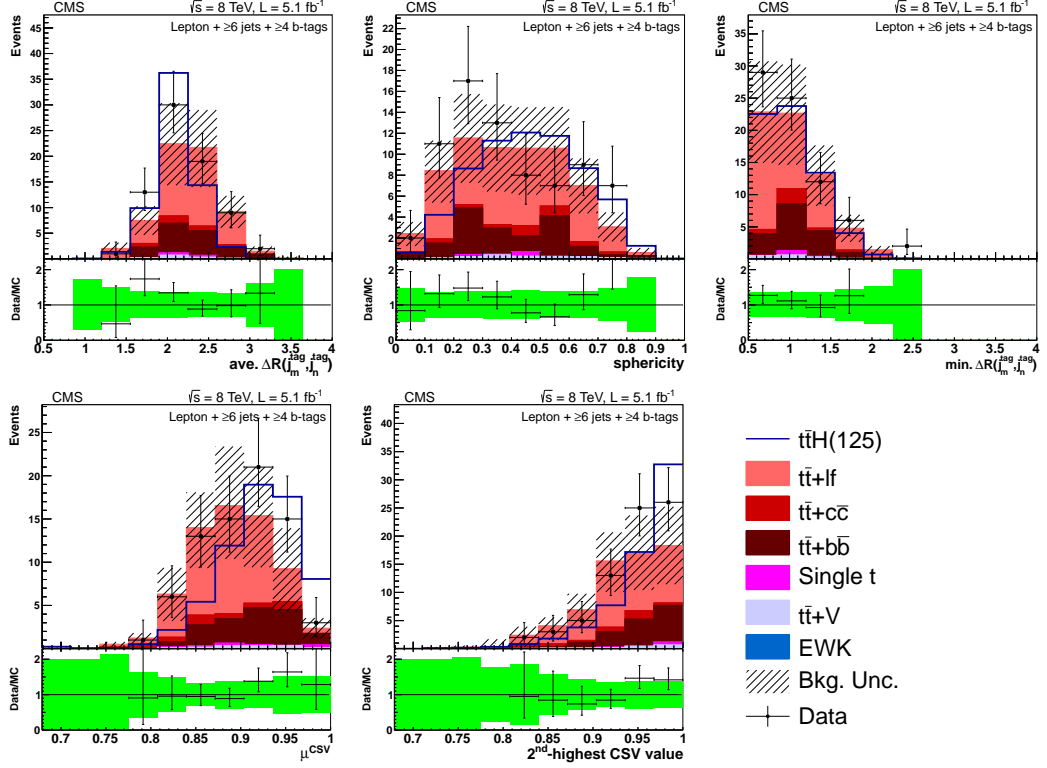


Figure 6.22: Lepton + jets data/MC comparison for the  $\geq 6$  jets + 4 tag category. The uncertainty band includes statistical and systematic uncertainties that affect both the rate and shape of the background distributions.

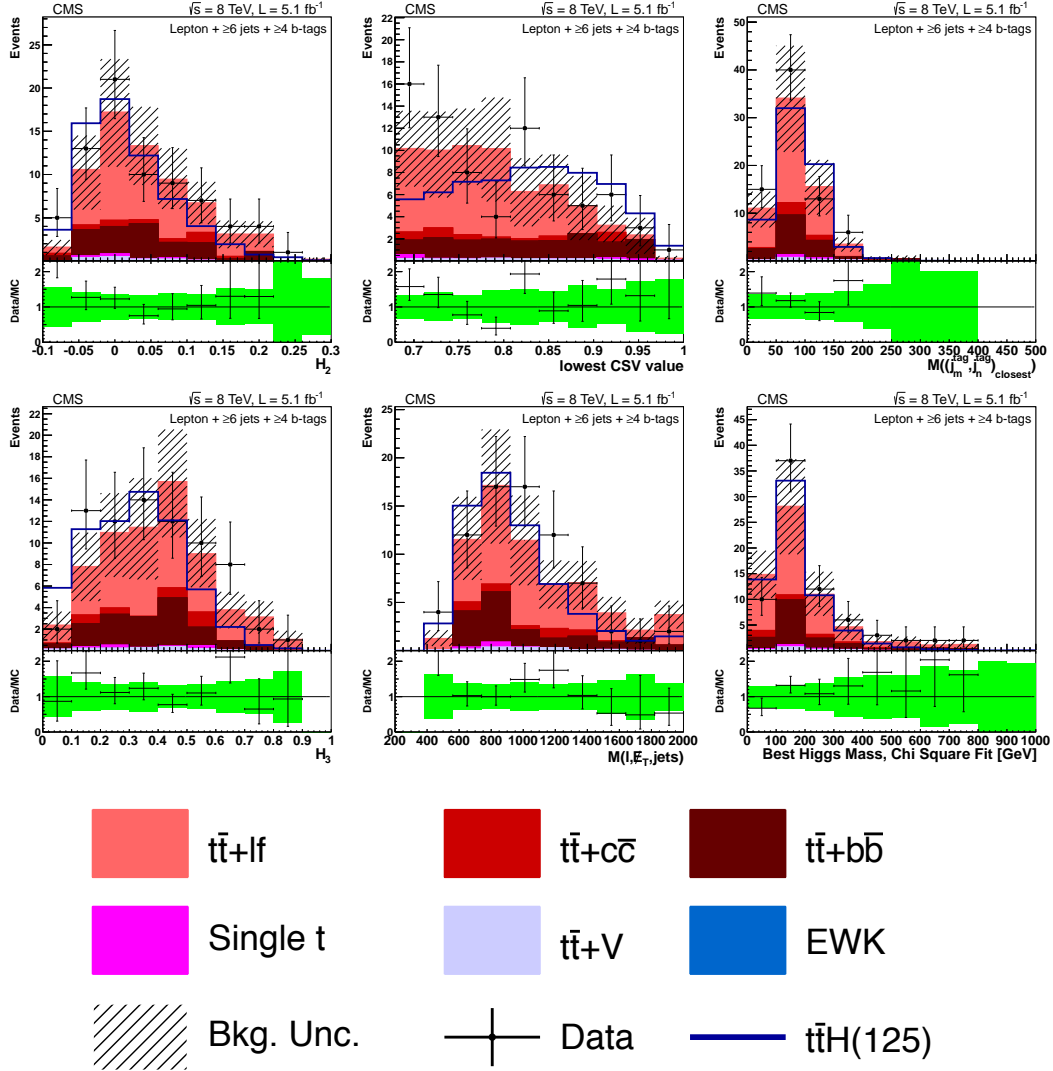


Figure 6.23: Lepton + jets data/MC comparison for the  $\geq 6$  jets + 4 tag category. The uncertainty band includes statistical and systematic uncertainties that affect both the rate and shape of the background distributions.

### 6.3.3 MVA Output, Data to Monte Carlo Comparisons

Data to Monte Carlo comparisons for the CFMlpANN output can be seen on figure 6.24. In the plots, the signal shape has been multiplied by a factor of 30 in order to make its shape visible, and in order to gauge a scale of the expected size of signal to background in each jet/tag category.<sup>2226</sup>

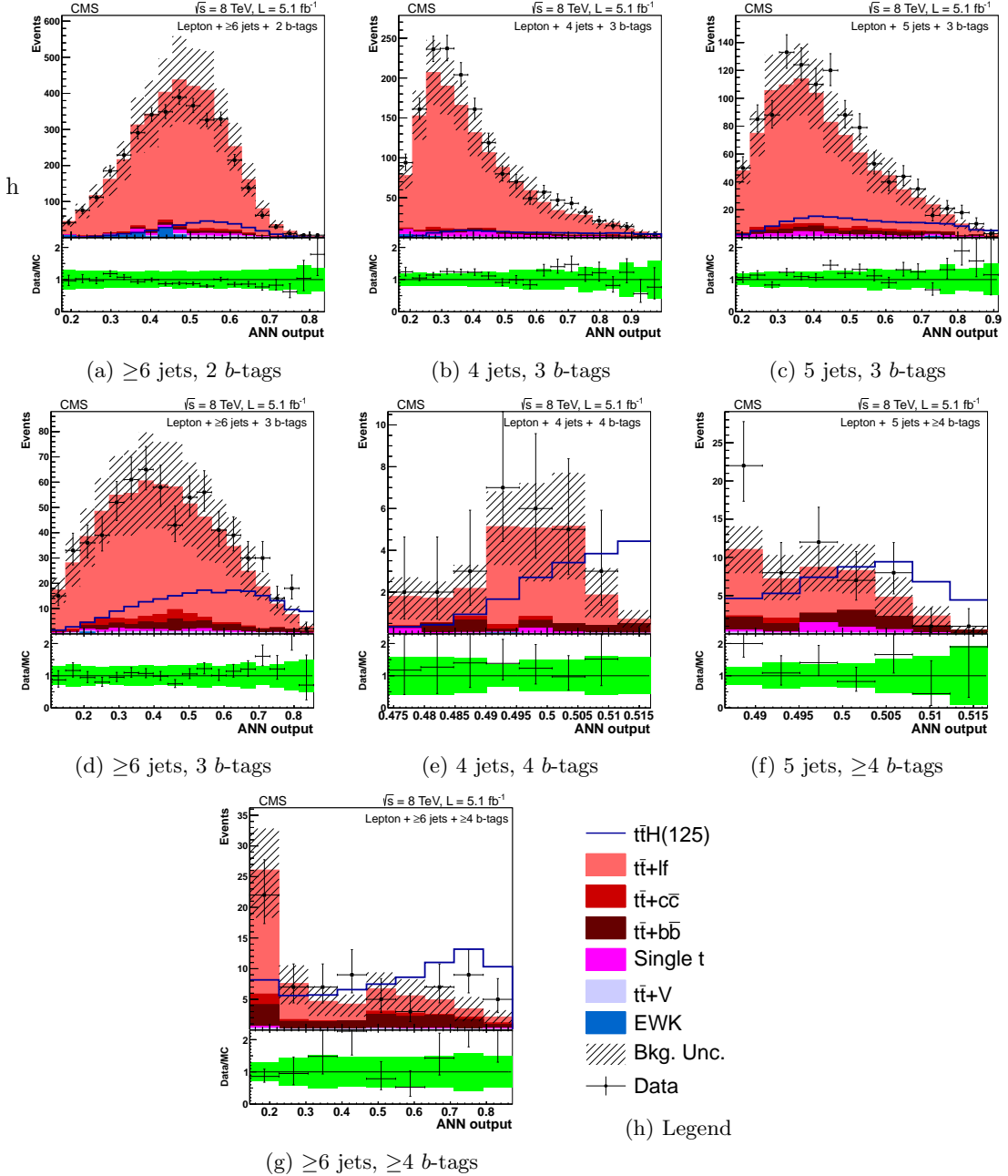


Figure 6.24: The distributions of the CFMlpANN output for lepton+jets events at 8 TeV in the various analysis categories. Background-like events have a low CFMlpANN output value. Signal-like events have a high CFMlpANN output value. The background is normalized to the SM expectation; the uncertainty (shown as a hatched band in the stack plot and a green band in the ratio plot) includes statistical and systematic uncertainties that affect both the rate and shape of the background distributions. The  $t\bar{t}H$  signal ( $m_H = 125 \text{ GeV}/c^2$ ) is normalized to  $30 \times$  SM expectation.

## 2230 6.4 Systematic Uncertainties

2231 There are three types of systematic effects considered in this analysis: those that affect only the  
 2232 rates of signal or background processes, those that affect only the shapes of the CFMlpANN  
 2233 discriminants for signal or background processes, and those that affect both the rate and the  
 2234 shape. In the last case, the rate and shape effects are treated simultaneously so that they are  
 2235 considered completely correlated. Unless otherwise noted, all of the uncertainties listed here  
 2236 apply equally to signal and background and are treated as 100% correlated between the two.  
 2237 Below is a list of systematic effects considered for this analysis:

Table 6.13: Summary of the systematic uncertainties considered on the inputs to the limit calculation. Except where noted, each row in this table will be treated as a single, independent nuisance parameter.

Source	Rate Uncertainty	Shape	Remarks
Luminosity (8 TeV)	2.2%	No	All signal and backgrounds
Lepton ID/Trig	4%	No	All signal and backgrounds
Pileup	1%	No	All signal and backgrounds
Additional Pileup Corr.	–	Yes	All signal and backgrounds
Jet Energy Resolution	1.5%	No	All signal and backgrounds
Jet Energy Scale	0-60%	Yes	All signal and backgrounds
b-Tag SF ( $b/c$ )	0-33.6%	Yes	All signal and backgrounds
b-Tag SF (mistag)	0-23.5%	Yes	All signal and backgrounds
MC Statistics	–	Yes	All backgrounds
PDF ( $gg$ )	9%	No	For $gg$ initiated processes ( $t\bar{t}$ , $t\bar{t}Z$ , $t\bar{t}H$ )
PDF ( $q\bar{q}$ )	4.2-7%	No	For $q\bar{q}$ initiated processes ( $t\bar{t}W$ , $W$ , $Z$ ).
PDF ( $qg$ )	4.6%	No	For $qg$ initiated processes (single top)
QCD Scale ( $t\bar{t}H$ )	15%	No	For NLO $t\bar{t}H$ prediction
QCD Scale ( $t\bar{t}$ )	2-12%	No	For NLO $t\bar{t}$ and single top predictions
QCD Scale (V)	1.2-1.3%	No	For NNLO $W$ and $Z$ prediction
QCD Scale (VV)	3.5%	No	For NLO diboson prediction
Madgraph Scale ( $t\bar{t}$ )	0-20%	Yes	$t\bar{t}$ + jets/ $bb$ / $c\bar{c}$ uncorrelated. Varies by jet bin.
Madgraph Scale (V)	20-60%	No	Varies by jet bin.
$t\bar{t} + bb$	50%	No	Only $t\bar{t} + bb$ .

2238 **Jet Energy Scale (JES):** The Jet Energy Scale systematic is based on the uncertainty on the  
 2239 L1, L2, L3, and L2L3 residual corrections to the reconstructed jet energy, as described  
 2240 in section 6.2.6. To evaluate the effect on the CFMlpANN output, the jet energy scale is  
 2241 shifted by one standard deviation up and down using the standard JetMET procedure [92].  
 2242 For each variation, the jet energies are recalculated, allowing for new jets to pass the selection  
 2243 where once they failed, or fail the selection where once they passed, resulting in a migration  
 2244 of events across jet/tag categories. Finally, the CFMlpANN response is recalculated, and  
 2245 the effect for signal and the  $t\bar{t} + jets$  background is shown in figure 6.25.

**Jet Energy Resolution (JER):** The jet  $p_T$  resolution in MC differs from that observed in  
 data by approximately 10% in a  $\eta$  dependent way, as described in table ??, as per the  
 recommendations of the JetMET group [93]. The value of the jet  $p_T$  is adjusted according

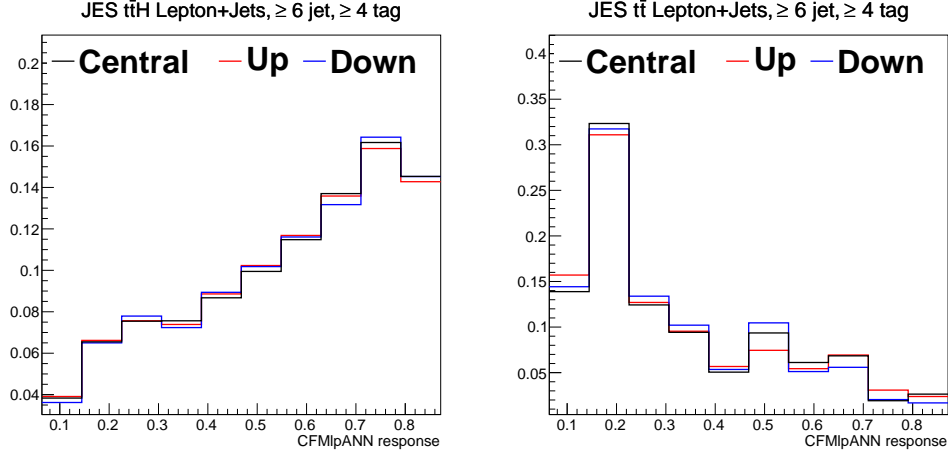


Figure 6.25: Comparison of the MVA discriminator for JES shift upwards (red) and downwards (blue) relative to the nominal (black) shape for the  $t\bar{t}H(120)$  signal (left) and the main background sample  $t\bar{t}$ + light flavor (right). The plots shown are from the  $\geq 6$  jet  $\geq 4$  tag category in the lepton+jets channel. All plots are normalized to unit area.

JES systematic yield change			
sys	shift	lepton+jets	
		$t\bar{t}H(120)$	$t\bar{t}$
JES	up	+8.6%	+12.1%
	down	-8.4%	-7.3%

Table 6.14: Relative yield change due to JES shift up/down for the  $\geq 6$  jets +  $\geq 4$  tags category in the lepton+jets channel.

to the formula:

$$p'_T = \max [0, p_T^{gen} + c(p_T^{reco} - p_T^{gen})] \quad (6.13)$$

2246 The correction factor  $c$  is taken from table ???. To assess the effect of the systematic  
 2247 uncertainty on the JER, the value of  $c$  is shifted up and down by standard deviation, the  
 2248 JER correction is applied to the jets using this new  $c$  value, and the event rates and ANN  
 2249 shapes are recalculated. The effect of the JER on the shape variation is negligible, so it is  
 2250 treated as a rate-only effect in limit setting.

2251 **b-tag Scale Factor:** The uncertainty in the  $b$ -tagging scale factor is assessed according to the  
 2252 prescriptions developed by the BTag POG [94]. Each per-jet  $b$ -tag scale factor is shifted  
 2253 up or down by its uncertainty, and the new CSV output value corresponding to that  
 2254 uncertainty is recalculated. This new CSV value is used to determine both the number of  
 2255 tags associated with that systematic and the new shape of variables that use the CSV  
 2256 output, such as the average CSV value for  $b$ -tagged jets. This uncertainty effects both rate  
 2257 and shape estimates. The effects of the  $b$ -tag scale factors on the ANN shape and event  
 2258 yields are summarized in Fig. 6.26 and Table 6.15 respectively.

2259 **Lepton ID and Trigger Scale Factors:** As discussed previously, an uncertainty of 4% covers

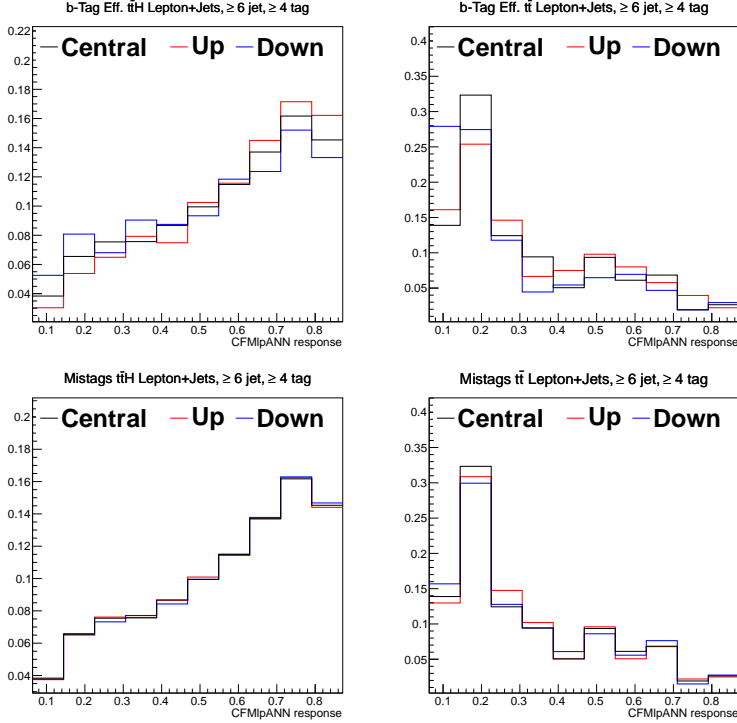


Figure 6.26: Comparison of the MVA discriminator for  $b$ -tag scale factor shift upwards (red) and downwards (blue) relative to the nominal (black) shape for the  $t\bar{t}H(120)$  signal (left) and the main background sample  $t\bar{t} + \text{light flavor}$  (right). The plots are from the  $\geq 6$  jets +  $\geq 4$  tags category in the lepton+jets channel. All plots are normalized to unit area.

$b$ -tag systematic yield change			
		lepton+jets	
sys	shift	$t\bar{t}H(120)$	$t\bar{t}$
heavy flavor SF	up	+14.9%	+23.7%
	down	-15.3%	-16.0%
light flavor SF	up	+0.7%	+5.7%
	down	-1.1%	-4.2%

Table 6.15: Relative yield change due to  $b$ -tag scale factor shift up/down for the  $\geq 6$  jets +  $\geq 4$  tags category in the lepton+jets channel.

variations of the combined trigger, ID, and isolation scale factor.

**Pileup Reweighting:** The uncertainty on the pileup reweighting comes from changing the minimum bias cross section used to calculate the pileup reweighting by  $\pm 7\%$  from the default value of 69.4 mb. The pileup reweighting is calculated using the shifted cross sections and the new weights are applied to determine the uncertainty on both the rate and shapes. Since the effect of the pileup on the shape variation is negligible, the effects of pileup are accounted through a rate-only uncertainty for the limit calculations.

**Additional Pileup Correction** The uncertainty associated with the additional pileup correction, described in section 6.1.5, is applied as a pure shape uncertainty to all processes. Fig. 6.27 shows the effects of the additional pileup correct uncertainty on the CFMlpANN shape.

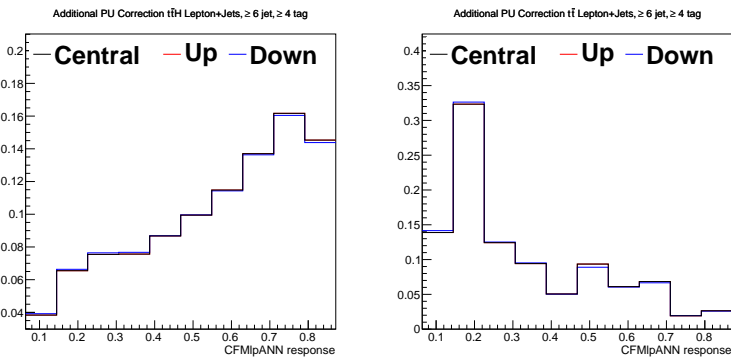


Figure 6.27: Comparison of the MVA discriminator for additional PU correction systematic upwards (red) and downwards (blue) relative to the nominal (black) shape for the  $t\bar{t}H(120)$  signal (left) and the main background sample  $t\bar{t} + \text{light flavor}$  (right). The plots are from the  $\geq 6$  jets +  $\geq 4$  tags category in the lepton+jets channel. All plots are normalized to unit area.

**Cross Sections:** The expectation for signal and background yields are derived from theoretical predictions of at least NLO accuracy. Uncertainties affecting these normalizations are summarized in table 6.16. Where appropriate, factors contributing to these uncertainties that are common to multiple processes are treated as 100% correlated. Note that for the  $t\bar{t}+\text{jets}$  (including  $t\bar{t} + b\bar{b}$  and  $t\bar{t} + c\bar{c}$  processes, as well as the  $V+\text{jets}$  processes, there is an additional uncertainty coming from the scale choice in Madgraph that effects these channels in a jet-bin specific way. This uncertainty is not included in the table 6.16, but is detailed in the next point.

**Luminosity:** The uncertainty on the luminosity estimate is 2.2%. This affects all rates.

**Madgraph  $Q^2$  Uncertainty:** Although that backgrounds are normalized using NLO accurate theoretical caluclations, these are only applicable to inclusive distributions. To extrapolate

Process	pdf			QCD Scale			
	$gg$	$qb$	$qg$	$t\bar{t}$	$V$	$VV$	$t\bar{t}H$
$t\bar{t}H$	9%						12.5%
$t\bar{t}+jets$	9%			12%			
$t\bar{t} + W$		7%		15%			
$t\bar{t} + Z$	9%			15%			
Single top			4.6%	2%			
$W+jets$		4.8%			1.3%		
$Z+jets$		4.2%			1.2%		
Dibosons						3.5%	

Table 6.16: Cross section uncertainties used for the limit settings. Each column in the table is an independent source of uncertainty, except for the last column which represents uncertainties uncorrelated with any others. Uncertainties in the same column for two different processes (different rows) are completely correlated.

late these inclusive predictions to exclusive rates in particular jet bins requires the use of a Monte Carlo sample. The MADGRAPH generator is used at the matrix element level and includes tree-level calculations for processes with multiple additional jets, matched to the PYTHIA parton shower to model additional soft and collinear radiation. Since the MADGRAPH + PYTHIA is tree-level, the choice of the renormalizations and factorizations scales in this calculation has a significant impact. To include the effects of this uncertainty, the factorization and renormalization scales are varied by a factor of two. The ideal way to study this effect would be to generate dedicated samples with the varied scale choice, however the required statistics to get a precise determination of the systematic effect is computationally prohibitive. Therefore, as an alternative, we reweight the amplitudes, dividing by the appropriate power of  $\alpha_s$  and the *pdf* values at the original scale, and multiplying by the values at the new scale choice. This reweighting procedure is supported by the CMS Monte Carlo Generators group, and has been validated against dedicated scale-varied samples and has been shown to produce consistent results [95]. This reweighting procedure provides both a rate and a shape uncertainty, separately for  $t\bar{t}$ +light flavor,  $t\bar{t} + c\bar{c}$ , and  $t\bar{t} + b\bar{b}$  components of the  $t\bar{t}$  sample. Figure 6.28 shows the shape and rate variations for selected event categories. To prevent the strength of the  $t\bar{t}+jets$  constraint from overconstraining the  $t\bar{t} + b\bar{b}$  and  $t\bar{t} + c\bar{c}$  components, we allow the Madgraph scale to vary independently for these three components.

**MC Statistics Uncertainty:** To account for the effect of limited MC statistics in the analysis, a method described by Barlow and Beeston, is used to select regions of the CFMlpANN output that should have additional nuisance parameters applied [?, ?]. For the CFMlpANN shapes of every MC process in all different categories, each bin is allowed to float within statistic uncertainty and a corresponding nuisance parameter is added. To make the limit

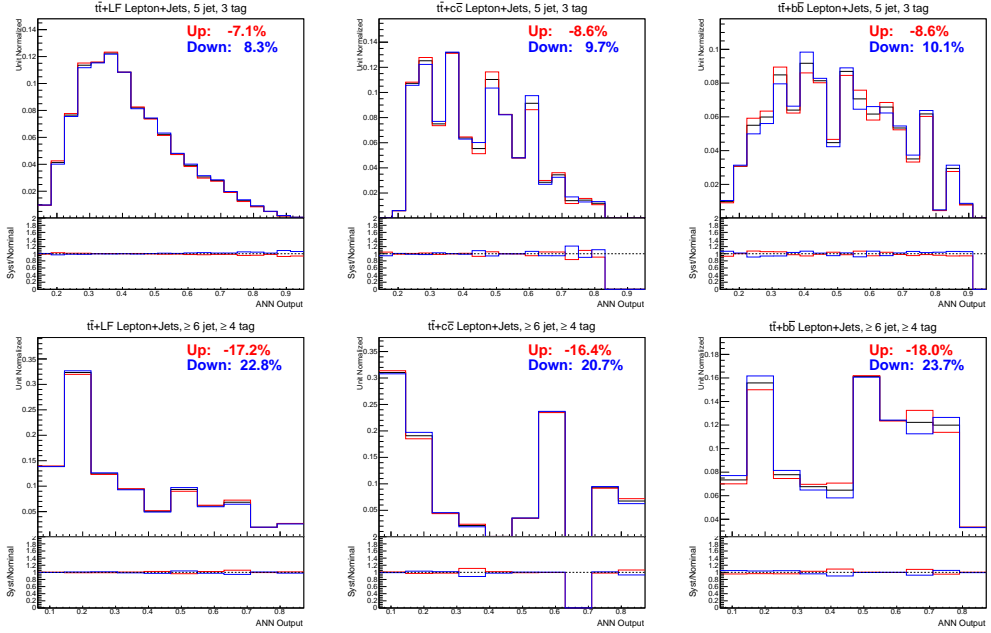


Figure 6.28: The rate and shape variations for selected categories due to the  $Q^2$  uncertainty.

computation more efficient and stable, bins are removed as nuisance parameters if the MC statistics uncertainty is negligible compared to the data statistics uncertainty or where there is no appreciable contribution from signal. In total, there are 60 nuisance parameters used to describe the MC statistics for this analysis. Tests show that the effect of neglecting bins as described above is smaller than 5%.

**Additional  $t\bar{t} + b\bar{b}$  Rate Uncertainty:**  $t\bar{t} + b\bar{b}$  background is very similar to our signal, the uncertainty on its rate and shape will have a big impact on our search. Due to the lack of more accurate next leading order(NLO) theoretical prediction for this process, we obtained this background and assessed its uncertainty based on the inclusive 8 TeV  $t\bar{t}$  sample. Since the inclusive  $t\bar{t}$  sample is generated with Madgraph + Pythia, we need to apply a K-factor to the Madgraph cross section. According to calculations done in [96], the K-factor from leading order(LO) to NLO ranges between 1.2 and 1.8, depending on the scale choice. To be conservative, an extra 50% rate uncertainty is assigned to  $t\bar{t} + b\bar{b}$  which corresponds to a K-factor of 1.7 for  $\sigma_{NLO}/\sigma_{Madgraph}$ . Studies also showed consistently that  $t\bar{t} + b\bar{b}$  rate is correct to within factor of 2 in control regions dominated by  $t\bar{t}$ +light flavor statistics. The extra 50% rate uncertainty should possibly include additional uncertainty beyond the 20% from  $Q^2$  scale to account for the differences between NLO and Madgraph.

In order to validate this assessment further, a dedicated CFMlpANN was trained to separate  $t\bar{t} + b\bar{b}$  from the  $t\bar{t} + jets$  background. In order to have sufficient statistics, two jet/tag categories are used: 5jets,  $\geq 3b$ -tags, and  $\geq 6$ jets,  $\geq 3b$ -tags. The nominal  $t\bar{t} + b\bar{b}$  cross sec-

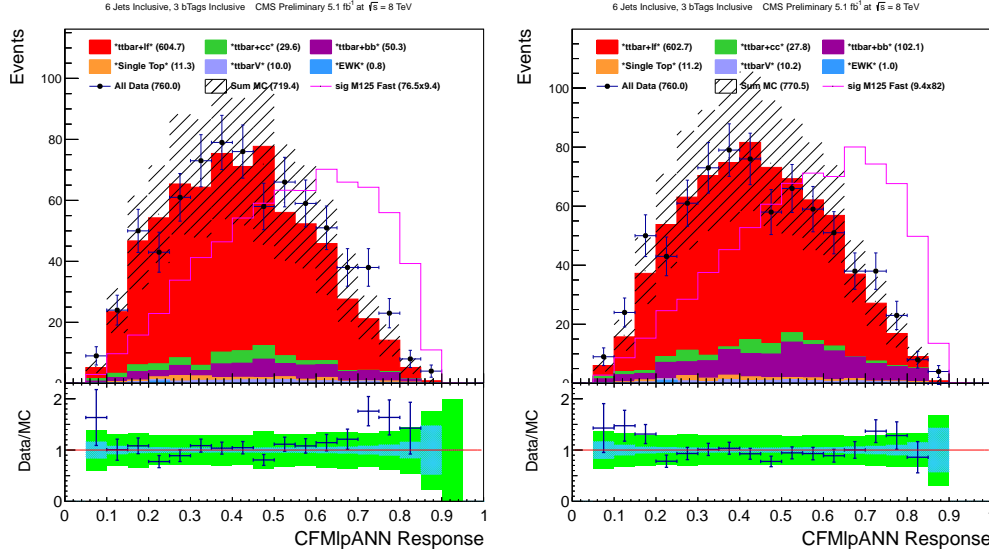


Figure 6.29: A dedicated CFMlpANN trained to isolate  $t\bar{t} + b\bar{b}$  from  $t\bar{t} + jets$ . The left plot shows is for the case of nominal  $t\bar{t} + b\bar{b}$  cross-section, the right plot shows the case for  $x2 t\bar{t} + b\bar{b}$  cross-section. The left-most region of both plots is the most sensitive to the  $t\bar{t} + b\bar{b}$  normalization, and shows no significant improvement in data to MC agreement, justifying the reasoning that an uncertainty larger than 50% is needed.

2326     tion was doubled, in an attempt to observe an improvement in the range of the discriminant  
2327     that was enriched in  $t\bar{t} + b\bar{b}$ . However, as figure 6.29 shows, no significant improvement  
2328     was seen, justifying the reasoning that an uncertainty much larger than 50% is needed.

## 2329     6.5 Statistical Methods

2330     In the lack of an observation of any deviation from SM predictions, upper limits are set on the  
2331     Higgs boson production cross section, with respect to the SM expectation,  $\sigma^{95\%}/\sigma^{SM}$ . Although  
2332     the analysis has been optimized for Higgs decays to  $b$ -quarks, there is still acceptance from  $WW$   
2333     and  $ZZ$  decays. As such, limits on the inclusive decay of the Higgs boson are set. The statistical  
2334     method used to report results is the modified frequentist approach, also known as  $CL_s$ .

2335     For the  $CL_s$  method, the likelihood function  $\mathcal{L}(\text{data}|\mu, \theta)$  is defined as

$$\mathcal{L}(\text{data}|\mu, \theta) = \text{Poisson}(\text{data}|\mu \cdot s(\theta) + b(\theta)) \cdot p(\tilde{\theta}|\theta) \quad (6.14)$$

$$= \prod_i \frac{(\mu s_i + b_i)^{n_i}}{n_i!} e^{-(\mu s_i + b_i)} \cdot p(\tilde{\theta}|\theta) \quad (6.15)$$

2336     where  $\mu$  is the signal strength modifier which is often reported in the upper limit results as the  
2337     ratio of the cross-section upper limit over the standard model cross-section and  $\theta$  represents a  
2338     full set of nuisance parameters that are used to incorporate systematic uncertainties [97]. The

2339 Probability Distribution Function (*pdf*) of the nuisance parameter  $p(\tilde{\theta}|\theta)$ , where  $\tilde{\theta}$  is the default  
 2340 value, reflects the degree of confidence in what the true value of  $\theta$  is.

2341 To compare the compatibility of the data with the *background-only* and *signal+background*  
 2342 hypotheses, where the signal is allowed to be scaled by some factor  $\mu$ , the test statistic  $\tilde{q}_\mu$  is  
 2343 constructed based on the profile likelihood ratio:

$$\tilde{q}_\mu = -2 \ln \frac{\mathcal{L}(\text{data}|\mu, \hat{\theta}_\mu)}{\mathcal{L}(\text{data}|\hat{\mu}, \hat{\theta})} \quad , 0 \leq \hat{\mu} \leq \mu \quad (6.16)$$

2344 where  $\hat{\theta}_\mu$  refers to the conditional maximum likelihood estimator of  $\theta$ , given the signal strength  
 2345 parameter  $\mu$  and data. The pair of parameter estimators  $\hat{\mu}$  and  $\hat{\theta}$  correspond to the global  
 2346 maximum of the likelihood.

2347 To perform the computation of the limits, RooStats-based statistical analysis tools recom-  
 2348 mended by Higgs PAG have been used. The corresponding software is the "Higgs Combination"  
 2349 package. There are two versions of the limit calculation technique that we use. The frequen-  
 2350 tist  $CL_s$  approach uses a large number of pseudo-experiments to extract the limit results. The  
 2351 "asymptotic" approach makes an analytic approximation of the full  $CL_s$  technique and there-  
 2352 fore avoids throwing pseudo-experiments [98]. The asymptotic approach is used for optimizing  
 2353 the analysis, for the results of this analysis. However, for the limits set from the combined Lep-  
 2354 ton+Jets and di-Lepton channels, using both 7 and 8 TeV data, the results are calculated using  
 2355 the full  $CL_s$  treatment. Comparisons have shown that limits obtained with the two techniques  
 2356 agree at the 10% level.

2357 In the limit calculation, the backgrounds are decomposed into the following distinct cate-  
 2358 gories:  $t\bar{t}$ +jets,  $t\bar{t} + b\bar{b}$ ,  $t\bar{t} + c\bar{c}$ , single top ( $s$ -channel,  $t$ -channel, and  $tW$ -channel combined),  
 2359  $W$ +jets,  $Z$ +jets,  $t\bar{t} + W$ ,  $t\bar{t} + Z$ , and dibosons ( $WW$ ,  $WZ$ , and  $ZZ$  combined). The rates and  
 2360 shapes of these background processes, as well as the signal are allowed to vary according to a set  
 2361 of nuisance parameters, and the values of these nuisance parameters are constrained according  
 2362 to the uncertainties summarized in Table 7.13. Except where noted below, each row in that table  
 2363 represents a single nuisance parameter, completely correlated across all categories and processes  
 2364 to which it applies. The exceptions to this approach are as follows:

- 2365 • In the case of the Madgraph  $Q^2$  uncertainty, there are separate nuisance parameters for  
 2366 each of the three components of the  $t\bar{t}$  background (+jets, + $b\bar{b}$ , and + $c\bar{c}$ ). Furthermore, for  
 2367 the  $t\bar{t}$ +jets component, the uncertainty is actually broken into three nuisance parameters  
 2368 for the contributions coming from diagrams with zero extra partons, one extra parton, or  
 2369 at least two extra partons.

- For the  $b$ -tagging efficiency and mistag rate uncertainties, the rate and shape components are described by separate, independent nuisance parameters. Furthermore, each event selection category has its own, independent nuisance parameter. This is to prevent the high statistics background rich regions from overconstraining the shape uncertainties in the lower statistics, more signal rich regions.

For systematic effects such as the jet energy scale or the rate component of the  $b$ -tagging scale factor that may cause migration between event categories, care has been taken to correlate properly the different categories so that, for example, increasing the jet energy scale will cause the appropriate increases and decreases in the yields in various categories. The binning of the CFMlpANN output is chosen to minimize the impact of MC statistics and, as described in section 6.4 the MC statistics for bins where the MC statistical uncertainty causes a significant impact are accounted for.

## 6.6 Results and Conclusions

The variable used for signal extraction is the shape of the MVA output discriminator distribution. The fit of the simulated samples to the measured data will test for the presence of signal and, in its absence, it will set upper limits on the Higgs boson cross section. Besides the MVA discriminator shapes for data, background and signal, inputs to the "Higgs Combination" package also include the number of events passing our selection for each of the above processes. Various systematic uncertainties described in section 6.4 have all been taken into account in our limit calculation. The Higgs mass points we set limits for are: 110, 115, 120, 125, 130, 135 and 140  $\text{GeV}/c^2$ . The upper limits are shown in Tab. 6.17 and Fig. 6.30.

Higgs Mass	Observed	Median	Expected 68% C.L. Range	Expected 95% C.L. Range
110 $\text{GeV}/c^2$	5.9	3.1	[2.1,4.6]	[1.6,6.8]
115 $\text{GeV}/c^2$	7.2	3.9	[2.7,5.7]	[2.0,8.1]
120 $\text{GeV}/c^2$	8.8	4.8	[3.4,6.9]	[2.5,9.7]
125 $\text{GeV}/c^2$	9.5	5.4	[3.8,7.9]	[2.8,11.1]
130 $\text{GeV}/c^2$	11.4	6.6	[4.6,9.6]	[3.4,13.7]
135 $\text{GeV}/c^2$	15.0	8.9	[6.3,12.8]	[4.7,18.1]
140 $\text{GeV}/c^2$	17.0	11.0	[7.7,15.9]	[5.7,22.5]

Table 6.17: Expected and observed upper limits for SM Higgs for lepton + jets channel using the first  $5.1\text{ fb}^{-1}$  of the 2012 dataset. These limits were extracted using the asymptotic method.

For this first  $5.1\text{ fb}^{-1}$  of data collected by the CMS detector, the first search for the Standard Model Higgs boson produced in association with top-quark pairs. Although there have been no observed sign of Higgs production in association with top quarks, upper limits are set on the production cross-section, using the statistical methods described above. If this data set

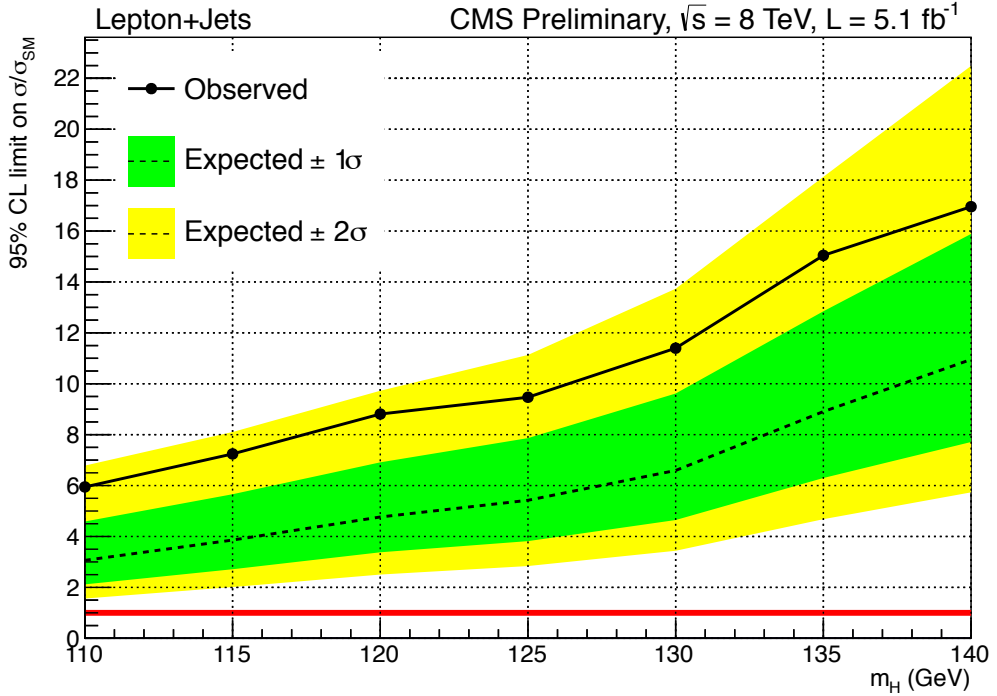


Figure 6.30: The expected and observed 95% CL upper limits on the signal strength parameter  $\mu = \sigma/\sigma_{SM}$  for the lepton+jets channel using the 2012 dataset. These limits were extracted using the asymptotic method.

2395 was repeatedly collected, allowing for statistical fluctuations, it should be expected that, for a  
 2396 Standard Model Higgs boson, with mass,  $m_H = 125$  GeV, that 95% of the results would fail to  
 2397 observe the  $t\bar{t}H$  signal unless its cross-section was modified by a factor of 9.5. From simulations  
 2398 alone, this exepcted factor is 5.4, an difference of less than  $2\sigma$  from the observed data.

2399 The results of this analysis were combined with previous results in this channel from 7 TeV  
 2400 data and with a di-lepton final state channel and published in the Journal of High Energy Physics  
 2401 (JHEP) in May of 2013 [99]. The combined analytical power of all of the channels allowed for an  
 2402 upper limit of 5.8 times the predicted Standard Model cross section. This is less than  $1\sigma$  away  
 2403 from the expected factor of 5.2 from simulations alone.

2404 **Chapter 7**

2405 **Analysis II: The Complete 19.5**

2406  **$\text{fb}^{-1}$  of 8 TeV data**

2407 The CMS experiment recorded  $19.5 \text{ fb}^{-1}$  of data in the complete 8 TeV run during 2012.  
2408 The previous analysis was updated with the full dataset. A similar lepton and jet selection  
2409 is used, with the same classification scheme for events, based on the reconstructed jet and  $b$ -  
2410 tag multiplicity. New signal and background simulations were generated to account for the  
2411 increased dataset, requiring new calibration factors for the pileup, lepton and jet reconstruction,  
2412 and  $b$ -tagging efficiency. Additionally, a new type of multivariate analysis (MVA) technique was  
2413 employed, in place of the Clermont-Ferrand Multi-Layer Perceptron Artificial Neural Network  
2414 (CFMlpANN), a Boosted Decision Tree (BDT) is used for signal extraction and limit setting. The  
2415 number of input variables that were investigated for use in each jet/tag category, was expanded,  
2416 and some new variables were found to offer slightly more discriminating power. The discriminant  
2417 of a specialized BDT, trained to separate  $t\bar{t} + b\bar{b}$  from  $t\bar{t}H$ , was added as an input variable to  
2418 the BDT trained in the 5 jet,  $\geq 4$   $b$ -tag;  $\geq 6$  jet, 3  $b$ -tag; and  $\geq 6$  jet,  $\geq 4$   $b$ -tag categories.

2419 **7.1 Data and Simulated Samples**

2420 As described in the earlier chapters, data is collected through an HLT trigger path and stored  
2421 offline for analysis later. Simulated samples are generated with the latest theoretical and empir-  
2422 ical inputs for the proton PDF, standard model cross sections, and hadronic showering. These  
2423 events are processed with a simulation of the detector environment, and the subsequent elec-  
2424 tronic response of each of its elements. Finally, physics objects, such as electrons, and muons  
2425 are reconstructed with the particle-flow algorithm described in a previous chapter.

2426 **7.1.1 Data Samples**

2427 The results presented here are based on the full  $\sim 19.5 \text{ fb}^{-1}$  of the 2012 CMS dataset. Table 7.1  
2428 lists the datasets used for this analysis, based on single muon and single electron triggers used to  
2429 collect the data. Luminosities are quoted from the HF luminosity calculation and have a 2.2%  
2430 uncertainty.

Dataset	Run Range	Integrated Luminosity
/SingleMu/Run2012A-13Jul2012-v1/AOD	190456–193621	$0.81 \text{ fb}^{-1}$
/SingleMu/Run2012A-recover-06Aug2012-v1/AOD	190782–190949	$0.08 \text{ fb}^{-1}$
/SingleMu/Run2012B-13Jul2012-v1/AOD	193834–196531	$4.40 \text{ fb}^{-1}$
/SingleMu/Run2012C-24Aug2012-v1/AOD	198022–198523	$0.50 \text{ fb}^{-1}$
/SingleMu/Run2012C-PromptReco-v2/AOD	198941–203746	$6.39 \text{ fb}^{-1}$
/SingleMu/Run2012D-PromptReco-v1/AOD	203768–208686	$7.27 \text{ fb}^{-1}$
<b>Total SingleMu</b>	<b>190645–208686</b>	<b><math>19.5 \text{ fb}^{-1}</math></b>
/SingleElectron/Run2012A-13Jul2012-v1/AOD	190456–193621	$0.81 \text{ fb}^{-1}$
/SingleElectron/Run2012A-recover-06Aug2012-v1/AOD	190782–190949	$0.08 \text{ fb}^{-1}$
/SingleElectron/Run2012B-13Jul2012-v1/AOD	193834–196531	$4.40 \text{ fb}^{-1}$
/SingleElectron/Run2012C-24Aug2012-v1/AOD	198022–198523	$0.50 \text{ fb}^{-1}$
/SingleElectron/Run2012C-PromptReco-v2/AOD	198941–203746	$6.40 \text{ fb}^{-1}$
/SingleElectron/Run2012D-PromptReco-v1/AOD	203768–208686	$7.27 \text{ fb}^{-1}$
<b>Total SingleElectron</b>	<b>190645–208686</b>	<b><math>19.5 \text{ fb}^{-1}</math></b>

Table 7.1: The datasets analyzed for this analysis.

2431 **7.1.2 Signal Samples**

2432 The  $t\bar{t}H$  signal is modeled using the PYTHIA Monte Carlo generator. The samples and associated  
2433 cross sections used are listed in Table 7.2.

2434 **7.1.3 Background Samples**

2435 To model the backgrounds, this analysis primarily uses Monte Carlo (MC) samples from the  
2436 “Summer12” MC campaign, discussed in the previous chapter. Most of the samples are generated  
2437 either with the MADGRAPH tree-level matrix element generator matched to PYTHIA for the  
2438 parton shower, or with the NLO generator POWHEG combined with PYTHIA. These samples are  
2439 reconstructed with the same CMSSW version as the data samples listed above. Similarly to the  
2440 previous analysis, the pileup distribution in all MC samples is reweighted, using the procedure  
2441 listed below so that the MC pileup distribution matches the one expected for data. Table 7.3  
2442 lists the background MC samples and associated cross sections.

2443 For this analysis, the  $t\bar{t} + \text{jets}$  background, is decomposed into four components. The  $t\bar{t} + b\bar{b}$ ,  
2444 background is separated into two classes:  $t\bar{t} + b\bar{b}$  events in which both b-quarks are well separated  
2445 and energetic enough to be reconstructed, and events in which either the two b-quarks are so  
2446 close together they merge into the same jet or one of the b-quarks is too soft or forward to be  
2447 reconstructed as a jet. The latter contribution is referred to as  $t\bar{t} + b$ .

Mass	Higgs Decay	Dataset	Cross Sect.
$110 \text{ GeV}/c^2$	$H \rightarrow \text{all}$	/TTH_Inclusive_M110_8TeV_pythia6/Summer12_DR53X-PU_S10_START53_V7Av1/AODSIM	0.1887 pb
$115 \text{ GeV}/c^2$	$H \rightarrow \text{all}$	/TTH_Inclusive_M115_8TeV_pythia6/Summer12_DR53X-PU_S10_START53_V7Av1/AODSIM	0.1663 pb
$120 \text{ GeV}/c^2$	$H \rightarrow \text{all}$	/TTH_Inclusive_M120_8TeV_pythia6/Summer12_DR53X-PU_S10_START53_V7Av1/AODSIM	0.1470 pb
$122.5 \text{ GeV}/c^2$	$H \rightarrow \text{all}$	/TTH_Inclusive_M122.5_8TeV_pythia6/Summer12_DR53X-PU_S10_START53_V7Av1/AODSIM	0.1383 pb
$125 \text{ GeV}/c^2$	$H \rightarrow \text{all}$	/TTH_Inclusive_M125_8TeV_pythia6/Summer12_DR53X-PU_S10_START53_V7Av1/AODSIM	0.1302 pb
$127.5 \text{ GeV}/c^2$	$H \rightarrow \text{all}$	/TTH_Inclusive_M127.5_8TeV_pythia6/Summer12_DR53X-PU_S10_START53_V7Av1/AODSIM	0.1227 pb
$130 \text{ GeV}/c^2$	$H \rightarrow \text{all}$	/TTH_Inclusive_M130_8TeV_pythia6/Summer12_DR53X-PU_S10_START53_V7Av1/AODSIM	0.1157 pb
$135 \text{ GeV}/c^2$	$H \rightarrow \text{all}$	/TTH_Inclusive_M135_8TeV_pythia6/Summer12_DR53X-PU_S10_START53_V7Av1/AODSIM	0.1031 pb
$140 \text{ GeV}/c^2$	$H \rightarrow \text{all}$	/TTH_Inclusive_M140_8TeV_pythia6/Summer12_DR53X-PU_S10_START53_V7Av1/AODSIM	0.09207 pb
$110 \text{ GeV}/c^2$	$H \rightarrow \tau\tau$	/TTH_HToTauTau_M-110_8TeV_pythia6/Summer12_DR53X-PU_S10_START53_V7A-v1/AODSIM	0.0150 pb
$115 \text{ GeV}/c^2$	$H \rightarrow \tau\tau$	/TTH_HToTauTau_M-115_8TeV_pythia6/Summer12_DR53X-PU_S10_START53_V7A-v1/AODSIM	0.0150 pb
$120 \text{ GeV}/c^2$	$H \rightarrow \tau\tau$	/TTH_HToTauTau_M-120_8TeV_pythia6/Summer12_DR53X-PU_S10_START53_V7A-v1/AODSIM	0.0103 pb
$122.5 \text{ GeV}/c^2$	$H \rightarrow \tau\tau$	/TTH_HToTauTau_M-122.5_8TeV_pythia6/Summer12_DR53X-PU_S10_START53_V7A-v1/AODSIM	0.0093 pb
$125 \text{ GeV}/c^2$	$H \rightarrow \tau\tau$	/TTH_HToTauTau_M-125_8TeV_pythia6/Summer12_DR53X-PU_S10_START53_V7A-v1/AODSIM	0.0082 pb
$127.5 \text{ GeV}/c^2$	$H \rightarrow \tau\tau$	/TTH_HToTauTau_M-127.5_8TeV_pythia6/Summer12_DR53X-PU_S10_START53_V7A-v1/AODSIM	0.0072 pb
$130 \text{ GeV}/c^2$	$H \rightarrow \tau\tau$	/TTH_HToTauTau_M-130_8TeV_pythia6/Summer12_DR53X-PU_S10_START53_V7A-v1/AODSIM	0.0063 pb
$135 \text{ GeV}/c^2$	$H \rightarrow \tau\tau$	/TTH_HToTauTau_M-135_8TeV_pythia6/Summer12_DR53X-PU_S10_START53_V7A-v1/AODSIM	0.0046 pb
$140 \text{ GeV}/c^2$	$H \rightarrow \tau\tau$	/TTH_HToTauTau_M-140_8TeV_pythia6/Summer12_DR53X-PU_S10_START53_V7A-v1/AODSIM	0.0032 pb

Table 7.2: List of signal MC datasets and cross sections used to determine the SM expectation.

Sample	Dataset	Cross Sect.
$t\bar{t}$ + jets	/TTJets_MassiveBinDECAY_TuneZ2star_8TeVmadgraph-tauola/Summer12_DR53XPU_S10_START53_V7Av1/AODSIM	245.8 pb
$t\bar{t} \rightarrow$ all	/TTJets_MassiveBinDECAY_TuneZ2star_8TeVmadgraph-tauola/Summer12_DR53XPU_S10_START53_V7Av2/AODSIM	
$t\bar{t} \rightarrow$ jets	/TTJets_HadronicMGDecays_8TeVmadgraph/Summer12_DR53XPU_S10_START53_V7A_extv1/AODSIM	112.33 pb
$t\bar{t} \rightarrow \ell\nu + 4$ jets	/TTJets_SemiLeptMGDecays_8TeVmadgraph/Summer12_DR53XPU_S10_START53_V7A_extv1/AODSIM	107.66 pb
$t\bar{t} \rightarrow \ell\nu\ell\nu + 2$ jets	/TTJets_FullLeptMGDecays_8TeVmadgraph/Summer12_DR53XPU_S10_START53_V7Av2/AODSIM	25.81 pb
$t\bar{t} + W$	/TTWJets_8TeVmadgraph/Summer12_DR53XPU_S10_START53_V7Av1/AODSIM	0.249 pb
$t\bar{t} + Z$	/TTZJets_8TeVmadgraph_v2/Summer12_DR53XPU_S10_START53_V7Av1/AODSIM	0.208 pb
$W +$ jets	/WJetsToLNu_TuneZ2Star_8TeVmadgraphtarball/Summer12_PU_S7_START52_V9v1/AODSIM	36257.2 pb
$W + 1$ jet	/W1JetsToLNu_TuneZ2Star_8TeVmadgraph/Summer12_DR53XPU_S10_START53_V7Av1/AODSIM	6440.4 pb
$W + 2$ jets	/W2JetsToLNu_TuneZ2Star_8TeVmadgraph/Summer12_DR53XPU_S10_START53_V7Av1/AODSIM	2087.2 pb
$W + 3$ jets	/W3JetsToLNu_TuneZ2Star_8TeVmadgraph/Summer12_DR53XPU_S10_START53_V7Av1/AODSIM	619.0 pb
$W + 4$ jets	/W4JetsToLNu_TuneZ2Star_8TeVmadgraph/Summer12_DR53XPU_S10_START53_V7Av1/AODSIM	255.2 pb
$Z/\gamma^* +$ jets		
$10 \text{ GeV}/c^2 < M_{\ell\ell} < 50 \text{ GeV}/c^2$	/DYJetsToLL_M-10To50_TuneZ2Star_8TeV-madgraph/Summer12_DR53X-PU_S10_START53_V7A-v1/AODSIM	14702 pb
$M_{\ell\ell} > 50 \text{ GeV}/c^2$	/DYJetsToLL_M-50_TuneZ2Star_8TeV-madgraphtarball/Summer12_DR53X-PU_S10_START53_V7A-v1/AODSIM	3505.7 pb
$Z/\gamma^* + 1$ jet	/DY1JetsToLL_M-50_TuneZ2Star_8TeV-madgraph/Summer12_DR53X-PU_S10_START53_V7A-v1/AODSIM	666.7 pb
$Z/\gamma^* + 2$ jets	/DY2JetsToLL_M-50_TuneZ2Star_8TeV-madgraph/Summer12_DR53X-PU_S10_START53_V7A-v1/AODSIM	215.1 pb
$Z/\gamma^* + 3$ jets	/DY3JetsToLL_M-50_TuneZ2Star_8TeV-madgraph/Summer12_DR53X-PU_S10_START53_V7A-v1/AODSIM	66.07 pb
$Z/\gamma^* + 4$ jets	/DY4JetsToLL_M-50_TuneZ2Star_8TeV-madgraph/Summer12_DR53X-PU_S10_START53_V7A-v1/AODSIM	27.38 pb
Single $t$		
$s$ -channel	/T_s-channel_TuneZ2star_8TeV-powheg-tauola/Summer12_DR53X-PU_S10_START53_V7A-v1/AODSIM	3.79 pb
$t$ -channel	/T_t-channel_TuneZ2star_8TeV-powheg-tauola/Summer12_DR53X-PU_S10_START53_V7A-v1/AODSIM	56.4 pb
$tW$	/T_tW-channel-DR_TuneZ2star_8TeV-powheg-tauola/Summer12_DR53X-PU_S10_START53_V7A-v1/AODSIM	11.1 pb
Single $\bar{t}$		
$s$ -channel	/Tbar_s-channel_TuneZ2star_8TeV-powheg-tauola/Summer12_DR53X-PU_S10_START53_V7A-v1/AODSIM	1.76 pb
$t$ -channel	/Tbar_t-channel_TuneZ2star_8TeV-powheg-tauola/Summer12_DR53X-PU_S10_START53_V7A-v1/AODSIM	30.7 pb
$tW$	/Tbar_tW-channel-DR_TuneZ2star_8TeV-powheg-tauola/Summer12_DR53X-PU_S10_START53_V7A-v1/AODSIM	11.1 pb
$WW$	/WW_TuneZ2star_8TeV_pythia6_tauola/Summer12_DR53X-PU_S10_START53_V7A-v1/AODSIM	54.8 pb
$WZ$	/WZ_TuneZ2star_8TeV_pythia6_tauola/Summer12_DR53X-PU_S10_START53_V7A-v1/AODSIM	32.3 pb
$ZZ$	/ZZ_TuneZ2star_8TeV_pythia6_tauola/Summer12_DR53X-PU_S10_START53_V7A-v1/AODSIM	7.7 pb

Table 7.3: List of background MC datasets and cross sections used for normalization.

### 2448 7.1.4 MC pileup reweighting

2449 As discussed in section 6.1.4, the large instantaneous luminosities provided by the LHC result in  
 2450 the overlap of multiple proton-proton collisions during a single read-out window. These "pileup  
 2451 events" affect many aspects of the reconstruction, including lepton isolation and jet energy  
 2452 resolution, thus the simulated samples must accurately reproduce these effects.

2453 As with the last analysis, for the simulation, it is known how many additional interactions were  
 2454 added to every generated event. For the data, the number of pileup interactions for each unit of  
 2455 time depends on the instantaneous luminosity for each bunch pair and the total inelastic cross  
 2456 section,  $\sigma_{inelastic}$ . Empirically, it was found that  $\sigma_{inelastic} = 69.4 \text{ mb}$  described the data well.  
 2457 Changing of this value by  $\pm 7\%$  are used for the  $\pm 1\sigma$  variations for the associated systematic  
 2458 uncertainty. Figure 7.1 shows the number of reconstructed vertices for data and for the  $t\bar{t}$   
 2459 MC sample, both before and after pileup reweighting. After reweighting, the data and MC  
 2460 distributions agree very well, indicating that the pileup reweighting is working as expected.

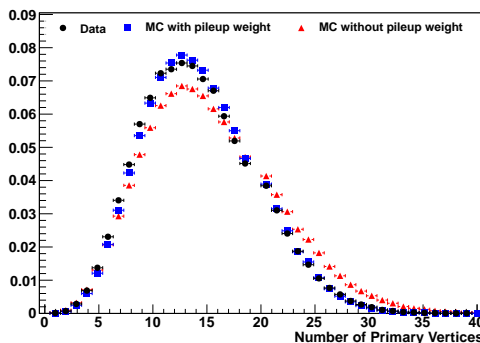


Figure 7.1: Comparison of number of reconstructed vertices for data (black) and the sum of all background MC samples before (red) and after (blue) pileup reweighting. After pileup reweighting, the MC matches the data well.

### 2461 7.1.5 Top $p_T$ Reweighting

2462 It has been observed that the spectra of leptons and jets produced from top quark decays have  
 2463 softer  $p_T$  distribution than are predicted by the Monte Carlo. Investigations have show that  
 2464 the  $p_T$  spectra of leptons and jets is softer than data and have traced this mismodeling to the  
 2465 top quark  $p_T$  distribution [100, 101]. Measurements of the differential cross section for top pair  
 2466 production as a function of the top quark  $p_T$ , have allowed for the creation of correction factors  
 2467 for this effect. These predictions of the  $t\bar{t}$  + jets Monte Carlo are also more consistent with  
 2468 calculations done at approximate NNLO accuracy. This correction factor replaces the additional  
 2469 pileup reweighting factor based on the  $H_T$  distribution, binned by number of reconstructed  
 2470 vertices.

2471 The scale factor used to correct the Madgraph top quark  $p_T$  distributions are shown in figure  
 2472 7.2. The associated uncertainty is a band shown in green, and corresponds to no correction factor  
 2473 for the down variation, and a doubling of the correction factor for the up variation. The scale  
 2474 factors are taken from a polynomial of the form:

$$SF = 1.18246 + 2.10061 \times 10^{-6} p_T (p_T - 2 \times 463.312)$$

2475 For  $p_T > 463.312 \text{ GeV}/c$ , a constant scale factor of 0.732 is used.

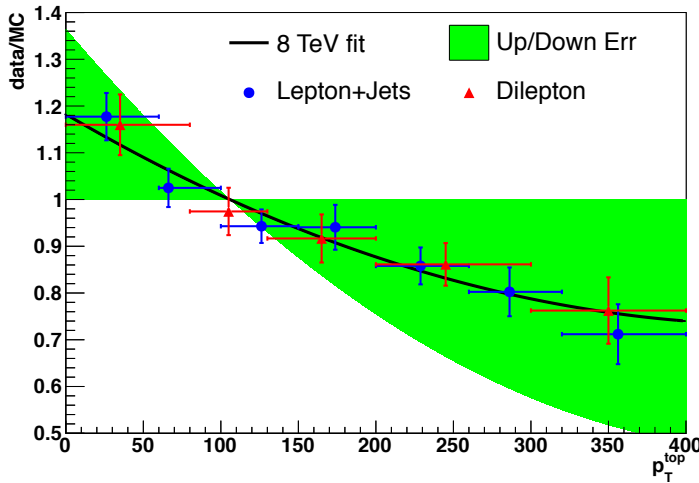


Figure 7.2: The scale factors from top differential cross section group, the fitting as well as the  $\pm 1\sigma$  variations.

2476 The top  $p_T$  scale factor improves the agreement between data and Monte Carlo. Figure 7.3  
 2477 compares the leading jet  $p_T$  distributions before and after reweighting. Before the correction,  
 2478 the leading jet  $p_T$  ratio plot forms a line with a slope, which is removed after the correction.

## 2479 7.2 Event Selection

2480 This section defines the common physics objects and event selection requirements. Events are  
 2481 required to pass quality filters, ensuring optimal operation of electronics and reconstruction, as  
 2482 described in section 6.2.1. The same lepton selection is used that was employed in the previous  
 2483 analysis, with events being selected by triggers described in section ???. Leptons are classified  
 2484 into two categories, tight and loose, defined for muons in section 6.2.3 and for electrons in 6.2.4.  
 2485 For this analysis, exactly one tight muon or exactly one tight electron is required and events  
 2486 with any additional loose leptons are rejected. Lepton reconstruction efficiency scale factors are  
 2487 discussed in 6.2.5. The selection for jets is also the same, with the same procedure for correcting

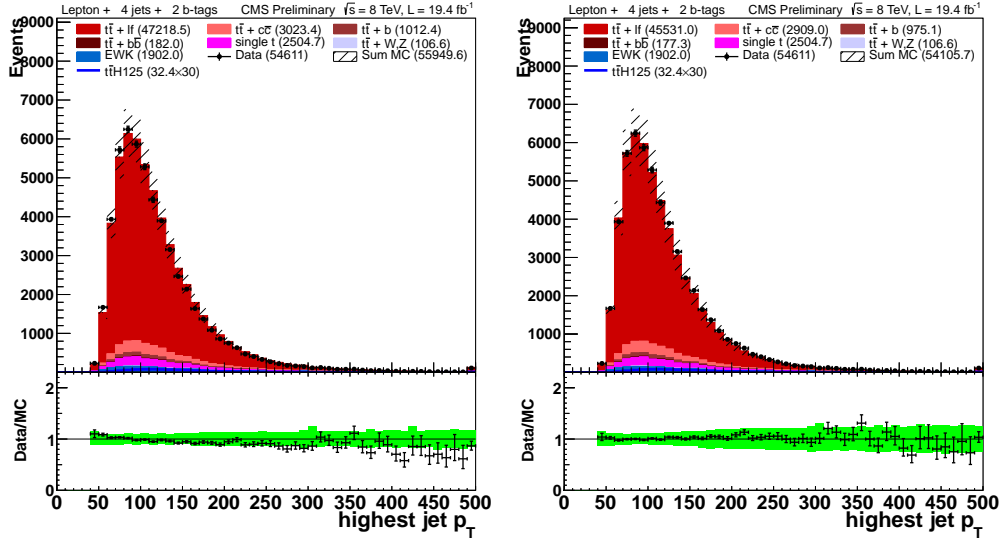


Figure 7.3: Leading jet  $p_T$  distribution for 8 TeV lepton plus jet events with  $\geq 4$  jets and  $\geq 2$  tags. The left-hand plot shows the distribution before top  $p_T$  reweighting. The right-hand plot shows the distribution after top  $p_T$  reweighting. Note that the ratio in the right-hand plot is flatter than the left-hand plot.

2488 the energy as in section 6.2.6. The only significant change to the event selection comes from the  
 2489  $b$ -tag scale factors used to calibrate the differences between efficiency in data and simulation for  
 2490 the CSV algorithm.

### 2491 7.2.1 $b$ -tag discriminant reweighting

2492 As described in section 6.2.7, the algorithm used to tag jets as coming from a  $b$ -quark, is the  
 2493 Combined Secondary Vertex (CSV) algorithm. Differences have been observed in the measured  
 2494 efficiency for  $b$ -tagging jets between data and simulation [87]. To account for these efficiency  
 2495 differences, a scale factor to correct the MC  $b$ -tagging efficiency. Moreover, we found that the  
 2496 CSV distribution of MC doesn't match that of data, there making it necessary to correct the  
 2497 shape of the discriminant distribution as well.

2498 A  $b$ -tag CSV reweighting method has been developed to address not only the difference in  
 2499 efficiency, but the difference in the shape of the discriminant distribution as well [102]. The  
 2500 method is based on a "tag and probe" approach. Events with two leptons, and exactly two jets  
 2501 are initially selected. One jet is required to pass a "tight" working point, characterised by a CSV  
 2502 value with  $\sim 90\%$  efficiency and  $\leq 1\%$  mistag rate. Then, the other jet is required to pass the  
 2503 analysis working point to assess the efficiency there. The results are binned by  $p_T$ ,  $\eta$ , jet flavour  
 2504 and CSV value.

2505 For MC the truth is available to assess the efficiency. For data, the full 8 TeV DoubleMu,  
 2506 DoubleElectron and MuEG datasets taken in 2012 are used. The scale factors for heavy flavor

2507 jets were derived in the dilepton channel, using a  $t\bar{t}$  enriched control sample dominated by events  
 2508 which have two  $b$  flavor jets from the top pair decay. The scale factors for light flavor jets in  
 2509 the dilepton channel, using a control sample dominated by  $Z+jets$  events where there are two  
 2510 light flavor jets. The scale factors for light flavor jets will account for the mis-tag efficiency  
 2511 discrepancy between data and MC. For events with one jet passing the tag requirements, the  
 2512 CSV distribution for the probe jet in given  $p_t$  and  $\eta$  bins. The total MC yields are normalized  
 2513 to the data yields. In order to account for heavy or light flavor contamination, the MC is divided  
 2514 into samples of heavy flavor and light flavor components and then non-relevant part from data  
 2515 is subtracted. The scale factor is then given by the ratio of subtracted data CSV distribution  
 2516 and the relevant MC CSV distribution, as shown below:

$$SF(CSV, p_t, \eta) = \frac{Data - MC_A}{MC_B} \quad (7.1)$$

2517 where A, B = heavy flavor component or light flavor component.

2518 Unlike the last analysis, where scale factors were applied to adjust the value of the CSV  
 2519 distribution, correction factor for this analysis is an event-by-event weight. If the jet is a  $b$  flavor  
 2520 jet, a heavy flavor scale factor is assigned to it; if it is a  $c$  flavor jet, a flat scale factor of 1.0 is  
 2521 applied, with the same uncertainty as a  $b$  flavor jet would receive; otherwise, if it is a light flavor  
 2522 jet, a light flavor scale factor is assigned. The total scale factor for the event is the product of  
 2523 all the scale factors of the jets:

$$SF_{total} = \prod_i^{N_{jets}} SF_{jet_i} = SF_{jet_1} \cdot SF_{jet_2} \cdot \dots \quad (7.2)$$

### 2524 7.2.2 Lepton + Jets Selection

2525 As with the previous analysis, the final selection requires events have exactly one tight lepton  
 2526 ( $e$  or  $\mu$ ), and at least four jets. Events with any additional loose or tight leptons are vetoed so  
 2527 this analysis can later be combined with a diLepton final state, without double counting events.  
 2528 Additionally, each event must have at least three jets with  $p_T > 40$  GeV/c.

2529 As before, events are further categorized by the reconstructed jet, and  $b$ -tagged jet multi-  
 2530 plicities:

- 2531 •  $\geq 6$  jets,  $=2$   $b$ -tags: At least 6 jets, 2 of which are  $b$ -tagged
- 2532 •  $=4$  jets,  $=3$   $b$ -tags: Exactly 4 jets, 3 of which are  $b$ -tagged
- 2533 •  $=5$  jets,  $=3$   $b$ -tags: Exactly 5 jets, 3 of which are  $b$ -tagged
- 2534 •  $\geq 6$  jets,  $=3$   $b$ -tags: At least 6 jets, 3 of which are  $b$ -tagged

2535 • ==4 jets, ==4 b-tags: Exactly 4 jets, 4 of which are b-tagged

2536 • ==5 jets, ==4 b-tags: Exactly 5 jets, 4 of which are b-tagged

2537 •  $\geq 6$  jets,  $\geq 4$  b-tags: At least 6 jets, with at least 4 of which are b-tagged

2538 Table 7.4 gives the event yield for MC backgrounds, both the total and each contribution,  
 2539 the expected event yield for signal  $t\bar{t}H$  ( $m_H = 125 \text{ GeV}/c^2$ ), and the data observed in each  
 2540 category. Figure 7.4 shows the data/MC comparison for the number of jets and the number of  
 2541 tagged jets distributions for events with one lepton ( $e$  or  $\mu$ ),  $\geq 4$  jets and  $\geq 2$  b-tags, it also  
 2542 includes a plot showing the event yields for data and each MC background in each category.

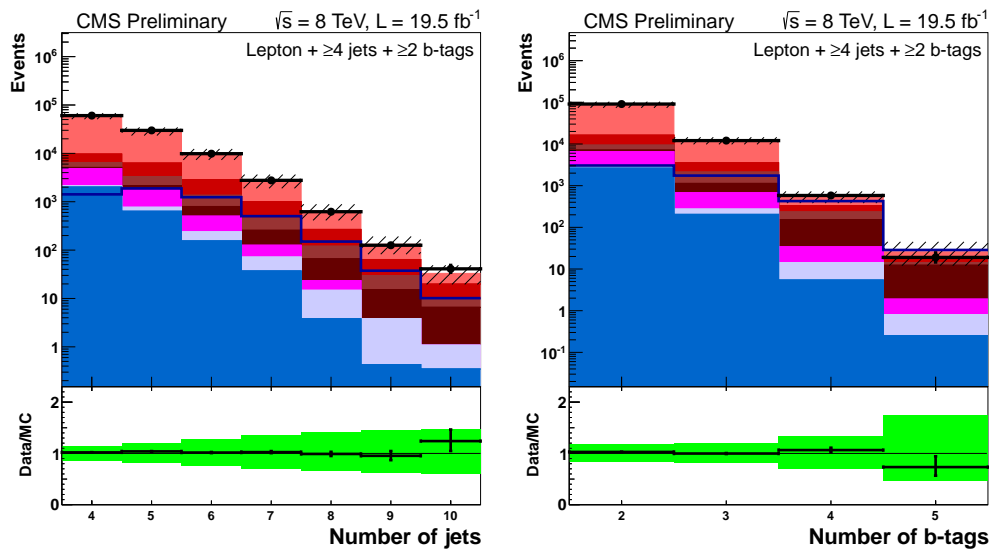


Figure 7.4: Comparison of yields for the different categories (top), number of jets (bottom left), and number of tagged jets (bottom right) in data and Monte Carlo for events with one lepton  $\mu$  or  $e$ ,  $\geq 4$  jets and  $\geq 2$  tags.

	$\geq 6$ jets 2 tags	4 jets 3 tags	5 jets 3 tags	$\geq 6$ jets 3 tags	4 jets 4 tags	5 jets $\geq 4$ tags	$\geq 6$ jets $\geq 4$ tags
$t\bar{t}H(125)$	$33.4 \pm 8.1$	$14.0 \pm 3.0$	$21.1 \pm 4.5$	$23.1 \pm 5.5$	$1.8 \pm 0.5$	$5.2 \pm 1.4$	$8.3 \pm 2.3$
$t\bar{t}+lf$	$7650 \pm 2000$	$4710 \pm 820$	$2610 \pm 530$	$1260 \pm 340$	$74 \pm 30$	$79 \pm 34$	$71 \pm 36$
$t\bar{t}+b$	$530 \pm 300$	$350 \pm 190$	$360 \pm 200$	$280 \pm 160$	$21 \pm 12$	$29 \pm 17$	$33 \pm 20$
$t\bar{t}+b\bar{b}$	$220 \pm 120$	$99 \pm 52$	$158 \pm 85$	$200 \pm 110$	$13.1 \pm 7.3$	$38 \pm 21$	$78 \pm 47$
$t\bar{t}+c\bar{c}$	$1710 \pm 1110$	$440 \pm 230$	$520 \pm 290$	$470 \pm 280$	$19 \pm 11$	$32 \pm 18$	$52 \pm 31$
$t\bar{t}V$	$99 \pm 27$	$16.2 \pm 3.8$	$23.9 \pm 5.7$	$28.8 \pm 7.4$	$1.1 \pm 0.4$	$2.5 \pm 0.7$	$5.8 \pm 1.8$
Single $t$	$264 \pm 54$	$235 \pm 41$	$116 \pm 22$	$55 \pm 14$	$3.4 \pm 1.6$	$10.3 \pm 5.3$	$7.3 \pm 3.1$
$V+jets$	$160 \pm 110$	$122 \pm 95$	$44 \pm 38$	$29 \pm 27$	$2.1 \pm 2.4$	$1.9 \pm 1.7$	$1.2 \pm 1.3$
Diboson	$5.9 \pm 1.6$	$6.3 \pm 1.4$	$2.4 \pm 0.7$	$1.0 \pm 0.4$	$0.3 \pm 0.2$	$0.1 \pm 0.1$	$0.2 \pm 0.1$
Total bkg	$10630 \pm 2790$	$5970 \pm 1060$	$3830 \pm 790$	$2310 \pm 620$	$133 \pm 44$	$193 \pm 62$	$249 \pm 90$
Data	10724	5667	3983	2426	122	219	260

Table 7.4: Observed data event yields, expected event yields in  $19.5 \text{ fb}^{-1}$  for signal and backgrounds in the lepton+jets channel.

## 2543 7.3 Multivariate Analysis

2544 The MVA technique used to analyze the full 8 TeV dataset is a Boosted Decision Tree (BDT).  
 2545 Each jet/tag category is trained with half of the simulated  $t\bar{t}H$  events for signal, and half of  
 2546 the simulated  $t\bar{t} + jets$  events as background. The top 10 variables, ranked with the separation  
 2547 figure of merit given in equation 6.10, are used as input variables. The BDT distribution of the  
 2548 discriminant is then used for signal extraction and limit setting.

### 2549 7.3.1 Boosted Decision Tree Overview

2550 A Boosted Decision Tree (BDT) is a code structure that makes a sequence of binary decisions  
 2551 to classify events as either signal-like or background-like [89]. For this analysis, the BDT uses  
 2552 10 input variables for each jet/tag category. The BDT looks at the distribution of events for  
 2553 signal and background, with 40 bins with a maximum and minimum value determined by the  
 2554 the largest and smallest values respectively for either the signal or the background. Out of these  
 2555 10 variables, the BDT selects the variable which maximizes the Gini Index, which is given by  
 2556 the equation:

$$GiniIndex = p \times (1 - p) \quad (7.3)$$

2557 where the purity,  $p = s/b$ , is the ratio of the integral number of signal,  $s$ , events and background,  
 2558  $b$ , events above or below the cut value chosen by the BDT. This effectively tries to find a cut on a  
 2559 variable that maximizes the amount signal in sample afterwards, creating a background-like set  
 2560 of events, and a signal-like set of events. After the first cut is chosen, the distributions for each  
 2561 of the variables above and below the cut value are re-examined. A second cut on a variable,  
 2562 at a point that maximizes the Gini Index is found, for each of the signal and background-like  
 2563 regions formed by the first cut. This process continues for a user-defined number of cuts. Since  
 2564 the input events are known to be singal-like or background-like, the purity of the final region  
 2565 that an event is classified as is used as the output for this set of decisions, known as a decision  
 2566 tree. Figure 7.5 shows a diagram of the general process.

2567 The BDT in this analysis uses 5 cuts for a single tree. The reason for using a small number, is  
 2568 that the BDT employs a process known as "boosting" to enhance its discriminating power.

2569 Boosting is the process of using multiple, or a forest, of individual decision trees to cast a  
 2570 majority vote for the decision to classify the event as signal-like or background-like [89]. Events  
 2571 from the training sample, which were misclassified, are given a larger weight, making their  
 2572 contribution to the distributions of the input variable more prominent, making it more likely  
 2573 for the next decision tree to classify the event correctly. The final discriminant,  $F(\hat{x}, P)$ , of the

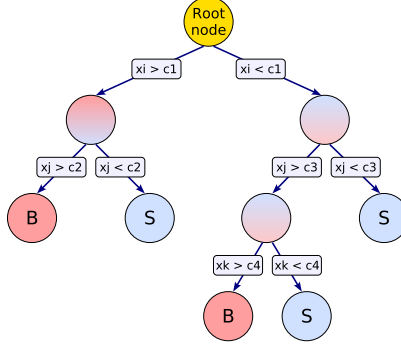


Figure 7.5: Example of a decision tree, which chooses a set of variables to cut on, in order to produce a region of events with high signal purity

2574 forest of decision trees is given by:

$$F(\hat{x}, P) = \sum_{m=0}^M \beta_m f(x; a_m); \quad P \in (\beta_m; a_m)_0^M \quad (7.4)$$

2575 where  $P$  is the set of parameter, whose values are optimized to create an optimized classification  
2576 decision. For  $M$  trees in the forest,  $\beta_m$  is the weight for the output of a single decision tree,  
2577  $f(x; a_m)$ , which is the purity,  $s/b$  of the final region of the tree an individual event is classified  
2578 into. The set of input variables for a single decision tree,  $m$ , is denoted by  $a_m$ .

2579 This analysis uses the "Gradient" method of boosting [89]. After the first tree is has been  
2580 built, the "loss function",  $L(F, y)$ , is calculated with the function:

$$L(F, y) = \ln \left( 1 + e^{-2F(\hat{x})y} \right) \quad (7.5)$$

2581 where  $y$  is the true value of the classification of the event (1 for signal, 0 for background).  
2582 This function has a minimum value when all of the events have been classified correctly. The  
2583 loss function is then minimized by varying the set of parameters,  $P \in (\beta_m; a_m)_0^M$ , using the  
2584 steepest-descent method. A random selection of events are reweighted, and the loss-function is  
2585 re-calculated. The error rate of classifying events for the previous tree is used to calculate the  
2586 new weight,  $\alpha$ , of events for the next tree:

$$\alpha = \frac{1 - err}{err} \quad (7.6)$$

2587 where  $err$  is the error rate. After events are re-weighted, a new decision tree is created and the  
2588 process is repeated, iteratively minimizing the loss function until a desired set of decision trees  
2589 are created. This analysis uses a forest of 100 decision trees to separate the  $t\bar{t}H$  signal from the  
2590  $t\bar{t} + jets$  background.

Overtaining was checked in a similar procedure that was used in the last analysis. Half the events for the signal and background samples are used to train the BDT, the other half are used to test it. The response to the BDT is calculated for both the testing and training sample, and the Kolomogrov-Smirnoff statistic is used as a figure of merit to judge the compatibility of the two samples. As seen in figure 7.6, there are no significant deviations between the testing and training samples, implying that no overtraining has occurred.

### 7.3.2 MVA Input Variables, Data to Monte Carlo Comparisons

The set of 10 input variables for each jet/tag category were chosen through their ranking using the separation figure of merit given in equation 6.10. The categories most sensitive to signal, 5 jets,  $\geq 4$   $b$ -tags;  $\geq 6$  jets,  $\geq 3$   $b$ -tags; and  $\geq 6$  jets,  $\geq 4$   $b$ -tags all include a variable, which is the output discriminant of a dedicated BDT trained to separate  $t\bar{t}H$  signal from  $t\bar{t} + b\bar{b}$  background. Table 7.5 gives a description of each of the input variables used. Table 7.6 describes which variables are used in each jet/tag category, and table 7.7 lists the variables used in the dedicated  $t\bar{t}H$ ,  $t\bar{t} + b\bar{b}$  BDT.

The modeling of the input variables is compared against data for each of the jet/tag diagrams in the the following figures:

- $\geq 6$  jets,  $\geq 2$   $b$ -tags: Figure 7.7
- $\geq 4$  jets,  $\geq 3$   $b$ -tags: Figure 7.8
- $\geq 5$  jets,  $\geq 3$   $b$ -tags: Figure 7.9
- $\geq 6$  jets,  $\geq 3$   $b$ -tags: Figure 7.10, and Figure 7.11
- $\geq 4$  jets,  $\geq 4$   $b$ -tags: Figure 7.12
- $\geq 5$  jets,  $\geq 4$   $b$ -tags: Figure 7.13, and Figure 7.14
- $\geq 6$  jets,  $\geq 4$   $b$ -tags: Figure 7.15, and Figure 7.16

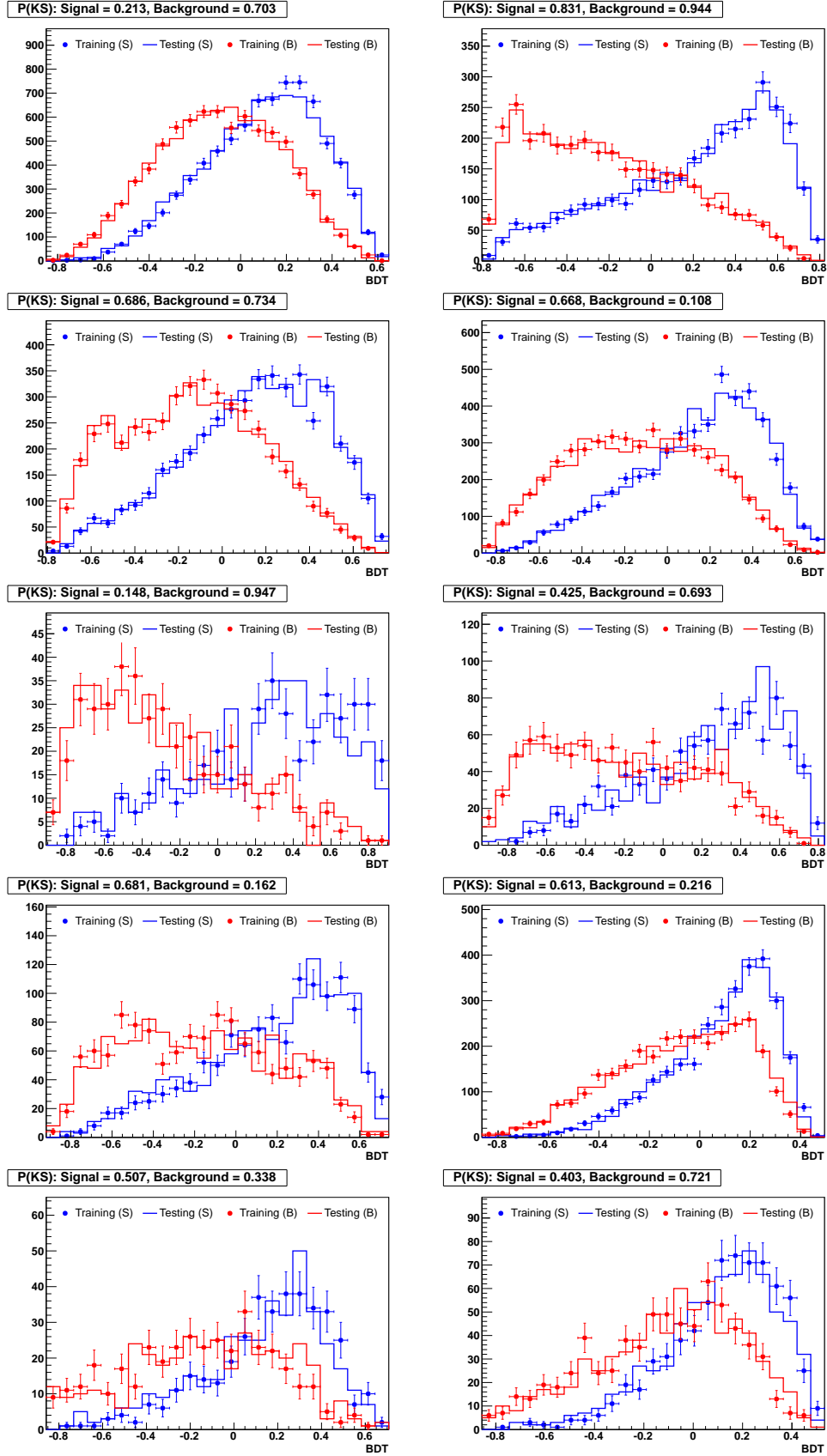


Figure 7.6: Comparisons of the testing and training samples used to optimize the BDT weights for each jet/tag category

Table 7.5: Event variables used in dilepton and lepton+jets BDT training and their descriptions.

abs $\Delta\eta$ (leptonic top, bb)	Delta-R between the leptonic top reconstructed by the best higgs mass algorithm and the $b$ -jet pair chosen by the algorithm
abs $\Delta\eta$ (hadronic top, bb)	Delta-R between the hadronic top reconstructed by the best higgs mass algorithm and the $b$ -jet pair chosen by the algorithm
aplanarity	Event shape variable equal to $\frac{3}{2}(\lambda_3)$ , where $\lambda_3$ is the third eigenvalue of the sphericity tensor as described in [?].
ave CSV (tags/non-tags)	Average $b$ -tag discriminant value for $b$ -tagged/non- $b$ -tagged jets
ave $\Delta R$ (tag,tag)	Average $\Delta R$ between $b$ -tagged jets
best higgs mass	A minimum-chi-squared fit to event kinematics is used to select two $b$ -tagged jets as top-decay products. Of the remaining $b$ -tags, the invariant mass of the two with highest $E_t$ is saved.
best $\Delta R(b,b)$	The $\Delta R$ between the two $b$ -jets chosen by the best higgs mass algorithm
closest tagged dijet mass	The invariant mass of the two $b$ -tagged jets that are closest in $\Delta R$
dev from ave CSV (tags)	The square of the difference between the $b$ -tag discriminant value of a given $b$ -tagged jet and the average $b$ -tag discriminant value among $b$ -tagged jets, summed over all $b$ -tagged jets
highest CSV (tags)	Highest $b$ -tag discriminant value among $b$ -tagged jets
$H_0, H_1, H_2, H_3$	The first few Fox-Wolfram moments [?] (event shape variables)
HT	Scalar sum of transverse momentum for all jets with $p_T > 30 \text{ GeV}/c$
$\sum p_T(\text{jets,leptons,MET})$	The sum of the $p_T$ of all jets, leptons, and MET
$\sum p_T(\text{jets,leptons})$	The sum of the $p_T$ of all jets, leptons
jet 1, 2, 3, 4 $p_T$	The transverse momentum of a given jet, where the jet numbers correspond to rank by $p_T$
lowest CSV (tags)	Lowest $b$ -tag discriminant value among $b$ -tagged jets
mass(lepton,jet,MET)	The invariant mass of the 4-vector sum of all jets, leptons, and MET
mass(lepton,closest tag)	The invariant mass of the lepton and the closest $b$ -tagged jet in $\Delta R$
max $\Delta\eta$ (jet, ave jet $\eta$ )	max difference between jet eta and avg eta between jets
max $\Delta\eta$ (tag, ave jet $\eta$ )	max difference between tag eta and avg eta between jets
max $\Delta\eta$ (tag, ave tag $\eta$ )	max difference between tag eta and avg eta between tags
median inv. mass (tag pairs)	median invariant mass of all combinations of $b$ -tag pairs
M3	The invariant mass of the 3-jet system with the largest transverse momentum.
MHT	Vector sum of transverse momentum for all jets with $p_T > 30 \text{ GeV}/c$
MET	Missing transverse energy
min $\Delta R$ (lepton,jet)	The $\Delta R$ between the lepton and the closest jet (LJ channel)
min $\Delta R$ (tag,tag)	The $\Delta R$ between the two closest $b$ -tagged jets
min $\Delta R$ (jet,jet)	The $\Delta R$ between the two closest jets
$\sqrt{\Delta\eta(t^{lep},bb) \times \Delta\eta(t^{had},bb)}$	square root of the product of abs $\Delta\eta$ (leptonic top, bb) and abs $\Delta\eta$ (hadronic top, bb)
second-highest CSV (tags)	Second-highest $b$ -tag discriminant value among $b$ -tagged jets
sphericity	Event shape variable equal to $\frac{3}{2}(\lambda_2 + \lambda_3)$ , where $\lambda_2$ and $\lambda_3$ are the second and third eigenvalues of the sphericity tensor as described in [?]
$(\Sigma \text{ jet } p_T)/(\Sigma \text{ jet E})$	The ratio of the sum of the transverse momentum of all jets and the sum of the energy of all jets
tagged dijet mass closest to 125 $t\bar{t}b\bar{b}/t\bar{t}H$ BDT	The invariant mass of the $b$ -tagged pair closest to $125 \text{ GeV}/c^2$ BDT used to discriminate between $t\bar{t}b\bar{b}$ and $t\bar{t}H$ in the LJ $\geq 6$ jets, $\geq 4$ tags, $\geq 6$ jets + 3 tags, and 5 jets + $\geq 4$ tags categories. See text for description and table 7.7 for list of variables.

4 jets, 3 tags	4 jets, 4 tags	
jet 1 $p_T$ jet 2 $p_T$ jet 3 $p_T$ jet 4 $p_T$ M3 $\sum p_T(\text{jets,lepton,MET})$ HT lowest CSV (tags) MHT MET	jet 1 $p_T$ jet 2 $p_T$ jet 4 $p_T$ HT $\sum p_T(\text{jets,lepton,MET})$ M3 ave CSV (tags) second-highest CSV (tags) third-highest CSV (tags) lowest CSV (tags)	
5 jets, 3 tags	5 jets, $\geq 4$ tags	
jet 1 $p_T$ jet 2 $p_T$ jet 3 $p_T$ jet 4 $p_T$ $\sum p_T(\text{jets,lepton,MET})$ $(\Sigma \text{jet } p_T)/(\Sigma \text{jet E})$ HT ave CSV (tags) third-highest CSV (tags) fourth-highest CSV (jets)	max $\Delta\eta$ (tag, ave jet $\eta$ ) $\sum p_T(\text{jets,lepton,MET})$ $(\Sigma \text{jet } p_T)/(\Sigma \text{jet E})$ ave $\Delta R(\text{tag,tag})$ ave CSV (tags) dev from ave CSV (tags) second-highest CSV (tags) third-highest CSV (tags) lowest CSV (tags) ttbb/ttH BDT	
$\geq 6$ jets, 2 tags	$\geq 6$ jets, 3 tags	
$\sum p_T(\text{jets,lepton,MET})$ HT mass(lepton,closest tag) max $\Delta\eta$ (jet, ave jet $\eta$ ) min $\Delta R(\text{lepton,jet})$ $H_2$ sphericity $(\Sigma \text{jet } p_T)/(\Sigma \text{jet E})$ third-highest CSV (jets) fourth-highest CSV (jets)	$H_0$ sphericity $(\Sigma \text{jet } p_T)/(\Sigma \text{jet E})$ max $\Delta\eta$ (jet, ave jet $\eta$ ) $\sum p_T(\text{jets,lepton,MET})$ ave CSV (tags) second-highest CSV (tags) third-highest CSV (tags) fourth-highest CSV (jets) ttbb/ttH BDT	$(\Sigma \text{jet } p_T)/(\Sigma \text{jet E})$ ave $\Delta R(\text{tag,tag})$ product( $\Delta\eta(\text{leptonic top, bb}), \Delta\eta(\text{hadronic top, bb})$ ) closest tag mass max $\Delta\eta$ (tag, ave tag $\eta$ ) ave CSV (tags) third-highest CSV (tags) fourth-highest CSV (tags) best higgs mass ttbb/ttH BDT

Table 7.6: BDT input variable assignments for the lepton+jets categories.

5 jets, $\geq 4$ tags	$\geq 6$ jets, 3 tags	$\geq 6$ jets, $\geq 4$ tags
ave $\Delta R(\text{tag,tag})$ max $\Delta\eta$ (tag, ave tag $\eta$ ) $(\Sigma \text{jet } p_T)/(\Sigma \text{jet E})$ tagged dijet mass closest to 125 $H_1$ $H_3$ $\sum p_T(\text{jets,lepton,MET})$ fourth-highest CSV (tags) aplanarity MET	tagged dijet mass closest to 125 $(\Sigma \text{jet } p_T)/(\Sigma \text{jet E})$ $\sqrt{\Delta\eta(t^{lep}, bb) \times \Delta\eta(t^{had}, bb)}$ $H_1$ $H_3$ M3 max $\Delta\eta$ (tag, ave tag $\eta$ ) max $\Delta\eta$ (tag, ave jet $\eta$ ) max $\Delta\eta$ (jet, ave jet $\eta$ ) abs $\Delta\eta$ (hadronic top, bb) abs $\Delta\eta$ (leptonic top, bb) sphericity aplanarity min $\Delta R(\text{tag,tag})$ jet 3 $p_T$	$H_3$ ave $\Delta R(\text{tag,tag})$ closest tagged dijet mass sphericity max $\Delta\eta$ (tag, ave jet $\eta$ ) max $\Delta\eta$ (tag, ave tag $\eta$ ) mass(lepton,jet,MET) $(\Sigma \text{jet } p_T)/(\Sigma \text{jet E})$ abs $\Delta\eta$ (leptonic top, bb) abs $\Delta\eta$ (hadronic top, bb) $\sqrt{\Delta\eta(t^{lep}, bb) \times \Delta\eta(t^{had}, bb)}$ ave CSV (tags) best $\Delta R(\text{b,b})$ best higgs mass median inv. mass (tag pairs)

Table 7.7: List of variables used as inputs in each of the ttbb/ttH BDTs. See table 7.5 for definitions.

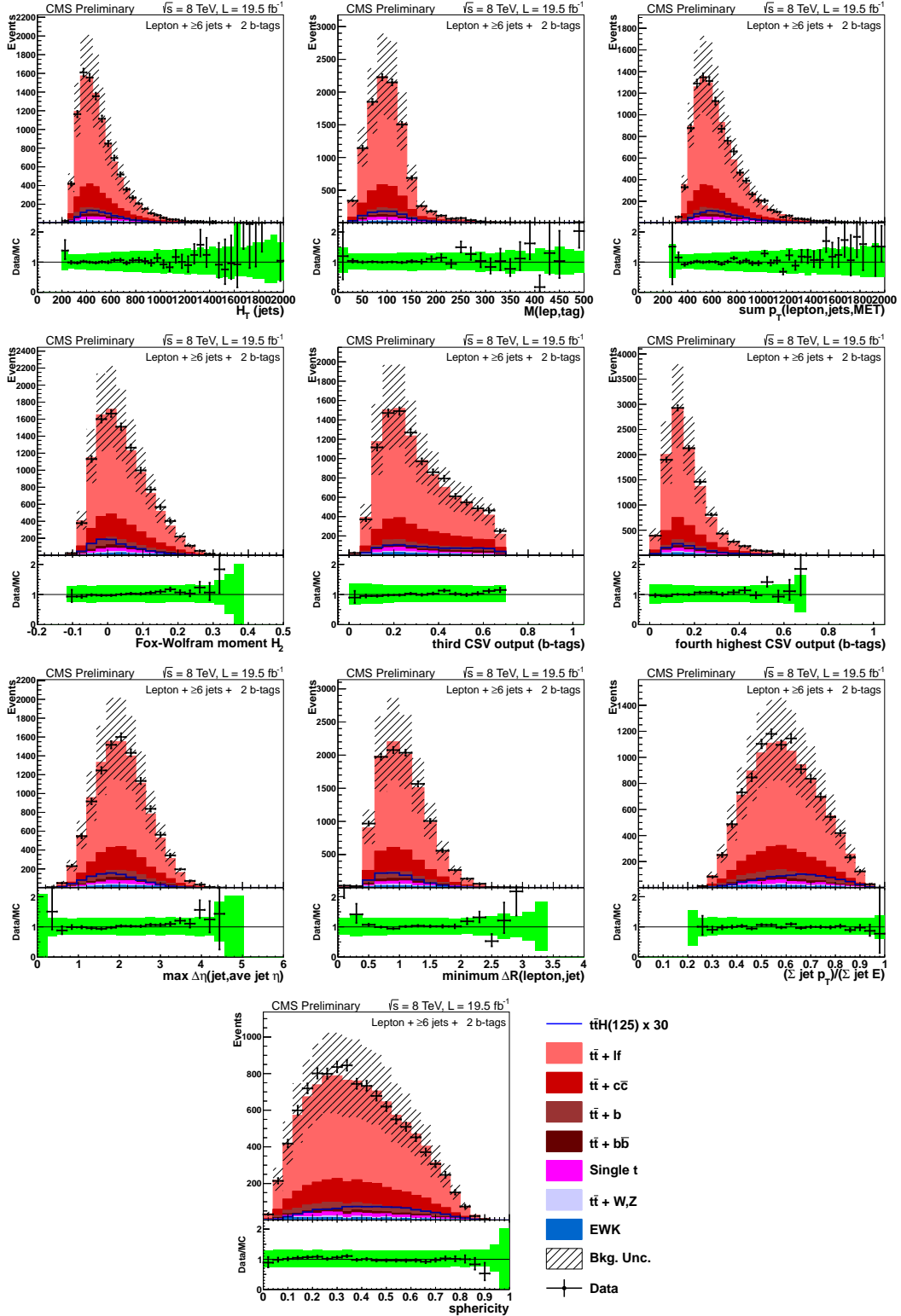


Figure 7.7: Data/MC comparisons for events with one lepton and  $\geq 6$  jets + 2 b-tags. The uncertainty band includes statistical and systematic uncertainties that affect both the rate and shape of the background distributions.

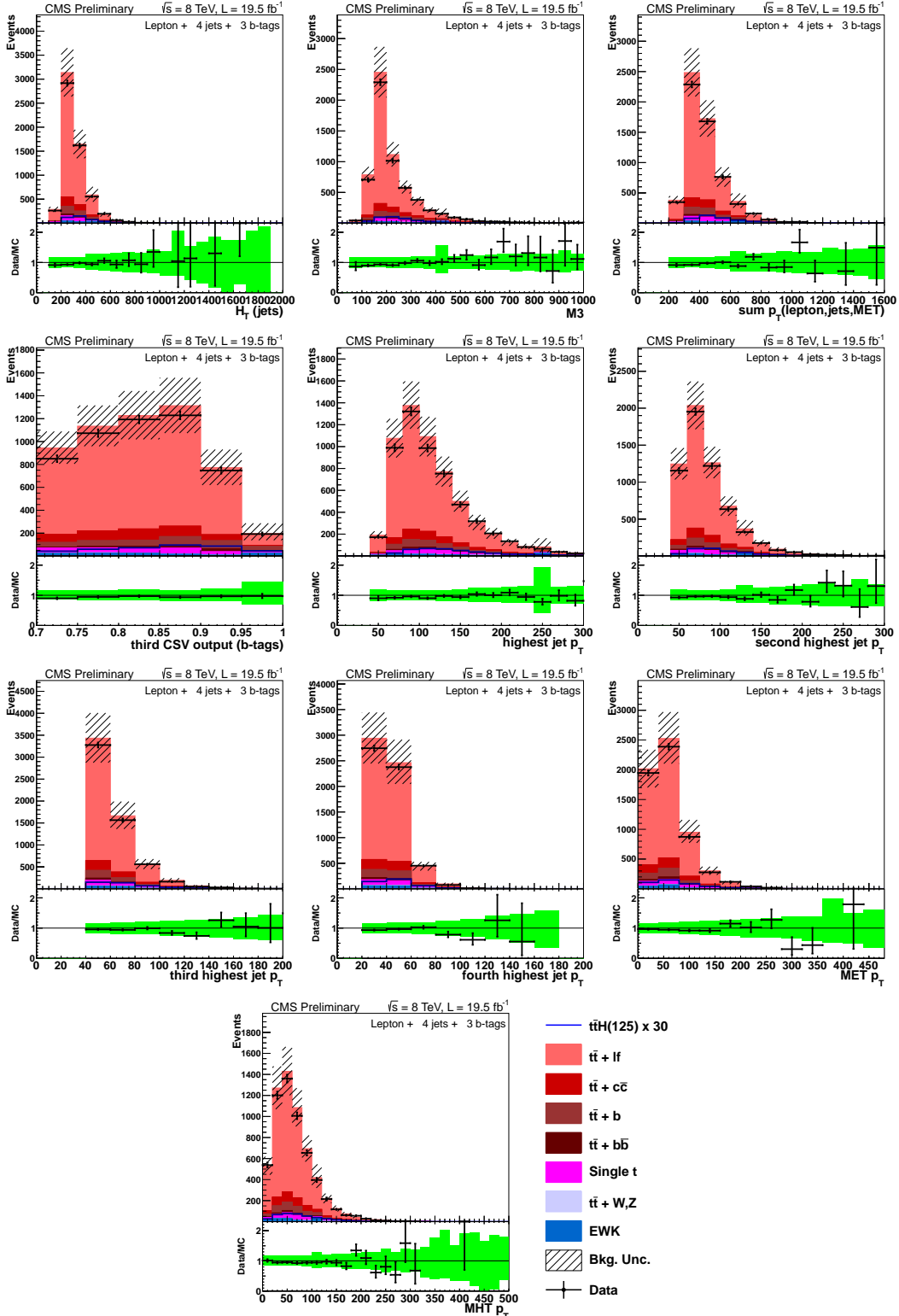


Figure 7.8: Data/MC comparisons for events with one lepton and 4 jets + 3 b-tags. The uncertainty band includes statistical and systematic uncertainties that affect both the rate and shape of the background distributions.

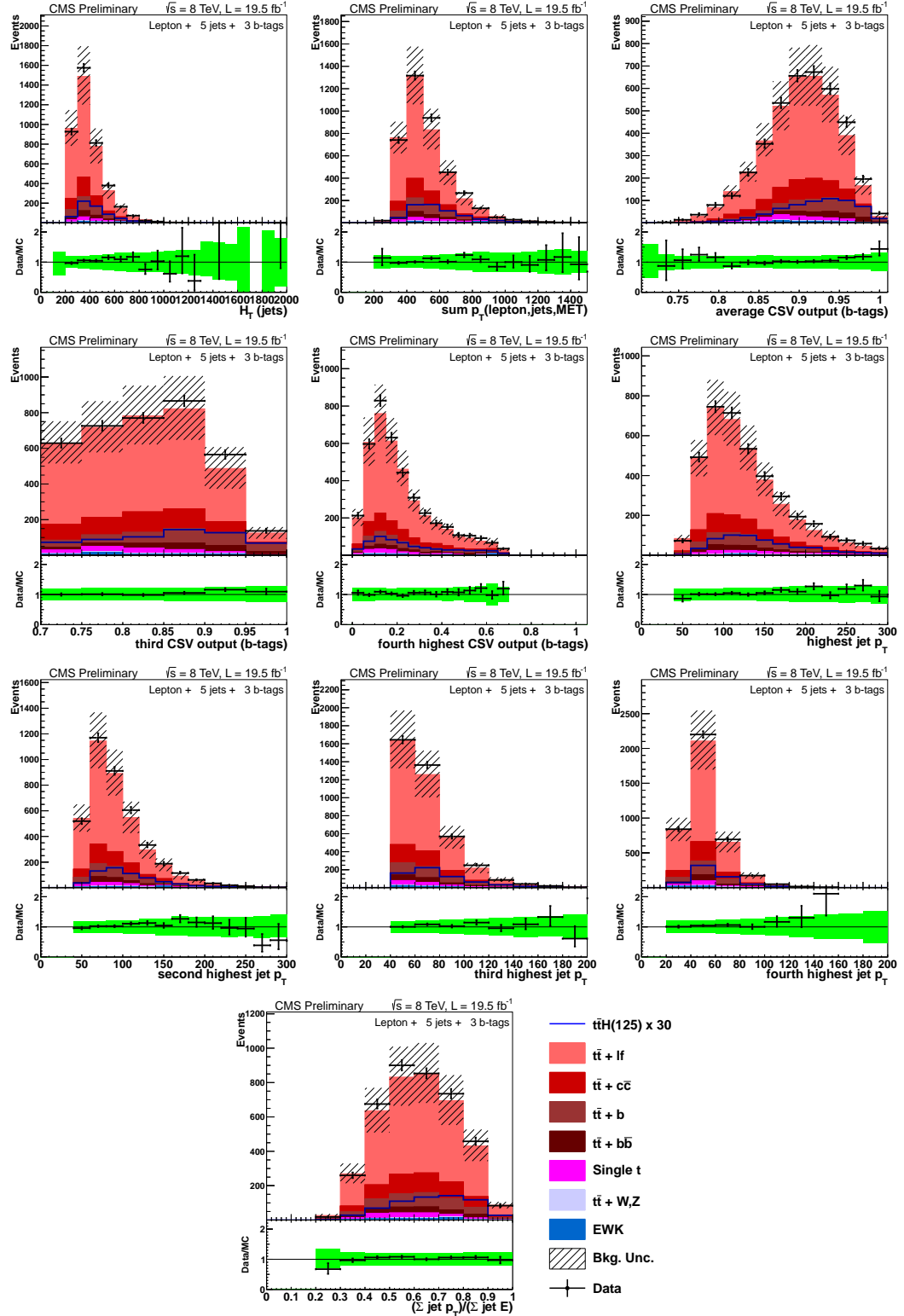


Figure 7.9: Data/MC comparisons for events with one lepton and 5 jets + 3 b-tags. The uncertainty band includes statistical and systematic uncertainties that affect both the rate and shape of the background distributions.

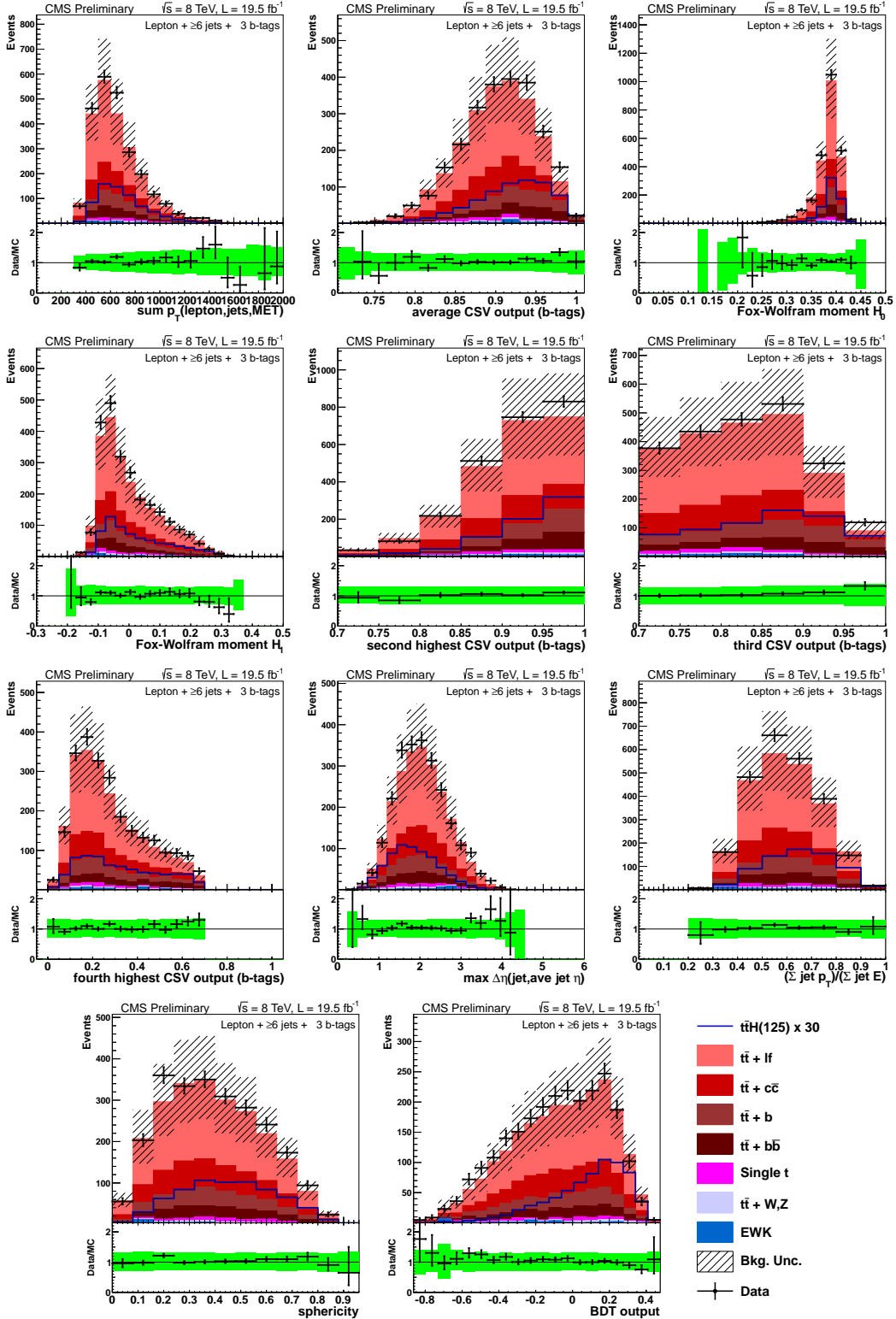


Figure 7.10: Data/MC comparisons for events with one lepton and  $\geq 6$  jets + 3 b-tags. The uncertainty band includes statistical and systematic uncertainties that affect both the rate and shape of the background distributions.

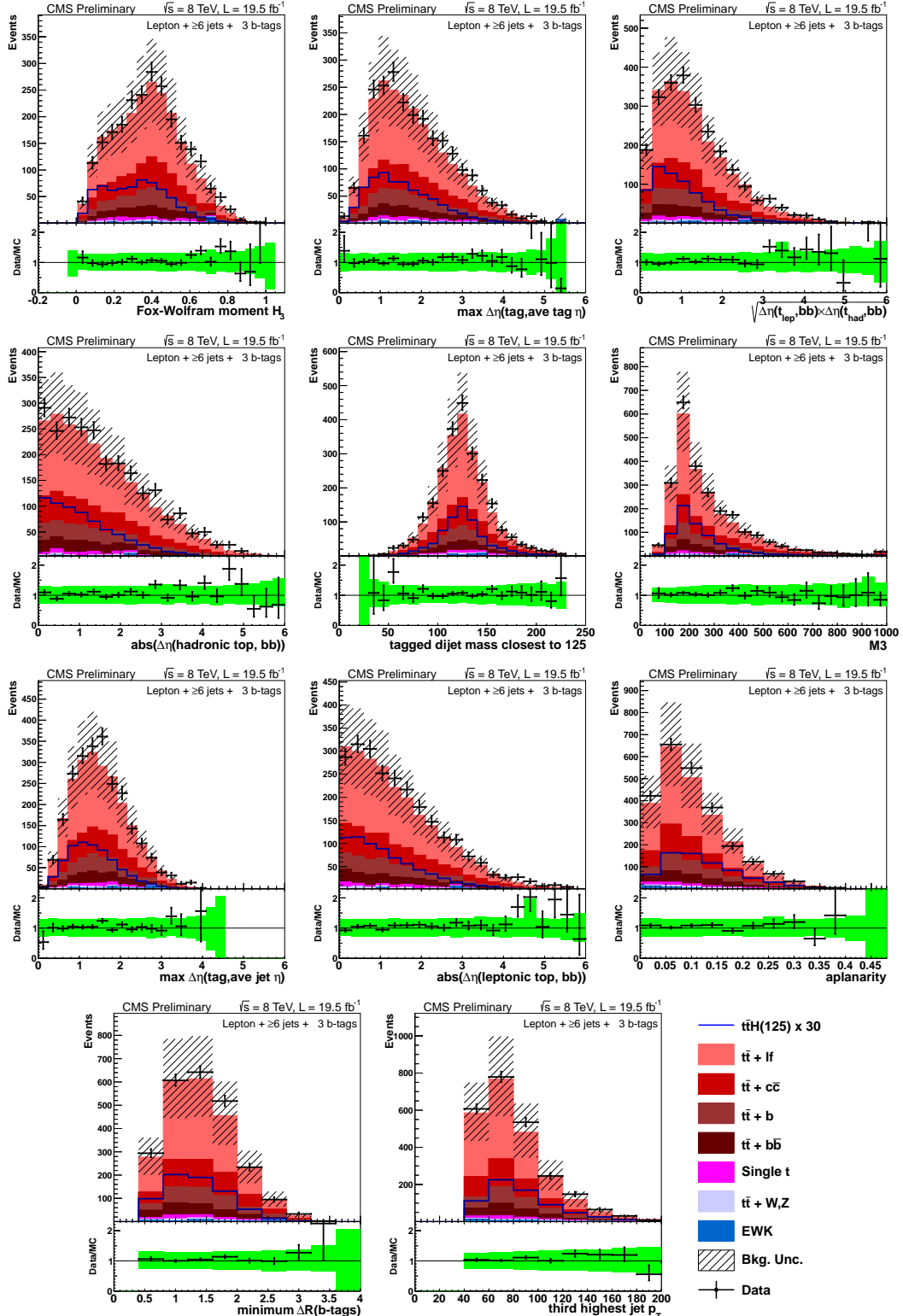


Figure 7.11: Data/MC comparisons for events with one lepton and  $\geq 6$  jets + 3 b-tags. The uncertainty band includes statistical and systematic uncertainties that affect both the rate and shape of the background distributions.

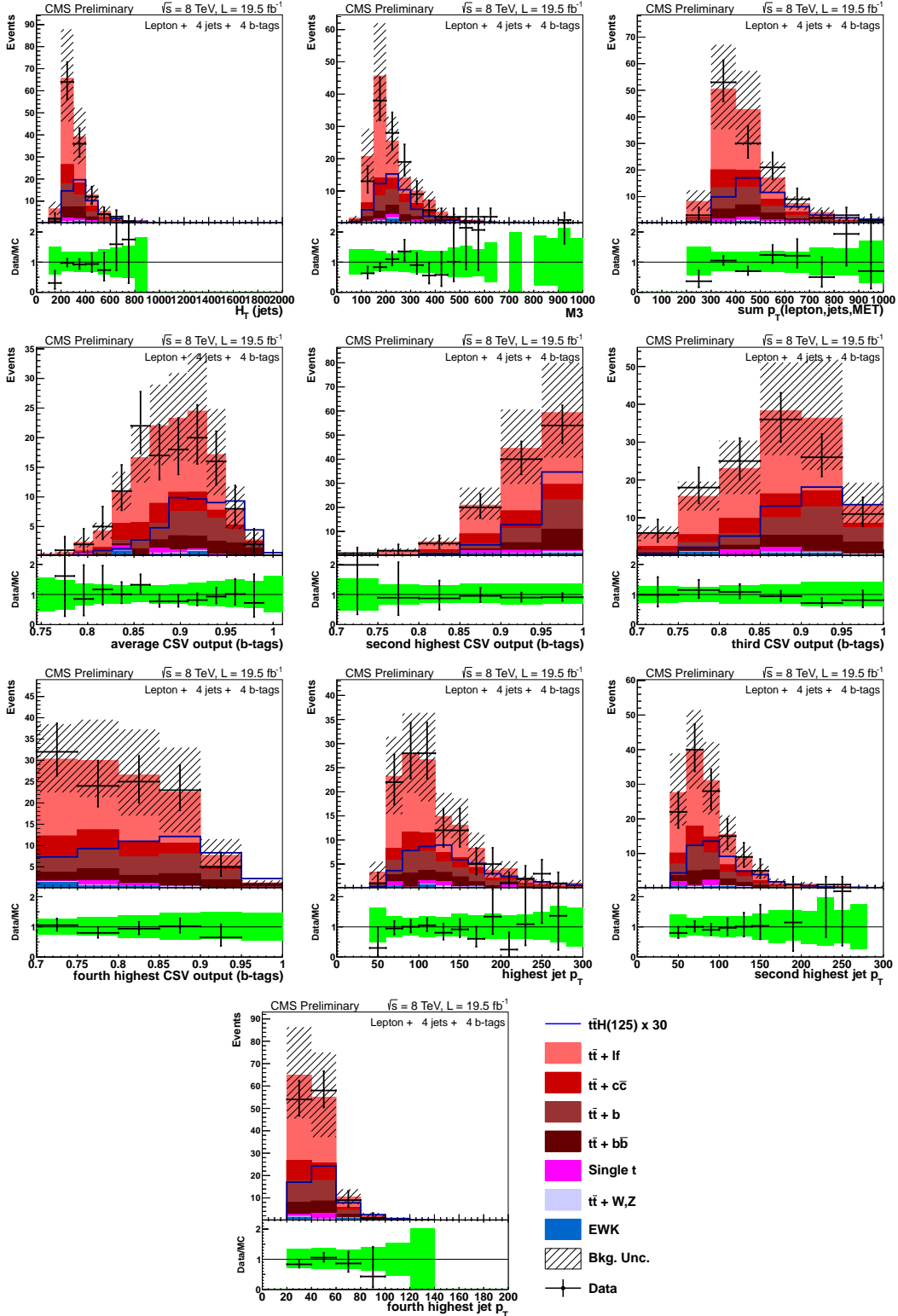


Figure 7.12: Data/MC comparisons for events with one lepton and 4 jets + 4 b-tags. The uncertainty band includes statistical and systematic uncertainties that affect both the rate and shape of the background distributions.

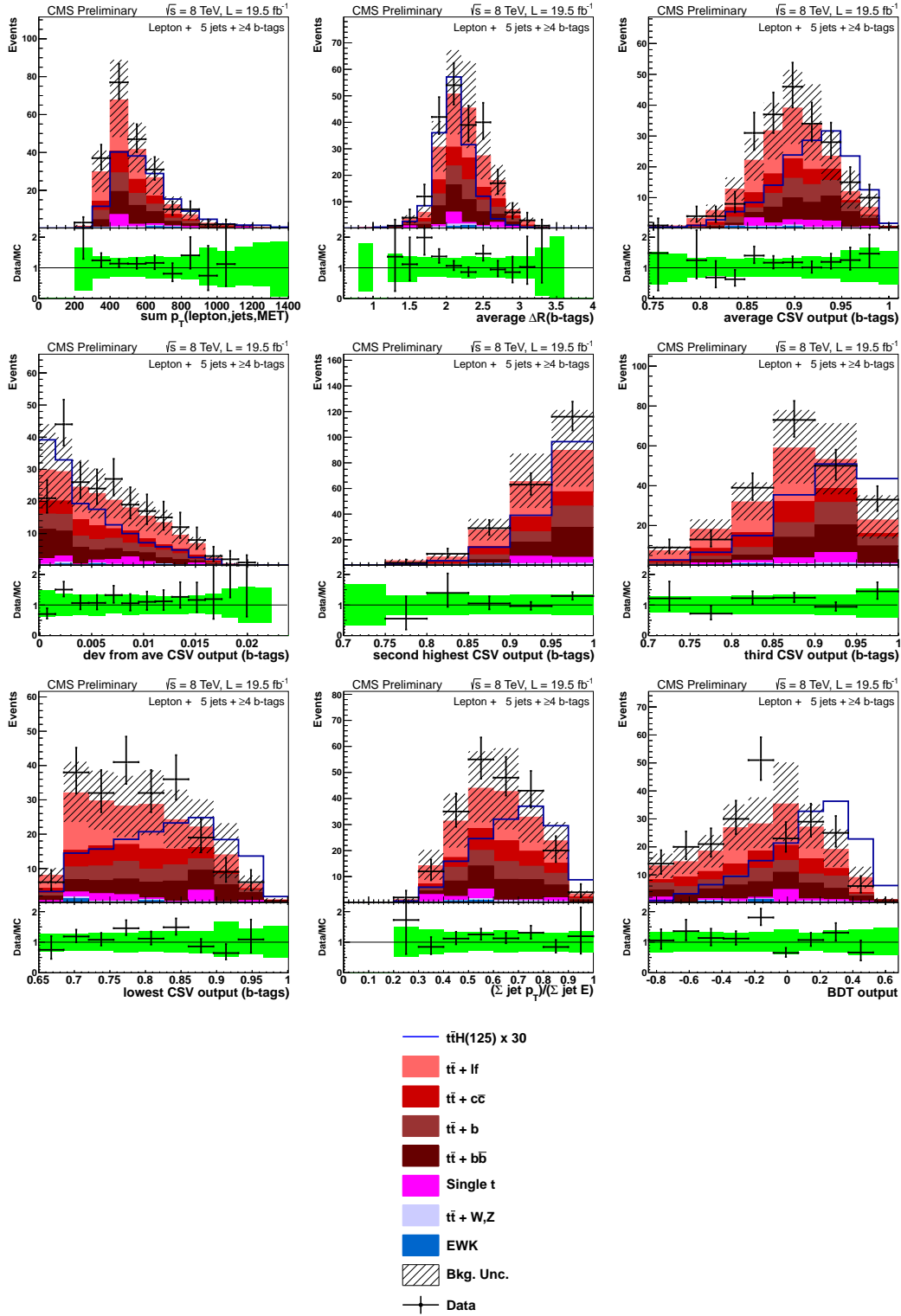


Figure 7.13: Data/MC comparisons for events with one lepton and 5 jets  $+ \geq 4$  b-tags. The uncertainty band includes statistical and systematic uncertainties that affect both the rate and shape of the background distributions.

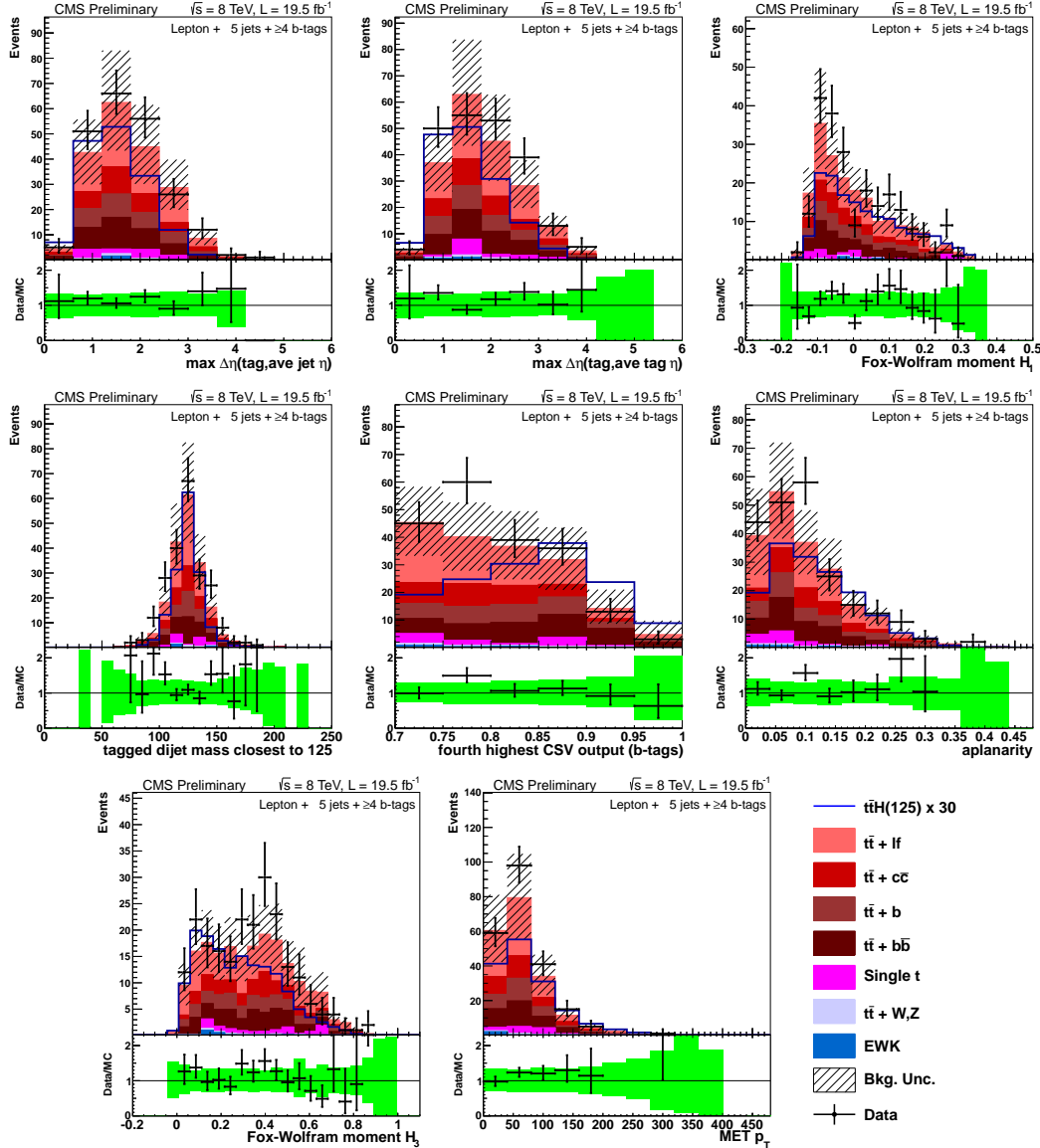


Figure 7.14: Data/MC comparisons for events with one lepton and 5 jets  $+ \geq 4$  b-tags. The uncertainty band includes statistical and systematic uncertainties that affect both the rate and shape of the background distributions.

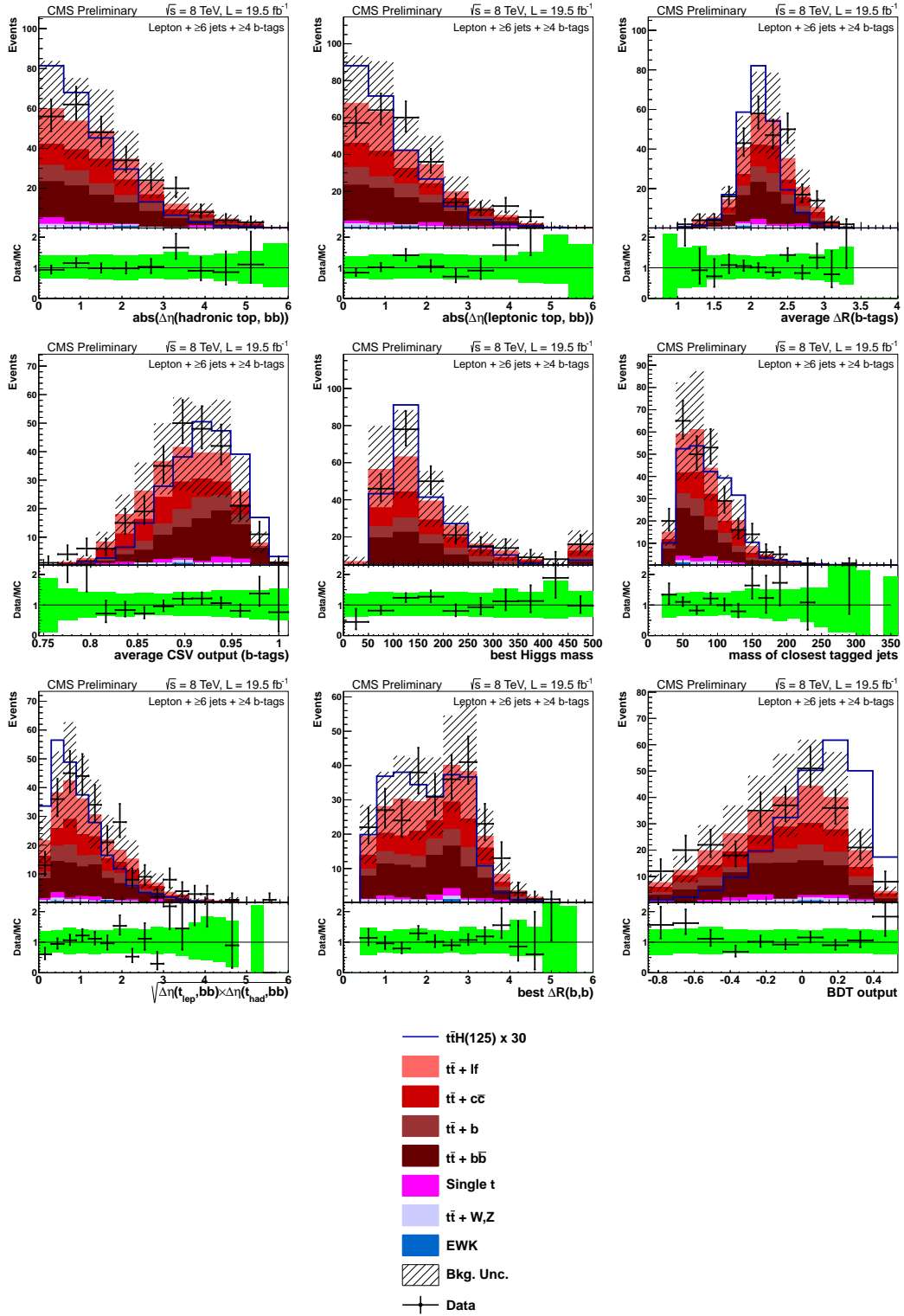


Figure 7.15: Data/MC comparisons for events with one lepton and  $\geq 6$  jets +  $\geq 4$  b-tags. The uncertainty band includes statistical and systematic uncertainties that affect both the rate and shape of the background distributions.

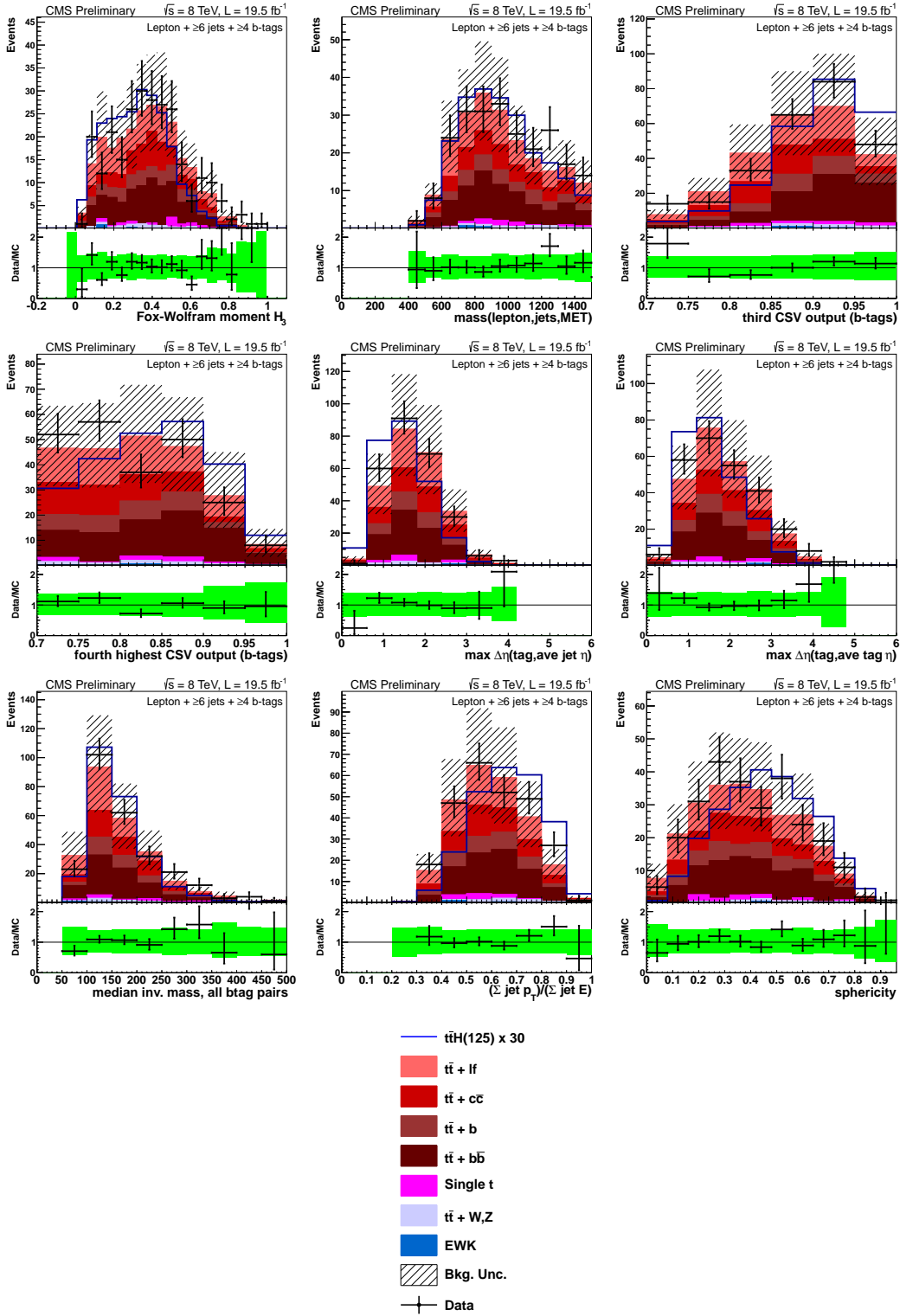


Figure 7.16: Data/MC comparisons for events with one lepton and  $\geq 6$  jets +  $\geq 4$  b-tags. The uncertainty band includes statistical and systematic uncertainties that affect both the rate and shape of the background distributions.

### 2614 7.3.3 MVA Output, Data to Monte Carlo Comparisons

2615 The distributions of the BDT output discriminators in each category are shown in Fig. 7.17. For  
 2616 these figures, the uncertainty band includes statistical and systematic uncertainties, e.g. JES  
 2617 and  $b$ -tag SF uncertainties, that are described in section 7.4.

## 2618 7.4 Systematic Uncertainties

2619 The evaluation of several of the systematic uncertainties follows the same procedure as described  
 2620 in the previous chapter. For these cases, the reader is directed to previous description of the  
 2621 uncertainty. Systematic uncertainties that are new to this analysis include those associated with  
 2622 the new  $b$ -tag calibration method and the top- $p_T$  reweighting. Where appropriate, comparisons  
 2623 between the shapes of the nominal and  $\pm 1\sigma$  variations are made.

2624 **Jet Energy Scale (JES):** See section 6.4 for a description of the evaluation of this systematic.  
 2625 Shape comparisons between the nominal and the  $\pm 1\sigma$  variations are shown in figure 7.18.  
 2626 Table 7.8 shows the effect on the rate for the  $\geq 6$  jets +  $\geq 4$  tags category.

JES systematic yield change			
		lepton+jets	
sys	shift	$t\bar{t}H(125)$	$t\bar{t} + bb$
JES	up	+9.1%	+8.3%
	down	-7.7%	-10.6%

Table 7.8: Relative yield change due to JES shift up/down for the  $\geq 3$  tag category in the dilepton channel and the  $\geq 6$  jets +  $\geq 4$  tags category in the lepton+jets channel.

2627 **Jet Energy Resolution (JER):** See section 6.4 for a description of the evaluation of this  
 2628 systematic.

2629  **$b$ -tag Scale Factors:** New scale factors to account for the differences in efficiency between  
 2630 data and simulation for the CSV  $b$ -tagging algorithm is described in section 7.2.1. There  
 2631 are three sources of systematic uncertainty on both the heavy flavor and light flavor scale  
 2632 factors: JES, purity, and statistics, and each source of variation is considered separately.  
 2633 The  $b$ -tag uncertainty associated with the JES is evaluated at the same time the overall  
 2634 JES uncertainty is considered. When the JES is shifted for the jet kinematics up or down  
 2635 by  $1\sigma$ , the  $b$ -tag scale factor values, which depend on the  $p_T$  of the jet in question, shift as  
 2636 well. This correlates the  $b$ -tag uncertainty from JES with the overall JES uncertainty. The  
 2637 other two sources of  $b$ -tag uncertainty are each evaluated independently for light-flavor and  
 2638 heavy-flavor. The purity uncertainty is controlled by a separate nuisance parameter for  
 2639 light and heavy flavor. Variation of this parameter is associated with changing the pre-

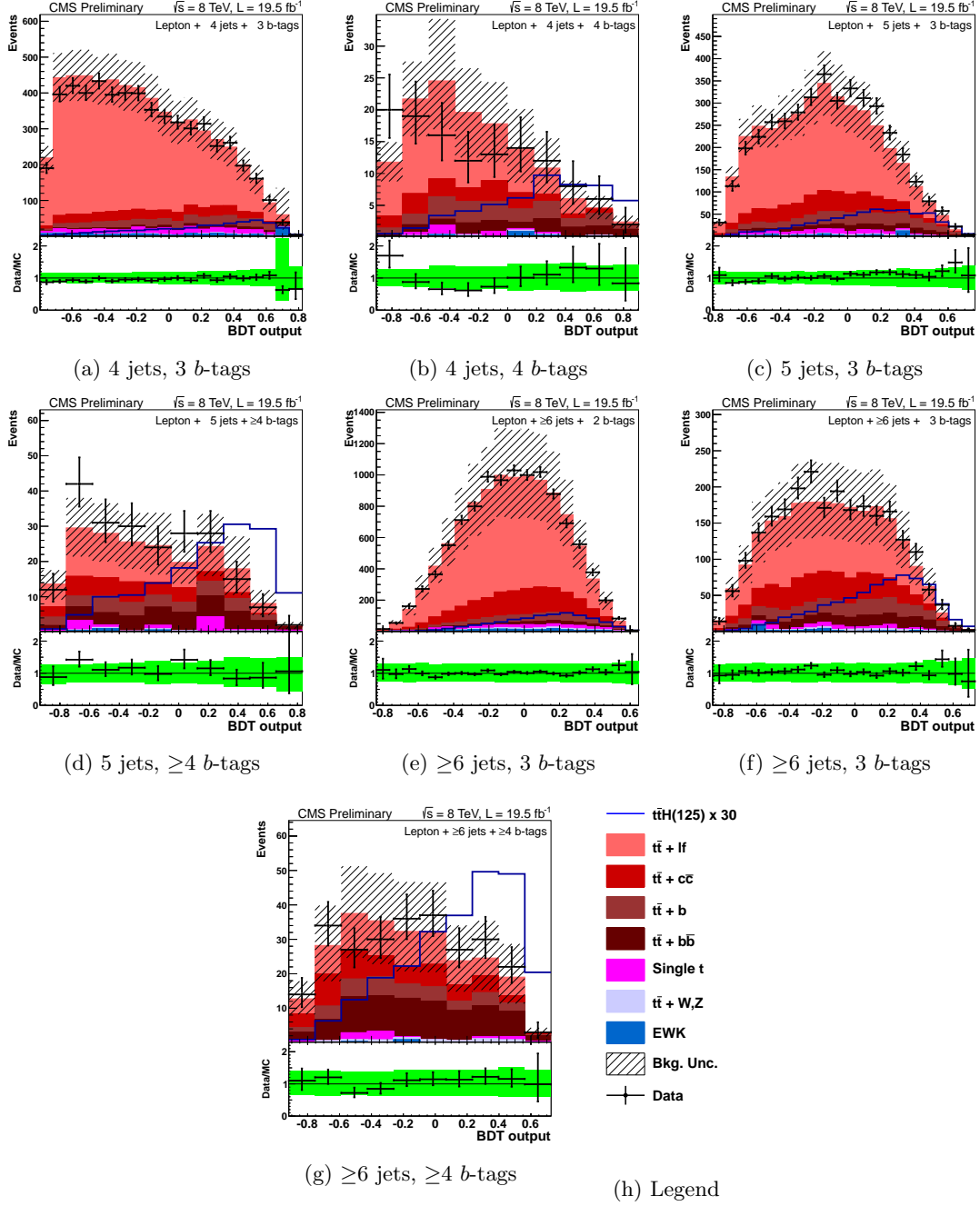


Figure 7.17: Final BDT output for lepton + jet events. Background-like events have a low BDT output value. Signal-like events have a high BDT output value. The uncertainty band includes statistical and systematic uncertainties that affect both the rate and shape of the background distributions. The top, middle and, bottom rows are events with 4, 5, and  $\geq 6$  jets, respectively, while the left, middle, and right-hand columns are events with 2, 3, and  $\geq 4$   $b$ -tags, respectively. The  $t\bar{t}H$  signal ( $m_H = 125$  GeV) is normalized to  $30 \times$  SM expectation.

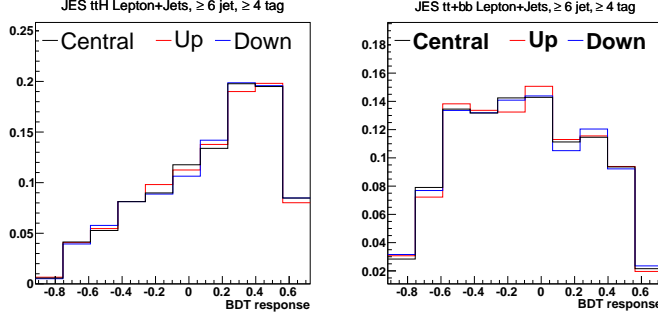


Figure 7.18: Comparison of the MVA discriminator for JES shift upwards (red) and downwards (blue) relative to the nominal (black) shape for the  $t\bar{t}H(125)$  signal (left) and the main background sample  $t\bar{t} + b\bar{b}$  (right). The plots are from the  $\geq 6$  jet  $\geq 4$  tag category in the lepton+jets channel. All plots are normalized to unit area.

2640           diction of simulated heavy-flavor events in the light-flavor control region, and visa versa.  
 2641  
 2642  
 2643  
 2644  
 2645  
 2646  
 2647  
 2648  
 2649  
 2650  
 2651  
 2652  
 2653  
 2654

Figures 7.19 and 7.20 and Table 7.9 show the effect of this uncertainty on the final BDT shapes. The impact of statistical uncertainties associated with the scale factor determination are controlled by means of four total nuisance parameters, two for heavy-flavor and two for light-flavor. For each jet flavor, the first nuisance parameter controls distortions in the CSV distribution corresponding to an overall tilt. This is consistent with a migration of events from one end of the CSV range to the other. The second nuisance parameter controls distortions of a more complicated nature, where the upper and lower ends of the distribution change relative to the center. Figures. 7.21 and 7.22, and Table 7.9 show the size of the shape and rate impact on the final BDT shape. For charm jets scale factors, the overall relative uncertainty is retained from the heavy flavor scale factors, doubled in size and used to construct two separate nuisance parameters to control the uncertainties. These two uncertainties associated with charm jets scale factors are not correlated with respect to all the uncertainties for the heavy flavor and light flavor scale factors. Figure 7.23 and Table 7.9 show the size of the shape and rate impact on the final BDT shape.

2655           **Electron and Muon ID and Trigger Scale Factors:** A rate uncertainty of 1.4% is assigned  
 2656           for single-lepton events. A single nuisance parameter is used for all lepton-related and is  
 2657           correlated between muons and electrons. Uncertainties for electrons and muons are treated  
 2658           identically, and in the case where there is a difference, the larger uncertainty is used.  
 2659  
 2660           Uncertainties from ID and isolation as fully uncorrelated and are combined in quadrature  
 for the value of the nuisance parameter.

2661  
 2662  
 2663

The total lepton efficiency uncertainty is composed of two parts. Both parts were measured using the method described in [103], which is a "tag and probe" method based on lepton events near the  $Z$  boson mass resonance. The first part is a 1% uncertainty on the lepton

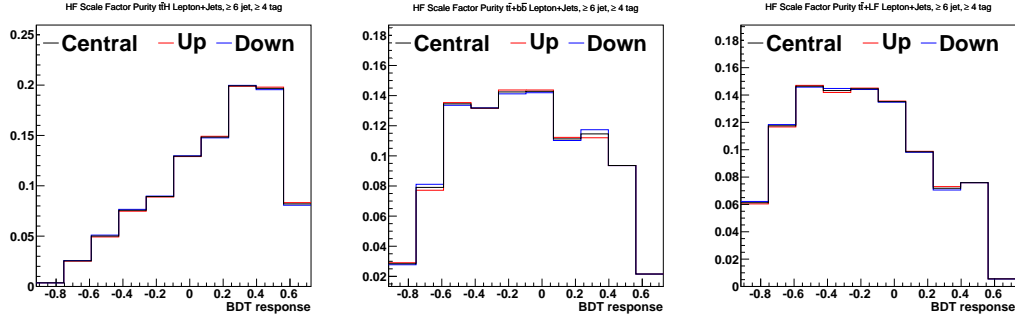


Figure 7.19: Comparison of the MVA discriminator when shifting the light flavor contamination in the heavy flavor scale factor determination shift upwards (red) and downwards (blue) relative to the nominal (black) shape for the  $t\bar{t}H(125)$  signal (top row) and  $t\bar{t} + b\bar{b}$  and  $t\bar{t} + \text{LF}$  background samples (middle row and bottom row respectively). The plots are from the  $\text{LJ} \geq 6 \text{ jet} \geq 4$  category. All plots are normalized to unit area.

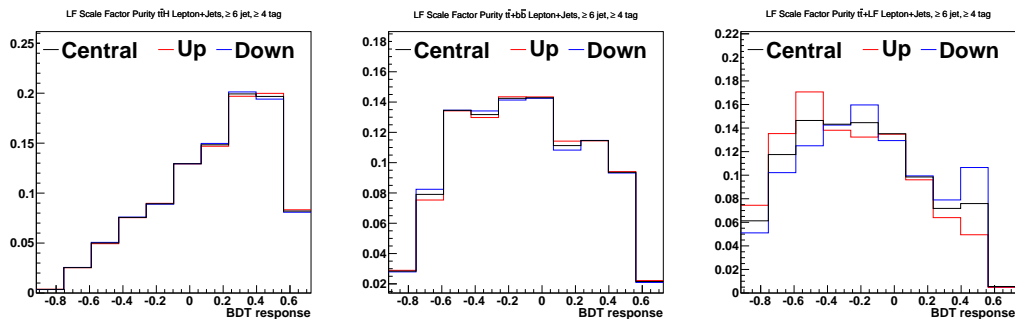


Figure 7.20: Comparison of the MVA discriminator when shifting the heavy flavor contamination in the light flavor scale factor determination shift upwards (red) and downwards (blue) relative to the nominal (black) shape for the  $t\bar{t}H(125)$  signal (top row) and  $t\bar{t} + b\bar{b}$  and  $t\bar{t} + \text{LF}$  background samples (middle row and bottom row respectively). The plots are from the  $\text{LJ} \geq 6 \text{ jet} \geq 4$  category. All plots are normalized to unit area.

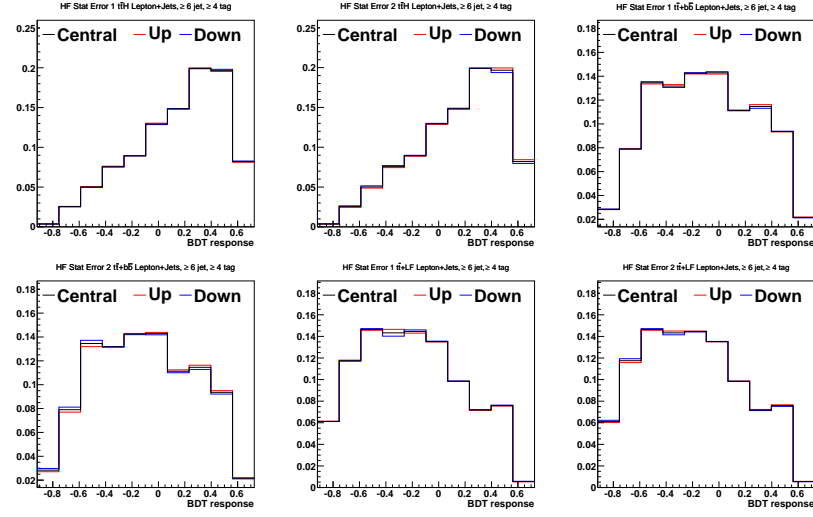


Figure 7.21: Comparison of the MVA discriminator when shifting to account for the statistical uncertainty on the heavy flavor scale factor extraction. Two classes of distortion in the scale factor are considered: linear distortions (labeled “Stat. Error 1”) and nonlinear distortions (labeled “Stat. Error 2”). Both shift upwards (red) and downwards (blue) relative to the nominal (black) shape for the  $t\bar{t}H(125)$  signal (top row) and  $t\bar{t} + b\bar{b}$  and  $t\bar{t} + \text{LF}$  background samples (middle row and bottom row respectively) are shown. The plots are from the  $\geq 6$  jet  $\geq 4$  tag category. All plots are normalized to unit area.

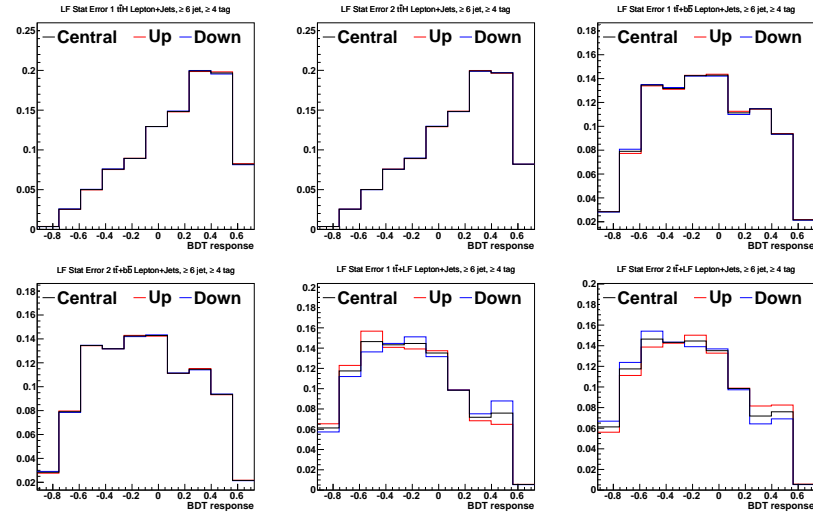


Figure 7.22: Comparison of the MVA discriminator when shifting to account for the statistical uncertainty on the light flavor scale factor extraction. Two classes of distortion in the scale factor are considered: linear distortions (labeled “Stat. Error 1”) and nonlinear distortions (labeled “Stat. Error 2”). Both shift upwards (red) and downwards (blue) relative to the nominal (black) shape for the  $t\bar{t}H(125)$  signal (top row) and  $t\bar{t} + b\bar{b}$  and  $t\bar{t} + \text{LF}$  background samples (middle row and bottom row respectively) are shown. The plots are from the  $\geq 6$  jet  $\geq 4$  tag category. All plots are normalized to unit area.

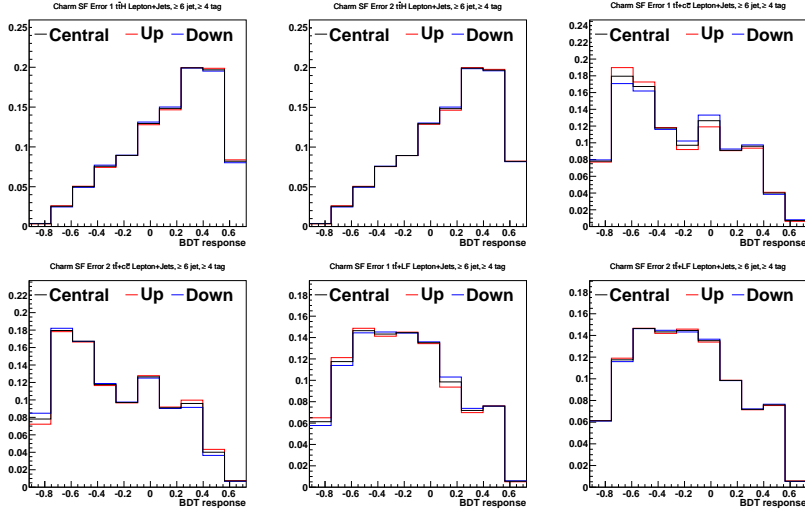


Figure 7.23: Comparison of the MVA discriminator when shifting to account for the uncertainty on the charm jets scale factor extraction. Two classes of distortion in the scale factor are considered: linear distortions (labeled “Error 1”) and nonlinear distortions (labeled “Error 2”). Both shift upwards (red) and downwards (blue) relative to the nominal (black) shape for the  $t\bar{t}H(125)$  signal (top row) and  $t\bar{t} + c\bar{c}$  and  $t\bar{t} + \text{LF}$  background samples (middle row and bottom row respectively) are shown. The plots are from the  $\geq 6$  jet  $\geq 4$  tag category. All plots are normalized to unit area.

b-tag systematic yield change					
		lepton+jets			
sys	shift	$t\bar{t} H(125)$	$t\bar{t} + \text{LF}$	$t\bar{t} + bb$	
Heavy Flavor SF Purity	up	+13.2%	+7.4%	+13.3%	
	down	-12.1%	-7.2%	-12.1%	
Light Flavor SF Purity	up	-3.4%	-32.2%	-4.4%	
	down	+3.4%	+43.9%	+4.4%	
Heavy Flavor SF Stat. Err. 1	up	-12.1%	-6.6%	-11.8%	
	down	+13.3%	+6.8%	+12.9%	
Heavy Flavor SF Stat. Err. 2	up	+8.9%	+5.0%	+9.1%	
	down	-8.3%	-4.9%	-8.5%	
Light Flavor SF Stat. Err. 1	up	+0.5%	-15.6%	+0.1%	
	down	-0.5%	+17.7%	-0.1%	
Light Flavor SF Stat. Err. 2	up	+1.8%	+10.1%	+2.1%	
	down	-1.7%	-8.9%	-2.0%	
sys	shift	$t\bar{t} H(125)$	$t\bar{t} + \text{LF}$	$t\bar{t} + cc$	
Charm jets SF Err. 1	up	+5.1%	-3.4%	-5.6%	
	down	-5.1%	+3.3%	+5.0%	
Charm jets SF Err. 2	up	+6.0%	+4.2%	+12.7%	
	down	-5.9%	-4.2%	-11.7%	

Table 7.9: This table summarizes the rate effect of the six independent nuisance parameters that characterize the  $b$ -tag uncertainties. (Note: The  $b$ -tag rate uncertainties associated with JES variations are already included with the JES rate uncertainties in Table 6.14. The impact of statistical uncertainties is in the heavy-flavor and light-flavor scale factor extraction is incorporated using two separate nuisance parameters, as described above. The uncertainty labeled “Stat. Err. 1” represents statistical uncertainties resulting a linear distortion of the CSV scale factor, while the one labeled “Stat. Err. 2” corresponds to nonlinear distortions.

identification and isolation scale factor. The second part of the total lepton efficiency uncertainty is a 1% trigger scale factor uncertainty.

**Pileup Reweighting:** See section 6.4 for a description of the evaluation of this systematic.

**Top Quark  $p_T$  Reweighting:** The systematic uncertainty on the top  $p_T$  reweighting is assessed as follows: the uncorrected Monte Carlo shapes are used as  $-1\sigma$  systematic uncertainty, and doubling the correction factor gives the  $+1\sigma$  variation. This creates a deviation that is the same size as the original observed difference between data and Monte Carlo. This uncertainty is shown in Fig. 7.2. Fig. 7.24 shows the effects of the uncertainty on the top quark  $p_T$  on the BDT shape and Table 7.10 shows the effect on the rates.

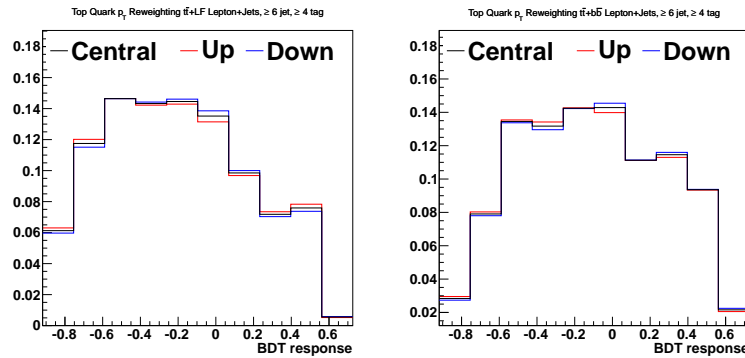


Figure 7.24: Comparison of the MVA discriminator for shifts in top quark  $p_T$  reweighting upwards (red) and downwards (blue) relative to the nominal (black) shape for the  $t\bar{t}$  +LF background (left) and the  $t\bar{t}$  + $b\bar{b}$  (right). The plots are from the  $\geq 6$  jets +  $\geq 4$  tags category in the lepton+jets channel. All plots are normalized to unit area.

Top quark $p_T$ reweighing systematic yield change			
		lepton+jets	
sys	shift	$t\bar{t}$	$t\bar{t} + b\bar{b}$
Top quark $p_T$ Reweighting	up	-5.2%	-7.0%
	down	+5.2%	+7.0%

Table 7.10: Relative yield change due to varying the top quark  $p_T$  reweighting. The “up” variation corresponds to apply twice as much correction to the top quark  $p_T$  distribution as the nominal, while the “down” correction corresponds to applying no correction to the default MC top quark  $p_T$  distribution.

**Cross Sections:** See section 6.4 for a description of the evaluation of this systematic. Uncertainties affecting these normalizations are summarized in Table 7.11.

**Luminosity:** The uncertainty on the luminosity estimate is 2.2%. This affects all rates.

**Madgraph  $Q^2$  Uncertainty:** See section 6.4 for a description of the evaluation of this systematic.

Process	pdf			QCD Scale			
	$gg$	$q\bar{b}$	$qg$	$t\bar{t}$	$V$	$VV$	$t\bar{t}H$
$t\bar{t}H$	9%						12.5%
$t\bar{t} + \text{jets}$	2.6%			3%			
$t\bar{t} + W$		7%		15%			
$t\bar{t} + Z$	9%			15%			
Single top			4.6%	2%			
$W + \text{jets}$		4.8%			1.3%		
$Z + \text{jets}$		4.2%			1.2%		
Dibosons							3.5%

Table 7.11: Cross section uncertainties used for the limit settings. Each column in the table is an independent source of uncertainty, except for the last column which represents uncertainties uncorrelated with any others. Uncertainties in the same column for two different processes (different rows) are completely correlated.

2678     Figure 7.25 shows the shape and Table 7.12 shows the rate variations for selected event  
 2679     categories.

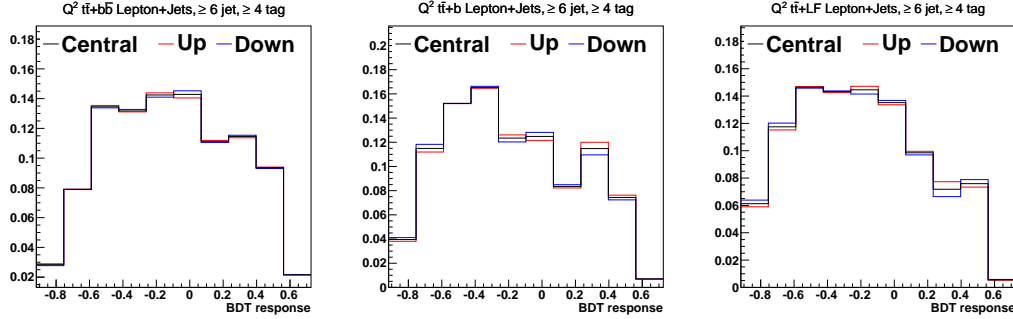


Figure 7.25: Comparison of the MVA discriminator when shifting the  $Q^2$  scale up and down by its uncertainties. Shown are the shift upwards (red) and downwards (blue) relative to the nominal (black) shape for the  $t\bar{t} + b\bar{b}$  (top row)  $t\bar{t} + b$  (middle row) and  $t\bar{t} + \text{LF}$  (bottom) background samples. The plots are from the  $LJ \geq 6$  jet  $\geq 4$  category. All plots are normalized to unit area.

$Q^2$ systematic yield change					
		lepton+jets			
sys	shift	$t\bar{t} + \text{LF}$	$t\bar{t} + b$	$t\bar{t} + b\bar{b}$	
$Q^2$ Uncertainty	up	-13.8%	-16.1%	-17.6%	
	down	+17.6%	+20.8%	+23.3%	

Table 7.12: This table summarizes the rate effect of shifting  $Q^2$  scale uncertainty for Madgraph. Note that the shifts are made independently for the following topologies:  $t\bar{t} + 0p$ ,  $t\bar{t} + 1p$ ,  $t\bar{t} + 2p$ ,  $t\bar{t} + c\bar{c}$ ,  $t\bar{t} + b$ , and  $t\bar{t} + b\bar{b}$ .

2680     **MC Statistics Uncertainty:** See section 6.4 for a description of the evaluation of this sys-  
 2681     tematic.

2682     **Extra  $t\bar{t}$ +HF Rate Uncertainty:** See section 6.4 for a description of the evaluation of this sys-  
 2683     tematic.

2684 Table 7.13 summarizes the systematic uncertainties assessed on the signal and backgrounds  
 2685 for this analysis. It describes how each systematic is treated in the fit used for signal extraction.

Source	Shape?	Notes
Luminosity	No	Signal and all backgrounds
Lepton ID/Trig	No	Signal and all backgrounds
Pileup	No	Signal and all backgrounds
Jet Energy Resolution	No	Signal and all backgrounds
Jet Energy Scale	Yes	Signal and all backgrounds
<i>b</i> -Tag HF fraction	Yes	Signal and all backgrounds
<i>b</i> -Tag HF stats (linear)	Yes	Signal and all backgrounds
<i>b</i> -Tag HF stats (quadratic)	Yes	Signal and all backgrounds
<i>b</i> -Tag LF fraction	Yes	Signal and all backgrounds
<i>b</i> -Tag LF stats (linear)	Yes	Signal and all backgrounds
<i>b</i> -Tag LF stats (quadratic)	Yes	Signal and all backgrounds
<i>b</i> -Tag Charm (linear)	Yes	Signal and all backgrounds
<i>b</i> -Tag Charm (quadratic)	Yes	Signal and all backgrounds
QCD Scale ( $t\bar{t}H$ )	No	Scale uncertainty for NLO $t\bar{t}H$ prediction
QCD Scale ( $t\bar{t}$ )	No	Scale uncertainty for NLO $t\bar{t}$ and single top predictions
QCD Scale ( $V$ )	No	Scale uncertainty for NNLO $W$ and $Z$ prediction
QCD Scale ( $VV$ )	No	Scale uncertainty for NLO diboson prediction
pdf ( $gg$ )	No	Pdf uncertainty for $gg$ initiated processes ( $t\bar{t}$ , $t\bar{t}Z$ , $t\bar{t}H$ )
pdf ( $q\bar{q}$ )	No	Pdf uncertainty for $q\bar{q}$ initiated processes ( $t\bar{t}W$ , $W$ , $Z$ ).
pdf ( $qg$ )	No	Pdf uncertainty for $qg$ initiated processes (single top)
Madgraph $Q^2$ Scale ( $t\bar{t} + 0p, 1p, 2p$ )	Yes	Madgraph $Q^2$ scale uncertainty for $t\bar{t} + jets$ split by parton number. There is one nuisance parameter per parton multiplicity and they are uncorrelated.
Madgraph $Q^2$ Scale ( $t\bar{t} + b\bar{b}/c\bar{c}$ )	Yes	Madgraph $Q^2$ scale uncertainty for $t\bar{t}+jets/b\bar{b}/c\bar{c}$ .
Madgraph $Q^2$ Scale ( $V$ )	No	Varies by jet bin.
$\tau$ Energy Scale	Yes	Tau signal and background
$\tau$ ID efficiency	Yes	Tau signal and background
$\tau$ Jet Fake Rate	Yes	Tau signal and background
$\tau$ Electron Fake Rate	Yes	Tau signal and background

Table 7.13: Summary for the of the systematic uncertainties considered on the inputs to the limit calculation. Except where noted, each row in this table will be treated as a single, independent nuisance parameter.

2686 Table 7.14 shows the results of the comparing the variation in rate for the sum of  $t\bar{t} + lf + b\bar{b} + c\bar{c}$   
 2687 backgrounds. The systematic that produces the largest variation of the backgrounds is the QCD  
 2688 scale uncertainty on the  $t\bar{t} + b\bar{b}$  background. The next largest variation comes from: the amount  
 2689 of  $t\bar{t} + b\bar{b}$ , the *b*-tagging efficiency and fake rate, and the jet energy scale. The next most important  
 2690 effect is the top quark  $p_T$  correction, and it is more than three times smaller than the QCD scale  
 2691 uncertainty on  $t\bar{t} + b\bar{b}$ .

## 2692 7.5 Statistical Methods

2693 The same procedure that was used in the previous analysis, and desrcied in section 6.5.

Uncertainties on the sum of $t\bar{t} + \text{lf}$ , $t\bar{t} + b$ , $t\bar{t} + b\bar{b}$ , and $t\bar{t} + c\bar{c}$ events with $\geq 6$ jets and $\geq 4$ b-tags		
Source	Rate	Shape?
QCD Scale ( $t\bar{t} + b\bar{b}$ )	17%	No
$b$ -Tag HF contamination	17%	Yes
QCD Scale ( $t\bar{t} + c\bar{c}$ )	11%	No
Jet Energy Scale	11%	Yes
$b$ -Tag LF contamination	9.6%	Yes
$b$ -Tag HF stats (linear)	9.1%	Yes
QCD Scale ( $t\bar{t} + b$ )	7.1%	No
Madgraph $Q^2$ Scale ( $t\bar{t} + b\bar{b}$ )	6.8%	Yes
$b$ -Tag Charm Uncertainty (quadratic)	6.7%	Yes
Top Pt Correction	6.7%	Yes
$b$ -Tag HF stats (quadratic)	6.4%	Yes
$b$ -Tag LF stats (linear)	6.4%	Yes
Madgraph $Q^2$ Scale( $t\bar{t} + 2$ partons)	4.8%	Yes
$b$ -Tag LF stats (quadratic)	4.8%	Yes
Luminosity	4.4%	No
Madgraph $Q^2$ Scale ( $t\bar{t} + c\bar{c}$ )	4.3%	Yes
Madgraph $Q^2$ Scale ( $t\bar{t} + b$ )	2.6%	Yes
Lepton ID/Trig	1.4 (2.8)%	No
QCD Scale ( $t\bar{t}$ )	3%	No
pdf ( $gg$ )	2.6%	No
Jet Energy Resolution	1.5%	No
Pileup	1%	No
$b$ -Tag Charm Uncertainty (linear)	0.6%	Yes

Table 7.14: Specific effect of systematics on predicted background yields for events with  $\geq 6$  jets and  $\geq 4$  b-tags. Here we only consider the sum of the largest backgrounds,  $t\bar{t} + \text{lf}$ ,  $t\bar{t} + b$ ,  $t\bar{t} + b\bar{b}$ , and  $t\bar{t} + c\bar{c}$ . These three backgrounds account for 94% of all background events. The signal is 3.5% of the yield of the three main backgrounds. The signal fraction is directly comparable to the variations of the background in the table. The table shows that the signal is much smaller than many of the background variations.

2694 **7.6 Results and Conclusions**

2695 In the lack of a significant excess of events in data, upper limits are once again set on the  
2696  $t\bar{t}H$  production rate. The shape of the BDT discriminator distribution is used to fit the simulated  
2697 signal and backgrounds samples to the data. Besides the BDT discriminator shapes for data,  
2698 background and signal, inputs to the limit setting include the number of events passing the  
2699 selection for each process. Systematics that are used are nuisance parameters are described in  
2700 the previous section. The Higgs mass points we set limits for are: 110, 115, 120, 125, 130, 135  
2701 and  $140 \text{ GeV}/c^2$ . For the lepton+jets channel, the limits are shown in Tab. 7.15 and Fig. 7.26.

Higgs Mass	Observed	Median	Expected 68% C.L. Range	Expected 95% C.L. Range
$110 \text{ GeV}/c^2$	3.6	3.3	[2.4,4.7]	[1.8,6.6]
$115 \text{ GeV}/c^2$	4.1	3.5	[2.4,4.9]	[1.8,6.9]
$120 \text{ GeV}/c^2$	4.3	4.0	[2.9,5.8]	[2.1,8.1]
$125 \text{ GeV}/c^2$	4.9	4.7	[3.3,6.7]	[2.5,9.4]
$130 \text{ GeV}/c^2$	6.8	6.0	[4.3,8.6]	[3.2,12.0]
$135 \text{ GeV}/c^2$	7.4	7.1	[5.0,10.2]	[3.7,14.2]
$140 \text{ GeV}/c^2$	9.0	9.6	[6.9,13.7]	[5.2,18.9]

Table 7.15: Expected and observed upper limits for SM Higgs for lepton + jets channel using the 2012 dataset. These limits were extracted using the asymptotic method.

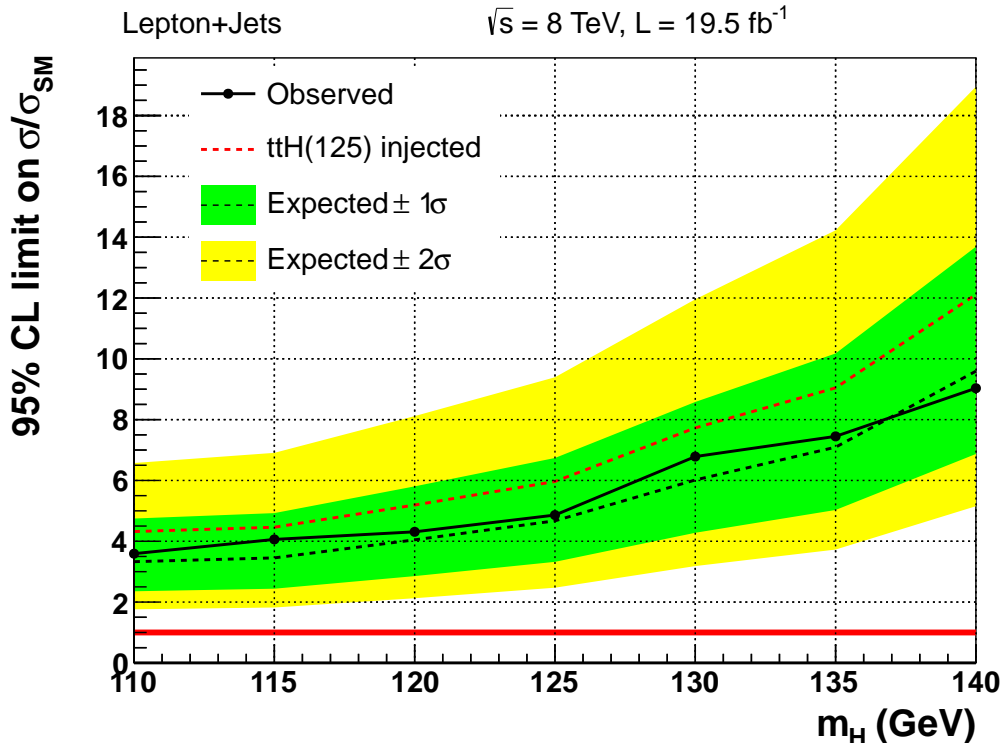


Figure 7.26: The expected and observed 95% CL upper limits on the signal strength parameter  $\mu = \sigma/\sigma_{SM}$  for the lepton+jets channel using the 2012 dataset. These limits were extracted using the asymptotic method.

2702 For the full  $19.4 \text{ fb}^{-1}$  of  $8 \text{ TeV}$  data collected by the CMS detector, an updated search

for the Standard Model Higgs boson produced in association with top-quark pairs has been performed. The increase in expected sensitivity did not increase by a factor of  $\sim 2$  that one would naively expect from increasing the statistics by a factor of  $\sim 4$ . This is because, largely due to the different set of systematic uncertainties used, the analysis entered a regime where statistical uncertainty was no longer the dominant factor that degraded sensitivity. If this data set was repeatedly collected, allowing for statistical fluctuations, it should be expected that, for a Standard Model Higgs boson, with mass,  $m_H = 125 \text{ GeV}$ , that 95% of the results would fail to observe the  $t\bar{t}H$  signal unless its cross-section was modified by a factor of 4.9. From simulations alone, this expected factor is 4.7, a difference of less than  $1\sigma$  from the observed data.

The results of this analysis were combined with previous results in this channel from 7 TeV data and with di-lepton, same-sign di-lepton, hadronic tau, di-photon, and multi-lepton final state channels and published in the Journal of High Energy Physics (JHEP) in September of 2014 [104]. The combined analytical power of all of the channels allowed for an upper limit of 4.5 times the predicted Standard Model cross section. This is slightly more than  $2\sigma$  away from the expected factor of 2.7 from simulations alone.

2718 **Chapter 8**

2719 **Analysis Improvements**

2720 The analyses described in the previous two chapters use sophisticated multivariate analysis  
2721 (MVA) techniques to perform signal extraction and limit setting. However, there are several  
2722 improvements that can still be made to optimize signal extraction and increase sensitivity. The  
2723 following section will describe the implementation of the latest simulation techniques in order  
2724 to improve the modelling the signal and background processes. The final section will discuss  
2725 variables from these new simulations that can be used to enhance the identification of final state  
2726 jets with their roles in the  $t\bar{t}$  system.

2727 **8.1 aMC@NLO, MadSpin, and Pythia8 Monte Carlo**

2728 One of the largest sources of uncertainty in each analysis comes from the theoretical uncertainty  
2729 of the Leading Order (LO) monte carlo sample used to estimate background rates and shapes.  
2730 In order to accurately model the high jet-multiplicity environment of the  $t\bar{t}H$  final state, higher-  
2731 order calculations in perturbation theory are necessary. Recently, the aMC@NLO framework  
2732 has been released, and is an automated tool for event generation that utilizes Next-to-Leading  
2733 Order (NLO) QCD predictions [105]. This framework takes advantage of recent theoretical  
2734 developments in the automation of calculating spin-entangled decays from heavy resonances,  
2735 which is packaged in the program MadSpin [106]. The event generator, aMC@NLO, using  
2736 MadSpin to calculate the decays of the top quark,  $W$  and  $Z$  bosons, is then interfaced to Pythia  
2737 8 to framework perform the parton shower and hadronization [107]. Each stage of this event  
2738 generation process uses the latest technological developments in monte carlo simulation, which  
2739 were unavailable at the time of the previous analyses.

2740 For process where additional jets are simulated in the final state, there will be an additional  
2741 complication since the parton shower and hadronization are performed separately and the con-

tributions for NLO processes will be double counted in several cases. This occurs when a process with an additional jet in the final state is created in the matrix element level by aMC@NLO and later, another event is created with no additional jets in the final state at the matrix element level, but when the parton shower occurs in Pythia 8, an additional jet can be generated, creating two event from a single underlying theoretical contribution. The removal of these overlapping events is carried out by a method known as FXFX merging [108]. This algorithm tracks the heritage of final state jets, in order to determine whether it was created as part of the matrix element or later during the parton shower. Due to the higher accuracy of modeling the kinematics of partons calculated in the matrix element stage, the algorithm removes events where additional jets are created in the parton shower, ensuring that the underlying process with an additional final state jets are created at the matrix element level, utilizing the NLO QCD calculations in aMC@NLO.

The utilization of these event generation techniques to simulate  $t\bar{t}H$  and  $t\bar{t}+jets$  backgrounds will improve the kinematic modeling of these high-jet multiplicity processes. A dedicated  $t\bar{t} + b\bar{b}$  sample with a large number of events generated with this framework would improve the modelling of the irreducible background. Unfortunately, these event generation tools were only recently released and the computational time required to generate samples with the equivalent statistical power of those used in the previous analyses is prohibitive on the time scale of this dissertation. However, each of the following samples were created using the process described above with 500,000 events each:

- $t\bar{t} + 0, 1, \text{ and } 2$  additional jets

- $t\bar{t} + b\bar{b}$

- $t\bar{t}H + 0, \text{ and } 1$  additional jets

The number of events generated is not sufficient to create a control region to assess calibrations of jet energy,  $b$ -tag efficiency, or lepton identification and reconstruction efficiency. However, since all of these processes are generated in an identical framework, it is reasonable to assume that calibrations applied will be similar for each, and as such comparisons amongst the samples can still provide insight into how they can be used to improve the analysis. Figure 8.1 shows a comparison between the number of reconstructed jets and  $b$ -tagged jets that pass the selection used in the previous analysis, with a lowered  $p_T$  threshold of 25 GeV. As before, the jet multiplicity of  $t\bar{t}H$  has a much longer distribution than the  $t\bar{t} + jets$  backgrounds, making it very important that these high-multiplicity events are modeled with the highest precision available.

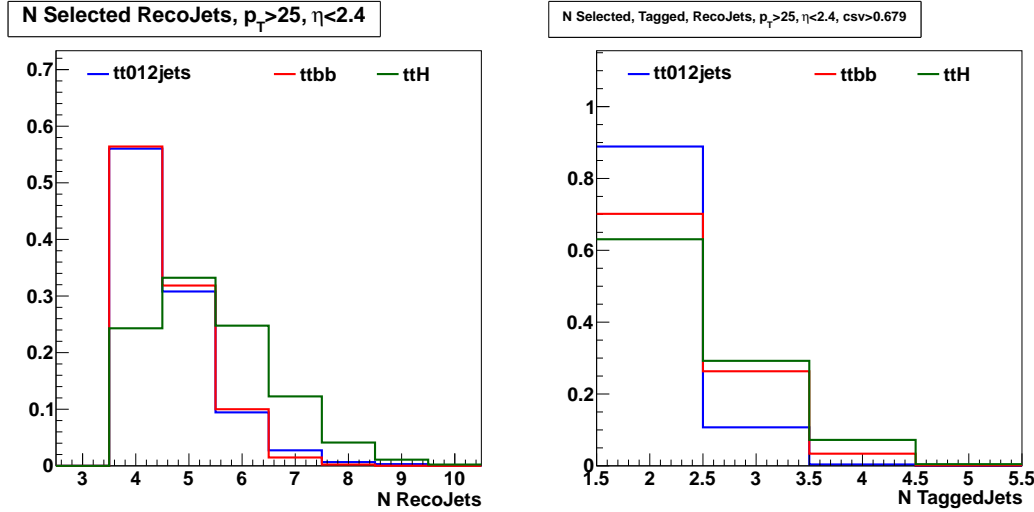


Figure 8.1: The number of reconstructed jets passing selection (left) and that have additionally been  $b$ -tagged (right) for  $t\bar{t}H$ ,  $t\bar{t} + jets$ , and  $t\bar{t} + b\bar{b}$  samples generated with the aMC@NLO and Pythia 8 framework

## 2774 8.2 Analysis Techniques Under Development

2775 One of the most difficult challenges of the  $t\bar{t}H$  final state is the combinatorics of possible  $b$ -jet  
 2776 candidates coming from the Higgs decay. The correct associate of jets to their roles in the decay  
 2777 of the top quarks would greatly reduce the number of jets as candidates for Higgs daughters.  
 2778 This is done, in some degree, in the analyses described in previous chapters via the "best Higgs  
 2779 mass" variable. This is a  $\chi^2$  minimization that relies only on the masses of the top quark,  $W$  and  
 2780 Higgs bosons in the event, to decide which jets are associated to the decays of which particles.  
 2781 These mass variable will be useful in identifying jets from the  $t\bar{t}$  system. Figure X shows the  
 2782 case for the  $W$  boson mass evaluated for jets which have been correctly associated to the MC  
 2783 truth generated partons in blue, and for the incorrect associations in green.

2784 The implementation of Madspin in the aMC@NLO framework allows for the highest precision  
 2785 on the spin correlations of the decay products from the  $t\bar{t}H$  and  $t\bar{t}$  systems. The angular  
 2786 relationships among the decay products provide additional discrimination power for the correct  
 2787 association of jets to their roles in the  $t\bar{t}H$  and  $t\bar{t}$  systems. The spin correlations of the decay  
 2788 products are enhanced by boosting to a reference frame that is more sensitive to differences in  
 2789 the angles between the correctly and incorrectly associated objects in the event. The reference  
 2790 frame of choice is formed by first identifying all of the potential candidates of the semi-leptonic  
 2791  $t\bar{t}$  decay:

- 2792 •  $\bar{b}$ -quark coming from the  $t$ -quark
- 2793 •  $b$ -quark coming from  $\bar{t}$ -quark
- 2794 • up-type quark from hadronic  $W$  boson decay

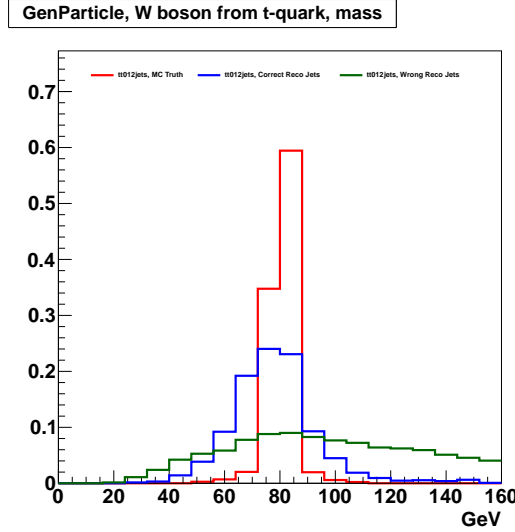


Figure 8.2: The invariant mass of the  $W$  boson in the  $t\bar{t}$  decay for the case of the MC truth (red), correctly associated reconstructed jets (blue), and incorrectly associated reconstructed jets (green)

- 2795 • down-type quark from the hadronic  $W$  boson decay

2796 The four-vector of the entire  $t\bar{t}$  system can be formed, and the hadronic candidates are  
 2797 boosted to a frame where the  $t\bar{t}$  system itself is at rest. Then, the  $t$ -quark, and its daughters  
 2798 are boosted to a frame such that the  $t$ -quark is at rest. Finally, the  $\bar{t}$ -quark, and its daughters  
 2799 are boosted to a frame such that the  $\bar{t}$ -quark is at rest. Then the angles between their decay  
 2800 products is evaluated. Typically, these studies are performed in the di-lepton channel since the  
 2801 angular resolution is much better in leptons than in jets. Figure 8.3 shows the cosine of the  
 2802 momentum 3-vector between the  $b$ -quarks from  $t$  and  $\bar{t}$ , the lepton and the up-type  $W$ -boson  
 2803 daughter, and the lepton and the down-type  $W$ -boson daughter.

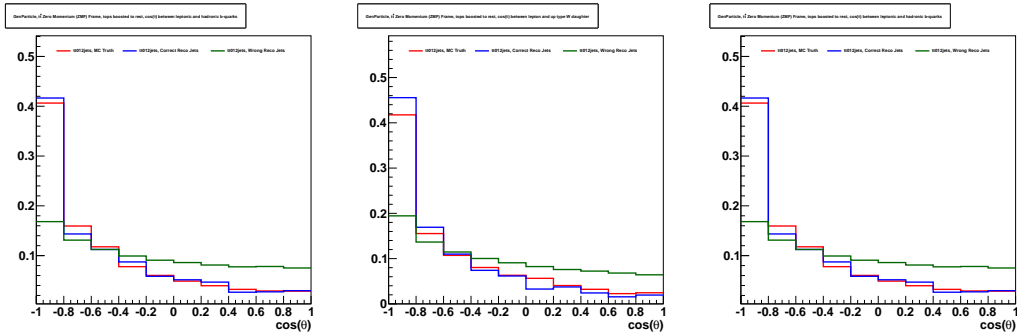


Figure 8.3: The cosine of the angle between the momentum three-vectors for the  $b$ -quarks from the top decays (left), the lepton and the up-type  $W$  boson daughter (center), and the lepton and the down-type  $W$  boson daughter (right)

- 2804 All three distributions have peaking values that provide discrimination between the jets correctly  
 2805 associated to the MC truth generator-level partons of the  $t\bar{t}$  decay, and the jets which are  
 2806 incorrectly associated. In each plot, the green represents the incorrect associations, while the

blue represents the correct associations, and the red represents the MC truth from the generated parton. An additional angle of interest is the difference in the  $\phi$  coordinate between daughters of the  $t\bar{t}$  decay. Figure 8.4 shows the distributions for the  $\Delta\phi$  between the  $b$ -quarks from the top decays, the lepton and up-type  $W$ -boson daughter, and the lepton and the down-type  $W$ -boson daughter. The case of the correctly associated jets has two sharp peaks near  $\phi = \pm 2$ , where the distribution is more uniform for incorrectly associated jets.

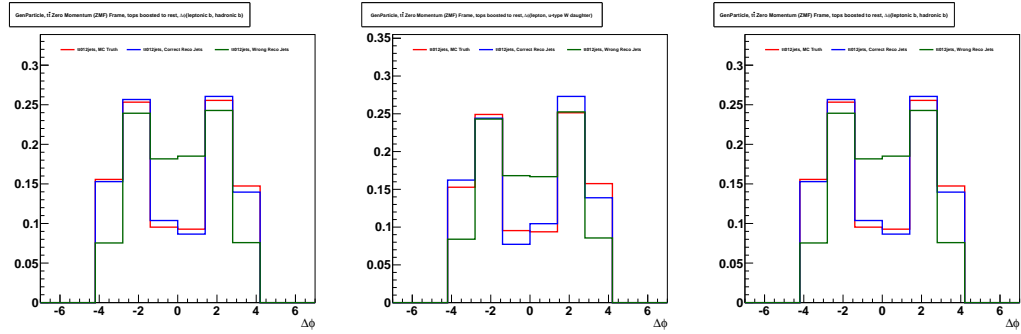


Figure 8.4: The difference in the  $\phi$  coordinate between the momentum three-vectors for the  $b$ -quarks from the top decays (left), the lepton and the up-type  $W$  boson daughter (center), and the lepton and the down-type  $W$  boson daughter (right)

A final variable of interest for jet association would be the charge of lepton multiplied against the charge of the  $b$ -quark that is associated with the same top-quark. These two values, due to charge conservation, will always be negative when multiplied. The charge of the jet is calculated from a  $p_T$  weighted sum of the tracks contained in the cluster, where the curvature of each track tells the charge of the hadron creating the signature. Since there are many hadrons clustered together to form a jet, there is a large degradation on resolution of the charge of the jet, however for the peak of this distribution is negative for correctly associated jets, and positive for incorrect jets, as shown in figure 8.5.

A jet association algorithm can be formed by using an MVA technique to provide a discriminant for how likely a certain combination of jets from an event are correctly associated to their roles in the decay of the  $t\bar{t}$  system. A training sample of correctly and incorrectly associated jets can be trained using the following variables:

- Invariant Mass of the Hadronic  $W$  boson
- Invariant Mass of the Leptonic  $W$  boson
- Invariant Mass of the Hadronic top-quark
- Invariant Mass of the Leptonic top-quark
- $\cos\theta_{b,\bar{b}}$  in the frame where  $t\bar{t}$  system and  $t$ -quarks are at rest respectively

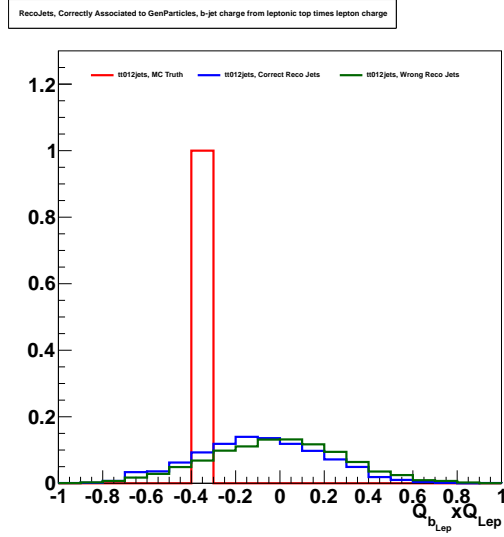


Figure 8.5: Jet times lepton charge, for the  $b$ -jet associated with the same top as the lepton. Green shows incorrectly associated reconstructed jets, blue shows correctly associated jets, and red is the MC truth

- $\cos \theta_{\text{lep}, \text{up-type}W\text{daughter}}$  in the frame where  $t\bar{t}$  system and  $t$ -quarks are at rest respectively

- $\cos \theta_{\text{lep}, \text{down-type}W\text{daughter}}$  in the frame where  $t\bar{t}$  system and  $t$ -quarks are at rest respectively

- $\Delta\phi(\theta_{b,\bar{b}})$  in the frame where  $t\bar{t}$  system and  $t$ -quarks are at rest respectively

- $\Delta\phi(\theta_{\text{lep}, \text{up-type}W\text{daughter}})$  in the frame where  $t\bar{t}$  system and  $t$ -quarks are at rest respectively

- $\Delta\phi(\theta_{\text{lep}, \text{down-type}W\text{daughter}})$  in the frame where  $t\bar{t}$  system and  $t$ -quarks are at rest respectively

- The product of the lepton and  $b$ -quark associated with the same  $t$ -quark

An additional improvement to the analysis will rely on a dedicated MVA for each of the

$t\bar{t} + X$  backgrounds, where  $X$  is light flavor, single  $c$ ,  $c\bar{c}$ , single  $b$ , and  $b\bar{b}$ . A dedicated  $t\bar{t} + b\bar{b}$  and even a  $t\bar{t} + c\bar{c}$  sample with sufficiently large enough events to train an MVA would be ideal. The discriminants from each of the backgrounds would be combined as input variables to a second MVA, in order to produce a discriminant for how likely the event is from a  $t\bar{t}H$  decay.

# 2844 Bibliography

- 2845 [1] “LHC Aerial View”.
- 2846 URL <http://www.coepp.org.au/files/coepp/images/cern-aerial2.jpg>.
- 2847 [2] CMS Collaboration, “Observation of a new boson at a mass of 125 GeV with the CMS  
2848 experiment at the LHC”, *Phys.Lett.B* (2012) [arXiv:1207.7235](https://arxiv.org/abs/1207.7235).
- 2849 [3] ATLAS Collaboration, “Observation of a new particle in the search for the Standard  
2850 Model Higgs boson with the ATLAS detector at the LHC”, *Phys.Lett.B* (2012)  
2851 [arXiv:1207.7214](https://arxiv.org/abs/1207.7214).
- 2852 [4] M. E. Peskin and D. V. Schroeder, “An Introduction to Quantum Field Theory”.  
2853 Westview Press, URL <http://www.westviewpress.com>, 1995.
- 2854 [5] K. G. Wilson, “Renormalization Group and Critical Phenomena. I. Renormalization  
2855 Group and the Kadanoff Scaling Picture”, *Phys. Rev. B* **4** (Nov, 1971) 3174–3183,  
2856 doi:[10.1103/PhysRevB.4.3174](https://doi.org/10.1103/PhysRevB.4.3174).
- 2857 [6] K. G. Wilson, “Renormalization Group and Critical Phenomena. II. Phase-Space Cell  
2858 Analysis of Critical Behavior”, *Phys. Rev. B* **4** (Nov, 1971) 3184–3205,  
2859 doi:[10.1103/PhysRevB.4.3184](https://doi.org/10.1103/PhysRevB.4.3184).
- 2860 [7] S. Bethke, “The 2009 World Average of alpha(s)”, *Eur.Phys.J. C***64** (2009) 689–703,  
2861 doi:[10.1140/epjc/s10052-009-1173-1](https://doi.org/10.1140/epjc/s10052-009-1173-1), [arXiv:0908.1135](https://arxiv.org/abs/0908.1135).
- 2862 [8] H. Weyl, “The theory of groups and quantum mechanics”. Dover Press,  
2863 URL <https://ia700807.us.archive.org/20/items/>  
2864 ost-chemistry-quantumtheoryofa029235mbp/quantumtheoryofa029235mbp.pdf,  
2865 1930.
- 2866 [9] C. N. Yang and R. L. Mills, “Conservation of Isotopic Spin and Isotopic Gauge  
2867 Invariance”, *Phys. Rev.* **96** (Oct, 1954) 191–195, doi:[10.1103/PhysRev.96.191](https://doi.org/10.1103/PhysRev.96.191).

- [10] M. Gell-Mann, “A Schematic Model of Baryons and Mesons”, *Phys.Lett.* **8** (1964) 214–215, doi:10.1016/S0031-9163(64)92001-3.
- [11] G. Zweig, “An SU<sub>3</sub> model for strong interaction symmetry and its breaking; Version 1”, Technical Report CERN-TH-401, CERN, Geneva, Jan, 1964.
- [12] G. Zweig, “An SU<sub>3</sub> model for strong interaction symmetry and its breaking; Version 2”,.
- [13] O. W. Greenberg, “Spin and Unitary-Spin Independence in a Paraquark Model of Baryons and Mesons”, *Phys. Rev. Lett.* **13** (Nov, 1964) 598–602, doi:10.1103/PhysRevLett.13.598.
- [14] P. Higgs, “Broken symmetries, massless particles and gauge fields”, *Physics Letters* **12** (1964), no. 2, 132 – 133, doi:[http://dx.doi.org/10.1016/0031-9163\(64\)91136-9](http://dx.doi.org/10.1016/0031-9163(64)91136-9).
- [15] S. Weinberg, “A Model of Leptons”, *Phys. Rev. Lett.* **19** (Nov, 1967) 1264–1266, doi:10.1103/PhysRevLett.19.1264.
- [16] S. L. Glashow, “Partial-symmetries of weak interactions”, *Nuclear Physics* **22** (1961), no. 4, 579 – 588, doi:[http://dx.doi.org/10.1016/0029-5582\(61\)90469-2](http://dx.doi.org/10.1016/0029-5582(61)90469-2).
- [17] A. Salam and J. Ward, “Electromagnetic and weak interactions”, *Physics Letters* **13** (1964), no. 2, 168 – 171, doi:[http://dx.doi.org/10.1016/0031-9163\(64\)90711-5](http://dx.doi.org/10.1016/0031-9163(64)90711-5).
- [18] Nobelprize.org, “The Nobel Prize in Physics 1957”. URL [http://www.nobelprize.org/nobel\\_prizes/physics/laureates/1957/](http://www.nobelprize.org/nobel_prizes/physics/laureates/1957/).
- [19] N. Cabibbo, “Unitary Symmetry and Leptonic Decays”, *Phys. Rev. Lett.* **10** (Jun, 1963) 531–533, doi:10.1103/PhysRevLett.10.531.
- [20] M. Kobayashi and T. Maskawa, “CP Violation in the Renormalizable Theory of Weak Interaction”, *Prog.Theor.Phys.* **49** (1973) 652–657, doi:10.1143/PTP.49.652.
- [21] G. Arnison et al., “Experimental observation of isolated large transverse energy electrons with associated missing energy at s=540 GeV”, *Physics Letters B* **122** (1983), no. 1, 103 – 116, doi:[http://dx.doi.org/10.1016/0370-2693\(83\)91177-2](http://dx.doi.org/10.1016/0370-2693(83)91177-2).
- [22] G. Arnison et al., “Experimental observation of lepton pairs of invariant mass around 95 GeV/c<sup>2</sup> at the {CERN} {SPS} collider”, *Physics Letters B* **126** (1983), no. 5, 398 – 410, doi:[http://dx.doi.org/10.1016/0370-2693\(83\)90188-0](http://dx.doi.org/10.1016/0370-2693(83)90188-0).
- [23] M. Banner et al., “Observation of single isolated electrons of high transverse momentum in events with missing transverse energy at the {CERN} pp collider”, *Physics Letters B*

- 2898       **122** (1983), no. 56, 476 – 485,  
 2899       doi:[http://dx.doi.org/10.1016/0370-2693\(83\)91605-2](http://dx.doi.org/10.1016/0370-2693(83)91605-2).
- 2900       [24] P. Bagnaia et al., “Evidence for Z0e+e at the {CERN} pp collider”, *Physics Letters B*  
 2901       **129** (1983), no. 12, 130 – 140,  
 2902       doi:[http://dx.doi.org/10.1016/0370-2693\(83\)90744-X](http://dx.doi.org/10.1016/0370-2693(83)90744-X).
- 2903       [25] The ALEPH, DELPHI, L3, OPAL, SLD Collaborations, the LEP Electroweak Working  
 2904       Group, the SLD Electroweak and Heavy Flavour Groups, “Precision Electroweak  
 2905       Measurements on the Z Resonance”, *Phys. Rept.* **427** (2006) 257,  
 2906       [arXiv:hep-ex/0509008](https://arxiv.org/abs/hep-ex/0509008).
- 2907       [26] The ALEPH, DELPHI, L3, OPAL Collaborations, the LEP Electroweak Working Group,  
 2908       “Electroweak Measurements in Electron-Positron Collisions at W-Boson-Pair Energies at  
 2909       LEP”, *Phys. Rept.* **532** (2013) 119, [arXiv:1302.3415](https://arxiv.org/abs/1302.3415).
- 2910       [27] F. Abe et al., “Observation of Top Quark Production in  $\bar{p}p$  Collisions with the Collider  
 2911       Detector at Fermilab”, *Phys. Rev. Lett.* **74** (Apr, 1995) 2626–2631,  
 2912       doi:[10.1103/PhysRevLett.74.2626](https://doi.org/10.1103/PhysRevLett.74.2626).
- 2913       [28] S. Abachi et al., “Search for High Mass Top Quark Production in  $p\bar{p}$  Collisions at  $\sqrt{s} =$   
 2914       1.8 TeV”, *Phys. Rev. Lett.* **74** (Mar, 1995) 2422–2426,  
 2915       doi:[10.1103/PhysRevLett.74.2422](https://doi.org/10.1103/PhysRevLett.74.2422).
- 2916       [29] LHC Higgs Cross Section Working Group Collaboration, “Handbook of LHC Higgs Cross  
 2917       Sections: 3. Higgs Properties”, doi:[10.5170/CERN-2013-004](https://doi.org/10.5170/CERN-2013-004), [arXiv:1307.1347](https://arxiv.org/abs/1307.1347).
- 2918       [30] W. Beenakker et al., “Higgs radiation off top quarks at the Tevatron and the LHC”,  
 2919       *Phys.Rev.Lett.* **87** (2001) 201805, doi:[10.1103/PhysRevLett.87.201805](https://doi.org/10.1103/PhysRevLett.87.201805),  
 2920       [arXiv:hep-ph/0107081](https://arxiv.org/abs/hep-ph/0107081).
- 2921       [31] W. Beenakker et al., “NLO QCD corrections to t anti-t H production in hadron  
 2922       collisions”, *Nucl.Phys.* **B653** (2003) 151–203, doi:[10.1016/S0550-3213\(03\)00044-0](https://doi.org/10.1016/S0550-3213(03)00044-0),  
 2923       [arXiv:hep-ph/0211352](https://arxiv.org/abs/hep-ph/0211352).
- 2924       [32] R. Frederix et al., “Scalar and pseudoscalar Higgs production in association with a  
 2925       top-antitop pair”, *Phys.Lett.* **B701** (2011) 427–433,  
 2926       doi:[10.1016/j.physletb.2011.06.012](https://doi.org/10.1016/j.physletb.2011.06.012), [arXiv:1104.5613](https://arxiv.org/abs/1104.5613).
- 2927       [33] M. Garzelli, A. Kardos, C. Papadopoulos, and Z. Trocsanyi, “Standard Model Higgs  
 2928       boson production in association with a top anti-top pair at NLO with parton showering”,

- 2929 [34] S. Dawson, L. Orr, L. Reina, and D. Wackerlo, “Associated top quark Higgs boson  
2930 production at the LHC”, *Phys.Rev.* **D67** (2003) 071503,  
2931 [doi:10.1103/PhysRevD.67.071503](https://doi.org/10.1103/PhysRevD.67.071503), [arXiv:hep-ph/0211438](https://arxiv.org/abs/hep-ph/0211438).
- 2934 [35] T. Gleisberg et al., “Event generation with SHERPA 1.1”, *JHEP* **0902** (2009) 007,  
2935 [doi:10.1088/1126-6708/2009/02/007](https://doi.org/10.1088/1126-6708/2009/02/007), [arXiv:0811.4622](https://arxiv.org/abs/0811.4622).
- 2936 [36] P. Artoisenet, R. Frederix, O. Mattelaer, and R. Rietkerk, “Automatic spin-entangled  
2937 decays of heavy resonances in Monte Carlo simulations”, *JHEP* **1303** (2013) 015,  
2938 [doi:10.1007/JHEP03\(2013\)015](https://doi.org/10.1007/JHEP03(2013)015), [arXiv:1212.3460](https://arxiv.org/abs/1212.3460).
- 2939 [37] F. Cascioli, P. Maierhofer, and S. Pozzorini, “Scattering Amplitudes with Open Loops”,  
2940 *Phys.Rev.Lett.* **108** (2012) 111601, [doi:10.1103/PhysRevLett.108.111601](https://doi.org/10.1103/PhysRevLett.108.111601),  
2941 [arXiv:1111.5206](https://arxiv.org/abs/1111.5206).
- 2942 [38] F. Krauss, R. Kuhn, and G. Soff, “AMEGIC++ 1.0: A Matrix element generator in  
2943 C++”, *JHEP* **0202** (2002) 044, [doi:10.1088/1126-6708/2002/02/044](https://doi.org/10.1088/1126-6708/2002/02/044),  
2944 [arXiv:hep-ph/0109036](https://arxiv.org/abs/hep-ph/0109036).
- 2945 [39] T. Gleisberg and F. Krauss, “Automating dipole subtraction for QCD NLO  
2946 calculations”, *Eur.Phys.J.* **C53** (2008) 501–523,  
2947 [doi:10.1140/epjc/s10052-007-0495-0](https://doi.org/10.1140/epjc/s10052-007-0495-0), [arXiv:0709.2881](https://arxiv.org/abs/0709.2881).
- 2948 [40] Planck Collaboration, “Planck 2013 results. I. Overview of products and scientific  
2949 results”, *Astron.Astrophys.* **571** (2014) A1, [doi:10.1051/0004-6361/201321529](https://doi.org/10.1051/0004-6361/201321529),  
2950 [arXiv:1303.5062](https://arxiv.org/abs/1303.5062).
- 2951 [41] V. Rubin, N. Thonnard, and J. Ford, W.K., “Rotational properties of 21 SC galaxies  
2952 with a large range of luminosities and radii, from NGC 4605 /R = 4kpc/ to UGC 2885  
2953 /R = 122 kpc/”, *Astrophys.J.* **238** (1980) 471, [doi:10.1086/158003](https://doi.org/10.1086/158003).
- 2954 [42] Super-Kamiokande Collaboration Collaboration, “Measurements of the solar neutrino  
2955 flux from Super-Kamiokande’s first 300 days”, *Phys.Rev.Lett.* **81** (1998) 1158–1162,  
2956 [doi:10.1103/PhysRevLett.81.1158](https://doi.org/10.1103/PhysRevLett.81.1158), [arXiv:hep-ex/9805021](https://arxiv.org/abs/hep-ex/9805021).
- 2957 [43] KamLAND Collaboration Collaboration, “Measurement of neutrino oscillation with  
2958 KamLAND: Evidence of spectral distortion”, *Phys.Rev.Lett.* **94** (2005) 081801,  
2959 [doi:10.1103/PhysRevLett.94.081801](https://doi.org/10.1103/PhysRevLett.94.081801), [arXiv:hep-ex/0406035](https://arxiv.org/abs/hep-ex/0406035).

- [44] MINOS Collaboration Collaboration, “Observation of muon neutrino disappearance with the MINOS detectors and the NuMI neutrino beam”, *Phys.Rev.Lett.* **97** (2006) 191801, doi:10.1103/PhysRevLett.97.191801, arXiv:hep-ex/0607088.
- [45] S. P. Martin, “A Supersymmetry primer”, *Adv.Ser.Direct.High Energy Phys.* **21** (2010) 1–153, doi:10.1142/9789814307505\_0001, arXiv:hep-ph/9709356.
- [46] J. Aguilar-Saavedra, R. Benbrik, S. Heinemeyer, and M. Prez-Victoria, “Handbook of vectorlike quarks: Mixing and single production”, *Phys.Rev.* **D88** (2013), no. 9, 094010, doi:10.1103/PhysRevD.88.094010, arXiv:1306.0572.
- [47] G. Burdman, M. Perelstein, and A. Pierce, “Large Hadron Collider tests of a little Higgs model”, *Phys.Rev.Lett.* **90** (2003) 241802, doi:10.1103/PhysRevLett.90.241802, arXiv:hep-ph/0212228.
- [48] M. Perelstein, M. E. Peskin, and A. Pierce, “Top quarks and electroweak symmetry breaking in little Higgs models”, *Phys.Rev.* **D69** (2004) 075002, doi:10.1103/PhysRevD.69.075002, arXiv:hep-ph/0310039.
- [49] H.-C. Cheng, I. Low, and L.-T. Wang, “Top partners in little Higgs theories with  $T$  parity”, *Phys. Rev. D* **74** (Sep, 2006) 055001, doi:10.1103/PhysRevD.74.055001.
- [50] H.-C. Cheng, B. A. Dobrescu, and C. T. Hill, “Electroweak symmetry breaking and extra dimensions”, *Nucl.Phys.* **B589** (2000) 249–268, doi:10.1016/S0550-3213(00)00401-6, arXiv:hep-ph/9912343.
- [51] M. S. Carena, E. Ponton, J. Santiago, and C. E. Wagner, “Light Kaluza Klein States in Randall-Sundrum Models with Custodial SU(2)”, *Nucl.Phys.* **B759** (2006) 202–227, doi:10.1016/j.nuclphysb.2006.10.012, arXiv:hep-ph/0607106.
- [52] C. T. Hill, “Topcolor: Top quark condensation in a gauge extension of the standard model”, *Phys.Lett.* **B266** (1991) 419–424, doi:10.1016/0370-2693(91)91061-Y.
- [53] R. Contino, L. Da Rold, and A. Pomarol, “Light custodians in natural composite Higgs models”, *Phys.Rev.* **D75** (2007) 055014, doi:10.1103/PhysRevD.75.055014, arXiv:hep-ph/0612048.
- [54] L. Evans and P. Bryant, “LHC Machine”, *JINST* **3** (2008) S08001, doi:10.1088/1748-0221/3/08/S08001.
- [55] M. Benedikt et al., “LHC Design Report Vol3 - The Injection Chain”. CERN, Geneva, 2004.

- 2991 [56] C. Hill et al., “Tests of the CERN proton linac performance for LHC - type beams”,  
 2992 *eConf* **C000821** (2000) TUD17, [arXiv:physics/0008102](https://arxiv.org/abs/physics/0008102).
- 2993 [57] K. S. Klaus Hanke, and Michel Chanel.
- 2994 [58] “Image, CERN PSbooster Layout”.  
 2995 URL <http://psb-machine.web.cern.ch/psb-machine/>.
- 2996 [59] S. Baird, “Accelerators for pedestrians; rev. version”, Technical Report  
 2997 AB-Note-2007-014. CERN-AB-Note-2007-014. PS-OP-Note-95-17-Rev-2.  
 2998 CERN-PS-OP-Note-95-17-Rev-2, CERN, Geneva, Feb, 2007.
- 2999 [60] “CERN Website, Super Proton Synchrotron”.  
 3000 URL <http://home.web.cern.ch/about/accelerators/super-proton-synchrotron>.
- 3001 [61] G. Dme, “The SPS acceleration system travelling wave drift-tube structure for the  
 3002 CERN SPS”,.
- 3003 [62] O. S. Brning et al., “LHC Design Report Vol1 - The Main Ring”. CERN, Geneva, 2004.
- 3004 [63] “CERN, List of All LHC Magnets”. URL [http://lhc-machine-outreach.web.cern.ch/lhc-machine-outreach/components/magnets/types\\_of\\_magnets.htm](http://lhc-machine-outreach.web.cern.ch/lhc-machine-outreach/components/magnets/types_of_magnets.htm).
- 3005 [64] M. Barnes, J. Borburgh, B. Goddard, and M. Hourican, “Injection and extraction  
 3006 magnets: septa”, [arXiv:1103.1062](https://arxiv.org/abs/1103.1062).
- 3007 [65] M. Barnes et al., “Injection and extraction magnets: Kicker magnets”,  
 3008 [arXiv:1103.1583](https://arxiv.org/abs/1103.1583).
- 3009 [66] “Outreach, CERN LHC, Cryogenic System”. URL <http://home.web.cern.ch/about/engineering/cryogenics-low-temperatures-high-performance>.
- 3010 [67] “The challenge of keeping cool”,.
- 3011 [68] P. Lebrun, “Large Cryogenic Helium Refrigeration System for the LHC”, Technical  
 3012 Report LHC-Project-Report-629. CERN-LHC-Project-Report-629, CERN, Geneva, Feb,  
 3013 2003. revised version number 1 submitted on 2003-02-19 11:44:11.
- 3014 [69] “Outreach, CERN LHC, Vacuum System”. URL <http://home.web.cern.ch/about/engineering/vacuum-empty-interplanetary-space>.
- 3015 [70] CMS Collaboration Collaboration, “Particle-Flow Event Reconstruction in CMS and  
 3016 Performance for Jets, Taus, and MET”, Technical Report CMS-PAS-PFT-09-001,  
 3017 CERN, 2009. Geneva, Apr, 2009.

- 3021 [71] CMS Collaboration, “Description and performance of track and primary-vertex  
 3022 reconstruction with the CMS tracker”, *JINST* **9** (2014), no. 10, P10009,  
 3023 [doi:10.1088/1748-0221/9/10/P10009](https://doi.org/10.1088/1748-0221/9/10/P10009), [arXiv:1405.6569](https://arxiv.org/abs/1405.6569).
- 3024 [72] R. Fruhwirth, “Application of Kalman filtering to track and vertex fitting”,  
 3025 *Nucl.Instrum.Meth.* **A262** (1987) 444–450, [doi:10.1016/0168-9002\(87\)90887-4](https://doi.org/10.1016/0168-9002(87)90887-4).
- 3026 [73] CMS Electromagnetic Calorimeter Group Collaboration, “Intercalibration of the barrel  
 3027 electromagnetic calorimeter of the CMS experiment at start-up”, *JINST* **3** (2008)  
 3028 P10007, [doi:10.1088/1748-0221/3/10/P10007](https://doi.org/10.1088/1748-0221/3/10/P10007).
- 3029 [74] K. Cankocak, Y. Onel, P. de Barbaro, and D. Vishnevskiy, “CMS HCAL Installation and  
 3030 Commissioning”, Technical Report CMS-CR-2008-047, CERN, Geneva, Jul, 2008.
- 3031 [75] CMS Collaboration Collaboration, “Commissioning of the CMS ECAL calibration with  
 3032 muons from cosmic rays and beam dumps”, Technical Report CMS-CR-2009-339, CERN,  
 3033 Geneva, Nov, 2009.
- 3034 [76] CMS Collaboration Collaboration, “Performance of the CMS Hadron Calorimeter with  
 3035 Cosmic Ray Muons and LHC Beam Data”, *J. Instrum.* **5** (Nov, 2009) T03012 . 35 p.
- 3036 [77] CMS Collaboration Collaboration, “HCAL performance from first collisions data”,.
- 3037 [78] CMS Collaboration Collaboration, “Particle-flow commissioning with muons and  
 3038 electrons from J/Psi and W events at 7 TeV”, Technical Report CMS-PAS-PFT-10-003,  
 3039 CERN, 2010. Geneva, 2010.
- 3040 [79] W. Adam, R. Frhwirth, A. Strandlie, and T. Todor, “Reconstruction of Electrons with  
 3041 the Gaussian-Sum Filter in the CMS Tracker at the LHC”,.
- 3042 [80] M. Cacciari, G. P. Salam, and G. Soyez, “The Anti-k(t) jet clustering algorithm”, *JHEP*  
 3043 **0804** (2008) 063, [doi:10.1088/1126-6708/2008/04/063](https://doi.org/10.1088/1126-6708/2008/04/063), [arXiv:0802.1189](https://arxiv.org/abs/0802.1189).
- 3044 [81] CMS Collaboration Collaboration, “Commissioning of the Particle-Flow reconstruction  
 3045 in Minimum-Bias and Jet Events from pp Collisions at 7 TeV”, Technical Report  
 3046 CMS-PAS-PFT-10-002, CERN, Geneva, 2010.
- 3047 [82] Particle Data Group Collaboration, “Review of Particle Physics”, *Chin.Phys.* **C38**  
 3048 (2014) 090001, [doi:10.1088/1674-1137/38/9/090001](https://doi.org/10.1088/1674-1137/38/9/090001).
- 3049 [83] “MET Optional Filters”.  
 3050 <https://twiki.cern.ch/twiki/bin/view/CMS/MissingETOptionalFilters>.

- [84] CMS Collaboration, “Jet Energy Resolution in CMS at  $\sqrt{s}=7$  TeV”,.
- [85] C. Weiser, “A Combined Secondary Vertex Based B-Tagging Algorithm in CMS”,  
Technical Report CMS-NOTE-2006-014, CERN, Geneva, Jan, 2006.
- [86] “Operating Points for  $b$ -Tag Algorithms”.  
<https://twiki.cern.ch/twiki/bin/viewauth/CMS/BTagPerformanceOP>.
- [87] “ $b$ -Jet Identification in the CMS Experiment”,.
- [88] VHbb Team, “Search for the SM Higgs Boson Produced in Association with W or Z and Decaying to Bottom Quarks (ICHEP 2012)”, CMS Note 2012/181, 2012.
- [89] A. Hocker et al., “TMVA - Toolkit for Multivariate Data Analysis”, *PoS ACAT* (2007) 040, [arXiv:physics/0703039](https://arxiv.org/abs/physics/0703039).
- [90] J. D. Bjorken and S. J. Brodsky, “Statistical Model for Electron-Positron Annihilation into Hadrons”, *Phys. Rev. D* **1** (1970) 1416, doi:10.1103/PhysRevD.1.1416.
- [91] G. C. Fox and S. Wolfram, “Event Shapes in  $e^+e^-$  Annihilation”, *Nucl. Phys. B* **149** (1979) 413, doi:10.1016/0550-3213(79)90003-8.
- [92] “Jet Energy Scale Uncertainties”. <https://twiki.cern.ch/twiki/bin/view/CMS/WorkBookJetEnergyCorrections>.
- [93] “Jet Energy Resolution Uncertainties”.  
<https://twiki.cern.ch/twiki/bin/view/CMS/JetResolution>.
- [94] “ $b$ -Tag Scale Factor Uncertainties”.  
<https://twiki.cern.ch/twiki/bin/viewauth/CMS/BtagPOG>.
- [95] T. Peiffer., “ $Q^2$  Systematic MC Samples re-weighting”. <https://indico.cern.ch/getFile.py/access?contribId=5&resId=0&materialId=slides&confId=177717>, 2012.
- [96] A. Bredenstein, A. Denner, S. Dittmaier, and S. Pozzorini, “NLO QCD corrections to top anti-top bottom anti-bottom production at the LHC: 2. full hadronic results”, (2010). [arXiv:1001.4006](https://arxiv.org/abs/1001.4006).
- [97] The ATLAS Collaboration, The CMS Collaboration, The LHC Higgs Combination Group Collaboration, “Procedure for the LHC Higgs boson search combination in Summer 2011”, Technical Report CMS-NOTE-2011-005. ATL-PHYS-PUB-2011-11, CERN, Geneva, Aug, 2011.

- 3080 [98] G. Cowan, K. Cranmer, E. Gross, and O. Vitells, “Asymptotic formulae for  
 3081 likelihood-based tests of new physics”, *Eur.Phys.J.* **C71** (2011) 1554,  
 3082 [doi:10.1140/epjc/s10052-011-1554-0](https://doi.org/10.1140/epjc/s10052-011-1554-0), [10.1140/epjc/s10052-013-2501-z](https://doi.org/10.1140/epjc/s10052-013-2501-z),  
 3083 [arXiv:1007.1727](https://arxiv.org/abs/1007.1727).
- 3084 [99] CMS Collaboration, “Search for the standard model Higgs boson produced in association  
 3085 with a top-quark pair in pp collisions at the LHC”, *JHEP* **1305** (2013) 145,  
 3086 [doi:10.1007/JHEP05\(2013\)145](https://doi.org/10.1007/JHEP05(2013)145), [arXiv:1303.0763](https://arxiv.org/abs/1303.0763).
- 3087 [100] CMS Collaboration, “Measurement of the differential top-quark pair production cross  
 3088 section in the dilepton channel in pp collisions at  $\sqrt{s} = 8$  TeV.”, CMS PAS TOP-12-028,  
 3089 2012.
- 3090 [101] CMS Collaboration, “Measurement of the differential top-quark pair production cross  
 3091 section in the lepton+jets channel in pp collisions at  $\sqrt{s} = 8$  TeV.”, CMS PAS  
 3092 TOP-12-027, 2012.
- 3093 [102] CMS Collaboration, “Calibration of the Combined Secondary Vertex b-Tagging  
 3094 discriminant using dileptonic ttbar and Drell-Yan events”, CMS Note 2013/130, 2013.
- 3095 [103] CMS Collaboration, “Dilepton trigger and lepton identification efficiencies for the top  
 3096 quark pair production cross section measurement at 8 TeV in the dilepton decay  
 3097 channel.”, CMS AN AN-12-389, 2012.
- 3098 [104] CMS Collaboration, “Search for the associated production of the Higgs boson with a  
 3099 top-quark pair”, *JHEP* **1409** (2014) 087,  
 3100 [doi:10.1007/JHEP09\(2014\)087](https://doi.org/10.1007/JHEP09(2014)087), [10.1007/JHEP10\(2014\)106](https://doi.org/10.1007/JHEP10(2014)106), [arXiv:1408.1682](https://arxiv.org/abs/1408.1682).
- 3101 [105] J. Alwall et al., “The automated computation of tree-level and next-to-leading order  
 3102 differential cross sections, and their matching to parton shower simulations”, *JHEP*  
 3103 **1407** (2014) 079, [doi:10.1007/JHEP07\(2014\)079](https://doi.org/10.1007/JHEP07(2014)079), [arXiv:1405.0301](https://arxiv.org/abs/1405.0301).
- 3104 [106] P. Artoisenet, R. Frederix, O. Mattelaer, and R. Rietkerk, “Automatic spin-entangled  
 3105 decays of heavy resonances in Monte Carlo simulations”, *JHEP* **1303** (2013) 015,  
 3106 [doi:10.1007/JHEP03\(2013\)015](https://doi.org/10.1007/JHEP03(2013)015), [arXiv:1212.3460](https://arxiv.org/abs/1212.3460).
- 3107 [107] T. Sjostrand, S. Mrenna, and P. Z. Skands, “A Brief Introduction to PYTHIA 8.1”,  
 3108 *Comput.Phys.Commun.* **178** (2008) 852–867, [doi:10.1016/j.cpc.2008.01.036](https://doi.org/10.1016/j.cpc.2008.01.036),  
 3109 [arXiv:0710.3820](https://arxiv.org/abs/0710.3820).
- 3110 [108] R. Frederix and S. Frixione, “Merging meets matching in MC@NLO”, *JHEP* **1212**  
 3111 (2012) 061, [doi:10.1007/JHEP12\(2012\)061](https://doi.org/10.1007/JHEP12(2012)061), [arXiv:1209.6215](https://arxiv.org/abs/1209.6215).

# <sup>3112</sup> List of Acronyms

<sup>3113</sup> **ATLAS** A Toroidal LHC Apparatus

<sup>3114</sup> **BSM** Beyond the Standard Model

<sup>3115</sup> **CERN** European Center for Nuclear Research

<sup>3116</sup> **CMS** Compact Muon Solenoid

<sup>3117</sup> **ECAL** Electromagnetic Calorimeter

<sup>3118</sup> **FSR** Final State Radiation

<sup>3119</sup> **HCAL** Hadronic Calorimeter

<sup>3120</sup> **ISR** Initial State Radiation

<sup>3121</sup> **JHEP** Journal of High Energy Physics

<sup>3122</sup> **LHC** Large Hadron Collider

<sup>3123</sup> **LO** Leading Order

<sup>3124</sup> **MVA** Multi-Variate Analysis

<sup>3125</sup> **NLO** Next to Leading Order

<sup>3126</sup> **QCD** Quantum Chromodynamics

<sup>3127</sup> **QED** Quantum Electrodynamics

<sup>3128</sup> **QFT** Quantum Field Theory

<sup>3129</sup> **SM** Standard Model